Influence of Shape of Solid Explosives on the Deformation of Circular Steel Plates-Experimental and Numerical Investigations

By

Salie Mahoi

UNIVERSITY OF CAPE TOWN

Thesis Presented for the Degree of

DOCTOR OF PHILOSOPHY

Department of Mechanical Engineering
University of Cape Town
February 2006

Contents

List of Figures

List of Tables

DECLARATION

I Salie Mahoi, declare that this thesis is essentially my own work except where reference is made to acknowledge other contributors. I also declare that this work has not been submitted in this or any other form for a degree or examination in any other University.

Sign this .....day of 2006

Salie Mahoi.....

DEDICATION

This thesis is dedicated to the entire Mahoi family especially to my father who passed away on the 3rd of June 2005. May his soul rest in perfect peace.

ACKNOWLEDGEMENTS

The author wish to thank Professor G.N. Nurick for his relentless effort in supervising this research. I also want to acknowledge the contributions of Mr. G. Newins in the Department of Mechanical Engineering, who greatly assisted me in the preparation of the experimental specimens for the blast and tensile tests. Many thanks also go to the National Research Foundation (NRF) and the Blast Impact and Survivability Research Unit (BISRU) including Mr. V. Balden, Mr. Chung Kim Yuen, Mr. Matt Theobald and Mr. Bonachis, for the financial and technical support of this research. I will also take this opportunity to thank the entire Mahoi family for their undivided support both financially and morally. Lastly, I will like to specifically thank my mother Mrs. Mary Mahoi, my wife Hawanatu Mahoi, my daughter Zwaibatu Mahoi and my friends including Sheku Kanu, Ibrahim Kamara, Dr. Sheikh Sesay, Jean-Marc Lucamba, Dr. Alhaji Bah, Mr. Ibrahim Bah, John Kabia, the Mthegha, Lavali, Gbondo-Tugbawa families, all of whom gave me their love and support throughout my studies.

NOMENCLATURE

Chapter 1

CY - Cylinder explosive

TC - Truncated-Cone explosive

ITC - Inverted-Truncated-Cone explosive

ALE - Abitrary Lagrange Elements

PE4 - Plastic Explosive (RDX/Wax)

JWL - Jones-Wilkins-Lee

EOS - Equation of State

ZND - Zeldovich-Neumann-Doering Model

Chapter 2

HMX - Cyclotetramethylenetetranitramine

RDX - Cyclotrimethylenetrinitramine

TNT - Trinitrotoluene

PETN - Pentaerithrytoltetranitrate

Teryl - 2,4,6-Trinitrophenylmethylnitramine

TATB - Triaminotrinitrobenzene

C-J - Chapman-Jouget state

$\mathbf{V_D}$ - Velocity of Detonation of Explosive

C - Characteristic Sound Speed of Explosive

U_P - Particle Velocity of Explosive

X_J - Reaction Zone Length

T_J - Reaction Zone Time

T_1 - Initial Time

P_1 - Pressure of the Reference Point

P_J - Pressure at the C-J state

σ, T, P, u_p - Stress, Temperature, Pressure and Particle Velocity in an Ideal Detonation

E_{CJ} - Energy of Explosive at the C-J state

E_0 - Initial Energy of Explosive

$E(V,S)$ - Specific Internal Energy of Explosive

$\nu, \gamma_\infty, m, \beta_j, \sigma^{\alpha j}, \alpha_j, \gamma_j$ - Parameters of the Williamburg Equation of State

$F\gamma, k, b, E_\nu^s$ - Parameters in the Equation of State for Detonation Products

A, B, ω, R_1, R_2 - JWL Equation of State Constants

D^*, a^* - Curve Fitting Constants

T_a - Time of Arrival of Shock Wave

T_d - Duration of blast load on structure

γ - 1.041

a - Sound Speed

$P_s(T)$ - Pressure With Time in a Triangular Blast Wave

P_s - Initial Pressure of a Blast Wave

$P_{ref\,max}$ - Maximum Reflected Pressure

I - Impulse per Unit Area of Blast

Z - Scaling Distance

W_{TNT} - Equivalent TNT Mass of Explosive

M_{exp} Mass of Explosive

τ, k - Duration and Decay Constant of a Blast Wave

Δh_f^0 - Heat of Formation of Explosion

ρ_0 - Initial Density of Explosive

MW - Molecular Weight

V_m - Terminal Velocity of Fragment From Gurney Equation

E_g - Specific Energy of Explosive in Gurney Equation

C, M - Mass of Explosive and Metal Case in Gurney Equation

CAX4R - Continuum Axi-symmetric 4-Noded Reduced Integraton Element

SAX1 - 2-Dimensional Axi-symmetric Elements

E - Young's Modulus of Steel

ε_{ln}^{pl} - Equivalent Plastic Strain

σ_{true} - True Stress

ε_{norm} - Nominal Strain

$\dot{\varepsilon}$ - Strain Rate

σ_0 - Stress at Zero Strain-Rate

ε^* - Equivalent Flow Strain

$\dot{\varepsilon}_0$ - Strain Rate $= 1.0s^{-1}$

C_p - Specific Heat

A, B, n, C, m - Johnson-Cook Constants

T - Temperature

T^* - Homogeneous temperature

T_{ref} - Reference temperature

T_{melt} - Melting temperature

$C_1, C_2, N, \alpha, T^{*M}$ - Parameters in the Modified Johnson-Cook Constitutive Equation

$C_1, C_2, C_3, C_4, C_5, N, \alpha$ - Parameters in the Revised Johnson-Cook Constitutive Equation

$C_1, C_2, C_3, C_4, C_5, n$ - Parameters in the Zerilli-Armstrong Constitutive Equation

σ' - Dynamic Flow Stress in the Cowper-Symonds Equation

σ_0 - Static Stress in the Cowper-Symonds Equation

D, q - Constants in the Cowper-Symonds Equation equal to $40.4s^{-1}$ and 5 Respectively

E, E_0 - Young's Moduli in the Masui Material Model

σ_0, σ_y - Static and Yield Stresses in the Masui Material Model

Chapter 3

σ_{true} - True Stress

σ_{nom} - Nominal Stress

σ_{eng} - Engineering Stress

ε_{nom} - Nominal Strain

ε_{Eng} - Engineering Strain

ε_{ln}^{pl} - Equivalent Plastic Strain

V_C - Cross Head Speed

Chapter 4

θ - Maximum diameter of explosive charge

M - Mass of explosive

CY-θ – M - Cylinder Explosive of Diameter Ranging from 18mm to 33mm and Mass Ranging from 2.6g to 5.9g respectively.

TC-θ – M - Truncated-Cone Explosive of Diameter Ranging from 18mm to 33mm and Mass Ranging from 2.6g to 5.9g respectively.

ITC-θ – M - Inverted-Truncated-Cone Explosive of Diameter ranging from 18mm to 33mm and Mass Ranging from 2.6g to 5.9g respectively.

θImp-Def-M - Impulse-Central Deformation for Diameters ranging from 18mm to 33mm and Mass Ranging from 2.6g to 5.9g respectively.

θ**CY** - Cylinder Explosive With Maximum Diameters of 18mm, 25mm and 33mm

θ**TC** - Truncated-Cone Explosive With Maximum Diameters of 18mm, 25mm and 33mm

θ**ITC** - Inverted Truncated-Cone Explosive With Maximum Diameters of 18mm, 25mm and 33mm

Chapter 5

$\mathbf{H_m}$ - Height of Mach Stem

$\mathbf{D_0}$ - Minimum Distance for a Mach Stem Formation

$\mathbf{H_b}$ - Height of Burst

$\mathbf{D_x}$ - Distance of Mach Stem Greater Than D_0

f - Critical Angle of Blast Wave

$\mathbf{M_x}$ - Mach Number

$\dot{\beta}$ - Degree of Chemical Reaction and

$\mathbf{H_e}$ - Height of explosive

I, G, r, x, y, z - Parameters in the Lee-Terva Equation of State

$f(p)$ - A Polynomial in Pressure Denoted Time Differentiation

$U, \dot{U}, \ddot{U}$ - Acceleration, Velocity and Displacement Vectors of a Finite Element Model

$\mathbf{F_I}(t)$,$\mathbf{F_D}(t)$,$\mathbf{F_E}(t)$ - Inertia Forces, Damping Forces and Elastic Forces

Δ_{stable} - Stable Time Increament

$\mathbf{L_e}$ - Length of Explosive Element

$\mathbf{C_d}$ - Detonation Wave Speed

M_{CY} - Effective Mass of Cylinder Explosive

M_{TC} - Effective Mass of Truncated-Cone Explosive

M_{ITC} - Effective Mass of Inverted Truncated-Cone Explosive

L - Length of Shock-wave Profile

t_d^{mp} - Time to detonation of a given material point

$\mathbf{X}^{mp}$ - Coordinates of the material point

$\mathbf{X}_d^N$ - Coordinate of the nth material point

t_d^N - Detonation delay time of the nth detonation point

$\mathbf{B}_s$ - Constant determining burn front width

- Burn fraction

Chapter 6

CYpress - Pressure distribution caused by CY Explosive

TCpress - Pressure distribution caused by TC Explosive

ITCpress - Pressure distribution caused by ITC Explosive

$\mathbf{V}_E$ - Initial Velocity of Shock-Wave After Detonation

$\mathbf{V}_R$ - Velocity of Detonation Particles at the Rear of an Explosion

BL - Bottom Line of Graph Showing Comparison of Experiment and Predicted Central Deformation

TL - Top Line of Graph Showing Comparison of Experiment and Predicted Central Deformation

Abstract

In recent years, explosive loads have received considerable attention from different events, accidentally or intentionally, over many structures around the world. The growing intensity of wars and terrorist attacks and the complexity of technological advancement to improve quality of life, also provide the need for a more detailed interpretation of the interaction of blast loads caused by explosives on structures. In addition, the risk of lives and property subjected to explosive loads, is also of great concern.

These issues have motivated researchers to extensively study the effect of blast loads on structures experimentally, analytically and numerically, for the past several decades in order to understand their effects. Two forms of loading conditions on structures have been studied, namely local and uniformly distributed loads. As regards localised loading on structures which is the focus of this research, Nurick and Radford [2] experimentally studied localised blast loads on circular plates by using small cylinder (CY) explosive charges in order to investigate the total deformation, burn diameter, inflection diameter, cap diameter and grain elongation of the plates. Charge diameters measuring 18mm, 25mm, 33mm and 40mm were centrally placed on top of a 12mm polystyrene foam pad in order to create a stand-off between the explosive and plate. The diameter of the loaded area and thickness of the plates are 100mm and 1.6mm respectively. The results range from Mode I (large inelastic deformation) to Mode II (capping at the central area).

Previous attempts to predict the effect of blast loading on structures have been carried out by many researchers using rectangular, triangular and other related loading conditions defined within a specified area on the plate's top surface. Although these previous attempts predicted the deformation reasonably well however, these conventional methods only consider the resulting blast load on the structure and not the shape and detonation point of the explosive charge. In order to take account of the shape (geometry) and material behaviour of the explosive charge on interaction with structures, Grobbelaar and Nurick [4] numerically modelled the experiments reported by Nurick and Radford [2]. The explosive pressure was modelled using the Jones-Wilkins-Lee (JWL) equation of state incorporated in the ABAQUS/Explicit 5.8 code. The spacial distribution of the explosive detonation products and their interaction with the plate were

investigated in order to understand the behaviour of the explosive. The central or midpoint deformation and profiles of the plate were investigated and compared reasonably well with those of the experiments as reported in Grobbelaar and Nurick [4].

However, these studies carried out by Nurick and Radford [2] and Grobbelaar and Nurick [4] and many other previous researchers focused on cylinder and sheet explosives and not other shapes of explosives. The effect of other shapes of explosives on interaction with a structure having the same masses have not been reported in the literature. The quest for a much wider understanding of the effect of other shapes of explosive on interaction with structures, forms the main objective of this current research. This current work is an extension of the research carried out by Nurick and Radford [2] and later numerically investigated by Grobbelaar and Nurick [4]. It is a three-part research in that it considers the influence of shapes of explosive on structures experimentally, theoretically and numerically. Cylinder explosives (CY), Truncated Cone explosive (TC) and Inverted Truncated cone (ITC) explosives are specifically investigated in this research.

A total of 33 experiments are carried out for the three different shapes of explosives, of varying masses detonated centrally above the test plates. The maximum diameters of the CY explosives are 18mm, 25mm and 33mm. For the TC and ITC explosives, the minimum diameters are 12.6mm, 17.5mm and 23.1mm with corresponding maximum diameters of 18mm, 25mm and 33mm. Also, the heights of the explosives range from 2.1mm to 14.7mm. A loaded area of diameter 100mm on the test plate is formed by two clamp plates measuring 200mm by 200mm, with central holes of diameter 100mm and thickness 20mm. Results of the central deformation range from Mode I (large inelastic deformation) to Mode IIc (capping at the central area) with the impulses ranging from 6.10Ns to 14.89Ns.

The mechanism of expansion of the detonation products based on the shape of the explosives is analytically and numerically investigated. In order to predict the various shock-wave profiles of the various shapes of explosives, it is assumed that the detonation front is circular and at the Chapman-Jouget (C-J) state (where the pressure and velocity remain unchanged during the process of detonation). A close correlation between the analytical and numerical predicted shock-wave profile is reported in this work. The numerical predictions of the plate deformation, are carried out using the ABAQUS/Explicit 6.4 and AUTODYN 6.0 hydrocodes. Non-linear geometric and material effects are considered in the numerical simulations for the plates using the Johnson-Cook constitutive equation. The explosive behaviour and loading on the structure is modelled using the Jones-Wilkins-Lee (JWL) equation of state. The explosive elements are modelled with Arbitrary-Lagrangian-Eulerian (ALE) mesh while those of the plates are modelled using Lagrangian mesh. Mesh sensitivity tests are carried out

for the explosive and plate in order to find a reasonble mesh size to predict the experiment. It is found that an initial mesh size of 0.4mm by 0.4mm and 0.4mm by 0.8mm used for the explosives in AUTODYN 6.0 and ABAQUS/Explicit 6.4 respectively predicted the experimental results reasonably well. For the plate, an initial element size of 0.4mm by 0.8mm is used in both codes.

In conclusion, it is generally found that the shape of an explosive influences the deformation of the plate and impulse measured by the pendulum. The TC explosive loaded plates show the highest central deformation, followed by the CY and ITC explosive loaded plates respectively. On the other hand, the ITC loaded plates generally show the highest impulse, followed by the CY and TC explosive loaded plates respectively. Furthermore, the results of the numerical predictions compare reasonably well with the experiments, as regards the central deformation and profile of the plates.

Chapter 1

Background to Study

1.1 Introduction

The study of the interaction of blast loads on structures has been carried out for many decades. This interaction on structures has been found to be very complex, and a better understanding of this process is essential. With regard to metal structures, this interaction may cause permanent deformation, which sometimes leads to undesired damage of the structure. Various modes of deformation of structures have been defined and reported in Menkes and Opat [1] and Nurick and Radford [2]. As defined by [1], the modes of failure of an aluminium beam subjected to impulsive loads are given as follows:

1. Mode I - large inelastic deformation
2. Mode II - tensile tearing at the support
3. Mode III - transverse tearing at the support

Nurick and Radford [2] and Nurick *et al* [3] further subdivided mode I and mode II deformations for circular plates as given in figure 1.1. Knowledge of the interaction of blast loads on structures can help to predict the effect and eventually lead to better designs in order to save lives. The search for answers regarding the influence of blast loads on structures is a growing research environment which has been going on for the past several decades.

Experimental, analytical and numerical research on localised and uniformly distributed blast loads on structures have been extensively studied. Previous

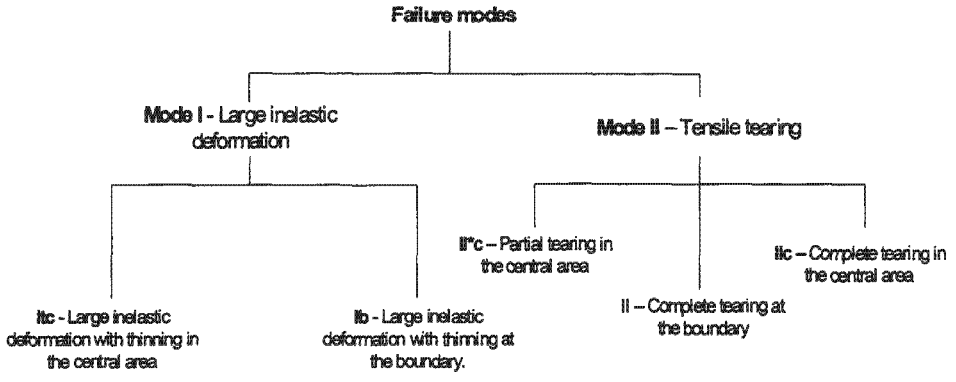

Figure 1.1: Figure showing subdivision of Mode I and Mode II failures for circular plates subjected to localised blast loading.

research reported in the literature did not consider the effect of TC (Truncated-Cone) and ITC (Inverted Truncated-Cone) explosives on interaction with structures. This research is therefore focused on the effect of TC and ITC explosives on interaction with a circular plate so as understand their effect. The experimental work in this research is an extension of previous research carried out experimentally by Nurick and Radford [2] and later numerically investigated by Grobbelaar and Nurick [4] in order to understand the spacial distribution and behaviour of explosives. With the exception of cylinder (CY) charges, experiments and simulations on small charges of Truncated-Cone (TC) and Inverted Truncated-Cone (ITC) explosive shapes are not reported in the literature and the author is unaware of any such work that has been carried out.

1.2 Objectives and Scope

In the past, most research work on explosive-structure interaction considered pressure loading on the surface of the structure, where the geometry of the explosive is not modelled as can be found in Chung Kim Yuen [5] and Bimha *et al* [6]. In order to realistically model the geometry of the explosive, Grobbelaar and Nurick [4] numerically modelled cylindrical (CY) explosives from experimental results reported in Nurick and Radford [2] incoporating the Jones-Wilkins-Lee (JWL) equation of state. The main objective of Grobbelaar and Nurick's work [4] was to model the blast loaded plates subjected to CY explosives of varying

mass using ABAQUS/Explicit 5.8 in which the geometry of the explosive was considered. Grobbelaar and Nurick [4] modelled cylinder-shaped (CY) explosives of a range of ratios of height-diameter shown in figure 1.2. In figure 1.2, the minimum ratio of explosive diameter to thickness represents a thin cylinder in diagram A and a maximum ratio represents a thicker explosive in diagram B.

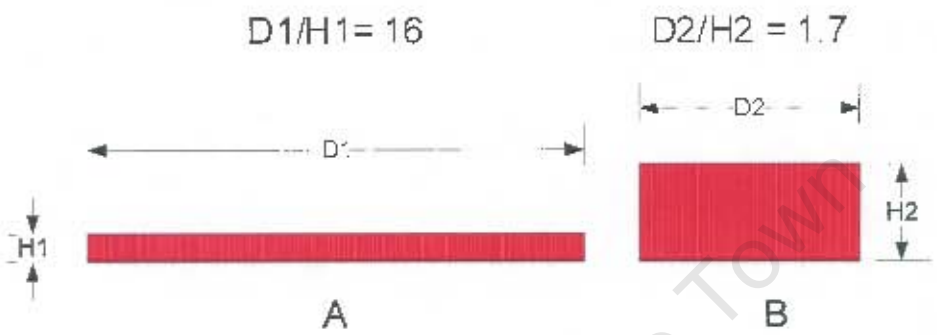

Figure 1.2: Figure showing range of diameter to thickness ratio of CY explosive.

The main objective of carrying out this current research however, is to extend the work carried out experimentally by Nurick and Radford [2] and numerically by Grobbelaar and Nurick [4] in order to investigate experimentally, theoretically and numerically the influence of other shapes of explosives. The mechanism of expansion and the prediction of shock-wave profiles from the explosives during and after detonation are both investigated theoretically and numerically, in order to further understand the load distribution on structures. The dimensions and shapes of the three explosives investigated in this work are shown in figure 1.3.

In order to investigate the effects of shape of the explosives, masses of the CY, TC and ITC explosives are kept equal and the deformation of the plate and impulse compared for each shape of explosive. The masses, diameters, and height of the cylinder explosives in this work are within the range of masses with those used in Nurick and Radford [2] with a minimum and maximum mass of 2.6g and 5.9g respectively. The burn diameter is also investigated in this work. As defined by Nurick and Radford [2], the burn diameter is a boundary of complete discolouration shown in figure 1.4.

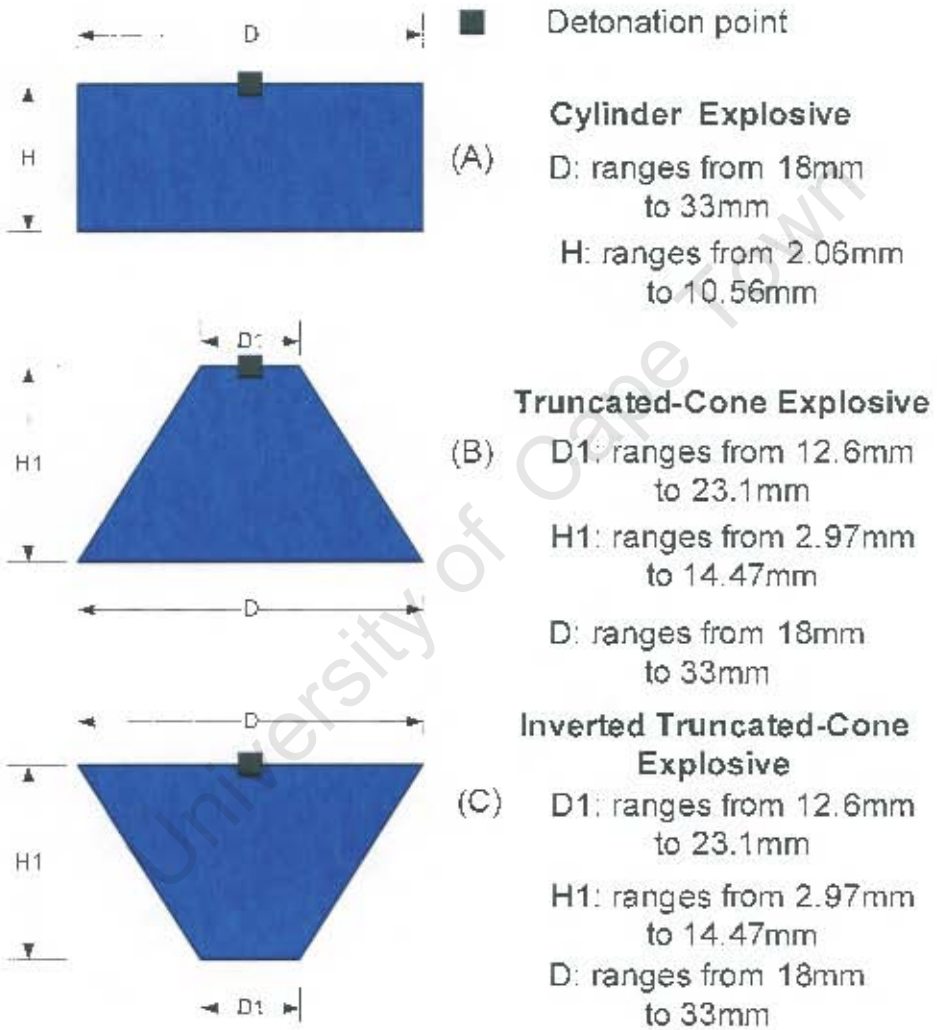

Figure 1.3: Figure showing range of dimensions of CY, TC and ITC explosives.

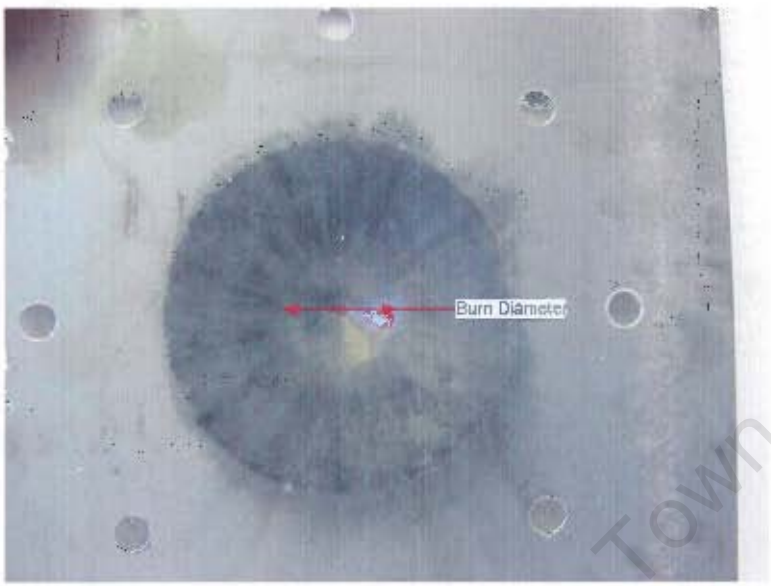

Figure 1.4: Figure showing burn diameter caused by blast load.

1.3 Methodology

Outlines of the methodology that is employed in this work in order to experimentally, analytically and numerically investigate the influence of shape of solid explosives on a structure are given below as follows:

1. The experimental work is a stand-off operation in which a polystyrene foam of thickness 20 mm is placed between the plate top surface and the explosive and carried out in a blast laboratory. The stand-off distance between the explosive and the plate is unchanged throughout the experiment. The type of explosives used in this research is plastic explosive (PE4). Each explosive is detonated at the center of the top surface as shown in figure 1.3. Plastic moulds with varying dimensions are used to form the various shapes of explosives. The target structure in this work is mild steel plate of diameter 100mm and thickness 1.6mm which are kept uniform throughout the experiments. Values of the central (midpoint) deformation, plate profile and impulse are recorded.

2. The various shapes of shock-waves generated by the explosives during and after detonation, are theoretically and analytically investigated. The detonation front is assumed to be spherical and also at the C-J state. A

2-dimensional approach is used to explain the mechanism of expansion of the detonation products and their spacial distribution.

3. The finite element simulation of the experiments are carried out using both ABAQUS/Explicit 6.4 and AUTODYN 6.0 codes. ALE (Abitrary-Lagrange-Eularian) mesh is used to model the explosive in both codes. An axi-symmetric model as opposed to a three-dimensional model is used to carry out the simulations in order to reduce computational time. The Jones-Wilkins-Lee (JWL) equation of state (EOS), reported in Lee *et al* [7] which relates the pressure, density, detonation wave speed and internal energy of the explosive, is incorporated in both numerical codes, in order to model the blast load on the plate. Adiabatic, strain-rate and non-linear geometric effects of the test plates are also incorporated in the numerical simulations using the Johnson-Cook constitutive equation.

1.4 Outline of Thesis Structure

1.4.1 Chapter 2

In chapter 2, a literature review of explosive detonation theory including the simple (ZND) and simplest (C-J) detonation theories are given. The development of equations of state of explosives and their applications to numerical simulations for the predictions of blast loaded structures are also discussed. More emphasis is given to the Jones-Wilkins-Lee (JWL) equation of state. A review of several constitutive equations for mild steel including the Johnson-Cook constitutive equation is discussed.

1.4.2 Chapter 3

In chapter three, the procedure for the experimentation of this work is described. The thickness and diameter of the plate measuring 1.6mm and 100mm respectively, remain unchanged throughout the experimentation. From the test plates, samples of nine "dog-bone" specimens are cut out in order to determine the stress-strain properties of the test plates at quasi-static conditions. Plastic moulds shaped in the form of CY, TC and ITC explosives are prepared in order to obtain the various shapes of explosives to carry out the experiments. A

total of 33 experiments are carried out for the investigations. The experiments focused on the deformation of the plate and impulse from the blast measured by the pendulum.

1.4.3 Chapter 4

This chapter presents and explains the experimental results. The results are presented in the form of photographs, tables and graphs. Results of the plate central deformation are presented in two forms. In the first set, plate deformation results subjected to varying shapes of explosives of the same mass are presented. In the second set of results where the masses of the explosives are varied, but of the same shape are also presented. The impulses of the blast loads measured by the pendulum are also presented in this chapter.

1.4.4 Chapter 5

This chapter focusses on the method of solution used to predict the experimental results presented in chapter 4 in order to investigate the effects of shape of a solid explosive on interaction with a structure. Method of constructing the shock-wave profiles theoretically are presented and compared to the shock-wave profile from the simulations using the ABAQUS/Explicit 6.4 and AUTODYN 6.0 software packages. Emphasis is placed on predicting the central deformation and final plate profiles. Furthermore, adiabatic conditions of the plate caused by high strain rate is incorporated in the numerical simulations using the Johnson-Cook constitutive equation. A test of convergence for the numerical simulation is addressed in order to find a solution for the element size of the plate and explosive that can be used to reasonably predict the experiments.

1.4.5 Chapter 6

Numerical investigations of the expansive nature of the three shapes of explosives are presented in this chapter. Details of the simulations of the experiments carried out in chapter 3 are presented. Interaction of the explosive load for each shape of explosive on the plate are investigated numerically and compared with the proposed theoretical shock-wave profiles discussed in chapter 5. Effect of changing the size of the explosive elements on the detonation speed and pressure

are also investigated.

1.4.6 Chapter 7

The numerical results from the simulations are presented in this chapter. The results are presented in the form of tables and graphs. Plots of the predicted central deformation and plate profiles for 18mm, 25mm and 33mm CY, TC and ITC are presented.

1.4.7 Chapter 8

The experimental and predicted central deformation and profile of the plates are compared in this chapter. Comparison is carried out in order to investigate the reliability of the ABAQUS/Explicit 6.4 and AUTODYN 6.0 codes to predict the effects of shape of explosive on a structure.

1.4.8 Chapter 9

Chapter nine discusses the results obtained from the experiments and predictions. The effective mass of each shape of explosive in relation to the central deformation of the plate is discussed. Discussion of the impulse in relation to the mass of explosive and the area of interaction of the blast load is also carried out in this chapter.

1.4.9 Chapter 10

In this chapter, conclusions recommendations and future work on the effects of shape of solid explosives are made based on the findings of this research. It is concluded that the shape of a solid explosive does have an effect on the deformation of a structure and the blast impulse.

Chapter 2

Literature Review

2.1 Introduction

Several attempts have been made in order to answer questions regarding the behaviour and performance of explosives. The quest for answers to some of these investigations has led to a growing research environment. Two main areas of interest in the search for answers are discussed in this chapter. First, an attempt is made to give a brief historical background and development of the theory of detonation including the development of equation of state for explosives. Secondly, a historical background and the development of hydrocodes for simulations of explosives is discussed which includes a review of the simulations of blast loaded plates.

2.2 Explosive Detonation Theory

An explosion is the effect produced by extremely rapid evolution of gases, usually at elevated temperatures, while an explosive is defined as any material or device which, by the rapid release of its potential energy, is capable of producing an explosion. The use of explosives is not new in the field of science and engineering. The Chinese are known to have used gunpowder prior to the thirteenth century as reported in Skidmore [8]. Alfred Noble's invention of dynamite in the latter half of the nineteenth century introduced the control and exploitation of detonating explosives in which the rate of material consumption is of the order of 10^5cm/s as reported in Skidmore [8]. Since then, various kinds of explosives and devices

have been developed including the invention of the initiator by Alfred Nobel as reported in Dremin [9].

The use of explosives during the Second World War, gave rise to the invention of several kinds of weapons including shaped charges. Some of the works on explosive technology focus on the use of explosive shaped-charges for mining and drilling purposes. A typical shaped charge and its effects on a target is shown in figure 2.1.

A shaped (hollow) charge consists of an explosive with cavity lined with metal as shown in figure 2.1 as defined in Meyers [10]. The effects of a shaped charge can be very devastating on a target as shown in figure 2.1. Detonation of the explosive accelerates the metal liner, in a convergent trajectory, producing a jet that travels with a velocity of V_2 higher than that of the detonation velocity V_0. Many works on shaped-charges have been carried out as can be found in Baker *et al* [11], Katayama *et al* [12], Molinari [13], Brown *et al* [14] and Held [15]. In Refs. [11] to [15], several metal liners with varying shapes and their effects were investigated.

Explosives can be divided into high and low explosives. High explosives are usually nitration products of organic substances, such as toluene, phenol, penataerythritol, amines, glycerine and starch. RDX and TNT are examples of pure high explosives. Pure explosives can be combined with wax, plasticizer or other additives so as to obtain a desired stability and performance. An example of such composition of a pure explosive and a plasticizer is PE4 (RDX/wax) explosive used in this research. High explosives detonate because the shock-wave speed during the process of detonation is greater than the characteristic sound speed of the explosive material. According to a published work found in [16], the pressure produced by an explosive can go up to 500,000 times that of the Earth's atmosphere, the detonation wave speed up to 10Km/s, temperature up to 5,500Kelvins and power up to 20×10^9Watts/cm^2. Low explosives are mostly solid combustible materials that decompose but do not normally detonate. This means that low explosives burn, a process referred to as deflagration. In deflagration, the shock-wave velocity is less than the characteristic sound speed of the explosive material.

The safety of the environment and people working with explosives is also of importance. Explosives not well handled or stored in an environment of favourable conditions can undergo self detonation which means that there is

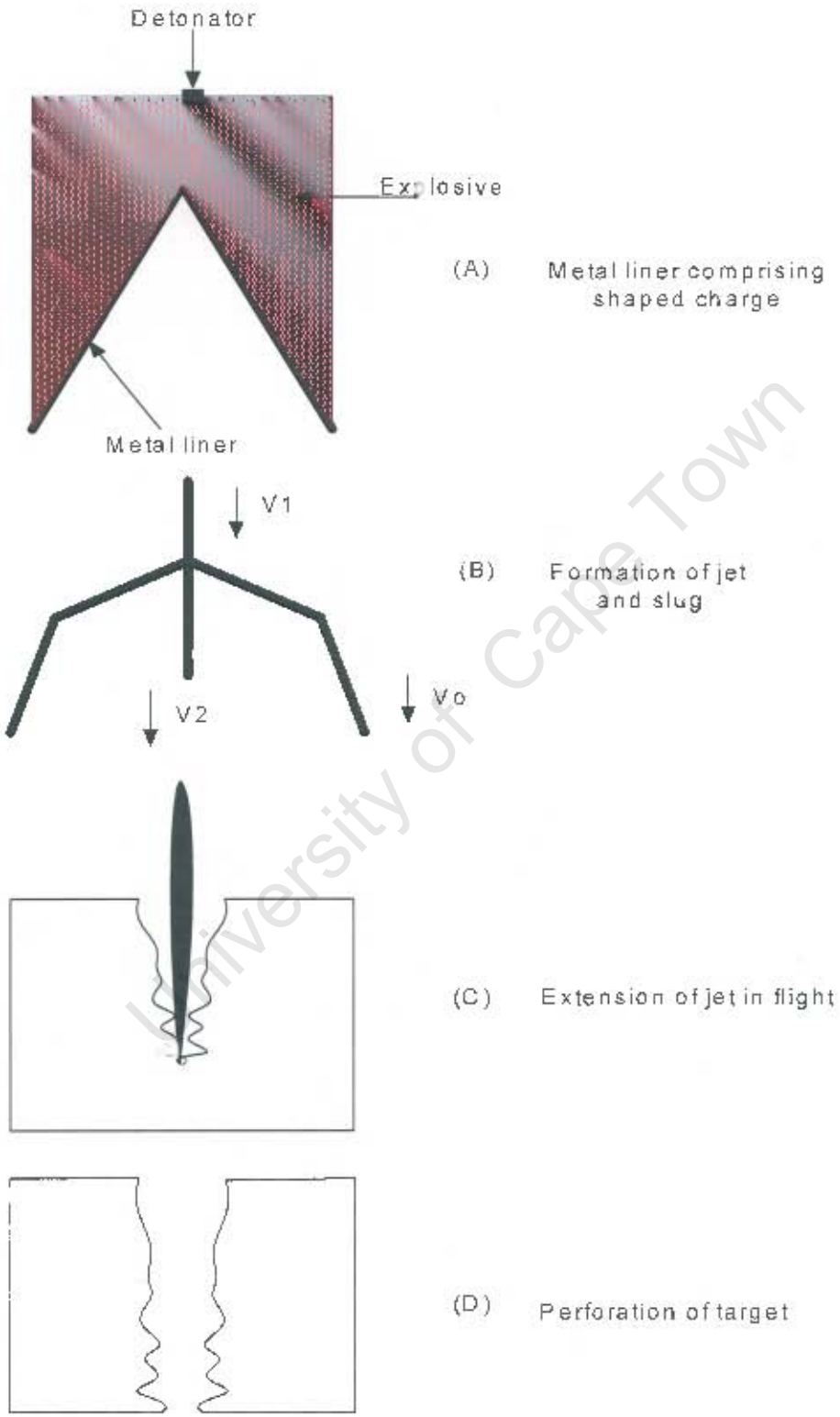

Figure 2.1: Figure showing schematic of a shaped charge and its effects on a target [10].

a cause for concern on the handling and storage of explosives. It has been well established that thermal runaway and ignition of different materials is dependent upon size, shape and surface and environmental temperature as well as the physical properties of the material. This means that for any given geometry, there is a critical size and surface temperature above which the heat generation within the solid exceeds the heat that is dissipated to the surroundings as reported in Shouman [17]. Research on the safety of explosives can be found in Shouman [17] and Jenkins *et al* [18]. In [18], studies were carried out for the detection of chemicals from landmines so as to reduce the effects of civilian casualties. Rogers and Rogers [19] studied the safety of explosives and specifically investigated several safety tests relating to impact, friction, shock and sparks. Thermal stability tests, time to explosion tests and critical temperature tests were all investigated by Rogers and Rogers [19]. Work on temperature effects on confined explosive charges can also be found in Chidester *et al* [20]. In [20], twenty large scale experiments were conducted on confined charges subjected to external heat. It was demonstrated that the rate of heating influenced the rate of decomposition of the explosive and was reported that slow heating causes a more violent thermal explosion than faster heating rate.

When the decomposition of an explosive with the evolution of gas and heat takes place exceedingly fast, proceeding through the explosive at a rate of several thousand meters per second and leaving in its wake gases at high temperatures and pressures, the process is called detonation as defined in Rinehart and Pearson [21]. With the rapid expulsion of gases at extremely high pressures, shock waves are generated during the process of detonation. Such waves are referred to as *detonation waves.*

Since the phenomenon of detonation was discovered by Berthelot, Vieille, Mallard and Le Chatelier in 1881 and 1882 as reported in Ficket and Davis [22], the study of explosive detonation theory has been widely researched and applied in the field of science and technology. Many studies have been carried out extensively as discussed in Langweiler [23], Guirguis *et al* [24], Ficket and Davis [22], Rinehart and Pearson [21], Leal-Crouzet *et al* [25], Skidmore [8], Dremin [9], Lubyatinsky and Loboiko [26] and Zukas and Walters [27]. It has also been a challenging and difficult subject to explain experimentally due to the extremely high rate of reaction of the explosive particles, generating pressures in the order of gigapascals (GPa) and temperatures over 5000 Kelvins which makes it very

difficult to measure the performance of explosives.

2.2.1 The ZND Model (Simple Model)

Following the discovery of detonation, was the formulation of the ZND theory. It was independently developed by Zeldovich (1940), Von-Neumann (1942), and Doering (1943) (ZND) as reported in Ficket and Davis [22]. The relatively simple description of steady plane detonation called the ZND theory is based on the Euler equations. In the ZND theory, the chemical reaction is initiated by a shock-wave and its pressure is greater than that of the detonation particles.

As reported in Ficket and Davis [22] the following assumptions of the ZND model, are given:

1. The flow is one-dimensional,
2. The shock is a jump discontinuity, because transport effects (heat conduction, diffusion, radiation, viscosity) are neglected,
3. The reaction rate is zero ahead of the shock and finite behind and the reaction is irreversible (proceeds in the forward direction only),
4. All thermodynamic variables other than the chemical reaction composition are in local thermodynamic equilibrium everywhere.

The zone in which the chemical reaction takes place is the detonation zone, which has a characteristic length depending on the rate of reaction of the explosive as shown in figure 2.2. At the start of the detonation process, a shock is generated which compresses the explosive material behind it. This pressure is referred to as the Von-Neumann spike as shown in figure 2.2.

As the material compresses behind the shock-wave, it heats up at local hot spots and initiates a chemical reaction for the detonation process. This process continues to regenerate itself throughout the process of detonation. With this self generating system within the explosive, the pressure and velocity of the explosive at the detonation front remain unchanged at steady detonation, throughout the process until all the charge is consumed. The Taylor-wave (rarefaction wave) following the reaction zone as shown in figure 2.2, represents the pressure of the detonation product after completely detonation. The length of the Taylor-wave is also dependent upon the thickness and boundary conditions at the rear of the

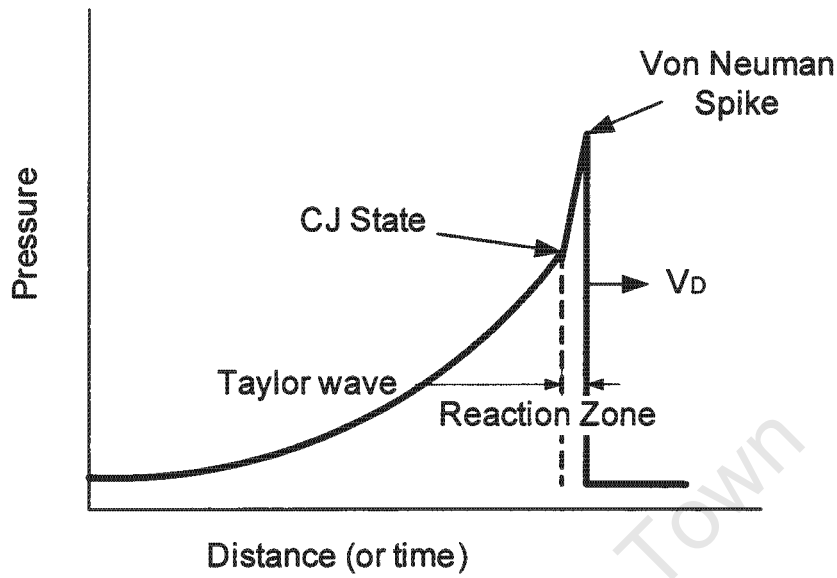

Figure 2.2: Figure showing structure of a detonation wave [31].

explosive. For unconfined and thin explosives, the Taylor-wave is shorter compared to confined and thicker explosives. For confined charges, it is well known that the speed of the detonation products is higher compared to an unconfined explosive as discussed in Aslam and Bdzil [28].

Since the reaction is not instantaneous, this means that a finite time as well as a finite distance of translation of the detonation products within the zone is a reasonable assumption. As shown in figure 2.3, the temperature, pressure and density in diagrams (a), (b) and (c) respectively, vary within the reaction zone as time proceeds. For diagram (d), it can be seen that the reaction is not instantaneous, and takes some time for any explosive material to completely react at the Chapman-Jouget (C-J) plane.

Investigations of the detonation reaction zone of solid explosives were carried out using a photoelectric technique as described in Lubyatinsky and Loboiko [26]. The reaction zone lengths and times for TNT, RDX, PETN and DATB based explosives were investigated and calculation of the length of the reaction zone was given as shown in equation 2.1.

$$X_J = \int_0^{T_J} (V_D - U_P)dt \tag{2.1}$$

where V_D is the detonation velocity, U_P the particle velocity and T_J the reaction

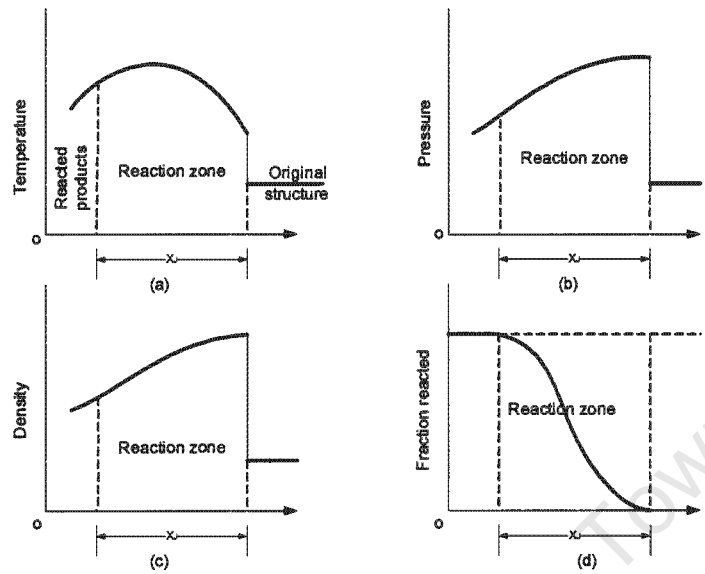

Figure 2.3: Figure showing schematic of variation of Temperature, Pressure, Density and Fraction of explosive reaction with detonation zone [21].

zone time. Table 2.1 summarises the reaction zone lengths and times calculated by Lubyatinsky and Loboiko [26] for HMX and TNT (hot pressed) based explosives.

Explosive	$\rho_{CJ}(g/cm^3)$	$X_J(mm)$	$T_J(\mu s)$
HMX	1.85	0.25	0.04
TNT	1.62	1.5	0.33

Table 2.1: Table showing reaction zone lengths and times for HMX and TNT based explosives

Studies of the reaction zone length in relation to the critical charge diameter of H6 (RDX/TNT) explosive for underwater blast weapons was carried out as reported in Swinton *et al* [29]. It was reported that the reaction zone length was estimated as 2.0mm, corresponding to a critical diameter of 4.4mm. Rinehart and Pearson [21] reported reaction zone lengths of 2mm for RDX and 3mm for TNT (fine powder). A formula for calculation of the reaction zone time is shown in equation 2.2 as reported in [26]. Equation 2.2 was derived by combining the data found in Dremin *et al* [9] and those found in Lubyatinsky and Loboiko [26] for the studied explosives with the exception of DATB explosives.

$$T_J = T_1 \exp\left(-\frac{P_J}{P_1}\right) \tag{2.2}$$

P_J is the pressure at the Chapman-Jouget (C-J) state, P_1 is the pressure of the reference point and T_1 the initial time. However, it was reported in Dremin [9] that the structure of a heterogenous charge as regards the particle size of the explosive, the nature of filler in pores and the state of the high explosive (liquid or solid) has a weak effect on the time of detonation transformation.

Determining the detonation velocity of explosives, is widely reported in Stewart and Yao [30], Cooper and Kurowski [31] and Scilly [32] and will be discussed later.

2.2.2 The Simplest Model and C-J State

In the simplest model, the length of the reaction zone is assumed to be zero and the reaction is instantaneous with the reaction zone and shock-wave collapsing into a single jump discontinuity at which the reaction is complete as shown in figure 2.4. In most applications, the simplest model is adopted for practical calculations of an EOS. As reported in Ficket and Davis [22], the following assumptions of the simplest model can be made:

1. The flow is one-dimensional,
2. The material emerging from the discontinuity is assumed to be in thermodynamic equilibrium, and is described by a thermodynamic equation of state,
3. The Jump discontinuity is steady (independent of time) so that the material emerging from the front is independent of time. The flow following this point may be time-dependent.

Consider the schematic diagram of an ideal detonation as shown in figure 2.4. The left side of the detonation front represents a stream of detonation products moving with velocity U_P and at elevated temperatures. The right hand side of the detonation front shows the unreacted explosive charge with zero velocity, and normal room temperature.

At the detonation front of negligible thickness, the velocity of detonation V_D, is at the Chapman-Jouget (C-J) state as given in equation 2.3.

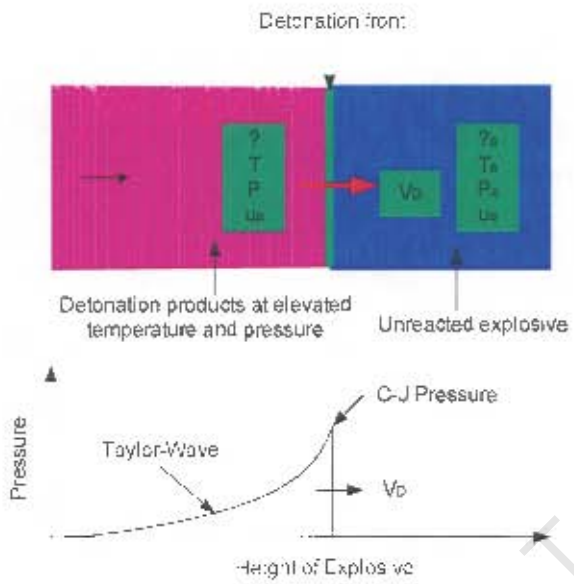

Figure 2.4: Figure showing schematic of an ideal detonation process of a solid explosive [21].

$$V_D = C + U_p \tag{2.3}$$

Equation 2.3 is referred to as the C-J condition, where C and U_p are the characteristic sound speed and particle velocity respectively. Figure 2.5 shows the state of an explosive during the process of detonation as given in Cooper and Kurowski [31]. The point A shows the state of the explosive with no shock whilst (C) shows the state of the material under the initial shock pressure, the Von-Nuemann pressure. At (C), the explosive is still not reacted but highly compressed and also at elevated temperatures.

The condition of the explosive at point (C) triggers the chemical reaction and hence the process of detonation. The hugoniot of the detonation products is defined along EBD whilst the hugoniot of the unreacted explosive at elevated pressure is defined along AFC. The lines ABC and AED, are defined as Rayleigh lines. These are lines showing the relationship between the initial and final state on a Pressure-Volume plane. Point (B) is referred to as the C-J point, the point at which the laws of conservation of mass, momentum and energy are applicable. The slope of the Rayleigh line is given as $-V_D^2/V^2$ and that at any other point on the hugoniot is given by $-U_p^2/V^2$. At point (E), the slope of the hugoniot is

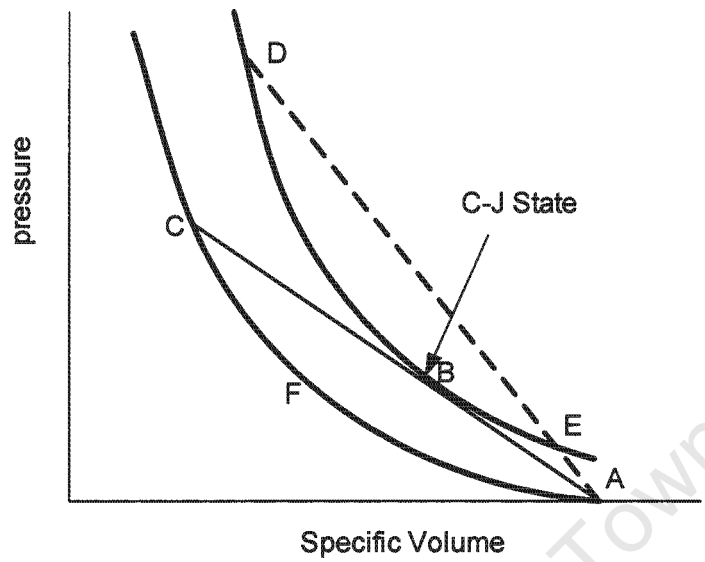

Figure 2.5: Figure showing detonation jump condition from the unreacted state to the CJ state on the Pressure-Volume plane [31].

less than that at the C-J point. This means that the velocity of the detonation products is less than that of the detonation front and hence the reaction zone will continually increase its length, an unrealistic assumption. At point D, the reaction zone and Taylor-wave will overtake the shock front, also an unrealistic assumption, which does not support the laws of conservation. The only possible point for the conservation of mass, energy, and momentum to exist is at point (B), referred to as the C-J point.

2.2.3 Conservation Equations

In summary, the basic jump equations of conservation at the C-J plane during the process of detonation as reported in Zukas and Walters [27], are given in equations 2.4, 2.5 and 2.6:

Conservation of Mass

$$\frac{\rho_{CJ}}{\rho_0} = \frac{V_0}{V_{CJ}} = \frac{V_D}{V_D - u_{CJ}} \tag{2.4}$$

Conservation of momentum

$$P_{CJ} = \rho_0 U_{CJ} D = \frac{U_{CJ} D}{V_0} \tag{2.5}$$

Conservation of Energy

$$E_{CJ} - E_0 = \frac{1}{2}(P_{CJ} + P_0)(V_0 - V_{CJ}) \tag{2.6}$$

The development of equations of state are generally based on the conservation equations given in equations 2.4, 2.5 and 2.6. The subscript CJ shows the state at the Chapman-Jouget condition whilst subscript 0 refers to the state at the initial condition. ρ is defined as the density, V, is the specific volume, D is the detonation Velocity and E, the specific energy. Langweiler [23] also reported equations containing directly measurable constants for the quantities involved in the hydrodynamic theory of detonation. It was revealed that the detonation velocity is the lowest possible value in the case of positive material velocity by finding the minimum of a $V_D - Up$ curve.

2.2.4 Equations of State (EOS)

Equations of state means some calibrated fitting form, describing material properties in a limited region, that allows a user to compute, in reasonable approximation, the behaviour of a physical system. The choice of a form of equation should be carefully made so as to realistically define the state of the material as it undergoes changes. Davis [33] discussed the concepts and formulae that are pertinent to the development and use of an EOS for explosive products, taken from hydrodynamics, thermodynamics and the physics of gases collected. The intention of the paper was to address the development of EOSs in which the equations of conservation of mass, momentum and energy for flow in one dimension are considered.

Two forms of EOS exist for explosives: Those that include temperature effects (complete EOS) and those that do not include temperature effects (incomplete EOS). For a complete equation of state, the mixture of the molecules and heat of formation are considered and it is a function of (p, ν, T). The EOS of each molecule that may be present is determined. A mixture rule is then used to determine the EOS for all possible combinations of the detonation products. The EOS at chemical equilibrium is finally determined by finding the combination with the minimum free energy.

A number of complete EOSs have been proposed as reported in Davis [34], Pastine [35], and Hueze [36]. In Davis [34], a simple complete EOS was formulated and calibrated for PBX9404 and PBX9501. Davis [34] formulated a complete EOS for unreacted solid explosives based on a reference isentrope (zero change in entropy) derived using walsh mirror image approximation and calibrated for unreacted PBX9501. However, Davis [34] further stated that the emphasis of the work was not to present a final perfect EOS, but on how calibration can be carried out. Pastine [35] developed E,V,T and PVT EOSs of reaction products at high pressure and temperature. The paper reported that the equation is predicted only on the independent particle concept, the existence of a pair potential that is function only of the molecular separation and on a model in which the substance described can be strictly solid-like, strictly fluid-like, or some combination of both. Hueze [36] proposed a complete EOS for both detonation products and initial explosives that provides access to all thermodynamic properties including temperature, entropy and free energy.

Development of the Williamburg equation of state to model the internal energy of non-ideal detonation was formulated by Brown and Braithwaite [37] as given in equation 2.7

$$E(V,S) = \frac{E_0}{\nu^{\gamma_\infty - 1}} \prod_{j=1}^{m} \left(\frac{1 + \beta_j \nu \sigma^{\alpha_j}}{1 + \beta_j} \right)^{\gamma_j} \tag{2.7}$$

where γ_∞ and α_j are given in equations 2.8 and 2.9

$$\gamma_\infty = \gamma + \sum_{j=1}^{m} \gamma_j \tag{2.8}$$

$$\sum_{j=1}^{m} \alpha_j \gamma_j = \gamma - 1 \tag{2.9}$$

The Williamburg EOS is a comparatively simple semi-empirical EOS for describing adiabats, shocks and other states from low to detonation pressures. It is based on a generalisation of a scaling law for the inverse-power potential and has shown to give excellent fits to single adiabats for the detonation products of two explosives, from which good fits to shocks can be calculated without further parameterization as reported in [37]. However, the Williamburg EOS does not apply to explosives of very high detonation velocities and that the thickness of the reaction zone is not considered negligible. Furthermore the energy and mo-

mentum in the Von-Nuemann spike cannot be neglected as reported in Dunnett [38].

An incomplete equation of state is in the form of (p, v). The Jones-Wilkins-Lee (JWL) EOS [7], is an example of an incomplete EOS used for the estimation of the pressure for detonation products in hydrocodes. Although the JWL EOS has its limitations as regards the lack of temperature effect, it has also proven to be a useful tool for practical engineering problems as regards its computational efficiency as discussed in Ficket and Davis [22] and Dunnett *et al* [38]. The JWL EOS is empirical and assumes a Grunneisen gamma constant. Jones *et al* [39] constructed an incomplete EOS for the reaction products of SX-2 using liquid-state pertubation theory for the simple fluid constituents and semi-empirical descriptions for the solid components. Cylinder tests were used to determine the JWL constants.

In Davis [41], an EOS for detonation products was proposed with the usual (p, v) form as given in equation 2.10.

$$p = \frac{E}{v}\left[k - 1 + F(v)\left\{1 + b\left(1 - \frac{E}{E^s(v)}\right)\right\}\right] \tag{2.10}$$

where $F(v)$ has a value of 0 at large specific volume and increases monotonically as the specific volume decreases, approaching a constant value at small volume, b is a constant and $E^s(v)$ is the specific internal energy on the principal isentrope. The equation allows independent calibration of the adiabatic gamma and the Gruneisen gamma. According to Davis [41], the basic premise of the work is to allow Engineers who normally make adjustments with EOS to compensate for errors using computer codes for practical applications.

Development of the JWL Equation of State

Prior to the formulation of the JWL EOS, numerous forms of equations were proposed for describing the adiabatic expansion of detonation products. (See Ficket and Davis [22], Cowan and Ficket [42], and Ficket and Wood [43]). These equations were believed to be inaccurate for the estimation of the explosive performance as reported in Ficket and Davis [22]. To improve the work carried out in [42], and [43], Wilkins [44] developed an equation of state which predicts with reasonable accuracy, results for experimental geometries emphasizing the early stages of detonation product expansion as given in equation 2.12. The

combination of a previous equation proposed by Jones and Miller [45] and that proposed by [44], gave rise to the formulation of the Jones-Wilkins-Lee (JWL) EOS given in equation 2.13. The equations proposed by [44] and [45] are given in equation 2.11 and 2.12 respectively.

Jones:

$$P = Ae^{-RV} - B + CT \tag{2.11}$$

Wilkins:

$$P = \frac{\alpha}{V^Q} + B(1 - \frac{\omega}{RV})e^{-RV} + \frac{\omega E}{V} \tag{2.12}$$

$$\text{where } \alpha = a\frac{(Q-1)}{(Q-1-\omega)}$$

JWL:

$$P = A(1 - \frac{\omega}{R_1 V})e^{-R_1 V} + B(1 - \frac{\omega}{R_2 V})e^{-R_2 V} + \frac{\omega E}{V} \tag{2.13}$$

The JWL EOS provides a simple empirical formula for the pressure of the detonation products which can be easily calibrated for use in hydrocodes. The JWL also has the ability to accurately describe the adiabat at the C-J state. However, the lack of temperature information limits the kind of thermodynamic information that can be deduced directly. The coefficients A and B are determined from E_0, D, P_{CJ} and ρ_0 once a guess is made for R_1, R_2 and ω using computer codes as described in Lee *et al* [7]. Cylinder and spherical tests were used to characterise the expansion behaviour used to describe the expansion behaviour of the detonation products.

The JWL EOS has been used in several numerical codes to model the pressure of detonation products with good correlation compared to experimental results as can be found in Grobbelaar and Nurick [4]. Yang [46] modelled and verified blast damage induced in rocks using ABAQUS/Explicit code. The blast load was modelled using the JWL EOS. It was however pointed out that further developments of the ABAQUS/Explicit code is needed in order to include non-ideal behaviour of the explosive gas particles and their ability to penetrate cracks in rocks.

2.2.5 Cylinder Test

The cylinder test is used to fit the parameters of a particular equation of state of an explosive. In brief, the cylinder test is a simple experiment in which a cylinder

filled with explosive is detonated at one end as shown in figure 2.6 in order to describe the adiabatic expansion of the detonation products at the C-J state. The subsequent motion of the cylinder accelerated by the expanding detonation products is measured using a diagnostic technique as described in Lee *et al* [7]. The radial motion of the wall is recorded by a streak camera using shadow graph technique also described in [7]. A computer code then uses the radial motion to calculate the radial velocities of the wall. Effects of explosive diameter and change in cylinder wall velocity as a function of position along the cylinder were investigated in Lee *et al* [7]. It was found that a 1" (2.5 cm) diameter of charge approximates to an infinite diameter behaviour.

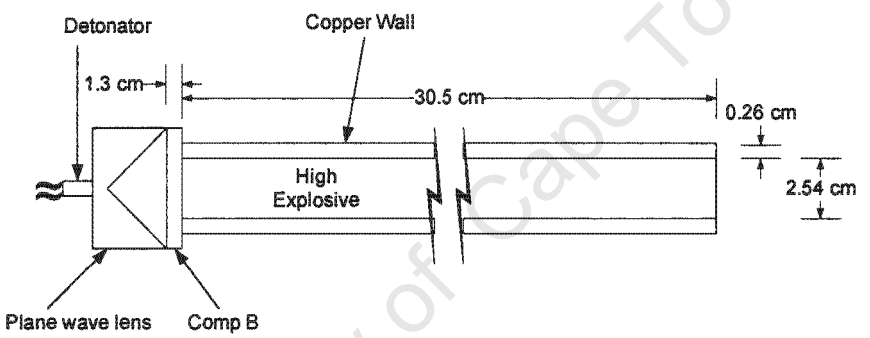

Figure 2.6: Schematic of a standard cylinder test geometry [7].

According to Merchant *et al* [47] however, EOS deduced in this way have typically failed to be of use in modelling weapon scenarios. This is as a result of the fact that the plane waves predicted in hydrocodes never really exists, as pertubations from the walls of the cylinder gave a drag to the edges of the detonation wave, curving it. This consequently increases the detonation velocity deduced, higher than that of a curved surface wave. It was addressed in Merchant *et al* [47], where EOS parameters for HMX based explosive EDC37 were successfully recalculated using the Withan-Bdzil-Lambourn (WBL) model which accurately models its wave-front characteristics. It is also mentioned that for the first time, a cylinder test derived EOS has successfully modelled varied scenarios without recourse to abitrary adjustment of the high explosive (HE) material parameters at a run time. Other works involving the cylinder test experiment can be found in Aslam and Bdzil [28] and Stewart [30].

2.2.6 Effect of Explosive Charge Diameter on Detonation Velocity

The effects of diameter on the detonation velocity is shown in figure 2.7 for confined and unconfined explosives. In both situations, the velocity of detonation increases as the charge diameter increases but reaches an asymptotic value as the diameter becomes very large. For a confined explosive, the detonation velocity reaches an asymptotic value much earlier compared to an unconfined charge as reported in Rinehart and Pearson [21].

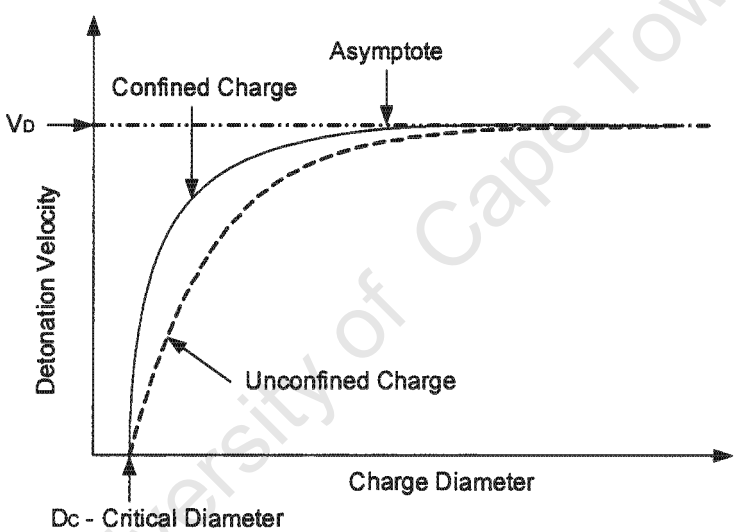

Figure 2.7: Graphs showing effect of diameter of explosive on detonation velocity for confined and unconfined charges.

Below a certain diameter referred to as the critical diameter (D_c), detonation does not take place as detonation only happens above this diameter as discussed in Rinehart and Pearson [21], Ficket and Davis [22] and Zukas and Walters [27]. The charge diameter in relation to the velocity of detonation V_D as formulated by Whelan *et al* [48], is given in equation 2.14 based on experimental results. The equation was formulated for cylindrically-shaped RDX-driven composite explosives, where D^* and a^* are curve fitting constants.

$$V_D^2 = (D^*)^2[1 - (a^*/d)^2] \tag{2.14}$$

The equation shows that the bigger the diameter of the charge, the velocity of detonation reaches its asymptotic value of D^*. For values of d equal to a^* (critical diameter), detonation does not occur. It was also reported by Whelan *et al* [48] that a simple relationship between the critical diameter and the reaction zone length can be formulated as given in equation 2.15.

$$d_c = 2.208a^* \tag{2.15}$$

2.2.7 Effect of Explosive Charge Height on Impulse

Figure 2.8 shows the detonation of an explosive charge and an increase in the length of the Taylor-wave as detonation takes place. However, it is shown in figure 2.8 (c), that at some distance from the detonation front, the particles at the rear end begin to lose momentum and move in the opposite direction. This means that the height does not contribute much to the impulse after a critical value which depends on the dimensions of the explosive, is reached.

In this regard, an effective height is reached, when the detonation particles moving away from the detonation front, do not actually contribute to the impulse. This height is referred to as the "effective height" and also addressed in Meyres [10]. According to Rinehart and Pearson [21], increasing the height of the explosive beyond 5/2 of its diameter, will not result in greater impulse.

2.3 Blast Waves

A blast wave is a shock-wave that moves through air as defined by Robertson *et al* [49]. A typical blast wave is shown in figure 2.9. As shown, the time taken for the blast pressure to meet its target from the source of the explosion is referred to as T_a, and T_d the time taken for the pressure to attenuate after reflection from the surface of the target material to atmospheric pressure.

As reported in Taylor [50], waves of finite amplitude as distinct from small amplitude or sound waves, cannot be propagated in any known gas without change of form as the wave travels along its path. But such waves can be propagated in one direction with a continuously changing form provided that the relation between the pressure and velocity is satisfied as given equation 2.16.

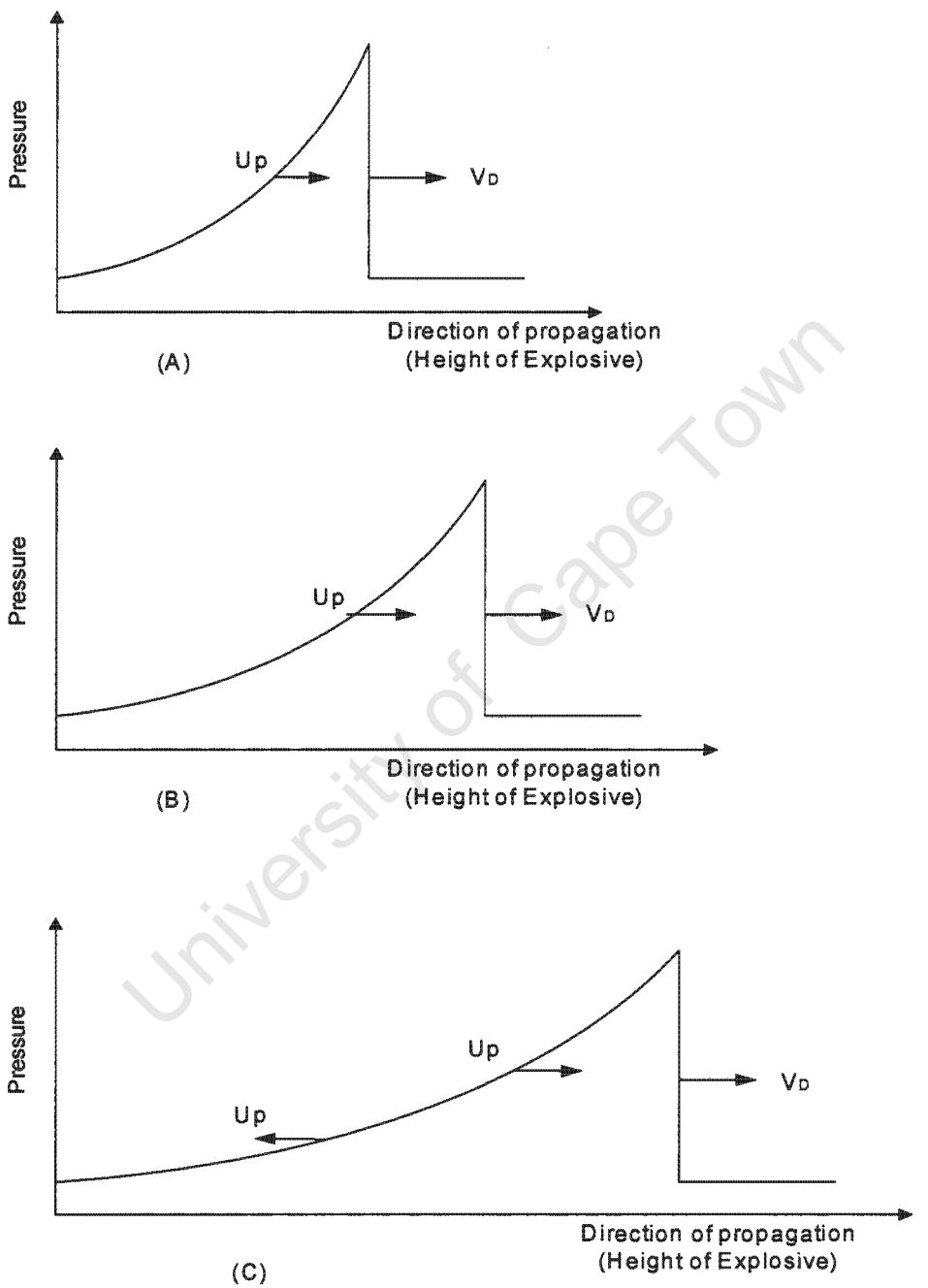

Figure 2.8: Figure showing propagation of a detonation wave with an increase in the Taylor-wave length and loss of momentum of rear particles [10].

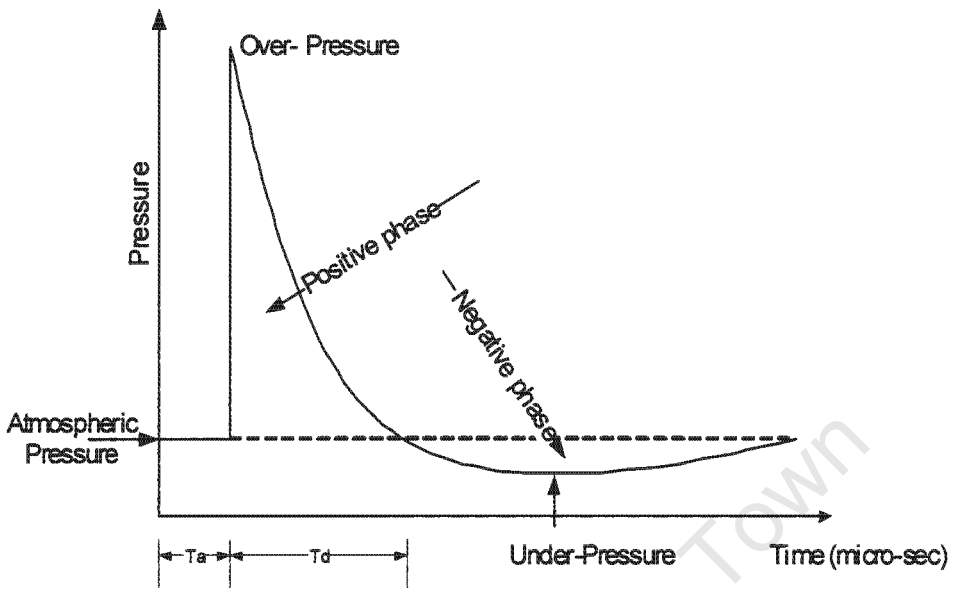

Figure 2.9: Figure showing typical blast wave pressure-time curve in air [21].

$$u = \frac{2a}{\gamma - 1}\left\{\left(\frac{p}{p_0}\right)^{(\gamma-1)/2\gamma} - 1\right\} \tag{2.16}$$

where a is the velocity of sound at the pressure p_0, and $u = 0$ at this pressure, γ is the ratio of the specific heats which for air may be taken as 1.045. Inside the pulse of length L, as shown in figure 2.10, the point at which pressure is p, the pressure will not be propagated at a velocity of a, but at a velocity of $(u + c)$ where c is given as shown in equation 2.17.

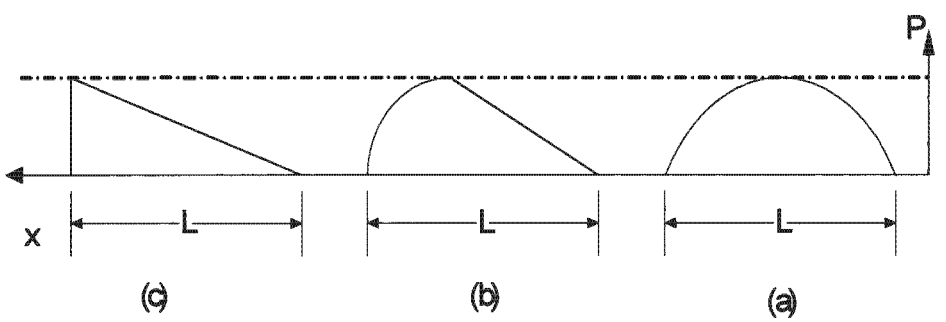

Figure 2.10: Formation of shock-wave in disturbance progressing from right to left [50].

$$c = a\left(\frac{p}{p_0}\right)^{(\gamma-1)/2\gamma} \tag{2.17}$$

When $p > p_0$, u is positive and $c > a$ so that the parts of the wave where the pressure is high are continually advancing relative to the parts of the wave where the pressure is lower as shown in figure 2.10. In figure 2.10, the top of the pulse is seen to be advancing from a symmetrical shape in (a) to an unsymmetrical form in (c) the point at which the left side of the graph becomes vertical or $\partial p/\partial x$ becomes infinite. At this stage, a shock-wave is formed and an irreversible conversion of kinetic and potential energy into heat as reported in Taylor [50].

It should be noted that the when a shock-wave strikes a rigid surface, it is reflected. The reflected wave moves back into the incident wave, the pressure thereby becoming redistributed as shown in figure 2.11.

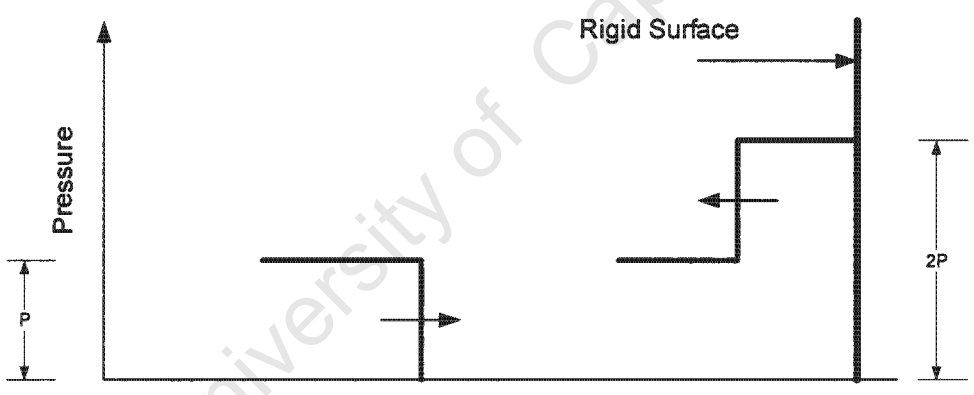

Figure 2.11: Interaction of incident shock-wave striking normally against a rigid surface [21].

The actual pressure on the surface of the rigid target is doubled for low intensity shock. As the intensity of the shock increases, however, the reflected pressure can go up to eight times the incident pressure as reported in Rinehart and Pearson [21]. The longer the Taylor-wave (rarefaction wave), the longer the time of the positive phase. For relatively small stand-off distances, the negative blast phase is neglected due to its minimal effects. For large stand-off distances, suction effects caused by significant negative pressures have been reported in Krauthammer and Altenberg [51]. According to Krauthammer and Altenberg [51], studies were carried out on glass panels subjected to blast loads.

It was found that at very small stand-off distances, glass panels deformed in the direction of the blast while the deformation occurred in the opposite direction as the stand-off distance increased. The impulse of the positive phase of the blast is much higher than that of the negative phase. Many researchers have discussed effects of shock-wave in air (blast loads) on structures as can be found in Whenhui *et al* [52], Guruprasad and Mukherjee [53], Chapman *et al* [54], Kinney and Graham [55], Hiroe *et al* [56] and Smith *et al* [57].

2.3.1 Estimating Blast Parameters

As reported in Olatidoye *et al* [58], the pressure decay with respect to time of a blast wave is given by equation 2.18.

$$P_s(T) = P_s \cdot (1 - \frac{T - T_a}{T_d})e^{-\alpha\frac{T-T_a}{T_t}} \tag{2.18}$$

where P_s is the maximum over-pressure (reflected pressure) at the point of interaction, α is the dimensionless wave-form parameter and T the time measured from the instant the shock front arrives. Equation 2.18, can also be simplified to equation 2.19.

$$P_s(T) = P_{ref\,max} \cdot e^{-\alpha T} \tag{2.19}$$

where $P_{ref\,max}$ is the maximum reflected pressure. As reported in Olatidoye *et al* [58], for practical reasons, the pressure time graph shown in figure 2.9 can be approximated to a triangular load as shown in figure 2.12 and also reported in Agbabian [59] and Baker [60].

From figure 2.12, the impulse of the blast can be calculated by the equation given in equation 2.20, I is impulse of blast per unit projected area, T_d the duration of the positive phase.

$$I = \frac{P_{ref\,max} \cdot T_d}{2} \tag{2.20}$$

2.3.2 Blast Scaling

A blast scaling law was first formulated by Hopkinson in 1915 as reported in Baker [60]. The law states that similar blast (shock) waves are produced at identical scaled distances when two explosive charges of the same geometry but

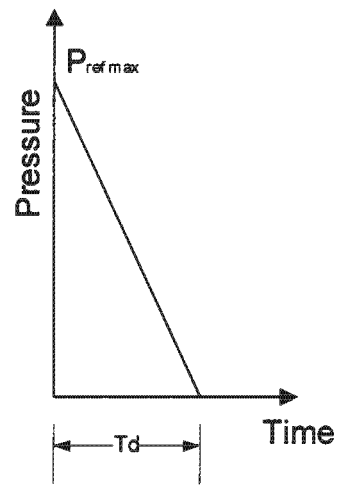

Figure 2.12: Triangular profile of blast load.

of different sizes, are detonated in the same atmosphere. The scaled distance is given as shown in equation 2.21.

$$Z = \frac{R}{W^{1/3}} \tag{2.21}$$

where R is distance from centre of explosive source and W is mass of the explosive. Figure 2.13 shows the sizes of two explosives whose densities are the same but of different masses.

For the pressures at A and B to be equal, the scaling factors Z1 and Z2 from the relationship given in equation 2.22 must be equal where $W1$ and $W2$ are the masses of the explosives at A and B respectively.

$$Z1 = Z2$$

$$\frac{R1}{R2} = \frac{W1^{1/3}}{W2^{1/3}}, \quad \frac{R1}{W1^{1/3}} = \frac{R2}{W2^{1/3}} \tag{2.22}$$

In 1944, Sachs formulated a more general blast scaling law which includes the effects of height and changes in ambient conditions. The law states that dimensionless groups can be formed that involve pressure, time, impulse and certain parameters of the ambient pressure. These groups are given in $(\frac{p}{p_0}, \frac{Ia_0}{E^{1/3}p_0^{2/3}}, \frac{ta_0 p_0^{1/3}}{E^{1/3}})$ as reported in Baker [60].

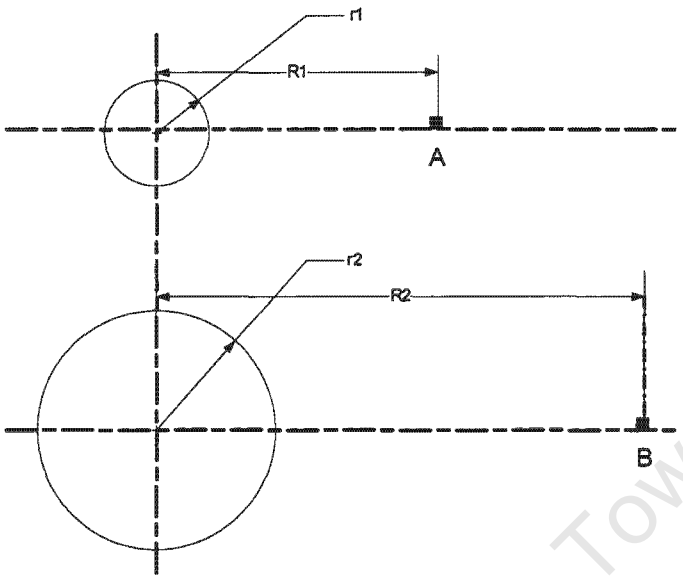

Figure 2.13: Figure showing illustration of similarity principle. Pressures at A and B are equal [60].

TNT Equivalent Method Using Scaling Law

The TNT equivalent method used to estimate blast loads has been widely discussed as can be found in Olatidoye *et al* [58], Jacinto *et al* [61], Formby and Wharton [62], Naumyenko and Petroskyi [63] and Wharton *et al* [64] in relation to scaling laws. The pressure of an explosive is estimated relative to that of the TNT. In this method, an equivalent mass of the explosive is found that produces the same amount of pressure as that of TNT using scaling laws. Brode [65] was the first to propose a relationship between the peak pressure with the scaled distance in the form given in equations 2.23 and 2.24.

$$P_{max} = \left(\frac{6.7}{Z^3} + 1\right) \text{ bar for } P_{max} \geqq 10\text{bars} \tag{2.23}$$

$$P_{max} = \left(\frac{0.975}{Z} + \frac{1.455}{Z^2} + \frac{5.85}{Z^3} - 0.019\right) \text{ bar for } 0.1\text{bar} \leqq P_{max} < 10\text{bars} \tag{2.24}$$

The equivalent TNT mass of the explosive is given in equation 2.25 as reported in Cooper and Kurowski [31], where M_{exp} is the mass of the explosive in Kg, P_{CJ} is the pressure at the C-J state and V_D, the detonation velocity of the explosive.

$$W_{TNT} = 0.078 M_{exp} \frac{P_{CJ}}{V_D} \tag{2.25}$$

Alternative equations proposed by Naumyenko and Petroskyi [63] are given in equations 2.26.

$$\begin{aligned} P_{max} &= \left(\frac{10.7}{Z^3} - 1\right) \text{ kp/cm}^2 \text{ for } Z \leqq 1 \\ (1\text{kp/cm}^2 &= 98\text{KPa}) \end{aligned} \tag{2.26}$$

$$P_{max} = \left(\frac{0.975}{Z} + \frac{1.455}{Z^2} + \frac{5.85}{Z^3}\right) \text{ kp/cm}^2 \text{ for } 1 \leqq Z \leqq 15$$

The equations given by Henrych [66] to estimate the maximum incident pressure are in three ranges according to the scaled distances as given below:

$$P_{max} = \left(\frac{14.072}{Z} + \frac{5.540}{Z^2} - \frac{0.357}{Z^3} + \frac{0.00625}{Z^4}\right) \text{ bar for } 0.05 \leqq Z < 0.3 \tag{2.27}$$

$$P_{max} = \left(\frac{6.194}{Z} - \frac{0.326}{Z^2} + \frac{2.132}{Z^3}\right) \text{ bar for } 0.3 \leqq Z < 1 \tag{2.28}$$

$$P_{max} = \left(\frac{0.662}{Z} + \frac{4.05}{Z^2} + \frac{3.288}{Z^3}\right) \text{ bar for } 1 \leqq Z \leqq 10 \tag{2.29}$$

Another alternative equation for the maximum pressure proposed by Mills [67], is given in equation 2.30. Since the pressure on the surface of the material is reflected, Mills [67] proposed another equation 2.31 for the maximum reflected pressure in KPa.

$$P_{max} = \left(\frac{1772}{Z^3} - \frac{114}{Z^2} + \frac{108}{Z}\right) \text{ KPa} \tag{2.30}$$

$$P_{ref\,max} = \left(\frac{2P_{max}(710 + 4P_{max})}{710 + P_{max}}\right) \text{ KPa} \tag{2.31}$$

Equations proposing estimate of the maximum pressure and total impulsive time were proposed by Kinney and Graham [55]. These are shown in equations 2.32 and 2.33 respectively.

$$P(Z) = \left\{ \frac{808[1 + (\frac{Z}{4.5})^2] \cdot 1.013 \cdot 10^5}{[1 + (\frac{Z}{0.048})^2]^{0.5}[1 + (\frac{Z}{0.32})^2]^{0.5}[1 + (\frac{Z}{1.35})]^{0.5}} \right\} \text{Pa} \tag{2.32}$$

$$T(Z) = \left\{ \frac{980[1 + (\frac{Z}{0.54})^{10}]W^{1/3}}{[1 + (\frac{Z}{0.02})^{3}]^{0.5}[1 + (\frac{Z}{0.74})^{6}]^{0.5}[1 + (\frac{Z}{6.9})]^{0.5}} \right\} \cdot 10^{-6} s \qquad (2.33)$$

where P(Z) is the incident pressure and T(Z) is the time of the positive blast wave.

2.3.3 Estimating Impulse of Blast

Bimha *et al* [6], carried out numerical studies in an attempt to model the overall deformation of a circular plate of fixed boundary condition. The explosive was centrally placed on a polystyrene as shown axi-symmetrically in figure 2.14.

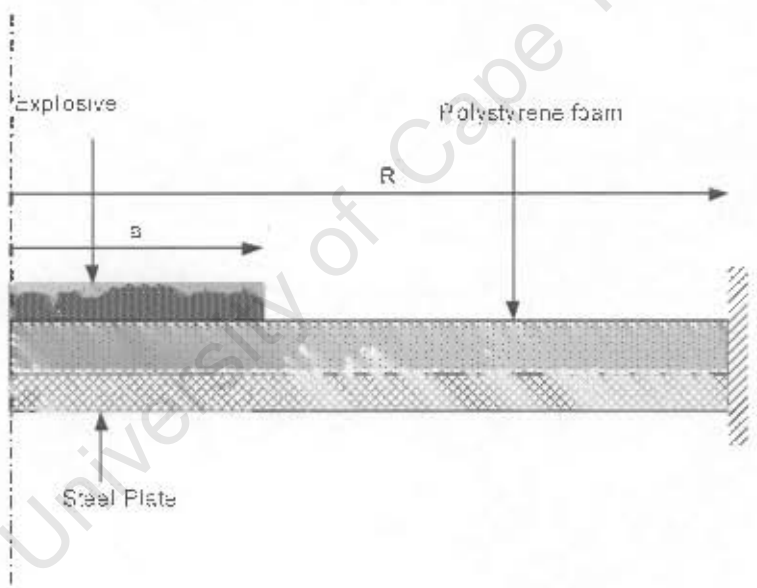

Figure 2.14: Schematic diagram of Bimha's model [6].

Values of $(\frac{a}{R})$ ranging from 0.15 to 0.6 with several impulses ranging from values causing Mode I to Mode II failures were considered in [6]. Given the area of interaction, the total pressure and duration of blast, the impulse given in equation 2.34 can be estimated.

$$I = PA\tau \qquad (2.34)$$

where I is the impulse, P the pressure on the target plate, A is the loaded area of plate and τ the duration of the blast. The pressure distribution of the blast is shown in figure 2.15.

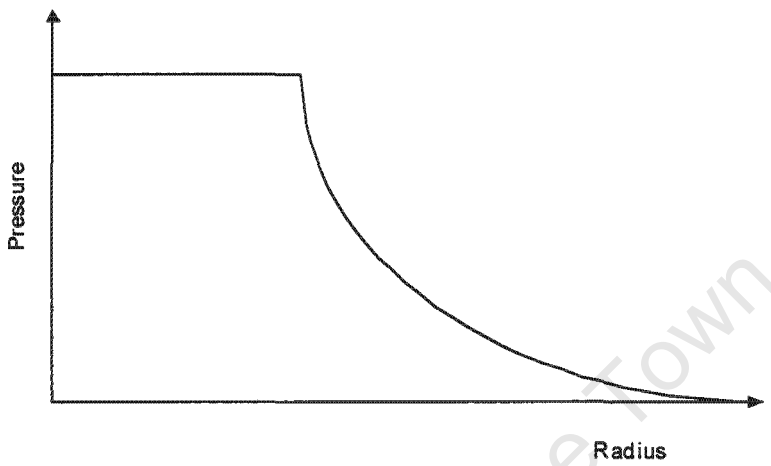

Figure 2.15: Pressure distribution with respect to radius of plate [6].

In figure 2.15, the pressure is assumed to be uniform from the centre of the plate to the edge of the explosive after which an exponential decay of the load is experienced up to the plate radius where the pressure is assumed to be at atmospheric. The blast duration is given in equation 2.35.

$$\tau = \frac{a}{V_D} \tag{2.35}$$

The area under the pressure curve also estimates the impulse of the blast. This is given below in equation 2.36.

$$I = r \int P(r) dA \tag{2.36}$$

By substituting the boundary conditions given in equations 2.38, 2.39 the impulse of the blast is estimated as given in equation 2.37.

$$I = \pi r \tau P_0 \left[a^2 + 2 \left\{ \left(\frac{a}{k} + \frac{1}{k^2} \right) - \left(\frac{R}{k} + \frac{1}{k^2} \right) e^{k(a-R)} \right\} \right] \tag{2.37}$$

$$P = P_0 \qquad \text{for } r \leq a \tag{2.38}$$

$$P(r) = P_0 e^{-k(r-a)} \qquad \text{for } a \leq r \leq R \tag{2.39}$$

where k is the decay constant as given in equation 2.40.

$$k = 130 - 261\left(\frac{a}{R}\right) + 948\left(\frac{a}{R}\right)^2 \qquad \text{for } 0.15 < \frac{a}{R} < 0.6 \qquad (2.40)$$

2.4 Explosive Performance

Various methods have been put forward to measure the performance of an explosive. Parameters such as overpressure, velocity, impulse and energy released, have been some of the most common parameters used for the determination of the performance of explosives. Some of the methods that have been used to determine the performance of explosive are well addressed in Scilly [32], Gurney [68] and Cooper and Walters [31].

As reported in Scilly [32], the *Trauzl block* test and the *Ballistic pendulum* tests energy release, are the two best known and probably most frequently used methods of assessing the energy released by detonating explosives. In brief, the Trauzl test consists of a standard cast cylindrical lead block of diameter 200mm and height 200mm with an axial recess of 25mm diameter and 125mm depth which accepts the 10g sample charge and detonator. When the charge is detonated, the volume of expansion of the cavity is recorded and compared with the expansion produced by 10g of picric acid.

In the ballistic pendulum test, a charge of explosive is fired in a mortar-like chamber at the end of a pendulum. The amount of explosive required to give the same pendulum deflection as a standardised amount of TNT is empirically determined. The ratio of these weights represents the relative TNT value of the second explosive as reported in Rinehart and Pearson [21].

A simple approach was put forward by Keshavarz [69], in order to measure the performance of explosives by considering their molecular compositions. The pressure at the C-J state of six well known explosives HMX, RDX, TNT, PETN, Teryl and DATB, at various loading densities with chemical formula $C_aH_bN_dO_n$, can be calculated by using equation 2.41, where ρ_0 is the loading density, MW is the molecular weight of the explosive and $\triangle h_f^\circ(g)$ the heat of formation in the gas phase. The results obtained compared well with experimental results as reported in Keshavarz [69].

$$P(\text{kbar}) = -2.6 + \left[\frac{-102a + 226b + 103c + 3150d + 30.7\triangle h_f^{\circ}(g)}{MW}\right]\rho_0^2 \quad (2.41)$$

For example, the C-J pressure of RDX using equation 2.41 is 278kbar (27.8GPa) compared to the experimental result of 263kbar (26.3GPa) as reported in Keshavarz [69].

An alternative formula is reported in Scilly [32] and Cooper and Walters [31] given in equation 2.42.

$$P_{CJ} = \frac{\rho_0 D^2}{4} \quad (2.42)$$

Result of the explosive pressure at the C-J state by using equation 2.42 for a density of 1600kg/m^3 and detonation velocity of 8190m/s^2 is 26.8GPa. Gurney [68] postulated the energy released from a confined explosive under standard conditions in a fixed proportion between the fragments from the casing and the detonation products for a variety of explosives and found that the characteristic velocity of the fragments is given by $\sqrt{(2E_g)}$. It is also reported in Gurney [68] that the terminal velocity is influenced by the shape of the casing and therefore formulated equations for spherically and cylindrically shaped charges given in equations 2.43 and 2.44 respectively. The fragment velocity data from exploding ordnance were used to determine the specific energy, E_g.

$$Vm = [2E_g/(M/C + 3/5)]^{1/2} \quad (2.43)$$

$$Vm = [2E_g/(M/C + 1/2)]^{1/2} \quad (2.44)$$

where M/C = [(outside diameter/inside diameter)^2 - 1]$\rho_m\rho_c$ and ρ_m and ρ_e are the densities of the metal and explosive, M is mass of metal and C is the mass of explosive. The efficiency factor to convert chemical energy into kinetic energy of the driven plate is given in equation 2.45

$$\epsilon = MV_m/\left(\sqrt{2E_g}\right)^2/C \quad (2.45)$$

For TNT and RDX explosives, the characteristic velocity of explosion from the cylinder test and Gurney parameters are given as (2.27 - 2.44)km/s and (2.83-2.93)km/s as reported in Scilly [32].

2.4.1 Effective mass of Explosive

The shaded portion in figure 2.16 represents the effective mass of the explosive that will contribute to the axial momentum of the metal plate. The outer rectangular boundary represents the total mass of explosive. According to Kennedy [70], the lateral edges of the explosive have to be subtracted from the total mass of explosive in order to estimate the mass of explosive that will drive a metal plate to its maximum velocity. For explosive charges of limited lateral dimension on accelerating plates, an effective mass is reached beyond which any increase will not contribute much to the maximum velocity of the plate in figure 2.16. The effective mass of the explosives shown in figure 2.16, is accounted for by taking off part of the expected unreacted explosive measured at 30^0 from the side of the explosive as reported in Kennedy [70]. This also means that after an effective mass is reached, the maximum velocity of the plate driven by the forms of explosives shown in figure 2.16 (A) and (B), will be similar irrespective of the difference in height.

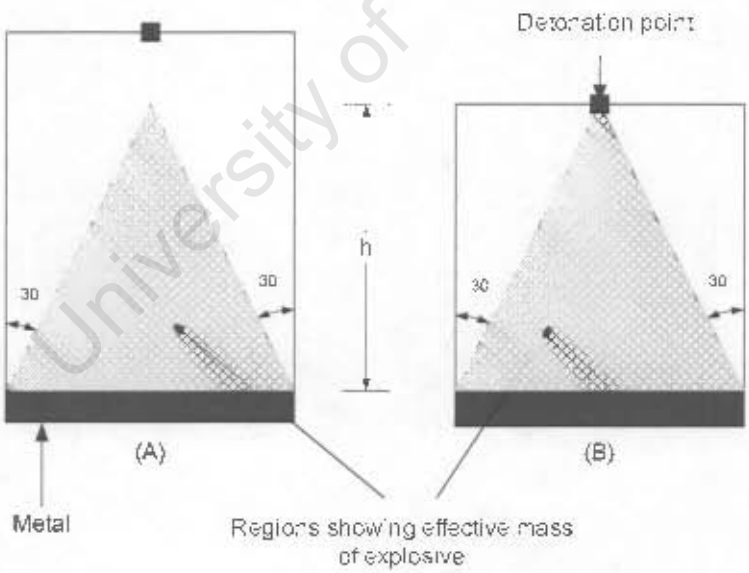

Figure 2.16: Discounting of sides of explosive to account for lateral release of explosive pressure; mass of unshaded region is not included [70].

2.5 Simulations of Explosives Using Hydrocodes

Hydrocodes are defined as numerical tools used for the simulation of continuum mechanics problems involving the deformation and flow properties of solids (computational solid mechanics - CSM) and fluids (computational fluid dynamics - CFD). Hydrocodes can also be defined as computational mechanics tools for the simulation of multi-material, compressible, wave propagation through multiple fluids and solids as reported in Mair [71]. According to Robertson *et al* [49], these numerical methods were used only for problems where very high pressures dominated material response and the materials were assumed to behave hydrodynamically (hence the term 'hydrocode'). Some of the wider applications of hydrocode simulations have been in the automobile industry for crash tests and sheet metal forming can be found in Frank and Gruber [72] and Galbrith and Finn [73] respectively.

Large-scale numerical simulations of explosions have been conducted for thirty-five years, but have historically been restricted to large and specialised computer programmes requiring substantial computer resources as reported in Robertson *et al* [49]. The main objective of developing hydrocodes was to illustrate and describe nonlinearity and hydrodynamic behaviour of an explosive during its rapid expansion and generation of high pressures as reported in Robertson *et al* [49]. Hydrocodes are also time dependent and are associated with wave propagation theory. The Rankine-Hugoniot jump equations of conservation of mass, momentum and energy at the C-J state can be solved by using hydrocodes. The formulations of such equations can be carried out by using either Lagrangian, Eulerian, or Arbitrary Lagrangian meshes to describe the deformation process. For a Lagrangian mesh, the material flows with the mesh (cell) as the deformation and flow of the material takes place, while in an Eulerian mesh, the mesh is fixed with the material flowing through it.

In a Lagrangian mesh, the length of an element during deformation affects the simulation negatively causing mesh distortion. When excessive distortion of the material occurs, leading to reduction in time steps, instability of the model causes the simulation to be aborted or gives very inaccurate results. In this regard mesh refinement of the model is important and has to be well investigated in order to obtain realistic results.

In the early 1960s and 1970s, some of the earliest codes were developed by

Mader [74]. These were the SIN code, a one-dimensional code and the two dimensional Lagrangian and Eulerian codes 2DL and 2DE, respectively. These codes dealt with the explicit chemistry and kinetics of the detonation or burning process. Since its inception, more sophisticated general purpose software codes have been developed such as the two dimensional Lagrangian HEMP code by Wilkins [75] and the Eulerian HELP code by Walsh *et al* [76] using the finite difference method and those that use the finite element method namely, DYNA, PRONTO, and ABAQUS. However, the AUTODYN code uses the finite difference, finite volume and finite elements methods. These codes have 2D and 3D versions.

2.6 Numerical Modelling of Blast Loaded Structures

Research in modelling the interaction of blast loads and structures has been going on for several decades. According to Nurick and Martin [77], [78], it was found that the initial focus of investigations was on blast loads that are distributed over the entire surface area of the structure in order to predict the central deformation and shape. This was believed to be too general as the load on the surface of the structure sometimes acts locally as in the case of a land mine explosion on a vehicle or in the case where a mach stem is formed very close to "ground zero" (point directly below the center of explosion on the target). In other words, localised loads occur, where the interaction area is far less than the total surface area of the structure. Some of the works which have considered using uniform rectangular loading on the entire surface of the structure can be found in Gelman *et al* [3], Olson *et al* [79], Teeling-Smith and Nurick [80] and Nurick and Lump [81]. The results in these works were reasonable with regard to the central deformation of the structure. The pressure generated using uniform rectangular loading on the entire surface area is estimated as given in equation 2.46

$$P = \frac{I}{A \cdot t} \tag{2.46}$$

where I is impulse, A is the loaded area and t the duration of blast.

Pan and Louca [82] carried out studies in which experimental and numerical

investigations on the response of stiffened plates subjected to gas explosions were reported. It was found that the stiffeners and boundary conditions influenced the response of the structure. Rudrapatna *et al* [83] numerically modelled clamped square stiffened steel plates subjected to blast loading. Geometric and material nonlinearity formed the basis of the numerical model. Failure was predicted using an interactive failure criterion comprising bending, tension and transverse shear. Schleyer and Hsu [84] analytically modelled the prediction of the response of elasto-plastic structures to pulse pressure loading. The load was modelled on the entire plate surface. The results compared reasonably well with the numerical simulation using the ABAQUS finite element code. The numerical approach was to address primarily the class of problems in which elastic effects are significant, pulse shape is irregular, boundary conditions are neither fixed nor simply supported and the loading is in the quasi-static to dynamic state.

However, as mentioned earlier, the load on a structure does not always act globally, but locally in some cases. In order to address the issue of localised loading on a structure, Nurick and Radford [2] Wierzbicki and Nurick [85], Symonds and Wiezbicki [86] modelled the load on a centralized area. Three decay loading conditions – linear, quadratic and cubic were suggested by [2]. Bimha *et al* [6] suggested the use of uniform pressure from the centre to the edge of the charge, after which the pressure begins to fall exponentially to the boundary of the plate assumed to be at atmospheric. Various other pressure profiles have been used to model the load distribution on the structure in order to predict the deformation and shape of structures subjected to blast loading as reported in Chung Kim Yuen and Nurick [87] and Muluh [88].

Balden and Nurick [89] published a paper on the numerical simulation of post-failure motion of blast loaded plates. The ABAQUS/Explicit code was used to carry out the simulations whilst the AUTODYN code was used to characterised the loading, time and spatial history on the structure. The paper is based on simulating previous experimental results published by Teeling-Smith and Nurick [80] and Nurick and Bryant [90]. The results compared reasonably well with experiments as regards the input energy, deformation and post-failure motion of the fragments. Chung Kim Yuen and Nurick [91] and Langdon *et al* [92] also recently published a two-part study on investigations of the response of blast loaded quadrangular plates of various stiffener conditions experimentally and numerically. Part one by [91], investigates the response of the structure

subjected to uniform loading, whilst part two by [92] investigates the response of the structure subjected to localised loading. The numerical model was carried out using the ABAQUS/Explicit 5.8 code for a 3-D quater-model incoporating adiabatic and high-strain rate effects in part one. The numerical simulations of the blast loaded structures were carried out by using the ABAQUS/Explicit 5.8 finite element programme. In both papers, tearing using temperature effects were predicted for various stiffened conditions.

However, one of the problems with these modelling techniques is that the shape of the explosives is not taken into consideration. Furthermore, it was assumed, that the blast wave is plane and is either partially or fully distributed uniformly on the surface of the structure on interaction. This assumption may not at all times be reasonable if the curvature and shape of the shock-wave are to be taken into consideration. The final shape of the shock wave after complete detonation is dependent on the initial shape of the explosive. As shown in figure 2.17, the shock-wave profile generated by a spherical charge has significant curvature which should be considered in the numerical model. This means that the shock wave first interacts with the structure at a point and eventually spreads within a localised central area.

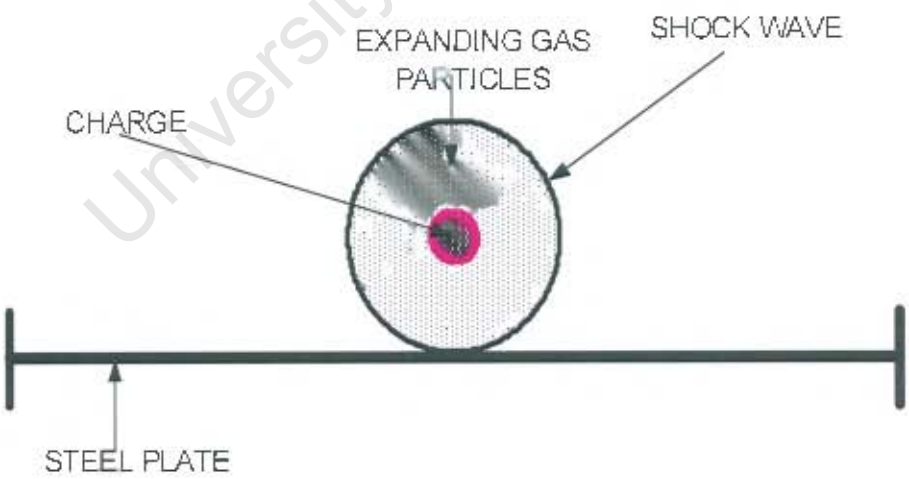

Figure 2.17: Interaction of a spherical shock-wave with a steel surface.

Numerical modelling of the medium between the explosive and target structure is also not considered in all these previous works. To consider modelling the

medium between the explosive and target structure, Yang [46] numerically simulated the response of buried shelters subjected to blast using the finite element package ABAQUS. The soil was modelled as a semi-infinite medium with an unbounded domain. The effects of the soil damping, the stiffness and dimensions of the structure, the depth of the weapon detonation and the stand-off distance on shock response were thoroughly discussed. Lain *et al* [93] also numerically simulated anti-tank mine detonations incoporating the soil in the material model. Various soil conditions were considered in the investigations. Simulation of energy absorption layer to protect structures against shock-waves was carried out by Wang *et al* [94] using a triple-layer absorptive structure designed to reinforce a missile silo against shock-wave blast. It was found that the absorption layer can significantly enhance survivability. Other related work that have considered numerical simulations of medium structure interaction can be found in O'Daniel and Krauthammer [95] using a 3-dimensional model in DYNA3D.

2.6.1 Numerical Simulation by *Grobbelaar and Nurick* [4]

Recent works which have considered modelling stand-off operations using the JWL equation of state can be found in Grobbelaar and Nurick [4]. The experimental results carried out by Nurick and Radford [2] were numerically modelled by Grobbelaar and Nurick [4] using the ABAQUS/Explicit 5.8 finite element code. The experiments were carried out for cylindrical shaped (CY) PE4 explosives at 12mm stand-off distance detonated at the centre of the top face. The explosive pressure on the structure was modelled using the JWL equation of state by considering the entire geometry of the explosive. The main objectives of Grobbelaar and Nurick's work were to numerically predict the central deformation and the plate profiles of the experiment.

Investigations were carried out on the element type of the plate and explosive used to predict the experiment. It was found that CAX4R (Continuum axi-symmetric 4 noded reduced integration) elements used for both the explosive and plate, predicted the experiment reasonably well compared to a 2-dimensional axi-symmetric elements (SAX1) as shown in figure 2.18. For SAX1 elements, the deformation of the plate did not match the experiments due to unrealistic increase in element elongation of the elements compared to CAX4R elements which gave a better and more realistic prediction of the plate deformation. Non-linear geometric and material effects were taken into account with regard to the steel

plate. However, adiabatic effects of the plate was not taken into consideration.

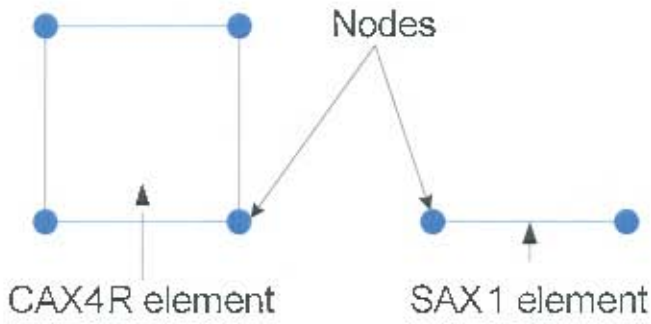

Figure 2.18: Figure showing schematics of a CAX4R and SAX1 elements.

The clamped boundary was modelled by encasting the top part of boundary of length (clamp length - plate thickness) from the end of the plate radius to the end of the outer boundary. This is because, it was observed that the top clamp end did not make contact with the plate up to one-plate thickness. Some of the works that have investigated modelling of the boundary of steel plates in various forms can be found in Gelman *et al* [3] and Thomas and Nurick [96]. In Gelman *et al* [3], it is reported that the radius of the plate at the boundary influences the central deformation and dimensionless impulse of the plate. Gelman *et al* [97] also modelled boundary conditions including fixed and clamped boundaries. The effect of radius at the boundary was also investigated and it was generally found that these conditions at the boundary influence the deformation.

Similar work has been carried out by Daykin [98]. In [98], V-shaped steel plates subjected to cylindrical explosives with adiabatic effects of the plate included in the numerical model were simulated. The results were reasonably predicted using the ABAQUS/Explicit code. Numerical modelling of explosives using the JWL EOS is also described in Hibbit *et al* [99] where a core formed by the placement of two pipes one inside the other was filled with plastic explosive. Four equally spaced detonation points around the circumference were detonated at the same time. It was observed that the inner pipe collapsed due to the explosive detonation products. The model represents a contact operation where the explosive is in direct contact with the target structure.

2.7 Material Modelling of Steel

When subjected to an applied force at various strain-rates, the physical nature and micro-structure of a steel change. For strain-rates higher than that at quasi-static condition, the result is a rise in the yield stress, due to strain hardening. On the other hand an increase in adiabatic heat occurs due to high frictional forces between molecules of the microstructure which further decrease the effective stress. Chung Kim Yuen [5], Wiehahn *et al* [113], and Muluh [88] considered adiabatic effects of steel plates subjected to blast loads in order to model the experiments. According to Soares *et al* [100], the temperature of steel subjected to high-strain rate can go up to several hundreds of degrees of Celsius. The increase in temperature of the steel reduces the effective stress of the steel which further accelerate the deformation process. Therefore it is of importance to incorporate adiabatic effects of the structure or material under high strain-rate.

To take account of strain-rate effects, various constitutive equations that have been formulated are discussed, including the Johnson-Cook material model [101], Zerilli-Armstrong [102], the constitutive equations relating stress, Young's modulus and temperature for steels developed by Cowper-Symonds [103] constitutive equation and the Masui *et al* [104] material model.

2.7.1 The Johnson-Cook Material model [101]

The Johnson-Cook [101] material model was proposed by Johnson and Cook in 1983 for materials subjected to large strain rates. Because of the development of powerful computer software packages, the Johnson-Cook material model can be used in software packages. It is a simple material model, yet gives reasonable results compared with more sophisticated models with more parameters, which may give better results but difficult to implement in commercial codes. The Von Mises flow stress of the material is a function of the strain, the strain rate and temperature as shown in equation 2.47.

$$\overline{\sigma} = [A + B\varepsilon^{n}][1 + C \ln \varepsilon^{*}][1 - \dot{T}^{*}] \tag{2.47}$$

ε^{*} is the equivalent flow strain, $\varepsilon^{*} = \frac{\dot{\varepsilon}}{\dot{\varepsilon}_0}$ is the dimensionless plastic strain rate for $\dot{\varepsilon}_0 = 1.0s^{-1}$, C is the strain-rate constant and T^{*} is the homogeneous temperature given in equation 2.48, where T_{ref} and T_{melt} are the reference and melting

temperatures.

$$T^* = \frac{T - T_{ref}}{T_{melt} - T_{ref}} \tag{2.48}$$

As strain-rate increases, the yield stress also increases with a corresponding increase in adiabatic heat in the material. The effects of an increasing adiabatic heat causes a corresponding decrease in flow stress. This interplay between the increase in flow stress caused by strain rate increase and a reduction of the flow stress caused by the increase in adiabatic effects occurs when a material deforms at high strain-rate. One of the advantages of using the Johnson-Cook model is that the fracture length of the material is not limited to a particular strain-rate as opposed to the other models which do not include the strain value beyond and below the true strain at quasi-static condition as discussed in Bonorchis, [105].

A modified Johnson-Cook (MJC) model was formulated by Holmquist and Johnson [106] and also discussed in Rule and Jones [107], Liang and Khan [108] and Bonorchis [105]. According to Rule and Jones [107], many ductile materials experience an enormous increase in yield strength, increasing more rapidly with increase in strain-rate in excess of $10^3 s^{-1}$, than that given in equation 2.47. To increase the strain-rate sensitivity, a modified Johnson-Cook model was proposed by Holmquist and Johnson [106] as given in equation 2.49.

$$\overline{\sigma} = [C_1 + C_2 \varepsilon^N][\varepsilon^{*\alpha}][1 - \dot{T}^{*M}] \tag{2.49}$$

where α is an empirical exponent. However, the MJC model does not appear to be used widely because the strain-rate sensitivity is not significantly enhanced over that provided by equation 2.47.

Following the formulation of the MJC model, is the revised Johnson-Cook (RJC) model given in Rule and Jones [107] in equation 2.50. The aim was to enhance strain-rates far in excess of $10^3 s^{-1}$ as opposed to that given in equation 2.47.

$$\sigma = (C_1 + C_2 \varepsilon^N)\left[1 + C_3 \ln \varepsilon^* + C_4 \left(\frac{1}{C_5 - \ln \varepsilon^*} - \frac{1}{C_5}\right)\right](1 - T^{*M}) \tag{2.50}$$

where C_4 and C_5 are additional empirical coefficients. The strain-rate sensitivity has been enhanced by the term $\frac{1}{C_5 - \ln \varepsilon^*}$, where C_5 is the natural logarithm of a critical strain level. The term tends to infinity as the strain-rate approaches the critical strain-rate.

2.7.2 Zerilli-Armstrong Material Model [102]

The material model proposed by Zerilli-Armstrong [102] is also a model which relates the flow stress with the strain, strain rate, and temperature of the material. It however specifically deals with each material based on its chemical structure such as FCC and BCC, as reported in Liang and Kahn [108]. The constitutive relations were proposed in order to better describe the individual material responses during the simulation of Taylor impact tests. In summary, two basic equations are proposed by Zerilli-Armstrong [102] for FCC and BCC material structures as given in equations 2.51 and 2.52 respectively.

$$\overline{\sigma} = C_0 + C_2 \varepsilon^{\frac{1}{2}} \exp(-C_3 T + C_4 T \ln \varepsilon) \tag{2.51}$$

$$\overline{\sigma} = C_0 + C_1 \varepsilon^{\frac{1}{2}} \exp(-C_3 T + C_4 T \ln \varepsilon) + C_5 \varepsilon^{n} \tag{2.52}$$

where $C_0 = \triangle\sigma_G^{'} + kl^{-\frac{1}{2}}$, $\triangle\sigma_G^{'}$ is included as an extra stress component which occur due to the influence of solute and the original dislocation density on the yield stress, $kl^{-\frac{1}{2}}$ accounts for the increased flow stress at low temperatures, T is the absolute temperature and n is the strain hardening constant. According to Liang and Kahn [108], one of the problems with equation 2.52 is that the strain hardening is independent of temperature, which is not true as most BCC metals have a work hardening behaviour which are dependent on strain-rate and temperature.

2.7.3 Cowper-Symonds Material Model [103]

The Cowper-Symonds [103] material model relates the stress and strain rate of a material as shown in equation 2.53. Temperature effects are not considered in the model. The equation also includes the flow stress at strain rate equal to zero. The Cowper-Symonds [103] material model is included in the ABAQUS/Explicit finite element code in which $\sigma_0^{'}$ is defined as the dynamic flow stress at a uniaxial plastic strain rate $\dot{\varepsilon}$, σ_0 is the static flow stress and D and q are material specific constants. For mild steel these constants are taken as $40.4s^{-1}$ and 5 respectively.

$$\frac{\sigma_0^{'}}{\sigma_0} = 1 + \left(\frac{\dot{\varepsilon}}{D}\right)^{\frac{1}{q}} \tag{2.53}$$

2.7.4 Masui *et al* Material Model [104]

Equations relating stress, Young's modulus and temperature of mild steel were proposed by Masui *et al* [104]. The Young's modulus and yield stress are related to the temperature as given in equations 2.54 and 2.55.

$$E = E_0 - 58.34 \cdot 10^6 \cdot T \quad \text{for } T \leq 600°C$$

$$E = 3.1 \cdot 10^5 (T - 1100)^2 + 97.9 \cdot 10^9 \quad \text{for } 600°C < T \leq 1100°C \tag{2.54}$$

$$\frac{\sigma_y}{\sigma_0} = 1 \quad \text{for } T \leq 200°C$$

$$\frac{\sigma_y}{\sigma_0} = 1 - 0.00178(T - 200) \quad \text{for } 200°C < T < 700°C \tag{2.55}$$

$$\frac{\sigma_y}{\sigma_0} = 0.133 - 0.000388(T - 700) \quad \text{for } 700°C \leq T \leq 1000°C$$

where σ_y is the yield stress at the reference temperature, σ_0 is the yield stress at the initial temperature of the material and T, the reference temperature of the material. The relationship between the Young's modulus, yield stress and temperature of the material are shown in figure 2.19.

The figure shows that the Young's modulus decreases linearly with temperature up to 600°C after which it decreases quadratically with increase in temperature. With regard to the Yield stress, the value remains constant up to 200°C and decreases as the temperature increases to 700°C. After 700°C, the yield stress continues to decrease with a lower gradient.

Coupled with the equations proposed by Cowper-Symonds [103], the material model by Masui *et al* [104] has been used to predict the behaviour of impulsively loaded steel plates with a reasonable degree of accuracy as found in Chung Kim Yuen [5], and Muluh [88].

2.8 Summary

A review of explosive detonation theory including the simple (ZND) and simplest (C-J) detonation theories has been carried out in this chapter. Following this,

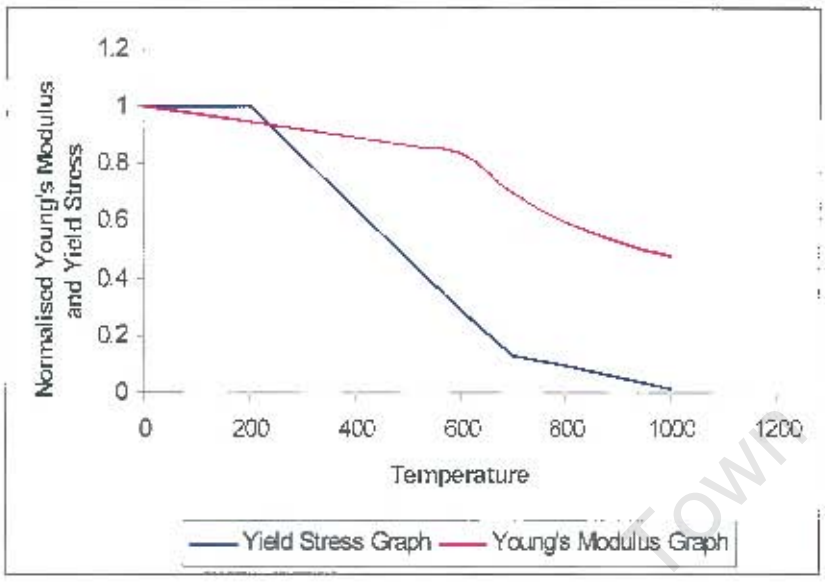

Figure 2.19: Normalised graphs for Young's modulus and Yield stress with temperature variation [104].

is the discussion of the development of equations of state of explosives and their applications to numerical simulations for the predictions of blast loaded structures. More emphasis is given to the Jones-Wilkins-Lee (JWL) equation of state. A review of several constitutive equations for mild steel with more emphasis on the Johnson-Cook constitutive equation is also discussed.

From a review of the experiments and predictions of blast loaded structures, it is established that studies of small charges of TC and ITC explosives have not been reported. The search for an answer to the influence of TC and ITC explosives on circular plates experimentally, analytically and numerically is the main objective of this current research.

Chapter 3

Experimentation

3.1 Introduction

This chapter describes the experimental procedure carried out in the blast laboratory for the various shapes and sizes of explosives considered in this research namely, CY, TC and ITC explosives. Experiments on the investigations of the effect of TC and ITC explosives have not been reported in the literature. The aim of this chapter is to experimentally investigate the influence of shape of solid explosives on interaction with a structure. Nine tensile tests of the steel plates at quasi-static conditions are carried out and presented in order to investigate the behaviour of the plate at high strain rates. Plastic moulds are also used in this research to form the various shapes of explosives in question. A total number of 33 experiments are performed with the masses and dimensions of the charges given in Appendix A. The ballistic pendulum on which the test rig is attached, is used to measure the impulse of the blast.

3.2 Experimental Procedure

3.2.1 Test and Clamp Plates

Before the experiments are carried out, the test and clamp plates are first prepared as shown in figures 3.1 and 3.2. The 100mm diameter hole formed by the clamp plates creates the loaded area on the test plate which then deforms on interaction with the blast load.

The explosive shapes are then formed using the required plastic mould and

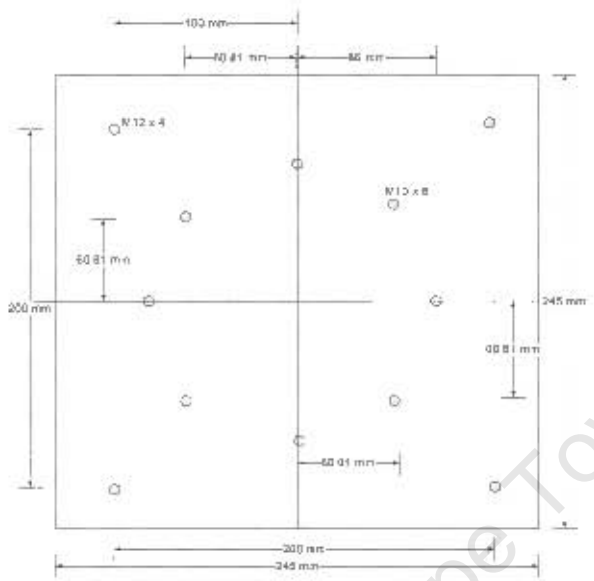

Figure 3.1: Figure showing schematic of 1.6mm thick test plate.

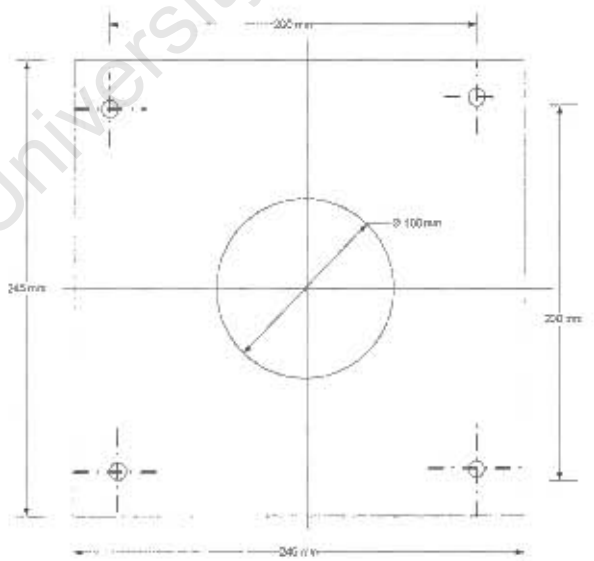

Figure 3.2: Figure showing schematic of 20mm thick clamp plate.

placed on top of a 20mm polystyrene foam pad, which forms a stand-off between the explosive and plate as shown in figure 3.3.

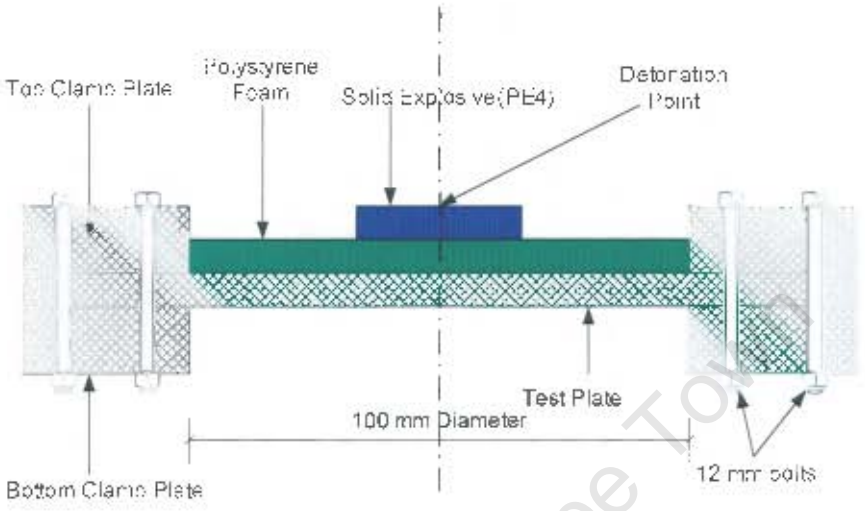

Figure 3.3: Figure showing schematic diagram of explosive, polystyrene and plate set up.

3.2.2 Material Properties of the Steel Plate

In order to carry out the tensile tests of the test plates at various strain-rates under quasi-static conditions, nine "dog-bone" specimens are cut out from the test plates as shown in figure 3.4. A gauge length of 45mm is used as the effective length of the specimen achieved with the use of an extensometer during the tensile tests.

The engineering stress-strain properties of the steel at various strain rates are shown separately in graphs (A), (B) and (C) of figure 3.5 and also shown in a single plot in figure 3.6. Nine experiments for the tensile tests of the steel are carried out at three different strain rate of $0.001s^{-1}$, $0.01s^{-1}$, $0.05s^{-1}$. For each strain rate, three repeated tests are carried out.

The curves in figures 3.5 and 3.6 are then converted to curves of zero strain-rates using the Cowper-Symonds equation [103] described in chapter 2 and given here in equation 3.1 for clarity.

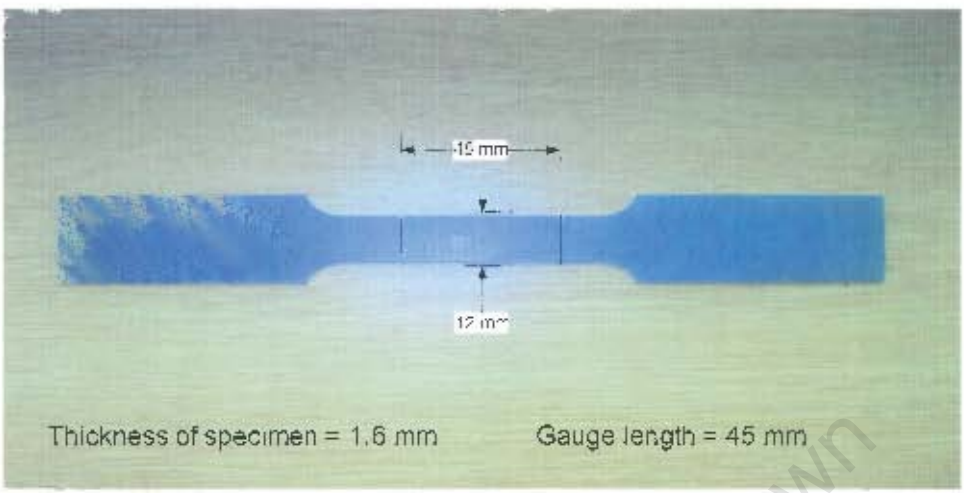

Figure 3.4: Photograph of "dog-bone" specimen used for tensile testing of the steel.

$$\frac{\dot{\sigma_{nom}}}{\sigma_0} = 1 + \left(\frac{\dot{\varepsilon}_{nom}}{D}\right)^{\frac{1}{q}} \tag{3.1}$$

The true stress-strain of the curves are shown in figures 3.7 and 3.8 obtained by using equations 3.2 and 3.3.

$$\sigma_{true} = \sigma_{nom}(1 + \varepsilon_{nom}) \tag{3.2}$$

$$\varepsilon_{ln}^{pl} = \ln(1 + \varepsilon_{norm}) - \frac{\sigma_{true}}{E} \tag{3.3}$$

where σ_{nom} is the nominal stress, ε_{norm} the nominal strain, E is the Young's modulus, $D = 40.4s^{-1}$ and $q = 5$.

From all the results, the average yield stresses at quasi-static condition (σ_0) using the Cowper-Symonds equation is 254MPa as shown in table 3.1 where V_C is the cross-head speed. To get an average stress-strain curve, the curve with a static yield stress (σ_0) of 253MPa (closest to average) corresponding to 283MPa (σ_{nom}) at strain-rate of $0.001s^{-1}$ in table 3.1 is chosen. The average true-stress true-plastic strain curve is shown in figure 3.9.

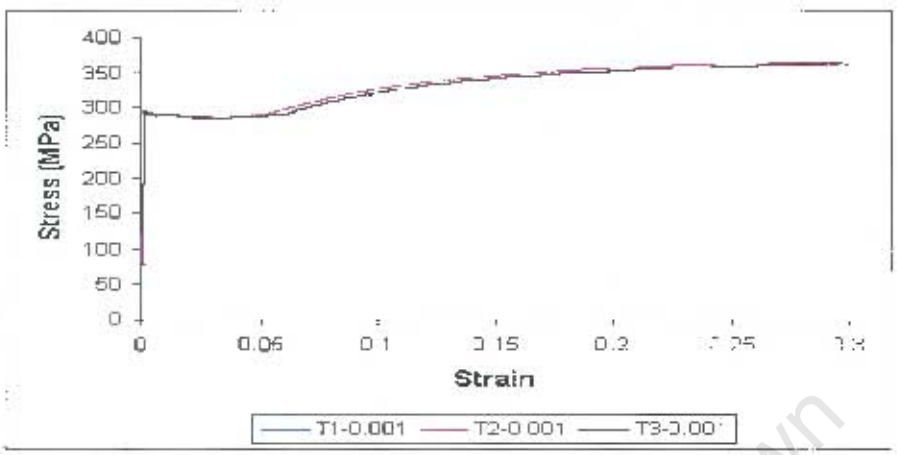

(A) Tensile tests at strain-rate of 0.001s^{-1}.

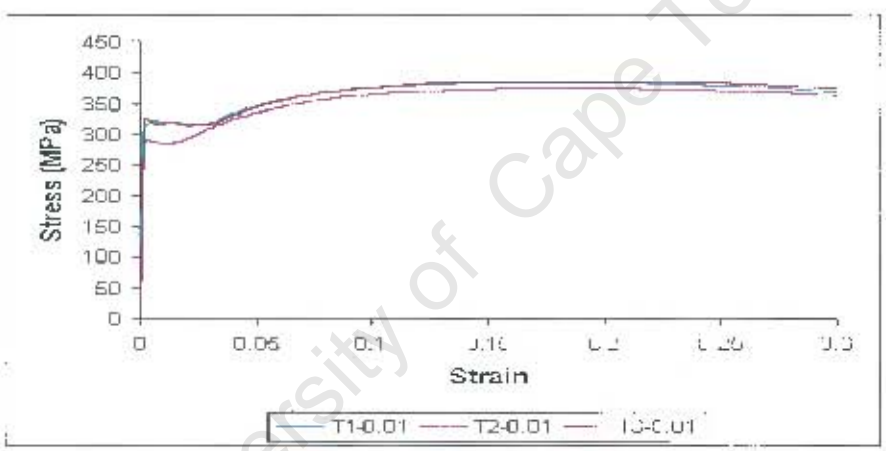

(B) Tensile tests at strain-rate of 0.01s^{-1}.

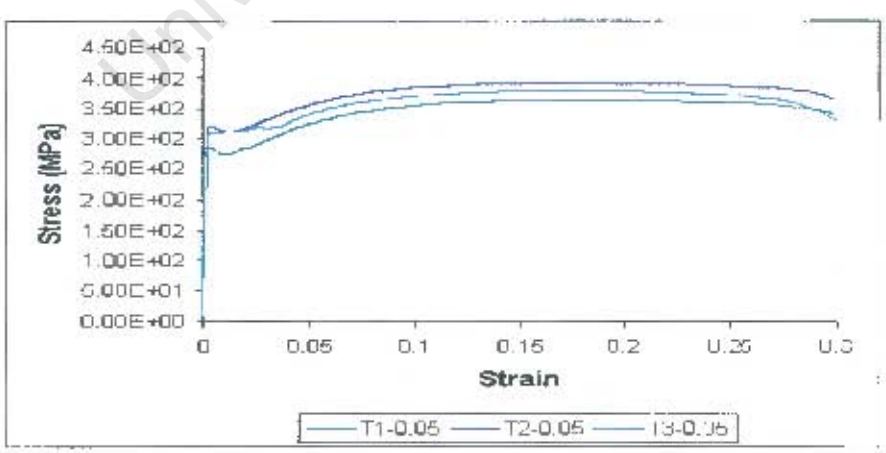

(C) Tensile tests at strain-rate of 0.05s^{-1}

Figure 3.5: Graphs showing engineering stress-strain relationship of mild steel at strain-rates of $0.001s^{-1}$, $0.01s^{-1}$and $0.05s^{-1}$ in (A), (B) and (C) respectively.

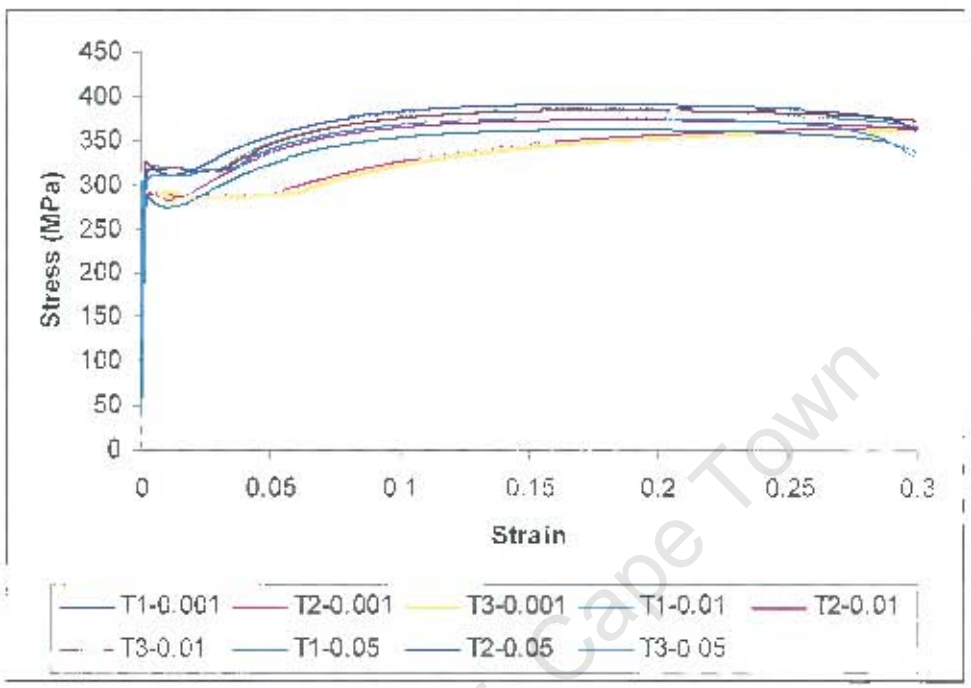

Figure 3.6: Graphs showing engineering stress-strain relationship of mild steel at various strain-rates.

No.	σ_{nom}(MPa)	$\dot{\varepsilon}(s^{-1})$	σ_0(MPa)	V_C(mm/s)
Test 1	283	0.001	253	0.045
Test 2	290	0.001	259	0.045
Test 3	293	0.001	262	0.045
Test 4	287	0.01	263	0.45
Test 5	302	0.01	259	0.45
Test 6	278	0.01	239	0.45
Test 7	284	0.05	239	2.25
Test 8	305	0.05	256	2.25
Test 9	307	0.05	259	2.25
		Average	**254**	

Table 3.1: Table showing values of yield stress at various strain rates and static conditions

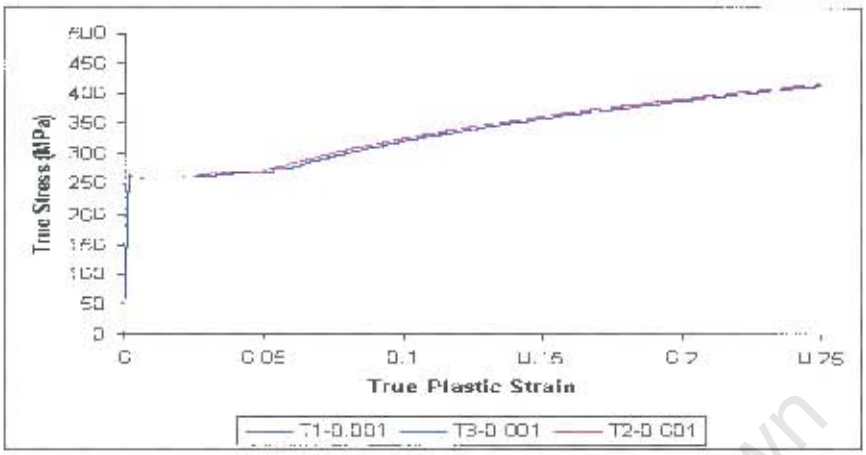

(A) True stress-strain curves at zero strain-rate with initial strain-rate of 0.001s^{-1}

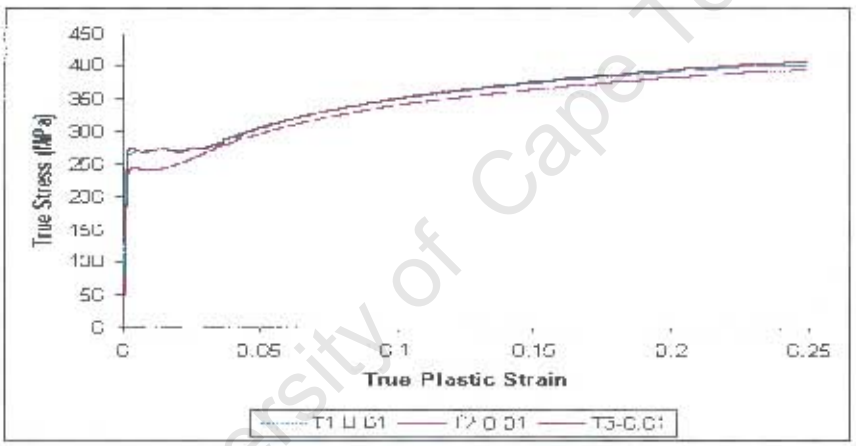

(B) True stress-strain curves at zero strain-rate with initial strain-rate of 0.01s^{-1}

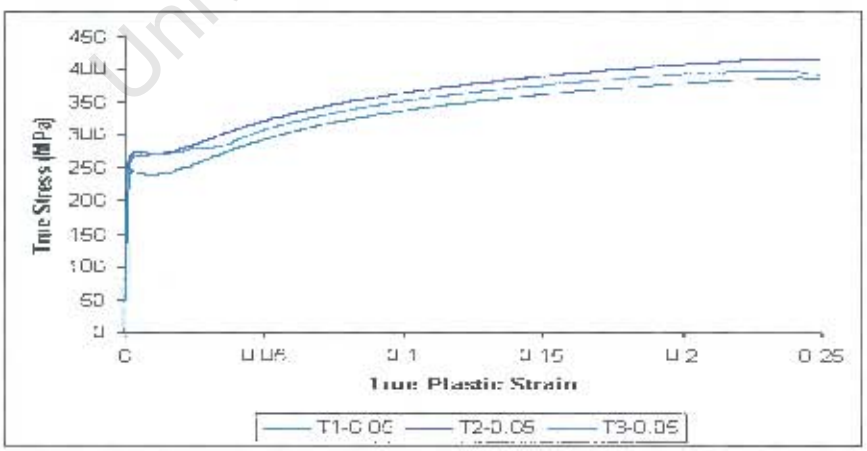

(C) True stress-strain curves at zero strain-rate with initial strain-rate of 0.05s^{-1}

Figure 3.7: Graphs showing true stress-strain relationship of mild steel at initial strain-rates of $0.001s^{-1}$, $0.01s^{-1}$and $0.05s^{-1}$ in (A), (B) and (C) respectively.

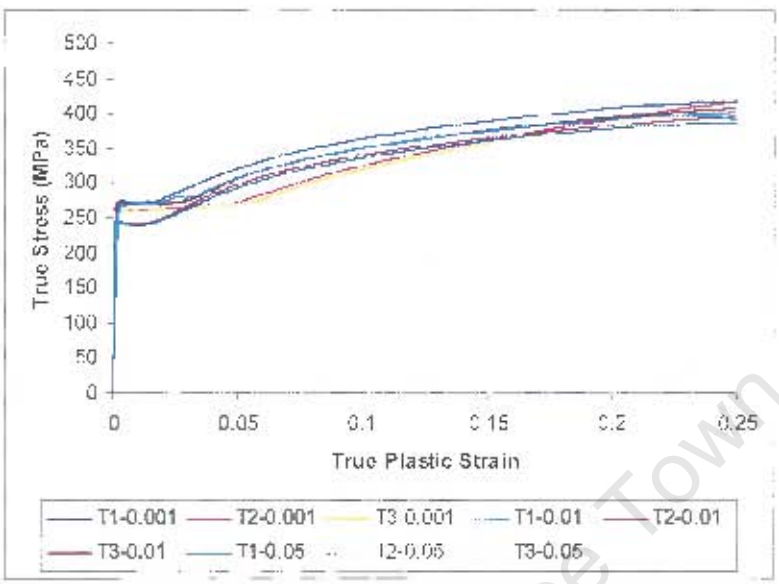

Figure 3.8: Graphs showing stress-strain relationship of steel at zero strain rate for all tensile tests.

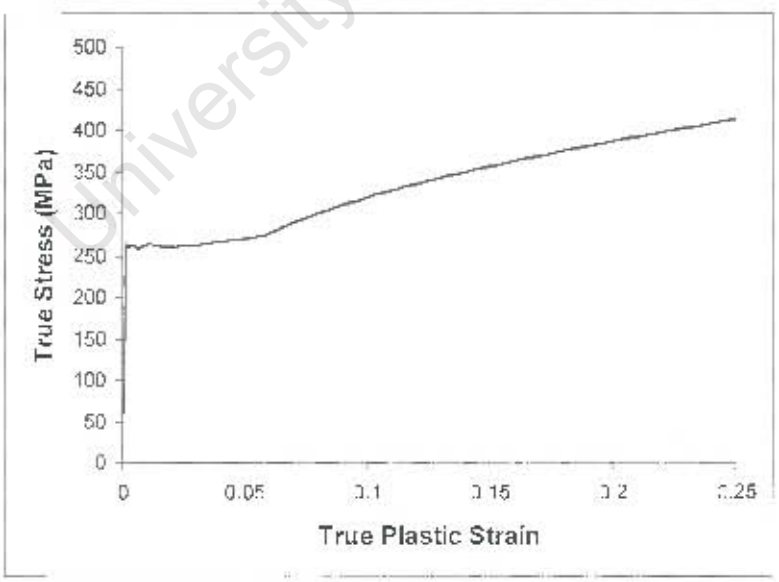

Figure 3.9: Graph showing average true-stress vs. true-strain for mild steel at static condition.

3.2.3 Forming the Explosive Shapes

The explosive shapes in this work are formed using plastic moulds as shown schematically and photographically in figures 3.10, 3.11 3.12 and 3.13 for a Cylinder explosive (CY) and for an Inverted Truncated Cone (ITC) respectively. The moulds shown in figure 3.12 and 3.13 are used to form both the ITC and TC explosives. The mass of the explosive is first estimated based on the dimensions and density of the explosive before being shaped by using the required mould. Appendix A lists the sizes and shapes of the various explosive charges used in the experiments. Photographs of all the moulds used to form the various explosive shapes and sizes are shown in appendix A.1.

An oblique view for 2.6g of 18mm CY, TC and ITC explosives formed by the required moulds is shown in figure 3.14.

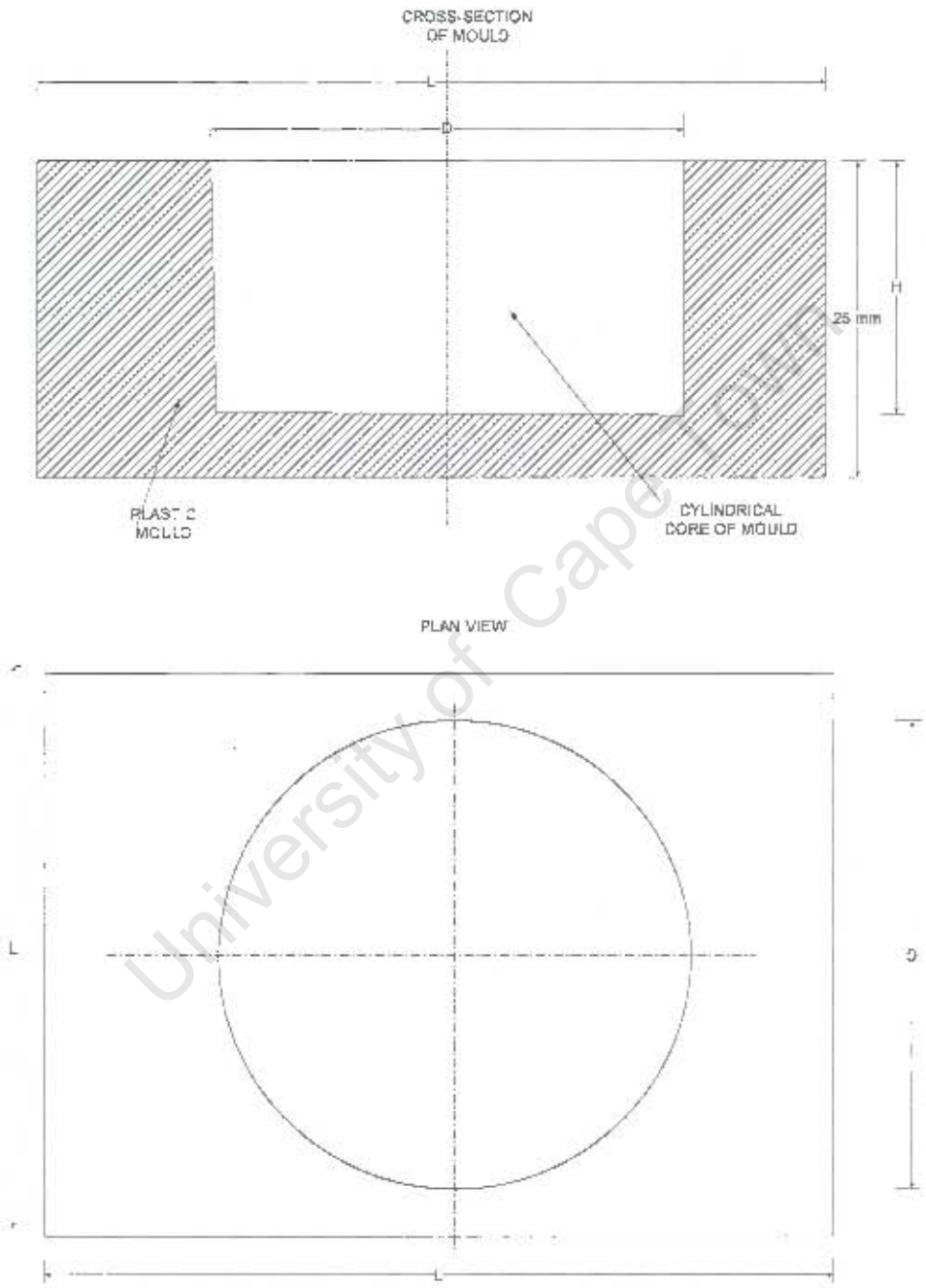

Figure 3.10: Schematic of cross-section of a CY explosive mould.

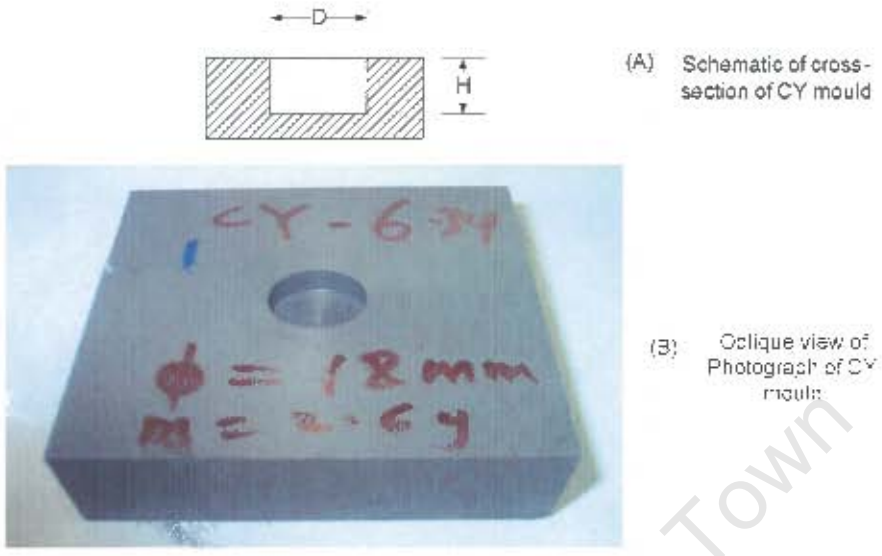

Figure 3.11: Photograph and schematic of a CY explosive mould.

3.3 The Ballistic Pendulum Test

The experimental procedure in this work is not new and has been well explained in Teeling-Smith and Nurick [80] and Bodner and Symonds [109]. A schematic diagram of the ballistic pendulum shown in figure 3.15 is used to carry out the test in order to measure the impulse of the blast. The pendulum is supported by four wires of equal lengths and tensions. The tensions of the wires must be equal in order to allow the recording pen to move in the axial direction of the blast load constantly.

At one end of the pendulum, a test plate sandwiched by two clamp plates is attached to a support plate, by way of connecting metal pipes of external diameters 12mm. Before each test, the pendulum is balanced by the use of masses attached to the other end of the pendulum. This is to ensure that the centroid of the pendulum is in the middle of the wires. A photograph of the set up is also shown in figure 3.16.

When the explosive is detonated, the pendulum moves in the axial direction of the blast. The maximum oscillations in the forward and backward movement of the pendulum is recorded. Appendix B gives the method of determining the impulse of the blast measured by the pendulum. After the test, the total deformation and specifically the central deformation of the plate and impulse of

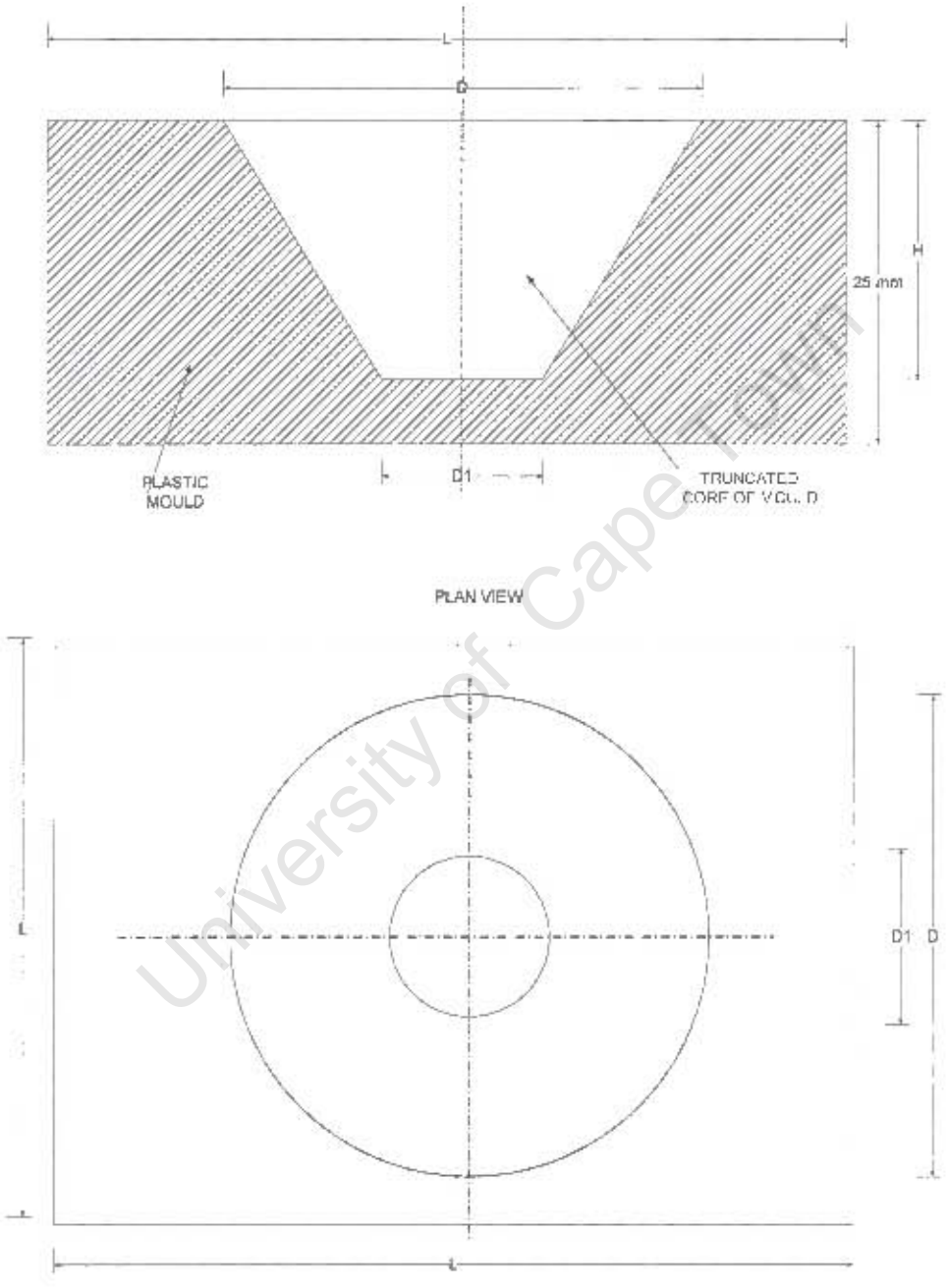

Figure 3.12: Figure showing schematic of cross-section and plan of a TC/ITC explosive mould.

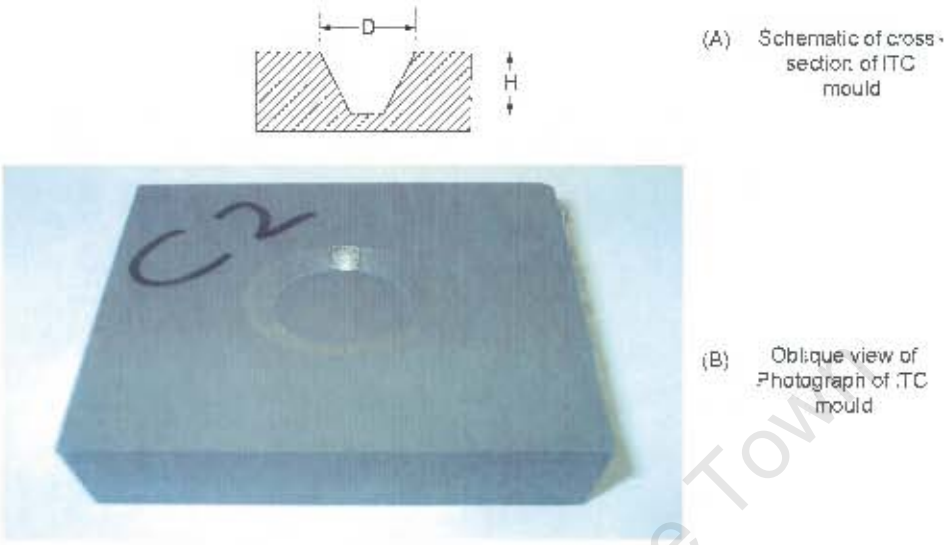

Figure 3.13: Photograph and schematic of an ITC/TC explosive mould.

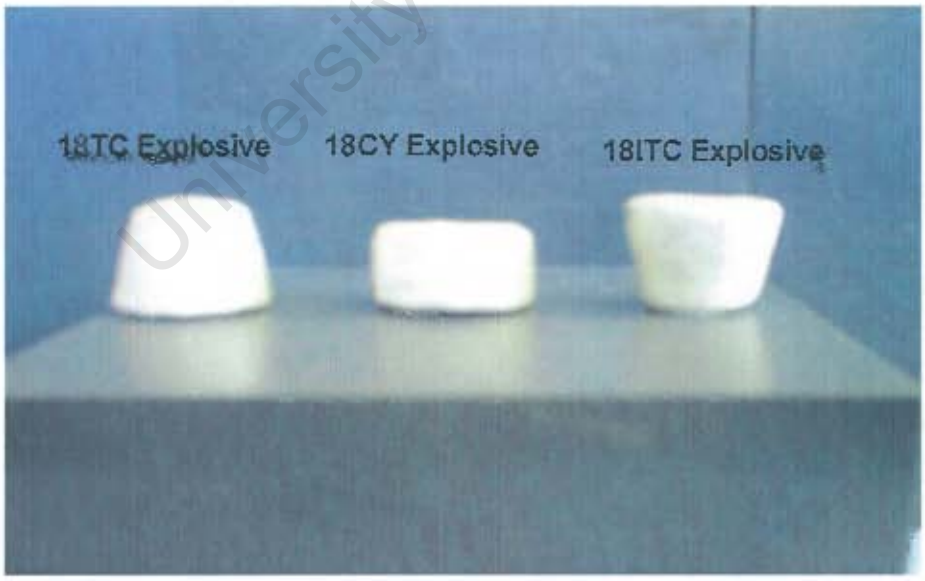

Figure 3.14: Photograph of TC, CY and ITC explosives of mass 2.6g each and maximum diameter 18mm.

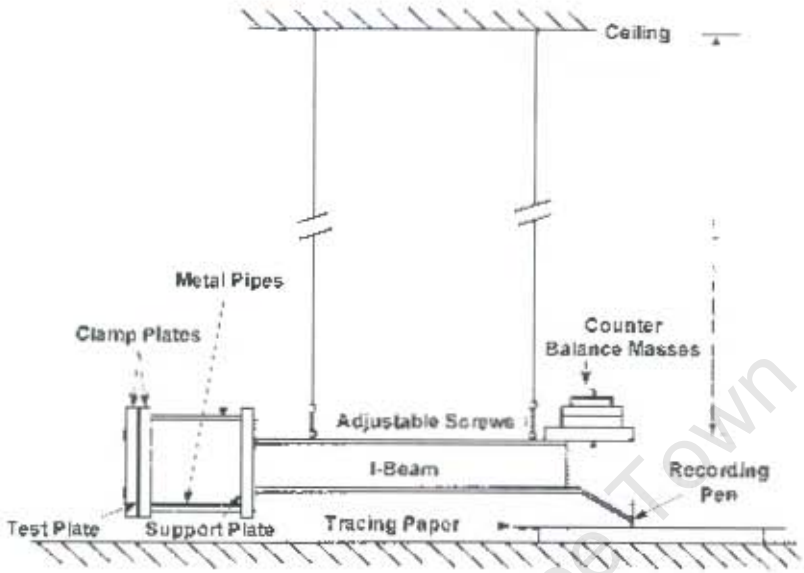

Figure 3.15: Figure showing schematic diagram of pendulum used to measure the blast impulse.

Figure 3.16: Photograph showing set up of experimentation in the blast lab.

the blast are measured and recorded as presented in chapter 4.

3.4 Summary

The experimental procedure in this work has been well described. A total of 33 test plates are used to carry out the experiments with a thickness measuring 1.6mm and loaded area of diameter 100mm. An average true stress-strain curve at quasi-static condition was obtained from nine tensile tests using a "dog-bone" specimen cut from the test plate. The use of plastic moulds to form the various shapes of explosives, will improve the repeatability of the experimental procedures. The ballistic pendulum to which the test rig containing the plate and explosive on one side is then used to measure the impulse of the blast. From the experiments, the total deformation of the plate and impulse of the blast measured by the ballistic pendulum are recorded and presented in chapter 4.

Chapter 4

Experimental Results

4.1 Introduction

The experimental results of the plates subjected to blast loads are presented in this chapter. The results are presented in the form of photographs, tables and graphs. The results of the plate deformation are presented in two forms: First, results of the plate deformations subjected to explosives of the same mass with varying shapes, followed by results, where the shape of the explosive is unchanged but with varying mass for each load diameters 18mm, 25mm and 33mm are presented. The impulse measured by the pendulum from the experiments are also presented.

4.2 Results for 18mm Load Cases

4.2.1 Effect of Shape of 18mm Explosive Charge on Central Deformation of Plate

The effect of shape of explosives on the deformation for 18mm load cases are shown in photographs 4.1, 4.2, 4.3 and 4.4. As shown in figures 4.1, 4.2, 4.3 and 4.4, where the masses of the explosive are the same for each shape of explosive, the TC explosive generally gives a higher central deformation with the ITC explosive having the lowest deformation. This is more evident in figure 4.4, in which the TC explosive causes a Mode IIc (capping) deformation, the CY causes a Mode II*c (partial capping) deformation and the ITC explosive causes a Mode

I deformation.

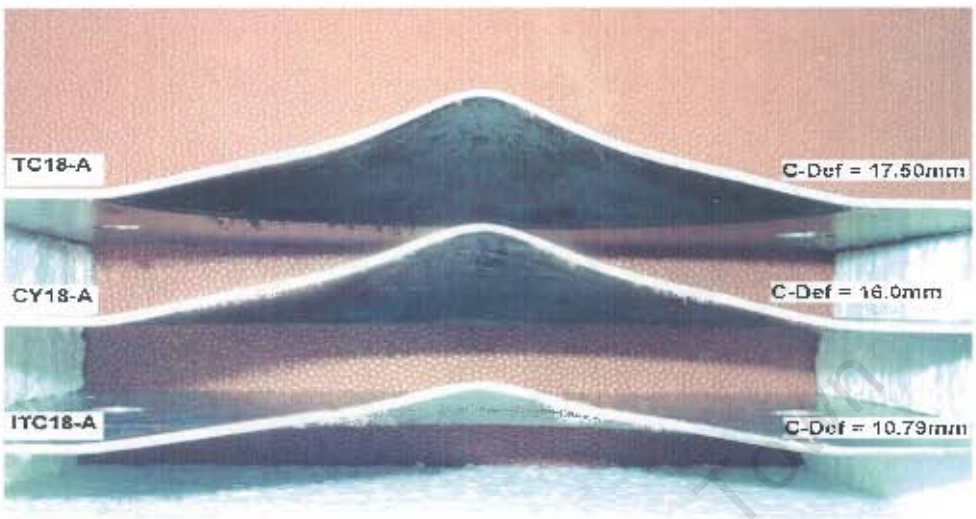

Figure 4.1: Photograph of cross-section of plates subjected to 2.6g CY, TC and ITC 18mm explosives.

4.2.2 Effect of Mass of 18mm Explosive Charge on Central Deformation of Plate

The effect of mass of explosive on the plates are shown photographically in figures 4.5, 4.6 and 4.7. Each result shows an increase in central deformation ranging from Mode I to rupture at the central part of the plates and graphically presented as shown in figure 4.8. It is observed that two of the TC explosively loaded plates show complete capping at the central area. No capping is observed for the ITC explosively loaded plates with one plate showing a Mode II*c (partial tearing) subjected to a CY explosive in figure 4.5.

Results of the central deformation of the plate for the CY explosives are higher than those of the ITC explosives and much closer to those given by the TC explosives. Also shown in figure 4.8, are the results of the TC and CY explosively loaded plates generally showing a higher deformation of the plate leading to rupture at the central area. The results of the central deformation of the plates caused by the ITC explosives are much lower than those caused by the CY and TC explosively loaded plates.

Figure 4.2: Photograph of cross-section of plates subjected to 3.2g CY, TC and ITC 18mm explosives.

Figure 4.3: Photograph of cross-section of plates subjected to 3.7g CY, TC and ITC 18mm explosives.

Figure 4.4: Photograph of cross-section of plates subjected to 4.3g CY, TC and ITC 18mm explosives.

Figure 4.5: Photograph of cross-section of plates subjected to 18mm CY explosives of varying mass.

Figure 4.6: Photograph of cross-section of plates subjected to 18mm TC explosives of varying mass.

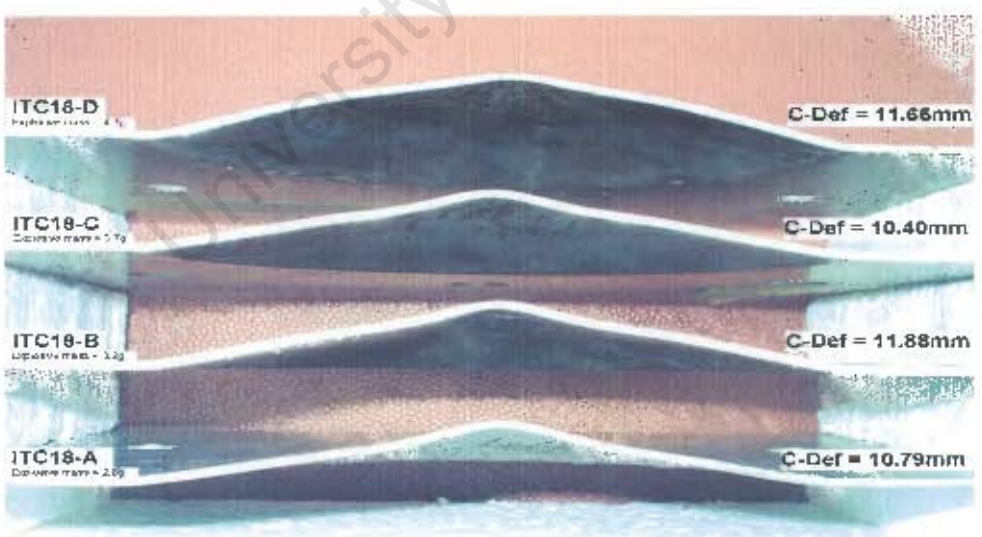

Figure 4.7: Photograph of cross-section of plates subjected to 28mm ITC explosives of varying mass.

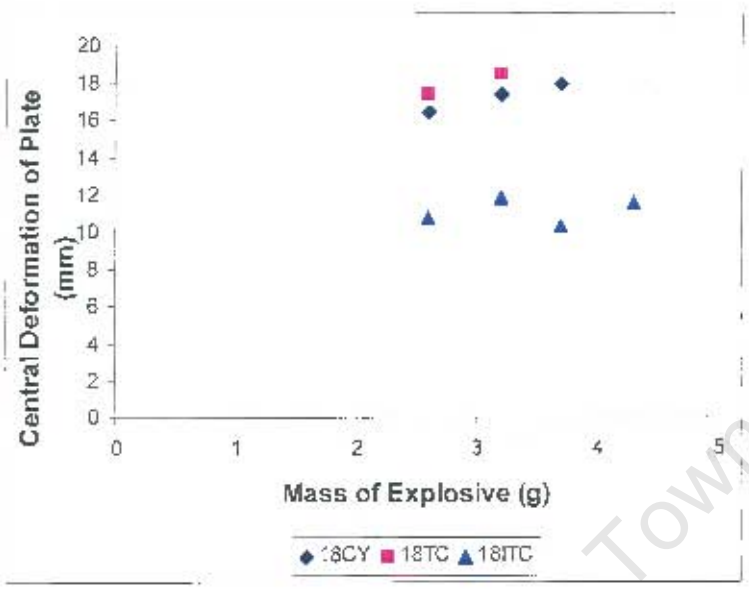

Figure 4.8: Graph showing central deformation of plate vs. mass of explosive for all 18mm TC, CY and ITC explosives.

Results of the central deformation and impulse are tabulated and presented for all 18mm load cases as shown in tables 4.1, 4.2 and 4.3.

Test No.	Mass of Explo.(g)	Def.(mm)	Imp.(Ns)	Comments
CY18-A	2.6	16.50	6.10	
CY18-B	3.2	17.47	7.09	
CY18-C	3.7	18.00	7.60	
CY18-D	4.3	-	8.71	ModeII*c

Table 4.1: Table showing central deformation of plate and impulse for 18mm CY explosives

Test No.	Mass of Explo.(g)	Def.(mm)	Imp.(Ns)	Comments
TC18-A	2.6	17.5	6.10	
TC18-B	3.2	18.59	6.30	
TC18-C	3.7	-	6.90	Capping
TC18-D	4.3	-	7.17	Capping

Table 4.2: Table showing central deformation of plate and impulse for 18mm TC explosives

Test No.	Mass of Explo.(g)	Def.(mm)	Imp.(Ns)	Comments
ITC18-A	2.6	10.79	6.90	
ITC18-B	3.2	11.88	7.20	
ITC18-C	3.7	10.40	7.85	
ITC18-D	4.3	11.66	8.86	

Table 4.3: Table showing central deformation of plate and impulse for 18mm ITC explosives

4.2.3 Effect of Shape and Mass of 18mm Explosive on Impulse of Blast

Results of the impulse of the blast measured by the pendulum are plotted out as shown in figure 4.9. Results of the impulse of the ITC loaded plates are slightly higher than those of the CY explosives, but much higher than those of the TC explosives. The results also show an increase in impulse with a corresponding increase in mass for each shape of explosive.

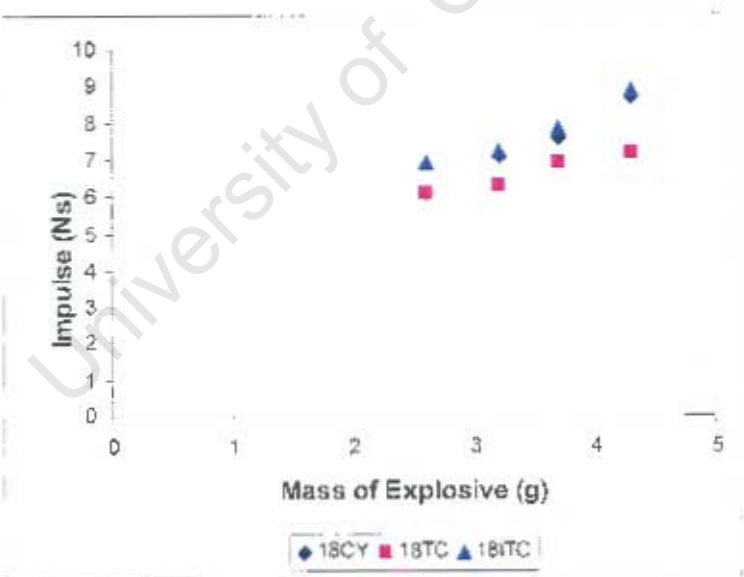

Figure 4.9: Graph showing mass of explosive vs. impulse of blast for 18mm CY, TC and ITC explosives.

4.3 Results for 25mm Load Cases

4.3.1 Effect of Shape of 25mm Explosive Charge on Central Deformation of Plate

Results showing the effect of comparing the deformation of the plates subjected to TC, CY and ITC explosives of the same mass, are presented for 25mm explosives as shown in figures 4.10, 4.11 and 4.12. The results show a similar pattern as those of the 18mm load cases in which the TC explosive causes a bigger central deformation leading to capping compared to those of ITC explosives which did not cause any tearing of the plates. In figure 4.13, the results graphically show a slight higher value of central deformation of the TC loaded plates than the CY loaded plates and far higher than the ITC loaded plates.

Figure 4.10: Photograph of cross-section of plates subjected to 3.0g CY, TC and ITC 25mm explosives.

4.3.2 Effect of Mass of 25mm Explosive Charge on Central Deformation of Plate

The effect of plate deformation on increasing the mass of explosive is shown in figures 4.14, 4.15 and 4.16. The results show that the central deformation of the

Figure 4.11: Photograph of cross-section of plates subjected to 3.6g CY, TC and ITC 25mm explosives.

Figure 4.12: Photograph of cross-section of plates subjected to 4.7g CY, TC and ITC 25mm explosives.

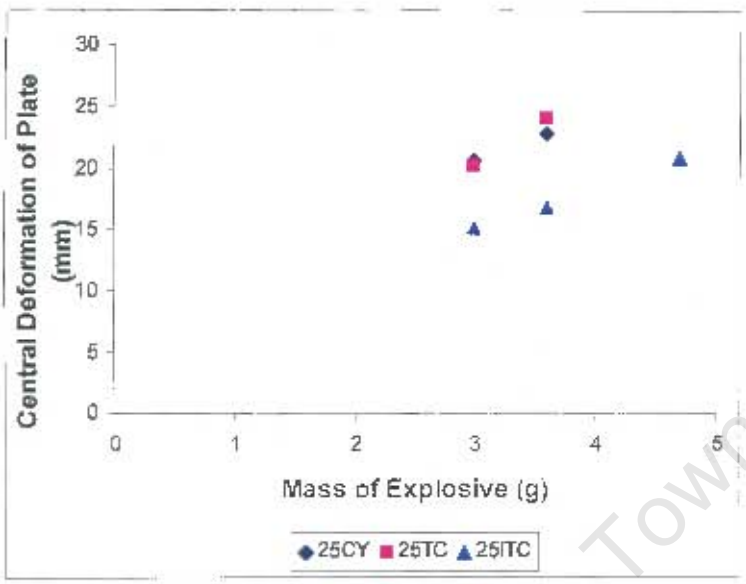

Figure 4.13: Graph showing central deformation of plate vs. mass of explosive for all 25mm TC, CY and ITC explosives.

plate increases as the mass of the explosive increases. The results also show a general pattern of deformation ranging from Mode I (large inelastic deformation) to Mode II (capping around central area) of the plate compared to the 18mm load cases.

4.3.3 Effect of Shape of 25mm Explosive Charge on Impulse of Blast

Results of the impulse of the blast and central deformation of the plate are presented in tables 4.4, 4.5, and 4.6 for all 25mm load cases. Also, results of the impulse of the blast measured by the pendulum in tables 4.4, 4.5, and 4.6 are shown graphically in figure 4.17. It can be seen in figure 4.17 that the ITC explosives causes a slightly higher impulse measured by the pendulum compared to the CY and TC explosives.

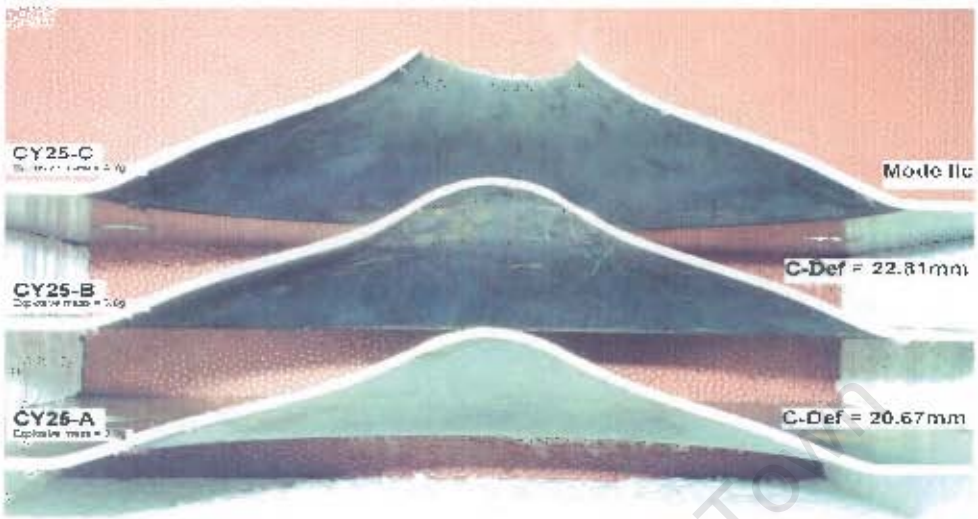

Figure 4.14: Photograph of cross-section of plates subjected to 25mm CY explosives of varying mass.

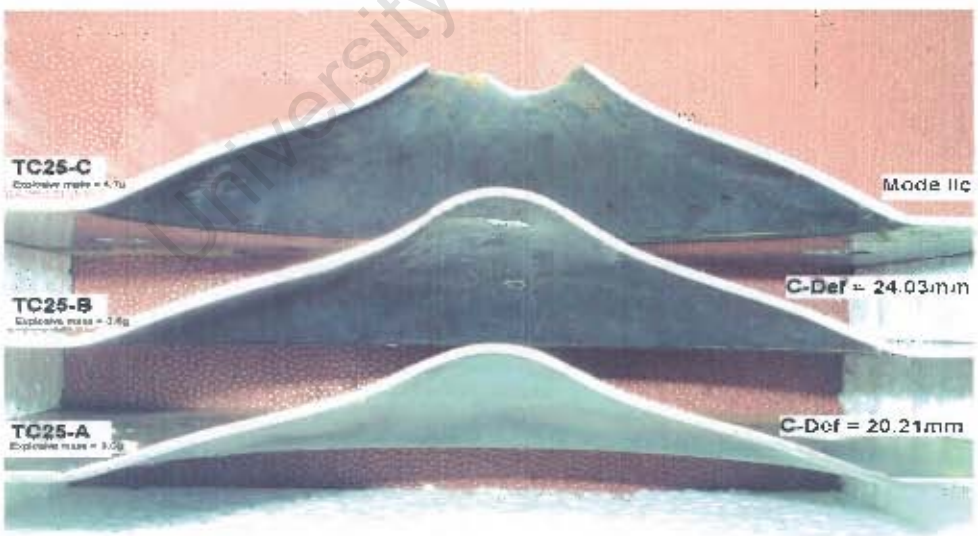

Figure 4.15: Photograph of cross-section of plates subjected to 25mm TC explosives of varying mass.

Figure 4.16: Photograph of cross-section of plates subjected to 25mm ITC explosives of varying mass.

Test No.	Mass of Explo.(g)	Def.(mm)	Imp.(Ns)	Comments
CY25-A	3.0	20.67	8.10	
CY25-B	3.6	22.81	9.20	
CY25 C	4.7	-	10.70	Capping

Table 4.4: Table showing central deformation of plate and impulse for 25mm CY explosives

Test No.	Mass of Explo.(g)	Def.(mm)	Imp.(Ns)	Comments
TC25-A	3.0	20.21	7.81	
TC25 B	3.6	24.03	8.93	
TC25-C	4.7	-	10.39	Capping

Table 4.5: Table showing central deformation of plate and impulse for 25mm TC explosives

Test No.	Mass of Explo.(g)	Def.(mm)	Imp.(Ns)	Comments
ITC25-A	3.0	15.08	8.62	
ITC25-B	3.6	16.69	9.47	
ITC25-C	4.7	20.79	11.46	

Table 4.6: Table showing central deformation of plate and impulse for 25mm ITC explosives

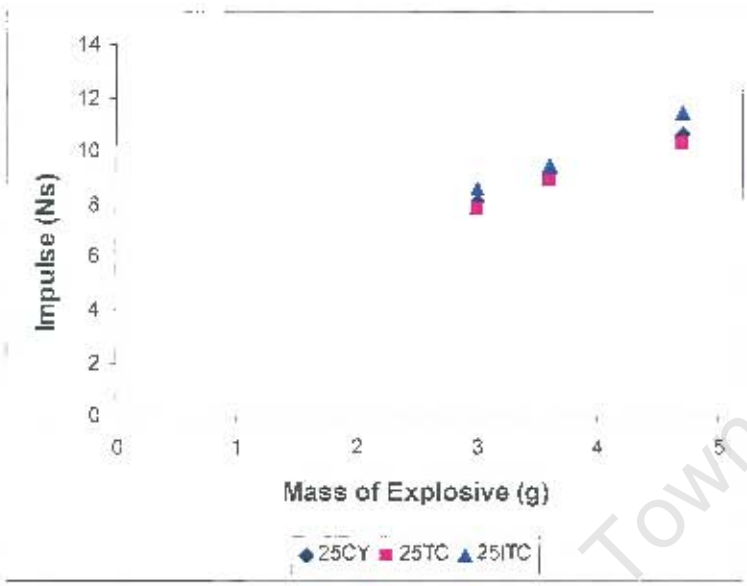

Figure 4.17: Graph showing mass of explosive vs. impulse of blast for 25mm CY, TC and ITC explosives.

4.4 Results for 33mm Load Cases

4.4.1 Effect of Shape for 33mm Explosive Charge on Central Deformation of Plate

Results of the effect of shape for 33mm load cases on the central deformation of the plates are shown in figures 4.18, 4.19, 4.20 and 4.21. The results show that the TC explosively loaded plate in figure 4.18 is slightly lower than that of the CY loaded plate. However, the ITC loaded plate in figures 4.18, 4.19, 4.20 and 4.21 are lower than those of the TC and CY loaded plates.

4.4.2 Effect of Mass of 33mm Explosive Charge on Central Deformation of Plate

Results from the experiments for 33mm diameter load cases are presented as shown in figures 4.22, 4.23 and 4.24. The deformation ranges from Mode I to Mode II as the mass of explosive increases for each shape of explosive. A plot of the central deformation against mass of explosive is shown in figure 4.25.

Figure 4.18: Photograph of cross-section of plates subjected to 3.0g CY, TC and ITC 33mm explosives.

Figure 4.19: Photograph of cross-section of plates subjected to 3.6g CY, TC and ITC 33mm explosives.

Figure 4.20: Photograph of cross-section of plates subjected to 4.7g CY, TC and ITC 33mm explosives.

Figure 4.21: Photograph of cross-section of plates subjected to 5.9g CY, TC and ITC 33mm explosives.

Figure 4.22: Photograph of cross-section of plates subjected to 33mm CY explosives of varying mass.

Figure 4.23: Photograph of cross-section of plates subjected to 33mm TC explosives of varying mass.

Figure 4.24: Photograph of cross-section of plates subjected to 33mm ITC explosives of varying mass.

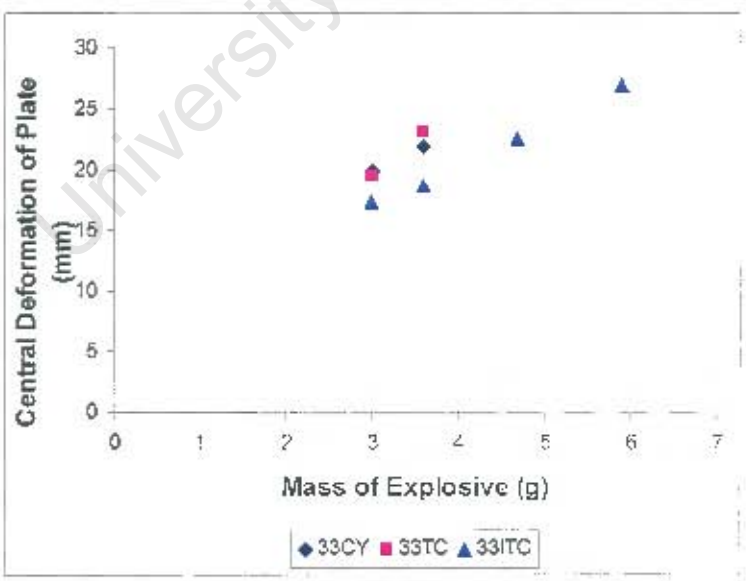

Figure 4.25: Graph showing central deformation of plate vs. mass of explosive for all 33mm TC, CY and ITC explosives.

4.4.3 Effect of Shape of 33mm Explosive on Impulse of Blast

The experimental results of the central deformation and impulse of the blasts for 33mm load cases are shown in tables 4.7, 4.8 and 4.9. It is observed that no Mode II*c or Mode II deformations are recorded for the plates subjected to the 33mm ITC explosives. Results of the effect of shape of 33mm explosives (CY, TC and ITC) on impulse are graphically presented as shown in figure 4.26. The impulses given by the TC, CY and ITC explosives are generally similar at lower masses, but show a higher value by the ITC explosive as the mass of explosive increases. This is seen in figure 4.26 at a mass of 5.9g, where the impulse by the TC explosive gives the lowest value compared to those caused by the ITC and CY explosives.

Test No.	Mass of Explo.(g)	Def.(mm)	Imp.(Ns)	Comments
CY33-A	3.0	19.92	8.48	
CY33-B	3.6	21.88	10.00	
CY33-C	4.7	-	12.07	ModeII*c
CY33-D	5.9	-	13.90	Capping

Table 4.7: Table showing central deformation of plate and impulse for 33mm CY explosives

Test No.	Mass of Explo.(g)	Def.(mm)	Imp.(Ns)	Comments
TC33-A	3.0	19.50	8.12	
TC33-B	3.6	23.05	9.92	
TC33-C	4.7	-	11.22	Capping
TC33-D	5.9	-	12.98	Capping

Table 4.8: Table showing central deformation of plate and impulse for 33mm TC explosives

4.5 Effect of Height to Charge Diameter Ratio on Impulse

A graphical presentation of the impulse against the ratio of the height to diameter of charge of all the experimental results is shown in figure 4.27. The results are

Test No.	Mass of Explo.(g)	Def.(mm)	Imp.(Ns)	Comments
ITC33-A	3.0	17.24	8.48	
ITC33-B	3.6	18.63	10.00	
ITC33-C	4.7	22.60	11.97	
ITC33-D	5.9	26.92	14.89	

Table 4.9: Table showing central deformation of plate and impulse for 33mm ITC explosives

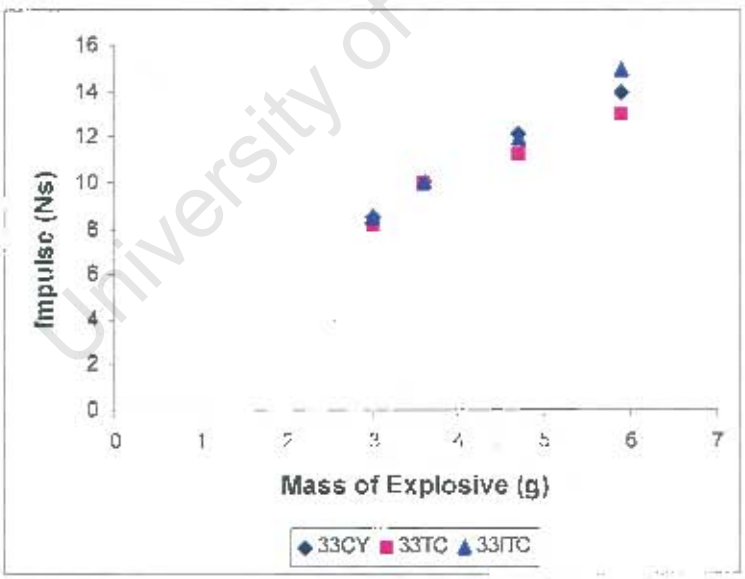

Figure 4.26: Graph showing mass of explosive vs. impulse of blast for 33mm CY, TC and ITC explosives.

similar to those presented by Nurick and Radford [2] in which the bigger diameter charge show a steeper gradient compared to charges of lower diameters. The results in figure 4.27 show that irrespective of the shape of the explosive, the impulse of the blast is influenced by the ratio of the height to maximum charge diameter. The results also show that the impulse is more sensitive to the ratio of the height to diameter as the charge diameter increases.

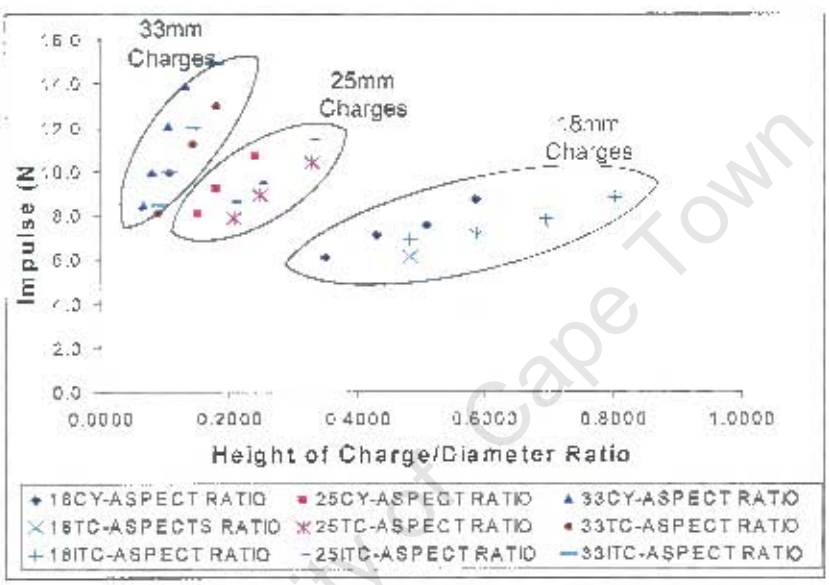

Figure 4.27: Graph showing impulse vs. ratio of charge height to diameter for 18mm, 25mm and 33mm CY, TC and ITC explosives.

4.6 Burn Diameter to Load Diameter Ratio

Results of the ratio of burn diameter to load diameter (BLDR) against height of explosive are shown in figure 4.28. The results show a similar pattern to those given in Nurick and Radford [2]. It can be seen generally in figure 4.28, that the burn to load diameter increases as the height of the explosive increases. However, it is acknowledged that there is a weak relationship between the height and burn load diameter ratio which needs further investigations.

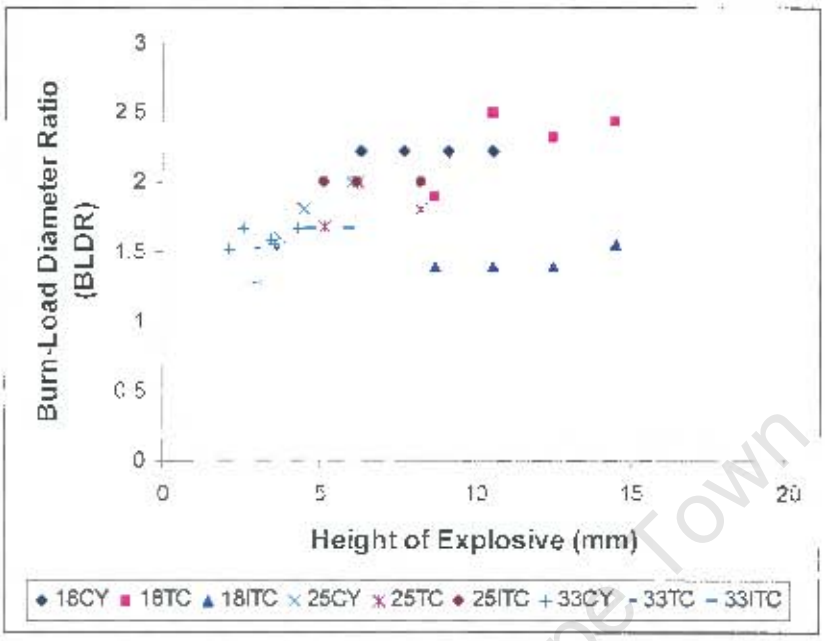

Figure 4.28: Burn diameter-load diameter ratio vs. height of explosive.

4.7 Summary

The experimental results presented for TC and ITC explosives have not been reported in the literature. The results show that irrespective of the fact that the masses of two or more explosives are the same, however, the influence of the shape plays a significant role in the deformation and impulse of a structure. From all the results presented photographically for all the load cases, it can be seen that the ITC explosive generally causes the lowest central deformation of the plates compared to the CY and TC explosives. As regards the impulse of the blast, the ITC explosives generally give the highest value measured by the pendulum compared to the CY and TC explosives. Furthermore, the results presented show that the ratio of the height to explosive charge diameter also influences the impulse measured by the pendulum.

Chapter 5

Method of Solution

5.1 Introduction

The objective of this chapter is to describe and illustrate both theoretically and numerically, the detonation mechanism of solid explosives as they expand. The spacial distribution of the detonation products based on the shape of the explosive, is investigated. Shock-wave profiles generated by CY, TC and ITC explosives, are specifically investigated in order to understand the interaction of explosive loads with structures. An attempt is made to construct the expected shock-wave profiles of the various explosives using their respective effective masses. The ABAQUS/Explicit 6.4 and AUTODYN 6.0 hydrocodes are used for the simulation of the experiments, in order to predict the total deformation of the plates. An axi-symmetric model is used in this work as it is computationally inexpensive compared to a three-dimensional model.

5.2 Generation of Shock-Wave Profiles

5.2.1 Shock-Wave Profiles of Cylinder Explosives

In order to predict the final shock-wave profile of CY explosives, figure 5.1 shows stages of the detonation process from diagram (A) to diagram (E). The simplest theory addressed in chapter 2 is used to explain the detonation process meaning that the detonation front is at the C-J state. However, a spherical shock wave is adopted as opposed to a plane wave in order to realistically predicts the final shock-wave profile and load distribution.

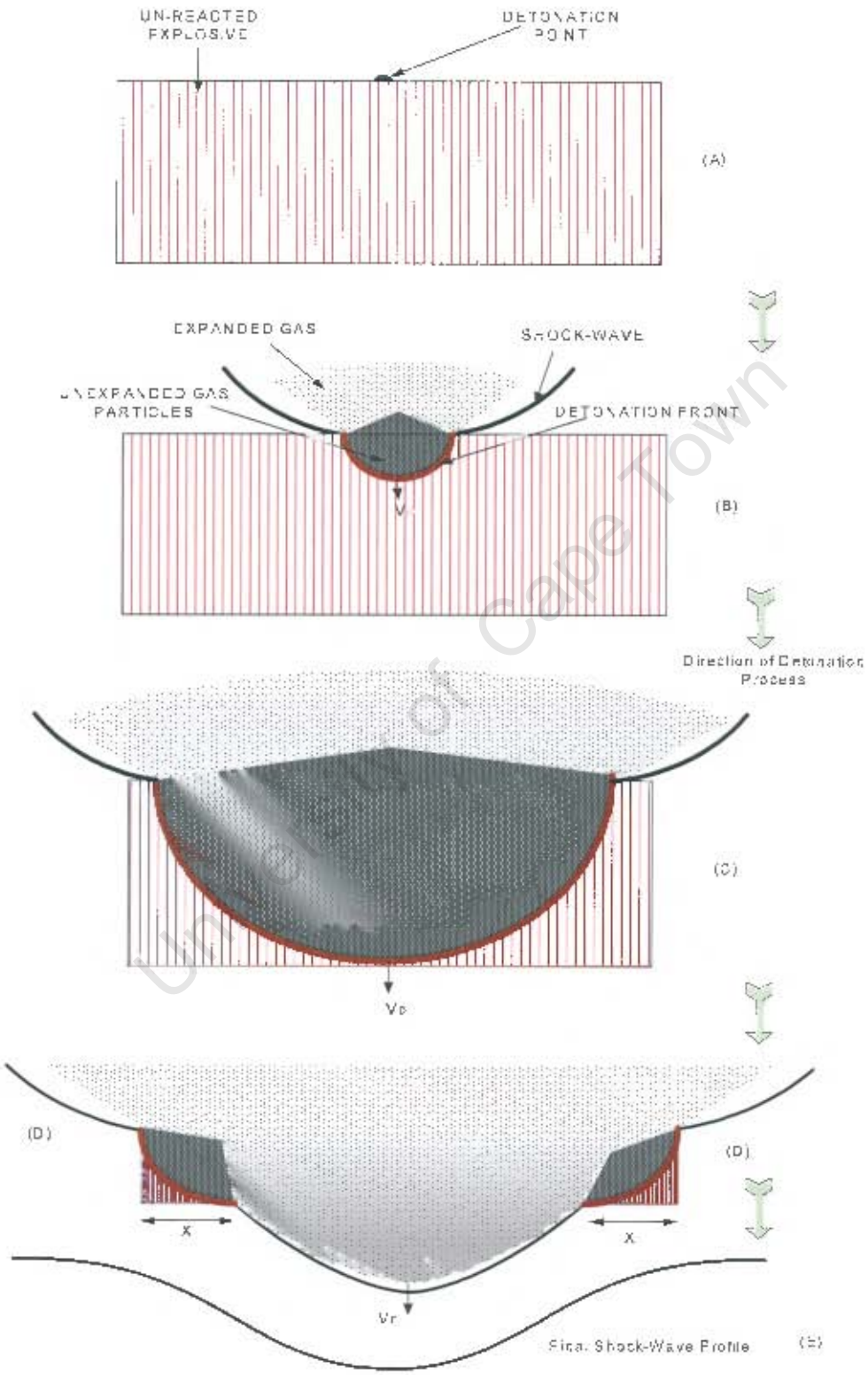

Figure 5.1: Figure showing schematic of detonation process of a CY explosive.

The detonation front is assumed to be in a state of thermodynamic equilibrium. The detonation front in figure 5.1 is followed by an upper and lower region. The upper region is comprised of expanded explosive gas particles of high pressure, whilst the lower region is of a much higher pressure of unexpanded gas particles. This lower region is formed immediately the process of detonation begins and is also reproducible until the chemical reaction of the explosive comes to completion. During the process of expansion of the gas particles (upper region), the surrounding fluid (air or water), slows down the momentum of the particles and eventually produces a shock or blast wave. For the laterally expanding gases, the shock is of lower intensity compared to the gas particles in the direction of the detonation front. This is so because the velocity of the laterally expanding gas particles is less than the velocity of the detonation front (V_D) as reported in Rinehart and Pearson [21].

The detonation front has a discontinuous pressure front as explained in chapter 2, but is reproducible during the process of detonation due to the heat and shock wave which move in the direction of flow of the front and thereby continually initiating the process of detonation. Furthermore, it should be noted that the C-J pressure at the detonation front in figure 5.1 remains unchanged, but reduces to about 1/300 of the C-J pressure as it initially travels through air as reported in Rinehart and Pearson [21]. From diagram (D) in figure 5.1, it can be observed that the unexpanded gas region following the reaction zone, has been formed in two separate regions in order to maintain the process of detonation as the reaction continues. Also, it can be observed that the detonation front experiences a change of curvature as a manifestation of a change of medium from solid to air. It can also be noted that the thicker the explosive, the longer the pressure will be maintained at the axis, hence a higher impulse in the central vertical direction. This means that the longer the Taylor-wave as discussed in chapter 2, the higher the load intensity at the centre of the explosive, hence, a higher momentum at the axis of the charge as shown in figure 5.2. In figure 5.2, the impulse at C is greater than those at A and B.

For a thicker (pencil-like) explosive in which the height is far greater than the diameter, the flow of particles along the vertical axis is greater than that of a thin cylinder (pancake-like) in which the height of the explosive is far less than the diameter. This also means that the dimensions of the charge influences the shape of the final shock wave profile. The shape of the shock-wave profile is

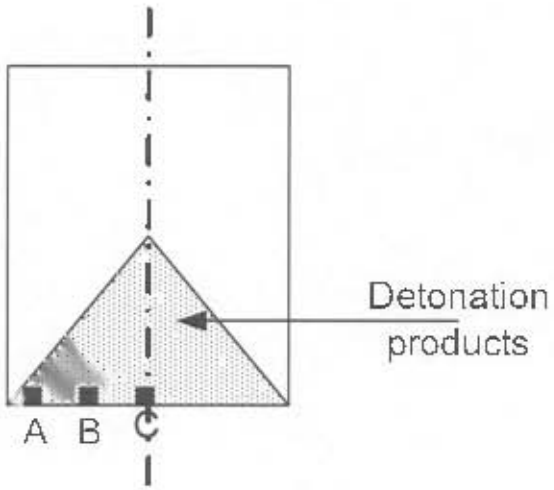

Figure 5.2: Figure showing positions of impulse intensity in an explosive [21].

confined in a smaller area for a thick explosive compared to a thinner and wider explosive, provided that the masses are the same.

From figure 5.1, it is shown that the detonation velocity V_D remains unchanged during the process of detonation until a change of medium occurs where the velocity becomes V_E $[> V_D]$ with a corresponding decrease in pressure of the front. The initial velocity of the shock-wave at the end of the detonation process in air, increases before reducing to zero with time. For example, the detonation velocity (V_D) of PETN is 7520m/s. In air, the detonation front moves with an initial velocity (V_E) of 7950m/s as reported in Rinehart and Pearson [21]. One characteristic of an explosive is that the detonation velocity remains fairly constant during the process of detonation after steady detonation is achieved. In the lateral direction, the velocity of the detonation particles is 3/4 of the detonation velocity, and the velocity of the rarefaction (Taylor-wave) , is 3/5 of the detonation speed as reported in Rinehart and Pearson [21].

5.2.2 Shock-Wave Profiles of Truncated-Cone and Inverted Truncated-Cone Explosives

Figures 5.3 and 5.4 show the propagation of the detonation profiles of a Truncated-Cone (TC) and Inverted Truncated-Cone (ITC) explosives. As shown in figure 5.3, the final shock-wave profile is similar to that of a CY explosive. It can

be seen in figures 5.3 and 5.4 (C), the detonation front remains spherical until it gets to the surface of the explosive where the detonation front increases its velocity from V_D to V_E in diagram (D). It can also be seen that the detonation front changes its shape as an indication of a change of medium from solid to air. The final shock wave profile shown in figure 5.4 (E), is a less localised load distribution compared to the shock-wave profile in diagram (E) of figure 5.3. On interaction with a target or structure, this kind of loading caused by the ITC explosive, is likely to cause a lower central deformation and less damage to the target structure. This means that irrespective of the masses of the CY, TC and ITC explosives being the same, tearing of the structure is likely to be caused by the TC and CY explosives as opposed to the ITC explosive. This is because the flow of particles are distributed in a much wider area, as shown in figure 5.4 (E), compared to that in figures 5.1 and 5.3 as manifested in the experimental results presented earlier.

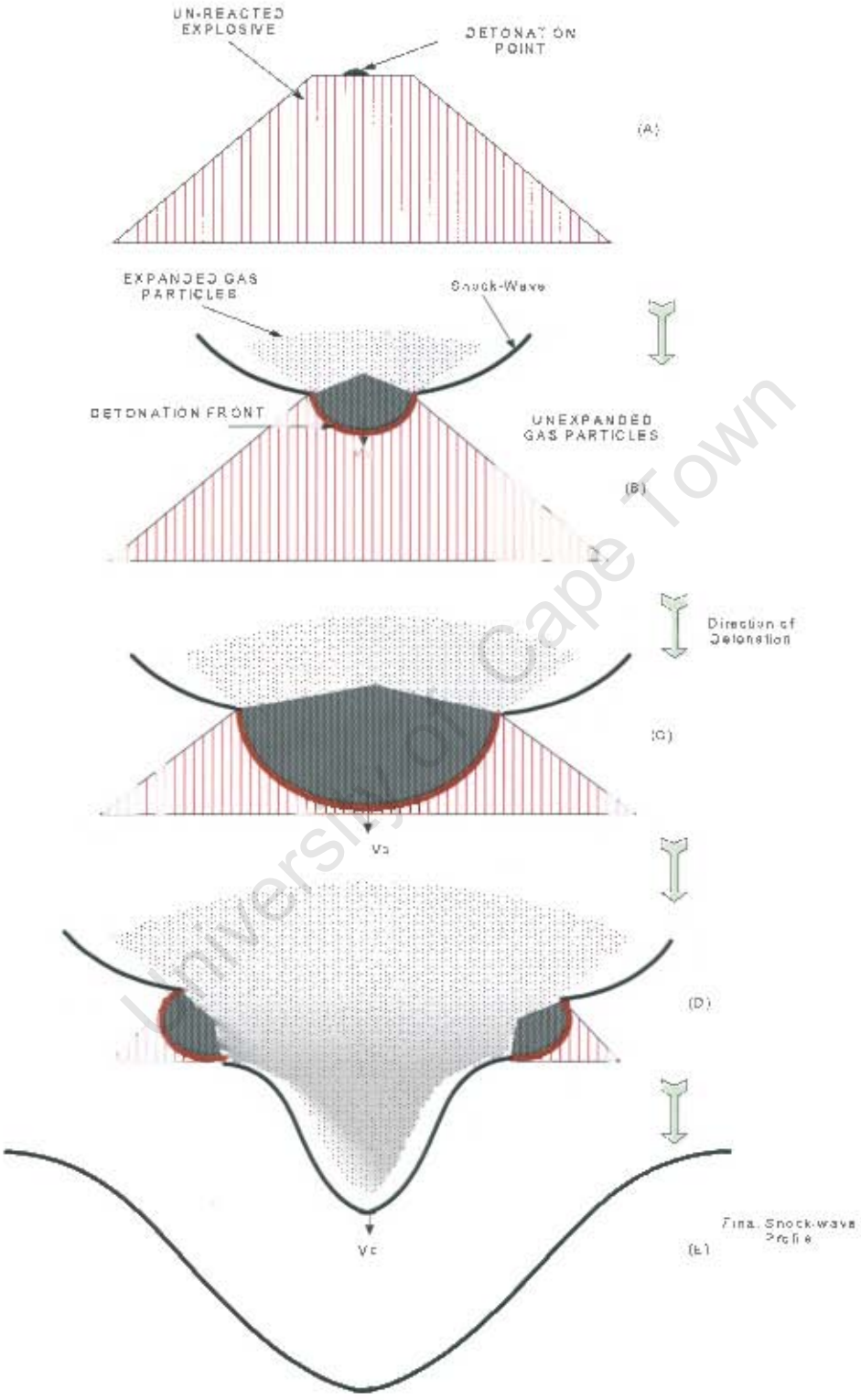

Figure 5.3: Figure showing schematic of the detonation process in a TC explosive.

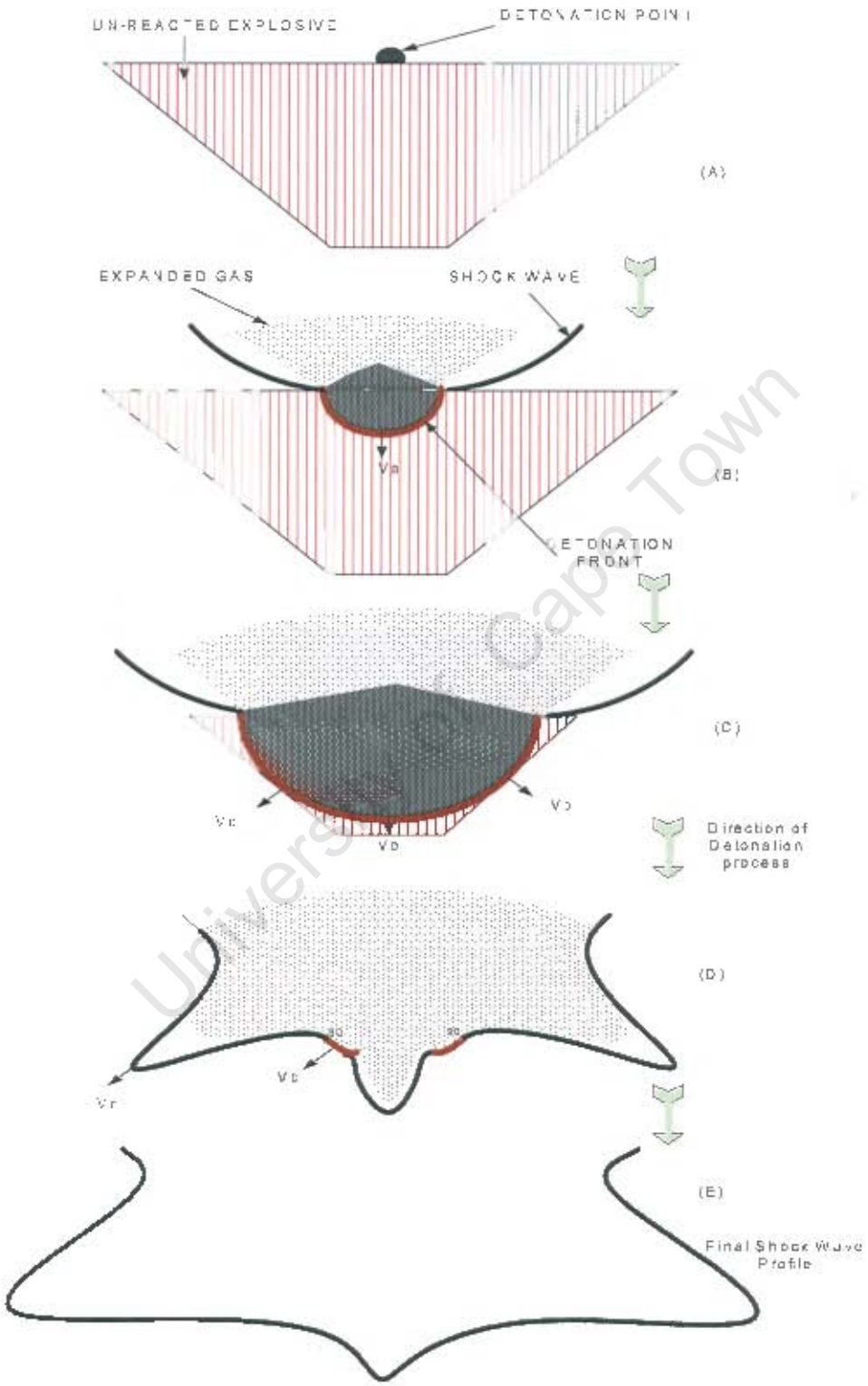

Figure 5.4: Figure showing schematic of the detonation process in an ITC explosive.

5.3 Constructing the Final Shock-Wave Profiles of CY, TC and ITC Explosives

In this section, an attempt is made to analytically construct the shape of the final shock-wave profiles in relation to the effective mass of the explosives. The effective mass of the explosives CY, TC and ITC explosives are shown in figure 5.5. As reported in Kennedy [70], a 30^0 angle is taken off-the sides in order to estimate the effective mass of the explosive that will contribute to the axial momentum of the target structure.

As shown in figure 5.5, the effective masses of the thick TC and CY are equal, meaning an equal central deformation of the plate is expected for both explosives. The depth of the shock-wave is directly proportional to the axial momentum as given in equation 5.1.

$$\text{Depth of shock-wave (L)} \propto \text{Axial momentum} \tag{5.1}$$

$$\text{Depth of shock-wave (L)} = \mathsf{K} \times \text{Effective mass} \times \text{Detonation velocity } (V_D)$$

where K is the constant of proportionality. Since the maximum deformation of the plates is caused by the TC explosive, the depth of the CY and ITC shocks in the axial direction are expressed as a ratio of the length of the TC explosive as given in equations 5.2 and 5.3 respectively.

$$L_{CY} = \frac{M_{CY}}{M_{TC}} L_{TC} \tag{5.2}$$

$$L_{ITC} = \frac{M_{ITC}}{M_{TC}} L_{TC} \tag{5.3}$$

where M_{CY} is the effective mass of the CY explosive, M_{ITC} is the effective mass of the ITC explosive and M_{TC} the effective mass of the TC explosive. The minimum widths of the shock-wave profiles are the same for the TC and CY explosives but much wider for the ITC explosives. However, for the central deformation, the length of the shock-wave (L) is most important.

For the thicker explosives, the effective masses of the CY and TC explosives are equal, meaning that the depths of their shock-wave profiles are also equal compared to the ITC explosive of smaller effective mass. By increasing the

height beyond the effective height of the explosive mass region in figure 5.5 in (A), the central deformation of the plate by the ITC, CY and TC explosives will not significantly increase. For the ITC explosive, the maximum effective mass is reached much earlier compared to the CY and TC explosives. For the thinner explosives in 5.5 in (B), it can be seen that the TC explosives uses all its mass whilst the ITC and CY explosives do not use all their masses in the explosive axially. However, the effective mass of the CY explosive is bigger than that of the ITC explosive. This means that the TC explosive will cause the highest central deformation followed by the CY and ITC explosives respectively.

As regards the impulse, it is expected that the explosive with the highest effective mass will cause the highest impulse. In figure 5.5, the thicker CY and TC explosives have the same effective mass meaning that the impulses must be equal. Although the effective mass of the ITC explosive is lower than those of the CY and TC explosives, however, the probability of the detonation products from the sides of the ITC explosive to interact with the target structure in a wider area is higher than that of a TC explosive. In this regard, equal impulses of the ITC, CY and TC explosives is expected if mass is only considered. On the other hand, the ITC explosive covers a wider area of interaction with the structure compared to those of the TC and CY explosives. This interplay between the effective mass of explosive and area of load application makes the impulse a more challenging analysis than that of the central deformation. As shown in figure 5.5 (B), the TC explosive is expected to give the highest impulse as all the charge is used to drive the structure with the highest axial momentum followed by the CY and ITC explosives if only mass is the varying factor. In this regard, both the influence of mass and shape has to be considered in order to estimate the impulse of the blast. The influence of mass and shape of explosive on the impulse is dealt with in the discussion chapter based on the experimental results.

It should be noted that the longer the length of the Taylor-wave of the blast, or the thicker the explosive, the less likelihood the particles at the rear end of the explosion can make contact with the plate. This means that beyond the length of the "effective Taylor-wave" (L), particles do not make effective contact with the plate or loses their momentum, hence a reduction of the impulse. This means that the TC and ITC explosive particles at the rear end are less likely to make contact with the plate compared to the CY explosive of shorter height. The reduction of the explosive particles momentum at the rear of the explosion

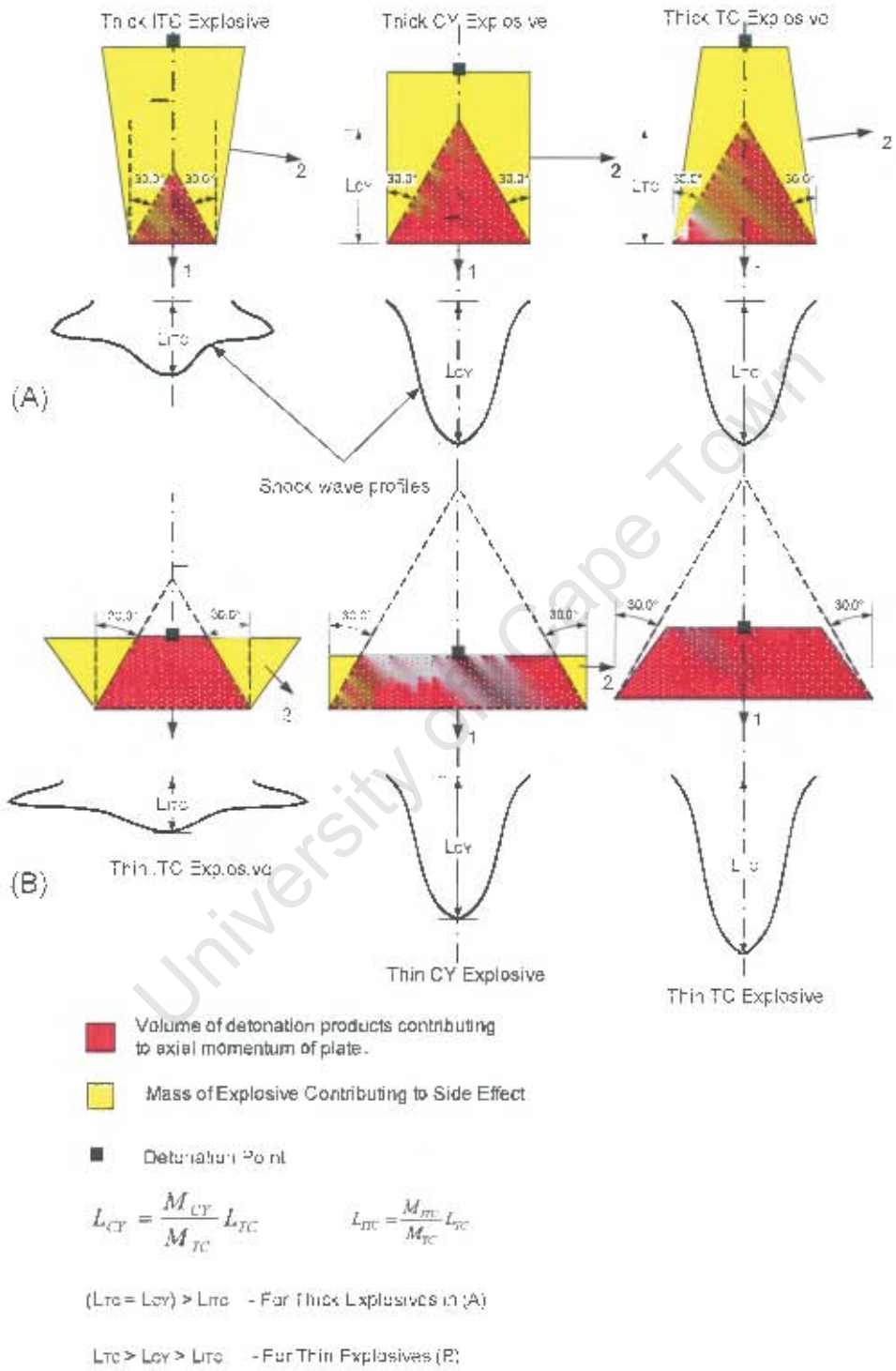

Figure 5.5: Figure showing schematics of the effective mass of explosive contributing to axial momentum of a structure.

causes a reduction of the total impulse.

5.4 Mach Stem Formation and Localised Loading

To discuss the issue of mach stem formation in relation to localised loading of structures, ideal incident and reflected spherical blast waves are assumed as shown in figure 5.6. At point O referred to as 'ground zero', that is the point directly below the centre of the explosive charge, to a point A, away from the centre of distance (D_O), the pressure on the surface of the structure is normal (regular) but decays with time. At point (A), where a reflected and incident wave meet, a mach stem is formed. The point at which the incident, reflected and mach stem meet is called the triple point. Estimate of the height of the mach stem is given in equation 5.4 proposed by Dharaneepathy *et al* [110].

$$H_m = 0.07 H_b \left[\left(\frac{D_x}{D_o}\right) - 1\right]^2 \tag{5.4}$$

where H_b is the height of burst, D_x is any distance away from ground zero and (D_O) the minimum distance for a mach stem formation. When D_x is equal to D_O, height of the mach stem is zero. According to Dharaneepathy *et al* [110], a mach stem is formed when the "critical" angle (f) is between 40^0 to 50^0. The region right of point (A), experiences a change in the direction of pressure horizontally as shown in figure 5.6 due to the formation of a mach stem.

In general, to estimate the critical angle, Robertson *et al* [49] reported on an equation relating the critical angle and the mach number as given in equation 5.5, where f is the "critical" angle and M_x, the mach number of the incident shock.

$$f = \frac{1.75}{M_x - 1} + 39 \tag{5.5}$$

The proposed pressure distribution of the blast wave for a TC and ITC explosives are given as shown in figures 5.7 and 5.9 respectively. For the TC and CY explosives, the load distributions are similar. The load is maximum in direction 1 as indicated in figure 5.7 (A) on interaction with the target structure at ground zero. $P_{r\,max\,1}$ is the maximum reflected pressure on the structure caused

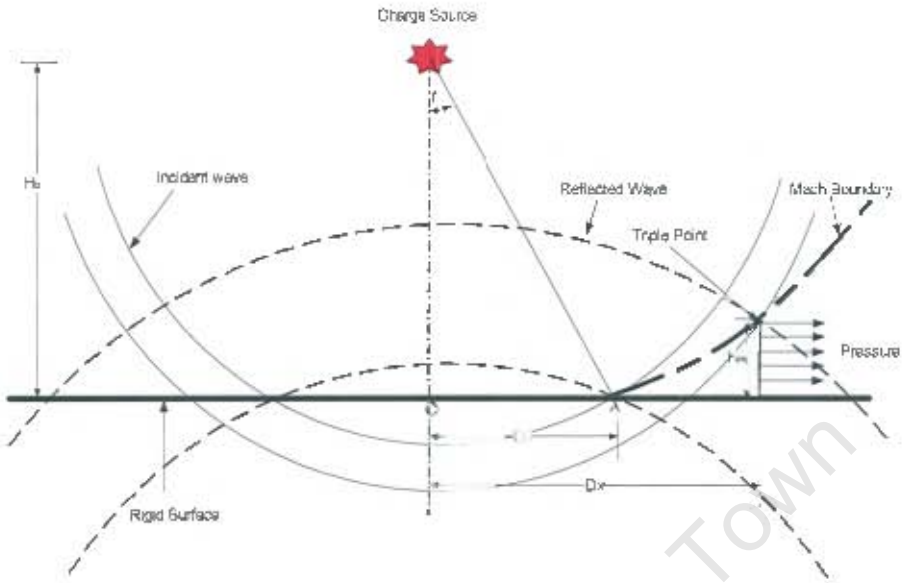

Figure 5.6: Figure showing schematic of Mach stem region formed by incident and reflected waves.

by the load in direction 1 and where P(t) is the magnitude of the pressure as time increases. M is the minimum vertical pressure after which a mach stem is formed. Beyond D_0, the normal load on the structure is reduced by the change in direction of the detonation products on the structure. The load in the mach region is maximum tangentially to the surface of the structure. The proposed load distribution shown in figure 5.7 is similar to that proposed by Bimha *et al* [6] in which two regions of load distribution on the structure is given. In Bimha *et al* [6] however, it is proposed that the load is constant from the center of the charge to the edge of the charge, and exponentially drops to atmospheric pressure to the boundary of the structure. This means that the load is planer from the center of the plate to the edge of the charge. This assumption cannot be entirely true if the load is spherical interacting at a point and eventually reduces exponentially. In figure 5.7, it is shown that the load decreases exponentially from the point of initial interaction to a point D_0 and rapidly drops exponentially along the surface to atmospheric pressure. The rapid drop is caused by the change in direction of the detonation products caused by the formation of a mach stem. Comparison of the proposed load distribution for CY and TC explosives and that proposed by Bimha *et al* [6] is shown in figure 5.8.

For an ITC explosive, the shock-wave profile of the explosive is shown in

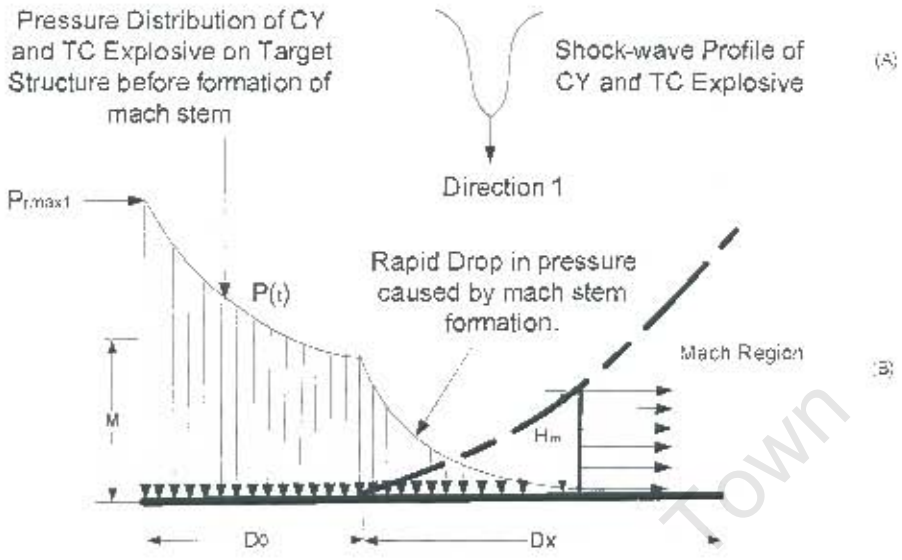

Figure 5.7: Figure showing schematic of proposed load distribution of TC and CY explosives on a target structure.

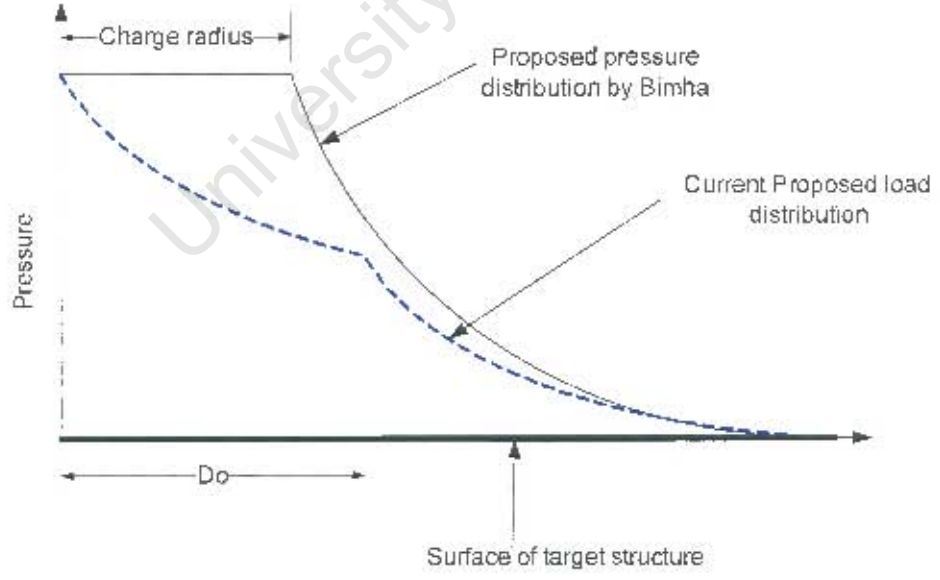

Figure 5.8: Figure showing comparison of proposed load distribution for CY and TC explosives and that proposed by Bimha *et al* [6].

figure 5.9, diagram (A). As shown in figure 5.9 (B), the load distribution which is dependent on the shape of the explosive, two high load intensity in directions 1 and 2 can be seen. P_{max1} is the maximum pressure in direction 1, P_{max2} the maximum pressure on the structure in direction 2, and M1 and M2 are minimum vertical pressures after which a mach stem begins to form. Between M1 and M2 a mach stem region is expected to form of high pressure due to interaction of the two horizontal pressures in opposite directions.

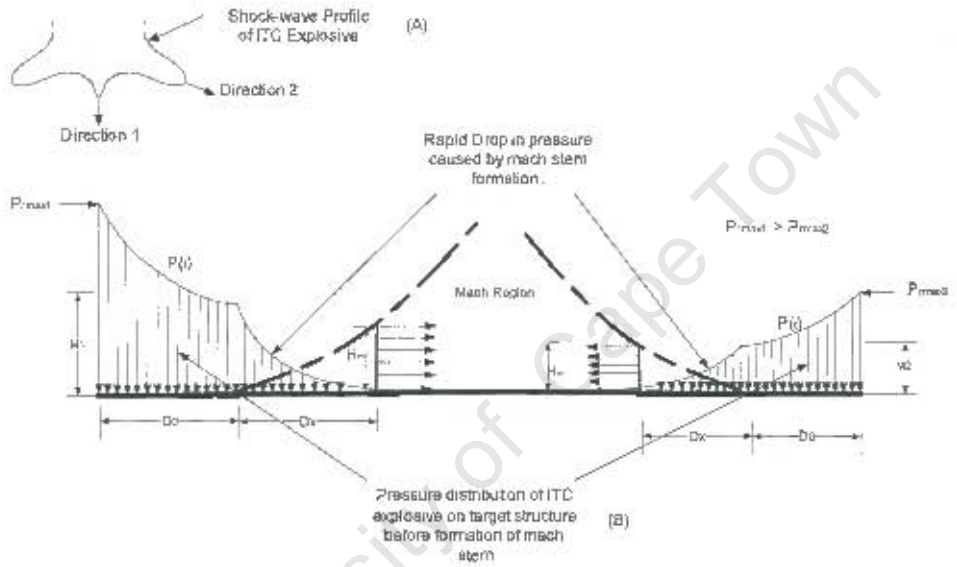

Figure 5.9: Figure showing proposed load distribution of ITC explosive on a target structure.

Because the intensity of the blast wave pressure caused by the TC and CY explosives are higher at ground zero than that of the ITC, the area of the regular reflected region will be much smaller than that caused by the ITC explosive. This means that the length of D_0 expected for the TC and CY explosive will be smaller than that formed by the ITC explosive.

5.5 Simulation of Explosive Behaviour

The increase in efficiency and power of computing in recent years has greatly increased the scope of the explosive designer to predict the performance of explosives reasonably well using hydrocodes. Two forms of generic explosive models have been developed for use in hydrocodes: a computationally cheap generic

method and a more complex reaction flow model as reported in Leiper and Kennedy [111]. In the former, the explosive is assumed to be that of a C-J wave moving through a mesh at a prescribed velocity in all directions simultaneously. The locust of the wave front is defined based on the Huygens construction which defines the front based on the number and position of the coordinates which are identified during the calculations. An EOS for the detonation products is essentially needed to model the pressure of the explosive at the C-J state. In the second approach, the behaviour of the explosive is based on explicit shock induced chemical reaction. In this method, an equation of state for the unreacted explosive, an equation of state for the reaction products and a set of reaction rate parameters are required as reported in Leiper and Kennedy [111]. This method considers the conversion of the unreacted state to the reacted state based on the local thermodynamic nature of the explosive material and a reaction rate law.

Studies of close-in blast of end-detonated cylindrical charges were carried out by Schraml *et al* [112]. The term "close-in blast" describes situation in which the explosive products from the detonation of an explosive charge interact with a structure at close stand-off distance. It also means that the explosive detonation products play a significant role in the response of the structure as reported in Schraml *et al* [112]. The paper documented a set of numerical simulations that were performed to complement an experimental study of the blast environment produced by the detonation of cylindrical charges. The purpose of the studies was to validate the ALE general application (ALEGRA) in simulating blast loading and to characterise the complex blast environments produced by the experiment. A reaction rate model was incorporated in the simulation in order to model the detonation process which is initiated by a shock. Characterisation of the blast environment was achieved by describing the evolution of dynamic pressure histories and peak pressure profile together with the impulses along a straight paths at various distances from the centre of the charge.

The Lee-Tarver model incorporated in the AUTODYN 6.0 material library is an example of an Ignition and Growth model given in equation 5.6.

$$\dot{\beta} = I(1-\beta)^x(v_0/v_e)^r + G(1-\beta)^x\beta^y p^z \tag{5.6}$$

where $\dot{\beta}$ is the degree of chemical reaction, v is specific volume, subscript 0 and e referred to the porous unshocked and dense shocked states respectively, and I, G, r, x, y, z are fitting factors. The reaction rate model in AUTODYN

6.0 material library comprises the JWL EOS for the detonation products, an EOS for the inert explosive and a reaction rate equation to describe the ignition and growth and completion of the burning. Other forms of reaction rate models have been formulated with the Forest fires [116] being one of the earliest ignition growth models as given in equation 5.7, where β is the degree of chemical reaction and $f(p)$ a polynomial in pressure and a point denoted time differentiation. Modelling of the explosive behaviour using an ignition growth model is beyond the scope of this work.

$$\dot{\beta} = (1 - \beta)f(p) \tag{5.7}$$

5.6 The Finite Element Method

The finite element method is an approximate numerical technique for the solution of the equations governing the response of a physical system. The method is characterised by three basic features:

1. The domain of the problem is represented by a collection of simple subdomains, called elements. The collection of elements is called the finite element mesh. A wide range of element types can be found in the ABAQUS manual [99].

2. Over each finite element, the physical process is approximated by functions of desired type (polynomials or otherwise) and algebraic equations relating physical quantities at selected points, called nodes, of the element are developed.

3. The element equations are assembled using continuity conditions of physical quantities.

Whereas the finite difference approach is a pointwise discretisation of the continuum, the finite element technique envisages the solution region as being composed of many small interconnected sub-regions or elements and nodes as shown in figure 5.10.

This implies that a piece-wise approach is adopted to solve the differential equations at the nodes using polynomials that represent the variable over the element. The degree of polynomial is dependent upon the number of nodes in the element and number of degrees of freedom. The displacements at the nodes are the unknowns of the problem. These displacement functions define the strain and strain-rate within each element. By using the constitutive equation representing the material behaviour, the stress can be determined. The internal and external forces, velocity, acceleration and displacements can all be determined at the nodes.

The development of the finite element method as a numerical tool began with the advent of the electronic digital computer as reported in Bathe [117]. The finite element method is used on computers, to solve the governing equations representing the physical system. The linear dynamic response of a physical system of finite elements is given in equation 5.8

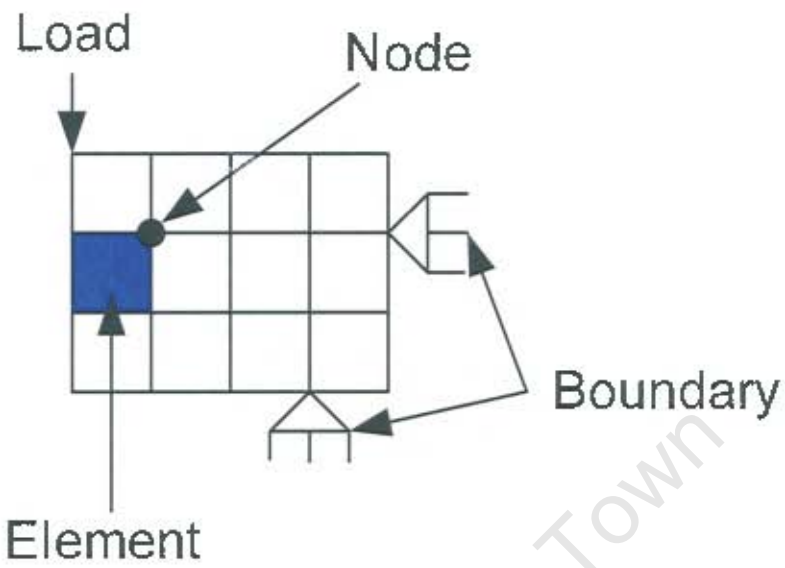

Figure 5.10: Schematic of structure with boundary subjected to load showing an element and a node of the finite element mesh.

$$M\ddot{U} + C\dot{U} + KU = R \tag{5.8}$$

where M, C and K are the mass, damping and stiffness matrices; R is the external load vector; and $\ddot{U}$, $\dot{U}$ and U are the acceleration, velocity and displacement vectors of the finite element model. In time discrete form, equation 5.8 can be written as

$$F_I(t) + F_D(t) + F_E(t) = R(t) \tag{5.9}$$

where $F_I(t)$ are the inertia forces, $F_I(t) = M\ddot{U}$, $F_D(t)$ are the damping forces, $F_D(t) = C\dot{U}$ and $F_E(t)$ are the elastic forces, $F_E(t) = KU$.

5.6.1 Overview of the Explicit Method

In this work the ABAQUS/Explicit 6.4 and AUTODYN codes are used for the numerical solution of the differential equations governing the explosive and plate. The explicit method is adopted in this work as it is suitable for impulsively loaded structures, complex contact problems, complex post-buckling problems, highly nonlinear and quasi-static problems and materials with degradation and failure

problems. The ABAQUS/Explicit code uses a central difference time integration scheme to solve the equations of motion (Newton's second law) with respect to time. The equations of motion are integrated with respect to time using the kinematic conditions at one increment to calculate the kinematic conditions at the next increment. The acceleration of a nodal mass with respect to time is given in equation 5.10

$$\ddot{u}_{(t)} = (M)^{-1} \cdot (P - I)_{(t)} \tag{5.10}$$

where $\ddot{u}$ is the nodal acceleration, M is the nodal mass matrix, P is the total applied force and I is the internal element forces. In the explicit procedure, there are no simultaneous equations to solve, making it an inexpensive method compared to the implicit method. If equation 5.10 is integrated with respect to time, the velocity and displacement of a node are obtained.

The issue of stability of the model must be addressed for the simulation to run to completion. Consider a bar subjected to stress wave as shown in figure 5.11. For stability, the time taken for the wave to propagate along the bar must be greater than that of the time increment chosen by the solver.

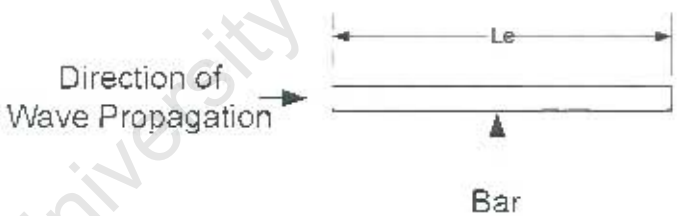

Figure 5.11: Figure showing schematic of a bar subjected to stress wave.

The stability limit can be calculated as given in equation 5.11.

$$\Delta t_{stable} = \min\left\{\frac{L_e}{C_d}\right\} \tag{5.11}$$

where Δt_{stable} is the stable time increment, L_e is the edge length of an element or diameter of an inscribe circle of a triangular element, C_d the wave speed of the material as given in equation 5.12, E is Young's modulus and ρ the density of the material.

$$C_d = \sqrt{\frac{E}{\rho}} \tag{5.12}$$

For computational efficiency, AUTODYN 6.0 and ABAQUS/Explicit 6.4 choose the time step to be as close as possible to the maximum stability limit. If the time increment of a model Δt, is larger than the stable time increment, then instability will occur which causes the simulation to terminate. The explicit methods require a small time increment that depends on the highest natural frequencies of the model and is independent of the type and duration of loading, whilst the implicit method does not place a limitation on the time increment. The increment of an implicit method is determined from accuracy and convergence of the solution. For the purpose of this research, the aspect ratio of the elements of the steel plate is initially 2:1 ($0.8mm \times 0.4mm$) whilst the aspect ratio of the explosive elements were kept initially at 1:1 ($0.8mm \times 0.8mm$) prior to loading in both codes.

5.6.2 Simulating the Explosive Behaviour in ABAQUS/Explicit 6.4 Code

The configuration of the experiment in the numerical simulation is shown in an axi-symmetric view in figure 5.12. A stand-off distance of 20mm is used throughout the simulation process. Three discrete steps are used in the simulation process.

In the first step the explosive is allowed to expand up to the point of first contact with the plate. A total time of $2\mu s$ (micro-seconds) is used in the first step, estimated approximately by dividing the stand-off distance by the detonation velocity assuming that the velocity of the detonation products remain constant until interaction is made.

In the second step, the interaction between the explosive and the plate is assumed to last for $65\mu s$. This time is achieved by assuming various values until an approximate value is reached and adopted for all the simulations. During this time, the explosive energy is transferred to the plate which eventually deforms with time. In the last step, the explosive is "frozen" for $1000\mu s$ during which the plate is allowed to settle with no energy from the explosive transferred to it.

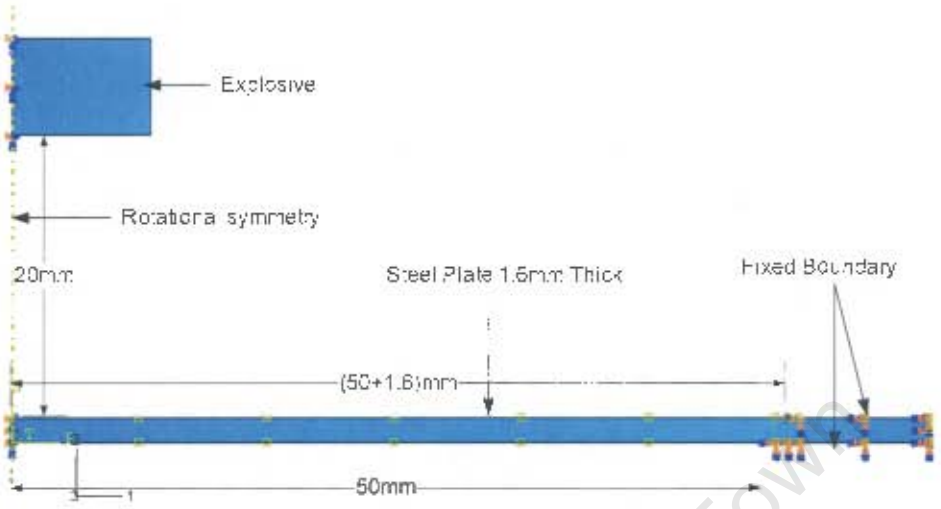

Figure 5.12: Figure showing set up of the experimental simulation of a CY explosive at 20mm stand-off distance from the top of the plate.

Modelling The Explosive Pressure

In modelling the explosive using the ABAQUS/Explicit code, CAX4R (Continuum Axi-symmetric 4-noded reduced integration) Arbitrary-Lagrangian-Eulerian (ALE) mesh is used. The JWL EOS [7] is used to model the explosive pressure of the detonation products as given in chapter 2 but repeated here for the sake of clarity in equation 5.13.

$$P = A(1 - \frac{\omega}{R_1 V})e^{-R_1 V} + B(1 - \frac{\omega}{R_2 V})e^{-R_2 V} + \frac{\omega E}{V} \tag{5.13}$$

According to Hibbit *et al* [99], the pressure generated by the release of chemical energy of the explosive is implemented in a form referred to as programmed burn. A programmed burn means that the reaction and initiation of the explosive is not determined by shock in the material. Instead, the initiation time is determined by a geometric construction using the detonation wave speed and the distance of the material point from the detonation points. The detonation time as given in the ABAQUS/Explicit programme is estimated as

$$t_d^{mp} = \min\left\{ t_d^N + \frac{\sqrt{(X^{mp} - X_d^N)(X^{mp} - X_d^N)}}{C_d} \right\} \tag{5.14}$$

where X^{mp}, is the position of the material point, X_d^N is the position of the nth detonation point, t_d^N, is the detonation delay time of the nth detonation point and C_d, the detonation wave speed. To obtain continuity of the burn wave over several elements, in the finite element model, the burn fraction F_b is incorporated and calculated as

$$F_b = \min\left\{1, \frac{(t - t_d^{mp})C_d}{B_s l_e}\right\} \tag{5.15}$$

where B_s is a constant which controls the width of the burn wave and l_e is the characteristic length of element. The pressure at time (t) within the explosive is estimated by multiplying the pressure from the JWL EOS and the burn fraction. The constants in the JWL EOS are given in Table 5.1.

A(GPa)	B(GPa)	R_1	R_2	ω	E(GJ/Kg)	ρ(Kg/m^3)	C_d(m/s)	P_{CJ}(GPa)
609	12.9	4.1	1.4	0.25	9	1600	8190	28

Table 5.1: Constants in the JWL Equation of State

Modelling the Geometry of the Steel Plate (Target)

The steel plate is modelled using CAX4R (Lagrangian) elements. Lagrangian elements are more suitable to model the plate as the deformation of the plate is not very large compared to the explosive elements. The elements aspect ratio is initially 2:1. Studies carried out by Grobbelaar and Nurick [4] show that the type of elements used to model the steel plate does affects the deformation of the plate.

Modelling the Boundary Conditions

The boundary conditions of the plate and explosive are modelled as described in Grobbelaar and Nurick [4] and shown in figure 5.12. On the left of figure 5.12, a line of rotational symmetry for both the explosive and steel plate is shown. The boundary on the right of figure 5.12 shows the dimensions of the boundary as proposed by Grobbelaar and Nurick [4]. A length of 1.6mm at the top boundary is not restrained in order to account for loss of contact at the top of the plate and the clamp.

Modelling the Contact

There are two algorithms in the ABAQUS/Explicit code for describing contact: the general contact algorithm and the contact pair algorithm as reported in Hibbit *et al* [99]. In the general contact algorithm, contact occurs between all regions of the model while in the contact pair algorithm, contact is defined between specific surfaces defined as master and slave surfaces. The general contact algorithm is suitable where less restriction of the contact surfaces is needed. The surfaces of the explosive making contact with the target surface is defined as the Master surface while the top face or loaded area of plate is the Slave surface.

Constraint on the interaction are normally applied by default. The default kinematic contact formulation chosen by ABAQUS/Explicit is used to model the surface-surface interaction in order to minimise the problem of overclosure. Overclosure occurs when significant amount of indent between the Master and the Slave surface takes place as shown in figure 5.13.

Figure 5.13: Figure showing overclosure caused by indent of the master (explosive) surface nodes into the plate (slave) surface.

In the numerical simulations, the penetration of a node into the plate is reduced by adopting a kinematic balanced master-slave approach. A penalty contact is not adopted as it does not prevent the penetration of a master surface into the slave surface.

5.6.3 Simulating the Explosive Behaviour in AUTODYN 6.0 Code

In simulating the detonation process using AUTODYN 6.0 code, the explosive is modeled with an ALE (Arbitrary Lagrangian Eulerian) mesh. In an ALE mesh, the explosive material moves across the mesh and the mesh simultaneously deforms and moves with the material. The plate is modeled with a Lagrangian mesh. A Lagrangian mesh is a material description in which the grid points are fixed to the material point as deformation takes place. The density, temperature, velocity and other related variables are computed as time progresses. In the Eulerian description, the material properties of mass, momentum and energy flow in and out of a cell across through a fixed mesh (grid) as time progresses.

A Lagrangian/Eulerian interaction is chosen to describe the interaction of the explosive load and the steel plate. The boundary conditions of the plate are modelled as suggested by Grobbelaar and Nurick [4]. The numerical set up of the experiment is shown axi-symmetrically in figure 5.14. Gauge points at 1mm intervals are chosen along the surface of the plate in order to investigate the stress distribution in the top surface of the plate. The explosive pressure is modelled using the JWL EOS and the steel plate material behaviour is modelled using the Johnson-Cook constitutive equation. The constants in both the JWL EOS and the Johnson-Cook constitutive equation used in the ABAQUS/Explicit 6.4 code are also used for the simulation in the AUTODYN 6.0 code. It should be noted that the AUTODYN 6.0 software does not generate a simplified input deck as opposed to the ABAQUS/Explicit code which generates a simplified input deck.

More emphasis is placed on the central deformation and plate profiles as regards the outcome of the numerical results. A total time of 1ms (1000μs) is used to run the simulation of the experiments corresponding to a total cycle of 1000000.

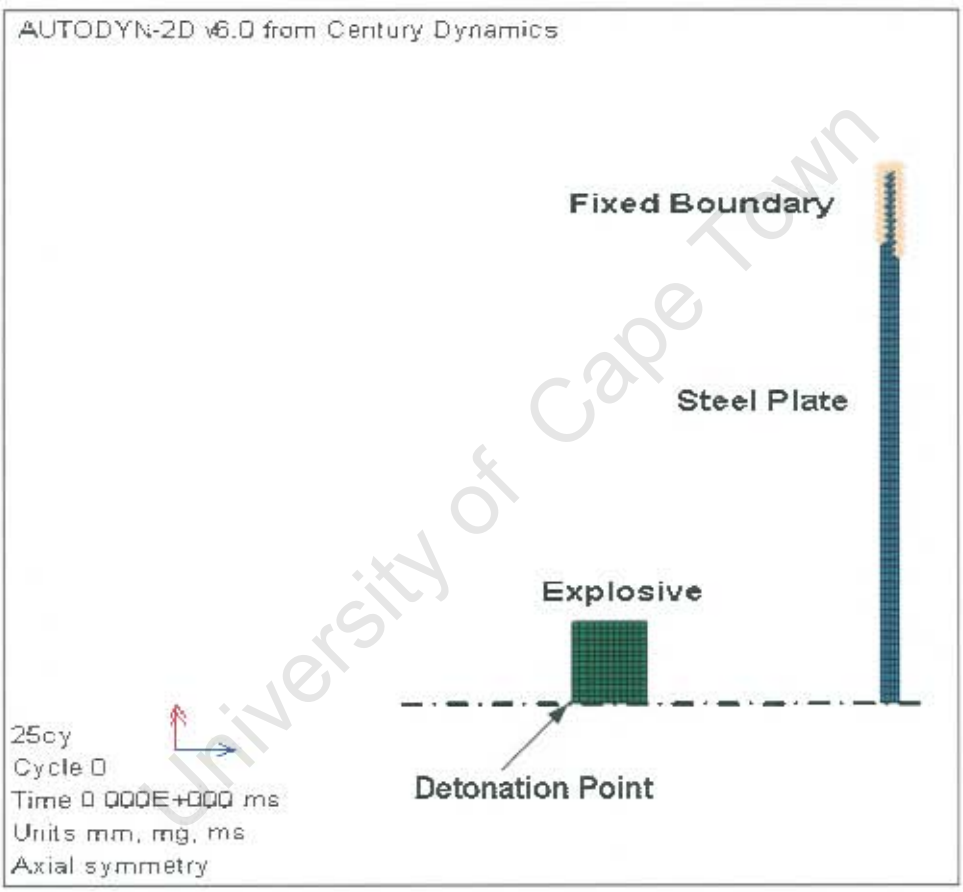

Figure 5.14: Figure showing setup of numerical simulation of explosive-plate interaction at cycle 0, using AUTODYN 6.0.

5.7 Material Properties of the Steel Plate

The material model used in this work for the steel is the Johnson-Cook [101] material model. The choice of using the Johnson-Cook [101] material model is made on the basis that it takes account of the effect of increase in yield stress due to strain hardening and a decrease in yield stress due to adiabatic effects simultaneously. The constants used in the Johnson-Cook material model with other material constants in the AUTODYN 6.0 and ABAQUS/Explicit 6.4 codes for the steel are shown in table 5.2. The value of the static yield stress is 253MPa and the true stress corresponding to that is 262MPa used as the value of A in the Johnson-Cook equation. The values of B and n, given in table 5.2 are obtained by substituting various trial values in order to obtain figure 5.15 that compares very closely with the average stress-strain curve from the experiment. The equation of the theoretical curve in figure 5.15 is given in equation 5.16. The values of the other parameters (Nos. 4-11) in table 5.2 are obtained from the AUTODYN 6.0 software materials library for mild steel 1006.

$$\sigma = 262 + 328.7\varepsilon^{0.56} \tag{5.16}$$

No	Constants	Value	Unit
1	A-static yield stress	262	MPa
2	B-work hardening coefficient	328.5	MPa
3	n-work hardening constant	0.56	-
4	m-thermal softening exponent	1	-
5	T_{ref}-room temperature	300	K
6	T_{melt}-melting temperature	1811	K
7	η-inelastic heat fraction	0.9	-
8	c_p-specific heat	452	J/kg/K
9	C-strain rate coefficient	0.02	-
10	E-Young's modulus	200	GPa
11	υ-poisson's ratio	0.3	-

Table 5.2: Johnson-Cook material constants for mild steel

5.8 Summary

The various methods used for the simulation of the experiment to predict the deformation of the structure have been addressed. Proposed shock-wave profiles

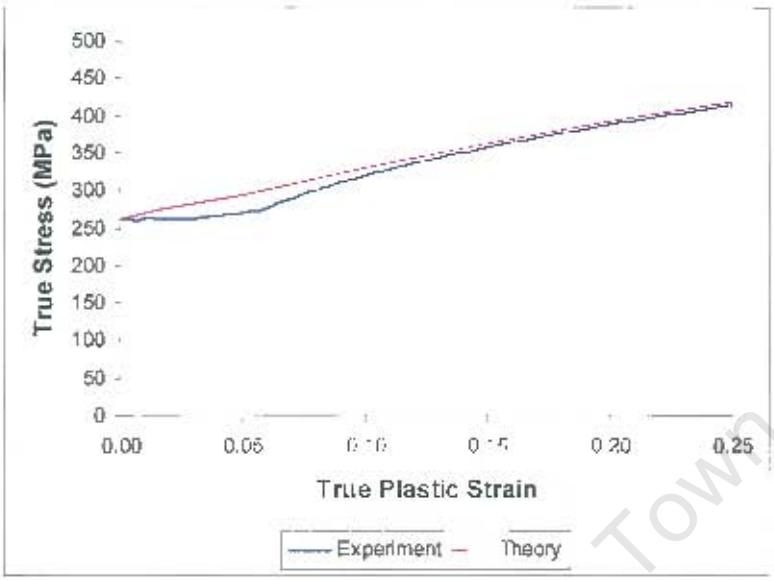

Figure 5.15: Comparison of theoretical and experimental stress-strain curves at zero-strain rate.

of the respective shapes of explosives have been constructed in order to address the load distribution on the steel plates using their respective effective masses. It is shown that the ITC explosive is less localised compared to the TC and CY explosives which are more localised. An attempt has also been made to propose alternative load distribution on the structure by the CY, TC and ITC explosives in relation to the formation of a mach stem. The numerical approach used for the prediction of the experiment using the ABAQUS/Explicit 6.4 software and AUTODYN 6.0 have been addressed with the JWL EOS and the Johnson-Cook constitutive equation incorporated in the numerical simulation for the explosive loads and plate behaviour respectively.

Chapter 6

Simulation of Explosive-Structure Interaction

6.1 Introduction

Central to this chapter is the simulation of the explosive-structure interaction using the ABAQUS/Explicit 6.4 and AUTODYN 6.0 hydrocodes. The codes predict the time evolution of the solution given the relevant flow equations and constitutive relations. The aim is to numerically investigate the final load distribution of the explosive on the plate surface and its influence on the deformation. Two simple methods of achieving convergence of the finite element solution of the model are used in both codes, by varying the element size of the explosive and plate in order to achieve the experimental deformation result. Investigations of the expansion of the CY, TC and ITC explosives and the spacial distribution of the detonation products at various time intervals during and after detonation are also carried out.

6.2 Test for Convergence of Finite Element Solution

6.2.1 Convergence of Solution in ABAQUS/Explicit 6.4 Simulation

The deformations at points P1, P2, P3 and P4 shown in the schematic of figure 6.1 are numerically investigated in order to test for convergence of the solution of the finite element model.

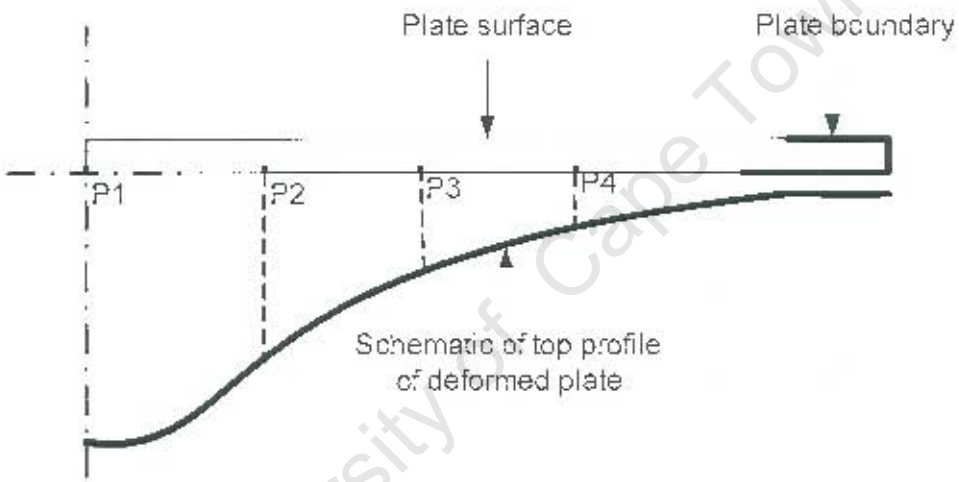

Figure 6.1: Schematics of plate showing points P1, P2, P3 and P4 and deformed profile.

An average element size of 0.8mm×0.8mm is used for the CY explosive of mass 2.6g and diameter 18mm, while the element size of the plate are varied from 0.2mm to10mm. Problems of excessive element deformation are reported at element sizes of 0.4mm of the explosive, which normally terminated the simulation. In this regard, an element size of 0.8mm of the explosive is used throughout the simulations. The experimental result of the central deformation is 15.6mm at P1 in figure 6.1. Table 6.1 shows the sizes and number of elements used for the numerical tests. The corresponding deformations of the points of reference are shown in column P1, P2, P3 and P4 of table 6.1.

A plot of the deformation against the number of elements of the plate is shown in figure 6.2. It can be seen that convergence is obtained at a minimum

Element Size	No. of Ele.	P1(mm)	P2(mm)	P3(mm)	P4(mm)
0.2mm × 0.4mm	1000	15.4	10.7	5.5	2.8
0.3mm × 0.3mm	889	15.1	10.6	5.39	2.7
0.4mm × 0.4mm	500	15.1	10.5	5.5	2.8
0.8mm × 0.4mm	250	14.89	10.1	5.35	2.66
5.0mm × 0.4mm	40	12.76	8.9	5.6	2.6
10.0mm × 0.4mm	20	9.62	7.1	4.7	2.44

Table 6.1: Number of elements of plate corresponding to deformations at P1, P2, P3 and P4.

number of 250 elements for P1 (central deformation) with an average asymptotic central deformation value of 15.2mm compared to 15.6mm for the experiment. This means that the deformation is independent of the number elements for a minimum number of elements greater than or equal to 250. In this regard, an element size of 0.8mm×0.4mm corresponding to a total of 250 elements for the plate is used to carry out all the numerical analysis whilst that of the explosive is 0.8mm×0.8mm.

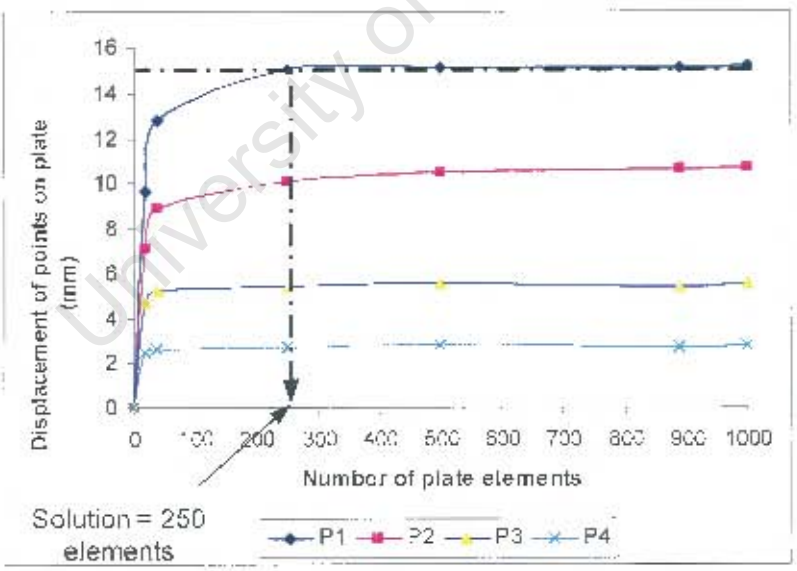

Figure 6.2: Figure showing test for convergence of the finite element solution from ABAQUS/Explicit 6.4 simulation for an 18mm CY explosively loaded plate.

6.2.2 Convergence of Solution in AUTODYN 6.0 Simulation

The relatively simple test for convergence of the finite element model in the AUTODYN 6.0 simulation is carried out by investigating the total deformation of the plate in relation to the element size of the explosive. An 18mm CY explosive of mass 2.6g is used to carry out the investigation. Element sizes of 0.8mm, 0.6mm and 0.4mm of the explosive are used to carry out the investigations by keeping the initial element size of the plate at 0.8mm×0.4mm unchanged as obtained in ABAQUS/Explicit code. Results of the predicted profiles and that of the experiments are shown in figure 6.3. It can be seen that the results is converging to the experiment as the element size is decreased. Element sizes less than 0.4mm of the explosive created problems of excessive element deformation causing termination of the simulation. In this regard, an initial element size of 0.4mm is used for the explosive throughout the simulations.

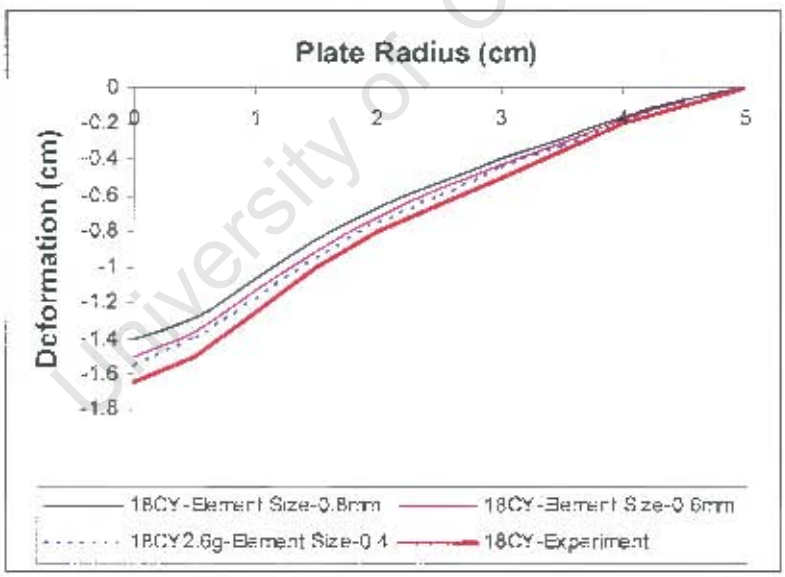

Figure 6.3: Figure showing test for convergence of the finite element solution from AUTODYN 6.0 simulation for an 18mm CY explosively loaded plate.

6.3 Effect of Element Size on Pressure and Velocity

6.3.1 Effect of Explosive Element Size and Duration on Detonation Pressure and Velocity in ABAQUS/Explicit 6.4

The magnitude of the pressure and velocity during the burning process in the simulation are also influenced by the size of the element. This is illustrated in figures 6.4 and 6.5. The results are obtained at a time of 0.7us. It can be seen that the pressure at the detonation front increases when the element size is decreased. For extremely fine mesh, the pressure can be so high and sometimes causes excessive element deformation of a structure as shown in figure 6.6.

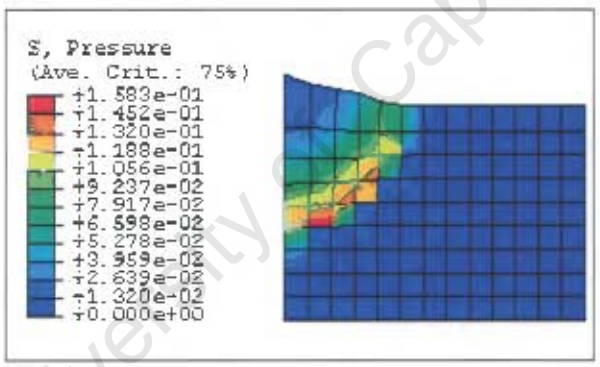

Figure 6.4: Pressure variation in (Mbars) for explosive element size of 0.8mm at time 0.7μs from ABAQUS/Explicit 6.4.

The velocity also increases as the element size decreases as shown in figures 6.7 and 6.8. The results clearly demonstrate that the pressure and velocity of detonation also vary with respect to element size of the explosive.

6.3.2 Effect of Explosive Element Size and Duration on Detonation Pressure and Velocity in AUTODYN 6.0

Effect of element size of explosive on the detonation pressure and velocity are shown in figures 6.9 and 6.10. Both figures show that the pressure and velocity

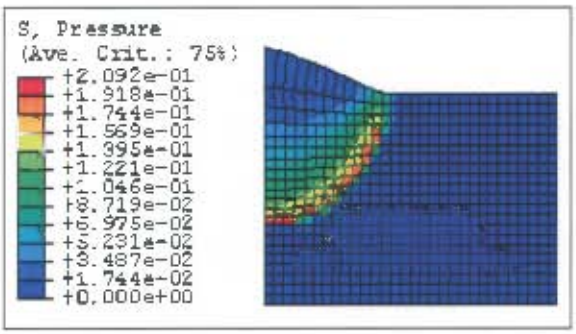

Figure 6.5: Pressure variation in (Mbars) for explosive element size of 0.3mm at a time of 0.7μs from ABAQUS/Explicit 6.4.

of the detonation front vary with a change in the element size. It is expected that after steady detonation is reached, the pressure and velocity should remain fairly constant. This variation is expected as steady detonation has not been modelled as the solution is based on a programme burn. The maximum pressure and velocity at an element size of 0.2mm in figures 6.9 and 6.10 are less than the values of 28GPa and 8190ms^{-1} as expected due to the fact that the finite element simulation gives the pressure and velocity of the detonation products.

Furthermore, figures 6.11 shows that for an explosive charge of diameter 18mm and height 15mm, the pressure of the detonation front increases with duration meaning that the solution does not converge or reaches an asymptotic values as in the case of the theory of detonation. The detonation pressure at a time of 20μs is less than the C-J pressure of 28GPa.

For a charge of diameter 18mm and height 6.34mm shown in figure 6.12, the velocity of the leading front V_E is greater than that at the detonation front V_D which is in accordance with the theory discussed in Rinehart and Pearson [21]. The velocity of the detonation products at the rear V_R is also less than that at the leading front which is also in agreement with the ABAQUS/Explicit 6.4 code.

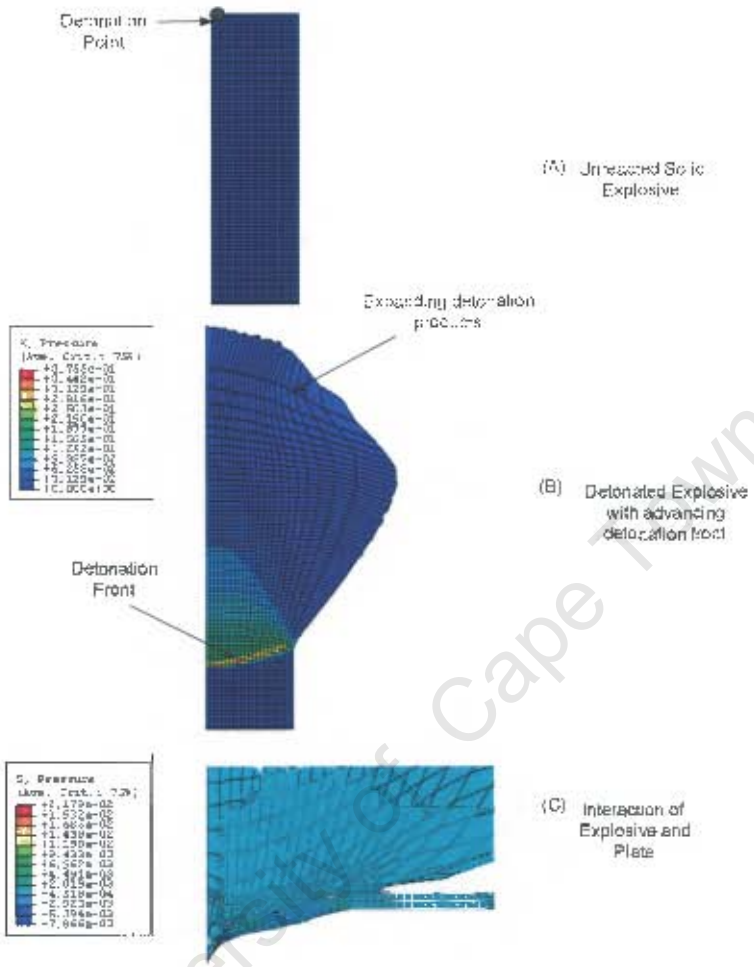

Figure 6.6: Excessive element deformation caused by a 0.4mm element size of explosive with a detonation pressure of over 37Mbars (37GPa) in diagram (B) from ABAQUS/Explicit 6.4.

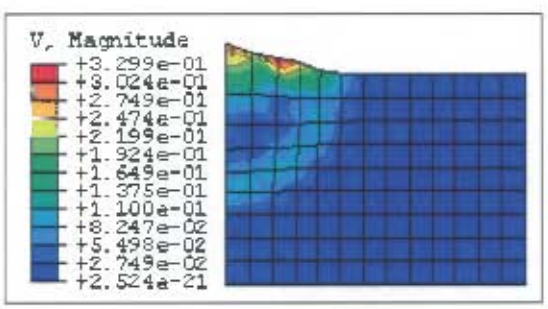

Figure 6.7: Velocity (cm/µs) of detonation products for explosive element size of 0.8mm from ABAQUS/Explicit 6.4.

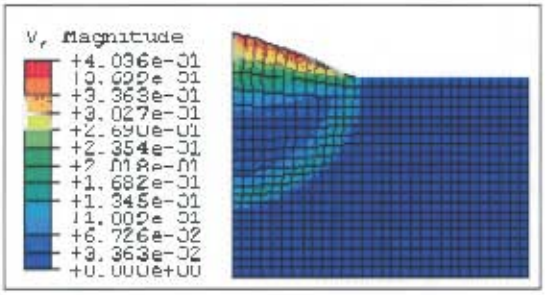

Figure 6.8: Velocity (cm/μs) of detonation products for explosive element size of 0.3mm from ABAQUS/Explicit 6.4.

6.4 Effect of Duration on Finite Element Model

6.4.1 Effect of Duration on Detonation Pressure in ABAQUS/Explicit 6.4

The effects of duration on pressure within the explosive during the detonation process is shown in figures 6.13, 6.14, and 6.15. The results show an increase in detonation pressure as the duration increases. The pressure can be seen to be lower at the rear of the explosion.

At 1.4μs, the leading pressure in the axial direction is of a lower pressure compared to that at the detonation front which still maintains a higher pressure until detonation is complete. The pressure of the explosive also depends on the dimensions of the explosive. Figure 6.16 shows pressure distribution within the explosive of a GY explosive of height 30mm and radius 9mm during detonation. The pressure as seen, is 25GPa which is close to the C-J pressure of 28GPa.

The pressure can go far beyond the magnitude of the C-J pressure of 28GPa for PE4 depending on the time and dimensions of the explosive. This is so because, the ABAQUS/Explicit programme does not limit the C-J pressure and does not also model steady detonation which is independent of time.

6.4.2 Effects of Duration on Detonation Velocity in ABAQUS/Explicit 6.4

The effects of duration on detonation velocity is shown in figures 6.17, 6.18 and 6.19. The velocity of the detonation products at the rear is higher than that at

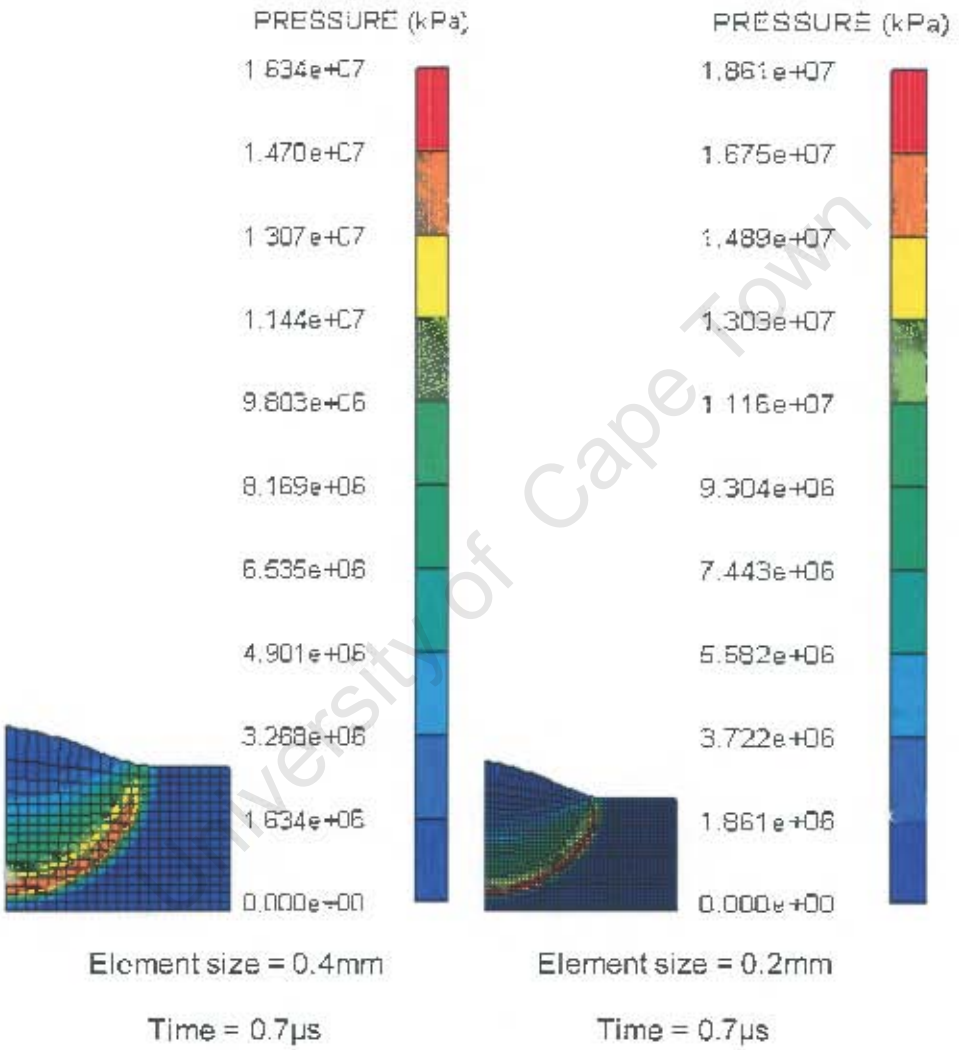

Figure 6.9: Figure showing effect of element size on the detonation pressure at a time of 0.7us.from AUTONYN 6.0.

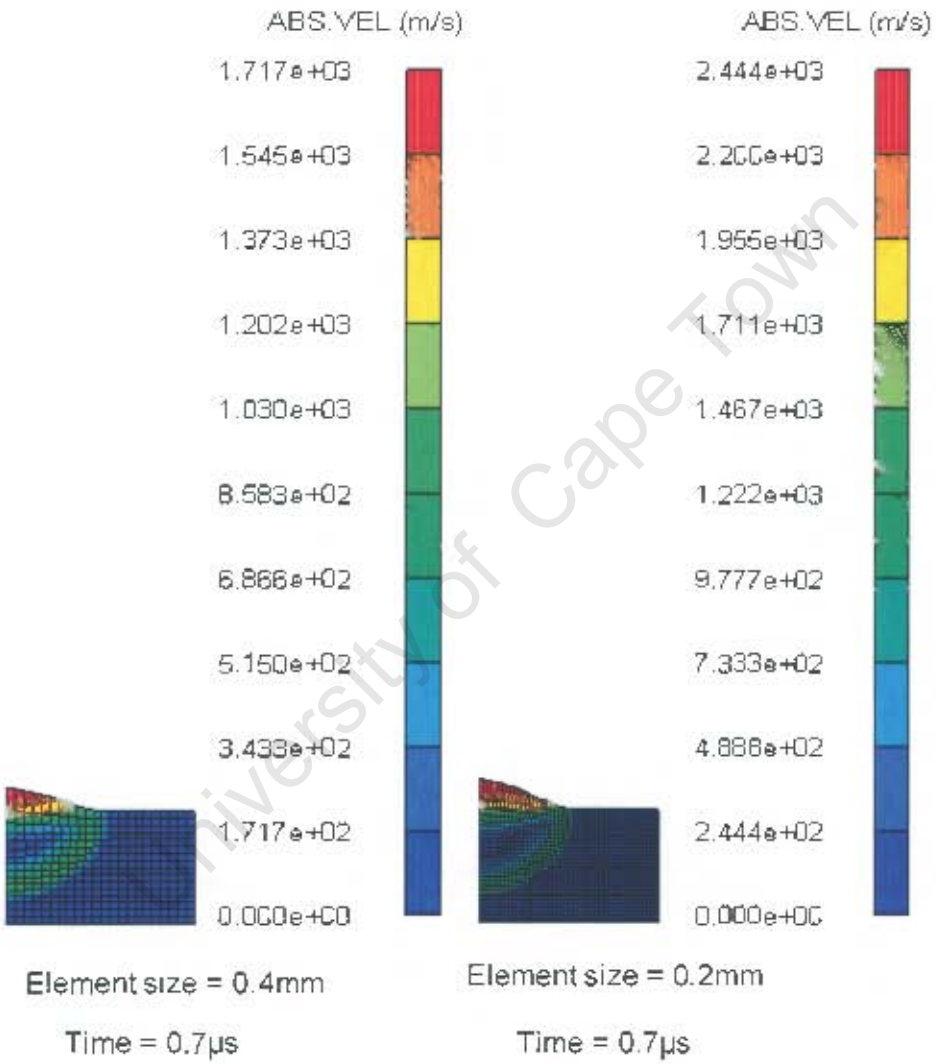

Figure 6.10: Figure showing effect of element size on the detonation velocity at a time of 0.7µs from AUTONYN 6.0.

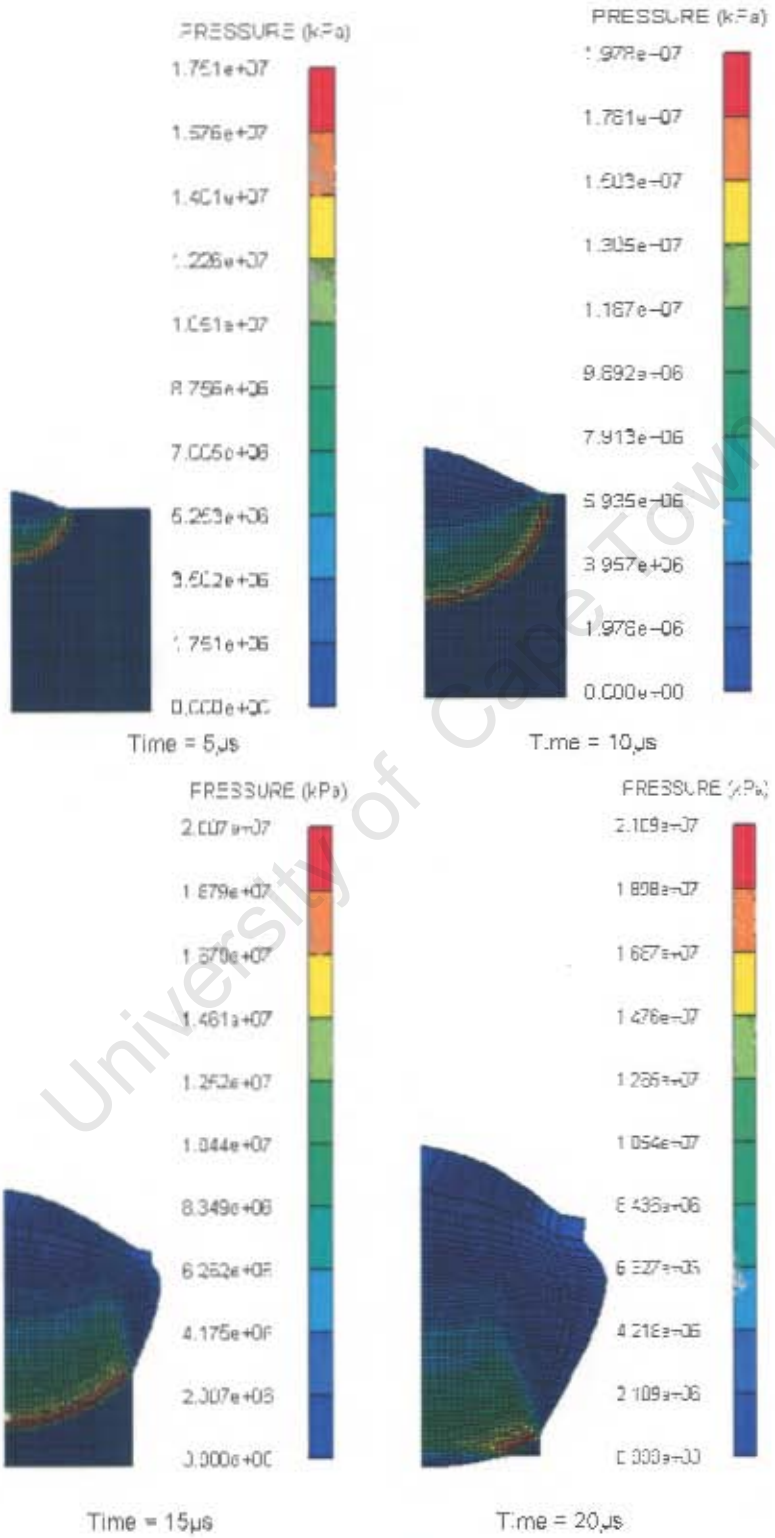

Figure 6.11: Figure showing change in pressure with respect to time for an explosive of height 15mm and diameter 18mm from AUTONYN 6.0.

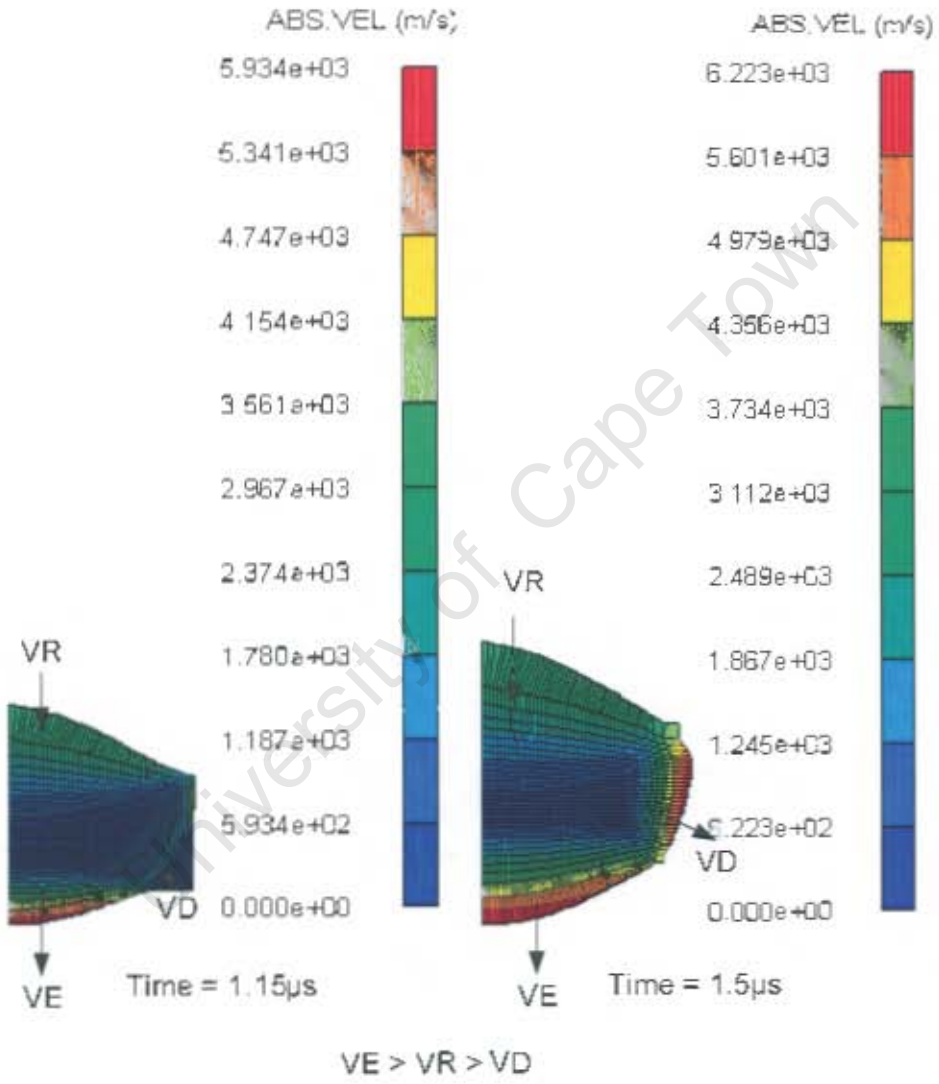

Figure 6.12: Effect of duration on detonation velocity from AUTODYN 6.0 for an element size of 0.2mm from AUTONYN 6.0.

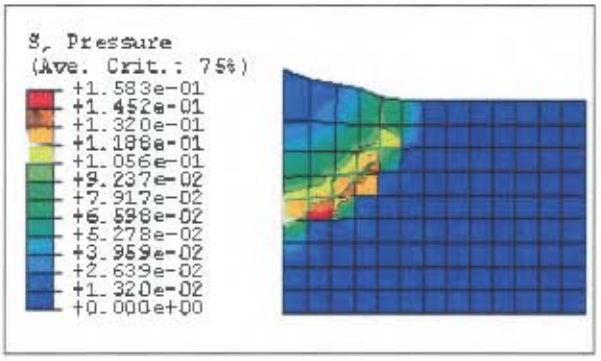

Figure 6.13: Pressure distribution in (Mbars) during detonation of explosive at time of 0.7μs from ABAQUS/Explicit 6.4.

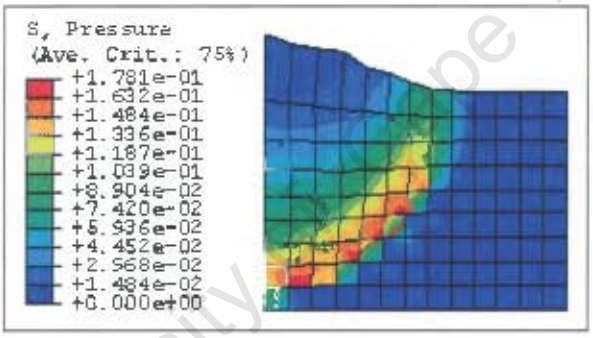

Figure 6.14: Pressure distribution in (Mbars) during detonation of explosive at a time of 1μs from ABAQUS/Explicit 6.4.

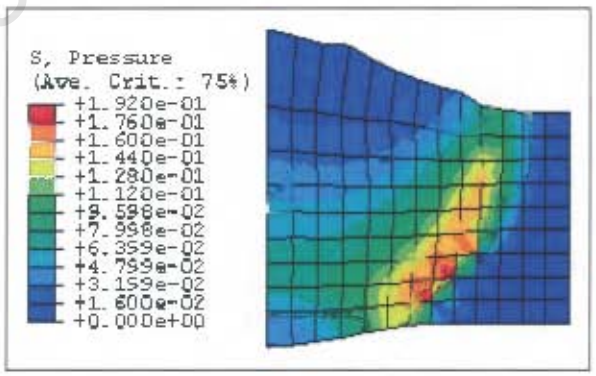

Figure 6.15: Pressure distribution in (Mbars) during detonation of explosive at a time of 1.4μs from ABAQUS/Explicit 6.4.

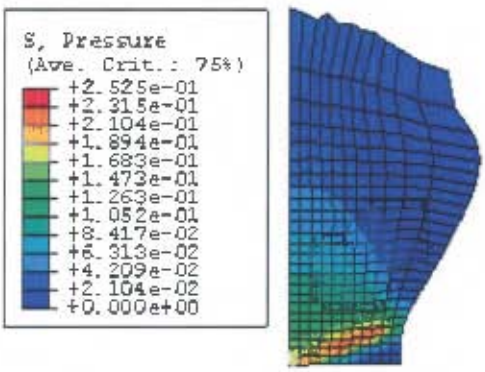

Figure 6.16: Pressure distribution in (Mbars), of a 30mm thick explosive of size 0.8mm during detonation from ABAQUS/Explicit 6.4.

the front. As reported in Rinehart and Pearson [21], the initial velocity of the explosive front increases just after detonation. The velocity at the detonation front and at the rear of the detonation front increases with duration. In theory, the detonation velocity at the front does not change once steady detonation is reached as opposed to the simulation. The velocity of the detonation products in the direction of the blast is higher than that at the rear and at the detonation front.

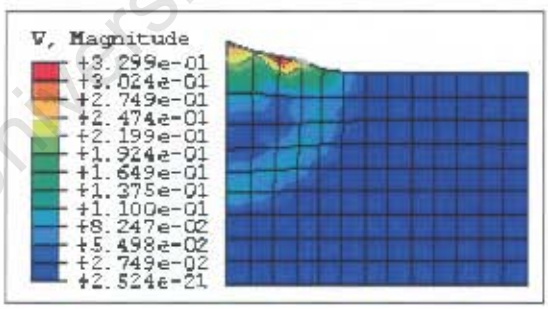

Figure 6.17: Velocity (cm/μs) of detonation products at a time of 0.7μs from ABAQUS/Explicit 6.4.

The results also show that the maximum detonation velocity is time dependent and increasing with respect to time. In figure 6.20, the velocity of the detonation products for a 20mm thick explosive and diameter 18mm is shown at a time of 2.7μs. The velocity of the front expanding particles move with a velocity of V_F and that at the rear moves with a velocity of V_R. The initial values

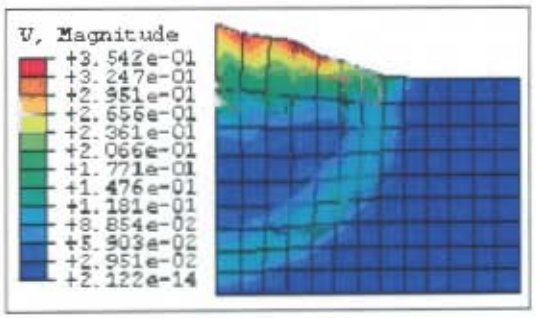

Figure 6.18: Velocity (cm/μs) of detonation products at a time of 1.0μs from ABAQUS/Explicit 6.4.

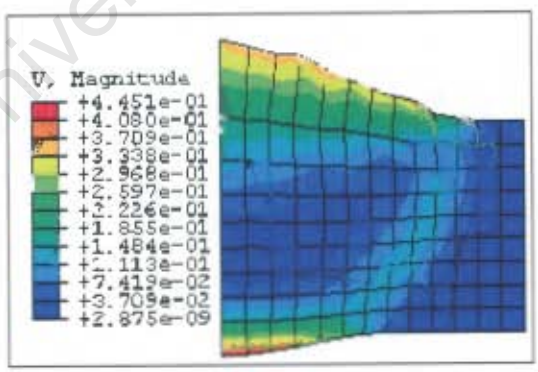

Figure 6.19: Velocity (cm/μs) of detonation products at a time of 1.4μs from ABAQUS/Explicit 6.4.

of V_F and V_R are both higher than that at the detonation front V_D as shown in the contour plot.

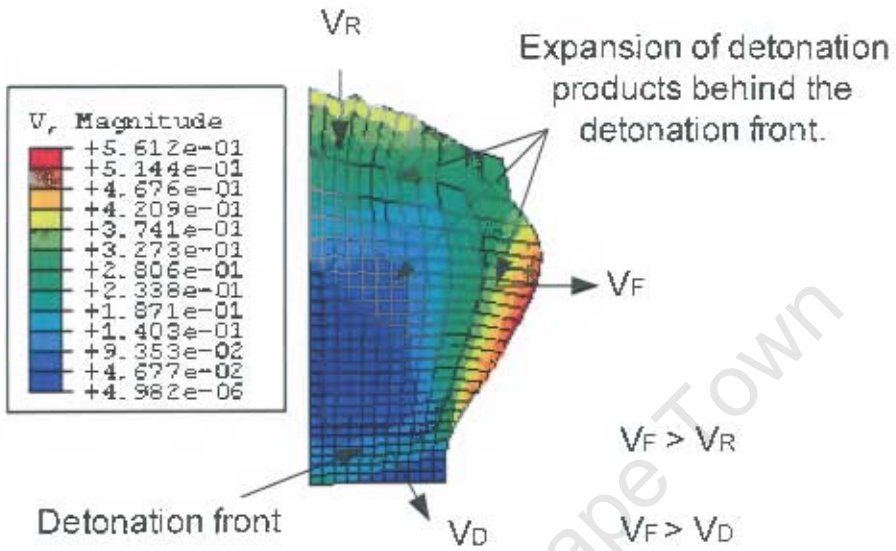

Figure 6.20: Simulation of a 20mm thick explosive showing variation in velocity at a time of 2.7s from ABAQUS/Explicit 6.4.

6.4.3 Effect of Duration on Detonation Pressure in AUTODYN 6.0

Effect of duration on detonation pressure from AUTODYN 6.0 is shown in figure 6.21. The simulation shows an increase in pressure with duration. The pressure of the detonation front is less than that at the C-J state. This variation is also expected as steady detonation has not been modelled as the solution is based on a programme burn.

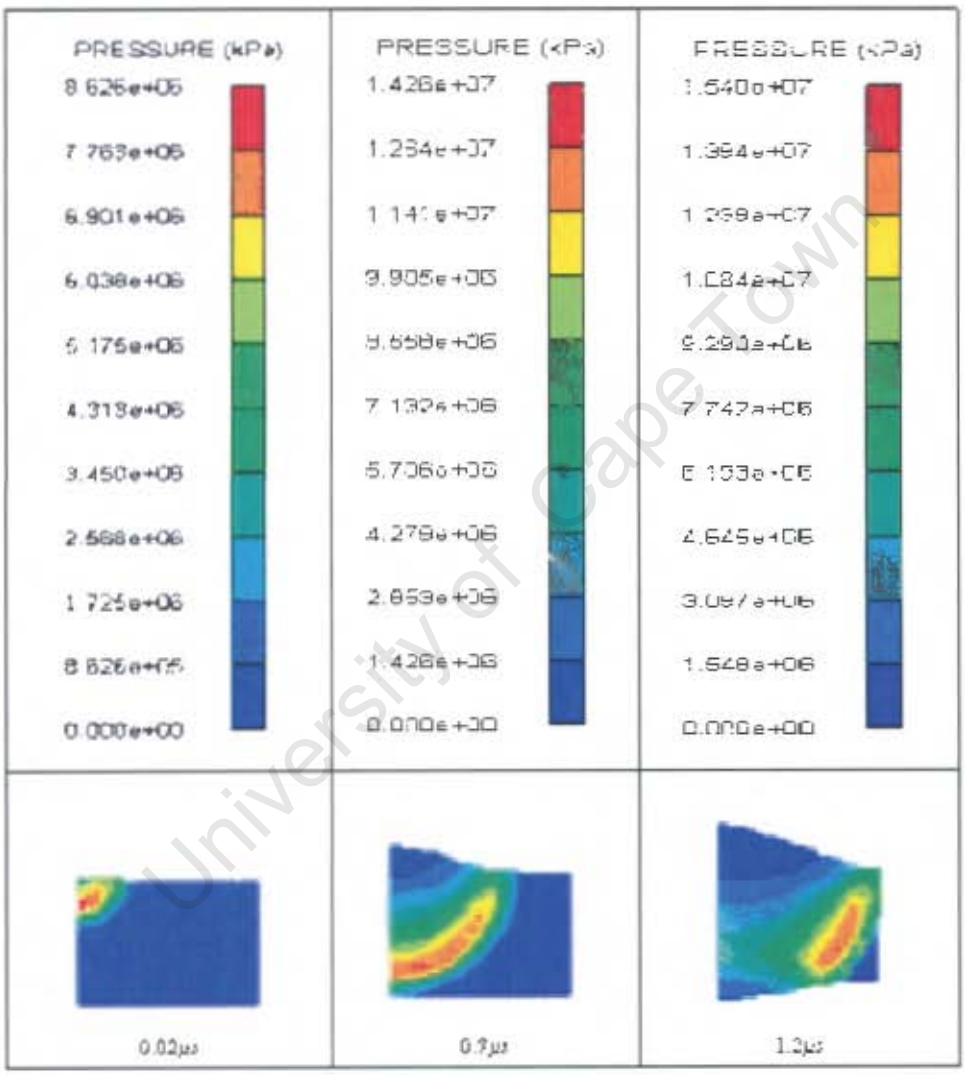

Figure 6.21: Pressure variation in CY explosive as duration increases from AUTODYN 6.0.

6.5 Effect of Shape of Explosive on Internal Energy

6.5.1 Internal Energy From ABAQUS/Explicit 6.4

The internal energy of the plate subjected to 18mm 25mm and 33mm CY, TC and ITC explosives are shown in figures 6.22, 6.23 and 6.24 respectfully. The TC loaded plates which generally show a higher central deformation, corresponding to a higher strain or plastic energy, absorbs a higher internal energy compared to the CY and ITC loaded plates. The graph of the internal energy of the 33mm TC loaded plate in figure 6.24, is not shown due to excessive element deformation which terminated the simulation.

6.5.2 Internal Energy From AUTODYN 6.0

At the start of the simulation during the detonation process, the internal energy and total energy of the explosive are the same. As expansion of the explosive continues, the internal energy of the explosive reduces rapidly to an asymptotic value as shown in figure 6.25 for a 2.6g of CY explosive whilst the total energy remain fairly constant. On interaction with the plate at 5.5μs, a slight increase in internal energy of the explosive and a corresponding drop in total energy as closely shown in figure 6.26. This behaviour of the slight drop in the total energy is not clear to the author and therefore needs further investigations.

The change in internal energy of the explosive with respect to time is shown in figure 6.27. It is shown that the internal energy of the explosive transmitted to the system increases during the initial interaction with the plate as the element size of the explosive decreases. This is shown in figure 6.27 diagram (B) in a more closer look at the influence of element size on internal energy. It is however shown that the internal energy converges for both element sizes as time progresses.

Comparison of the total energy absorbed by the plates from the TC, CY and ITC explosives are also shown in figure 6.28 from the AUTODYN 6.0 simulations. It is shown that the total energy absorbed by the plates subjected to the various shapes of explosives vary due to the load distribution. The higher internal energy absorbed by the plate is mainly associated with the increase in strain energy which is associated with the increase in deformation of the plate. Because a higher central deformation of the plate is generally associated with

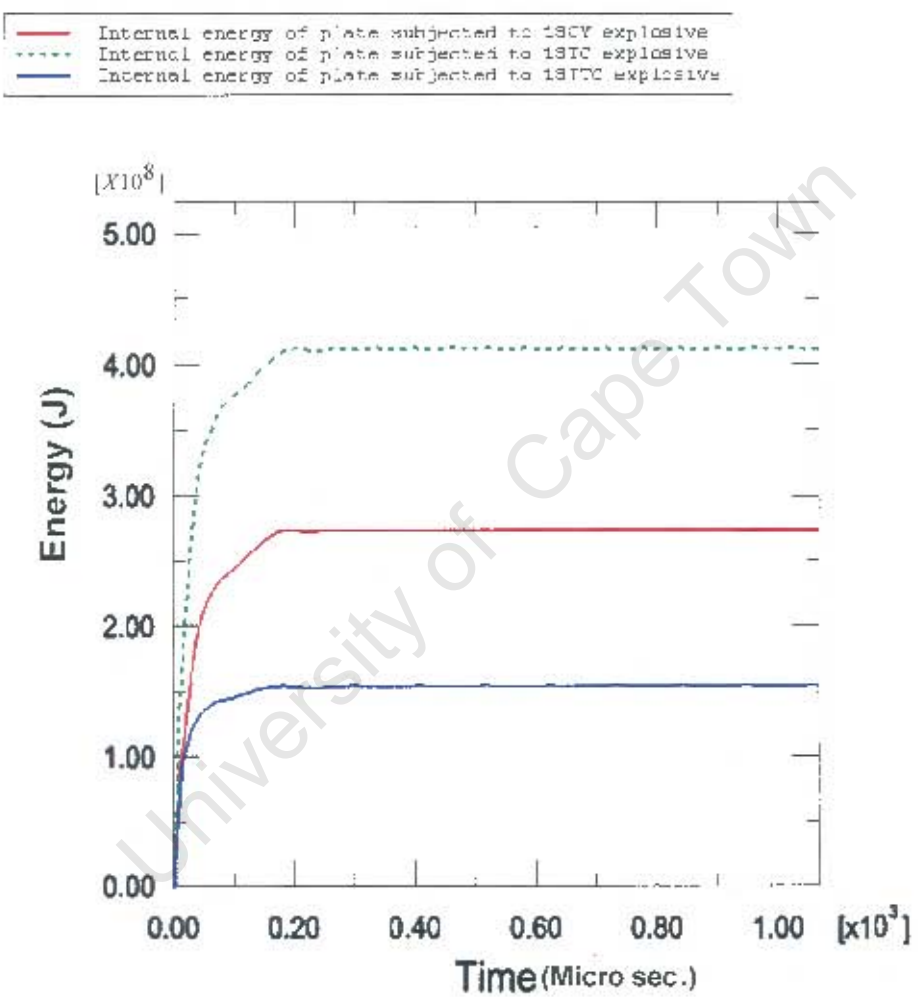

Figure 6.22: Graphs showing internal energy of plates subjected to 18mm CY, TC and TTC explosively loaded plates from ABAQUS/Explicit 6.4 simulation.

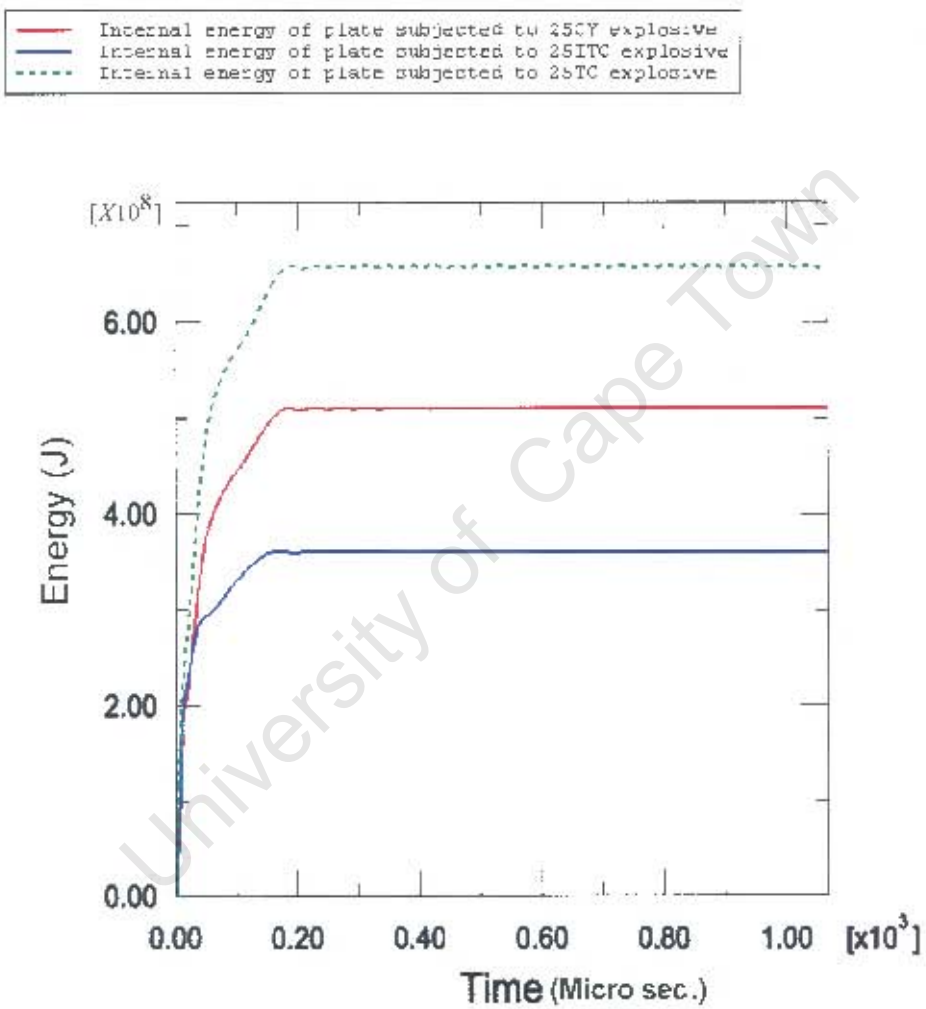

Figure 6.23: Graphs showing internal energy of plates subjected to 25mm CY, TC and ITC explosively loaded plates from ABAQUS/Explicit 6.4 simulation.

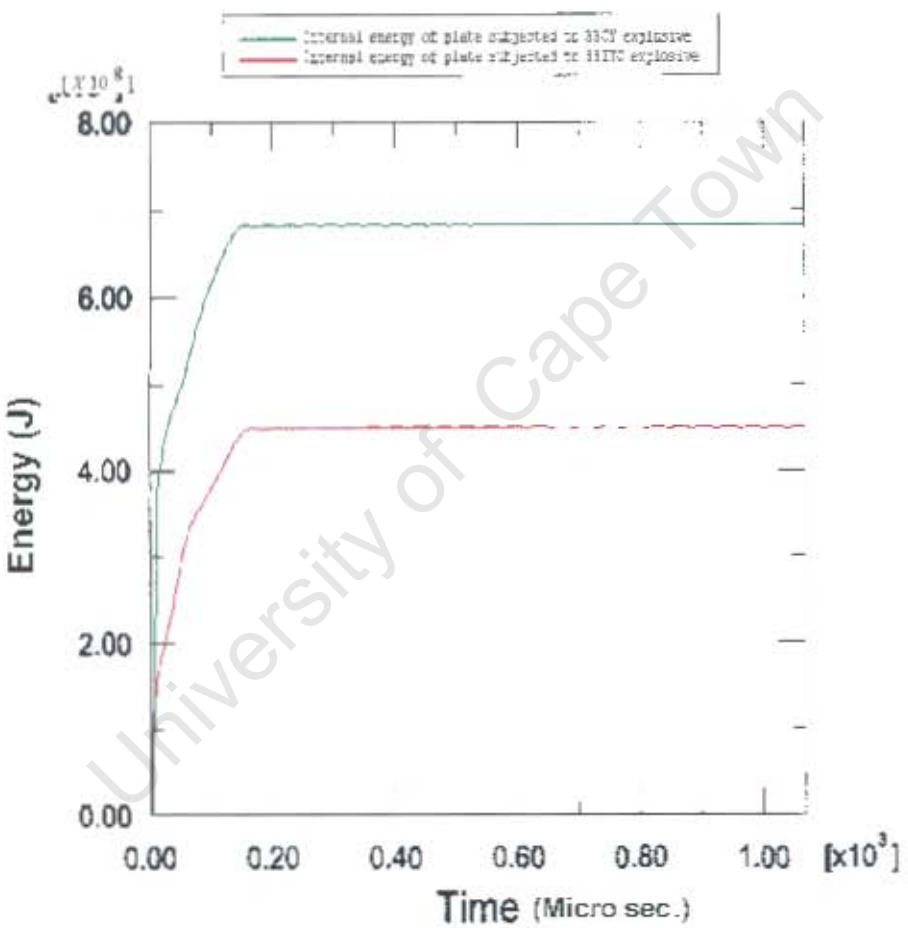

Figure 6.24: Graphs showing internal energy of plates subjected to 33mm CY and ITC explosively loaded plates from ABAQUS/Explicit 6.4 simulation.

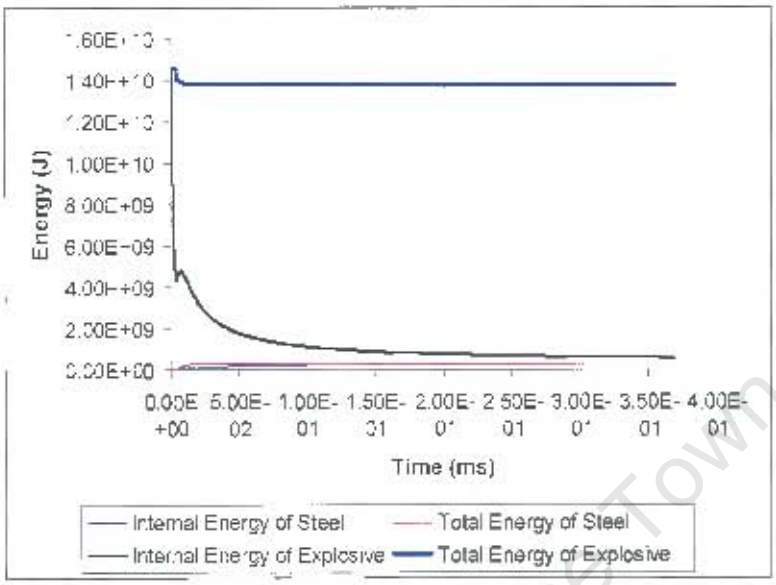

Figure 6.25: Graphs showing change in total and internal energy of TC explosive of mass 2.6g with time from AUTODYN 6.0.

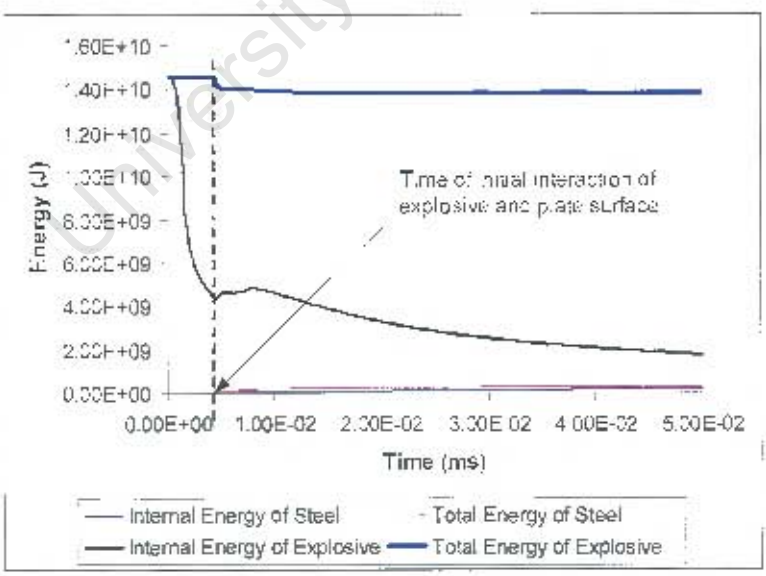

Figure 6.26: Graphs showing point at which plate and explosive interact for a TC explosive of mass 2.6g at 5.5µs.

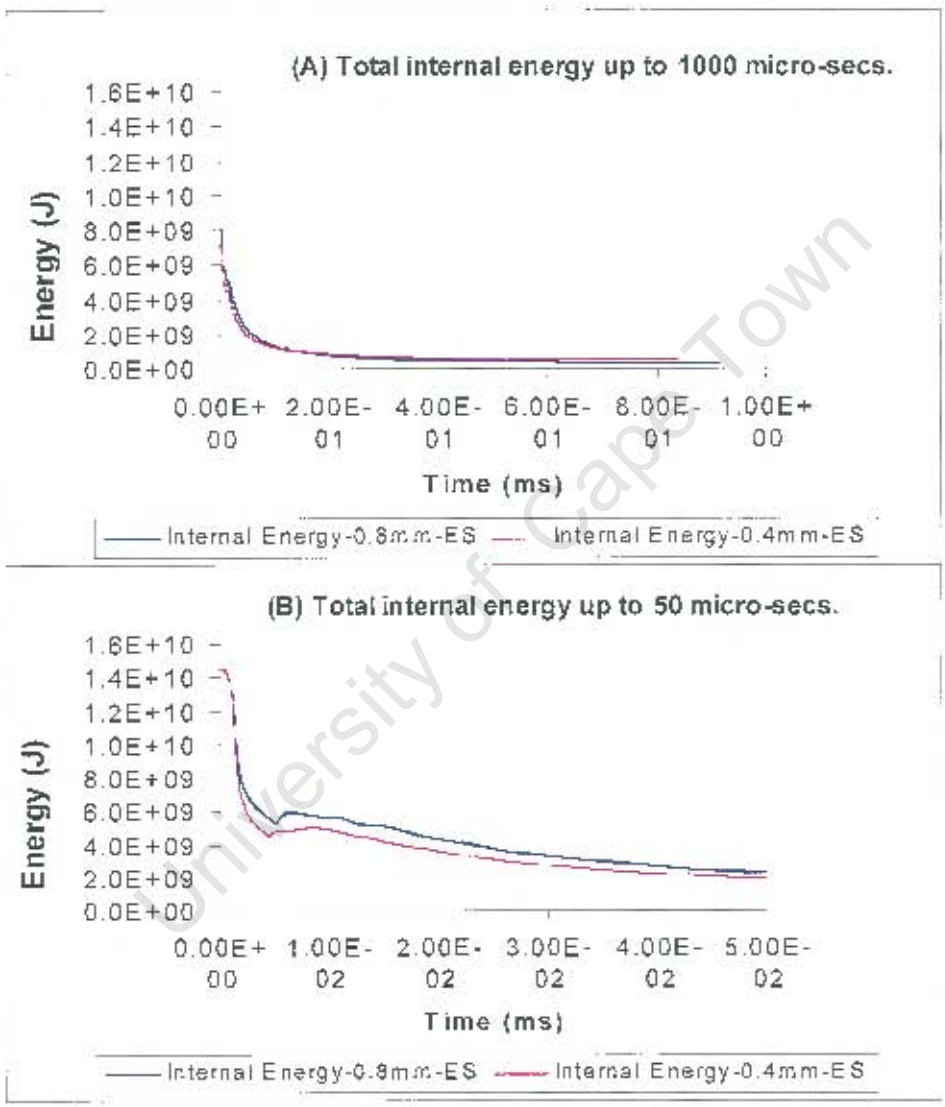

Figure 6.27: Graphs showing change in internal energy of explosive with time from AUTODYN 6.0.

the TC explosive, a higher total energy absorbed by the plate is expected for a TC-explosively loaded plate compared to a CY and ITC loaded plates.

6.6 Investigating the Detonation Process in ABAQUS/Explicit 6.4

Results of the expansion of the explosives during the detonation process are numerically investigated in three steps of the simulation. The spectrum of colours indicate the pressure (stress) distribution of the model as shown in figure 6.29.

For illustrations of the detonation process, a mass of 2.6g of 18mm CY, TC and ITC explosives are used to show the progression of the wave front during and after detonation. The element size of the explosive is 0.8mm×0.8mm, while the size of plate elements is 0.8mm×0.4mm. The colours corresponding to pressure from the simulation indicate the strength of the pressure or stress distribution but does not represents the true values in reality.

Step I

Simulation of the detonation process of the explosive is shown in a contour plot in figure 6.30. Progression of the detonation front from 0.45μs to 2μs for all three explosive shapes indicate a circular detonation front at high pressure.

It can be seen in figure 6.30, that the CY explosive is consumed faster in the vertical direction due to its shorter height compared to the TC and ITC explosives due to its shorter height. At 1.5μs, the CY and ITC explosives are completely consumed whilst the TC explosives is completely consumed at a time of 1.8μs.

It can be seen in figure 6.30, that the pressure increases at the centre of the explosive due to residual heat and pressure which is still present after generation of the first (primary) shock-wave as in the case of a real detonation process. This can be clearly seen at a time of 2μs, at which the centre is at a higher pressure compared to the other areas of the explosion. The presence of the high pressure detonation particles normally at very high pressure and temperature within the explosion, causes a multiple of shocks of lesser magnitude compared to the primary shock. The issues of multiple shocks are well addressed in Baker [60] and Ohashi *et al* [115].

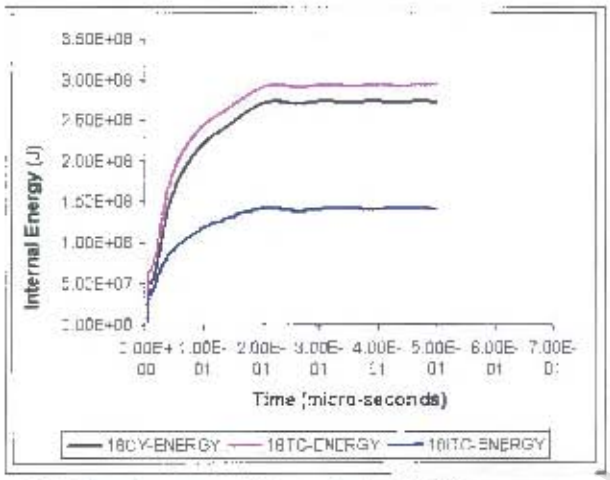

(A) Internal energy of plate subjected to 18mm charges

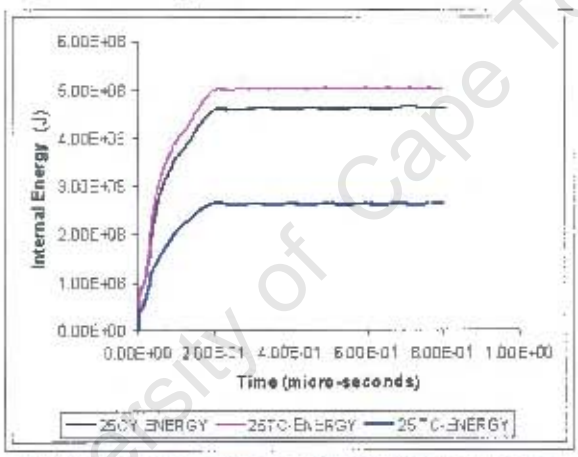

(B) Internal energy of plate subjected to 25mm charges

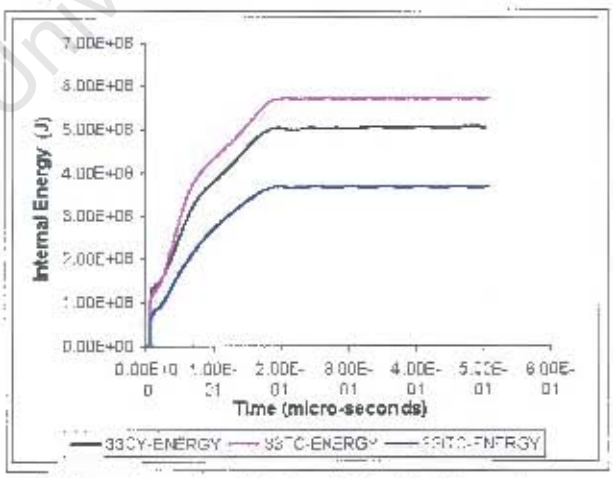

(C) Internal energy of plate subjected to 33mm charges

Figure 6.28: Graphs showing internal energy of plates subjected to 18mm 25mm and 33mm CY, TC and ITC explosively loaded plates from AUTODYN 6.0 simulation.

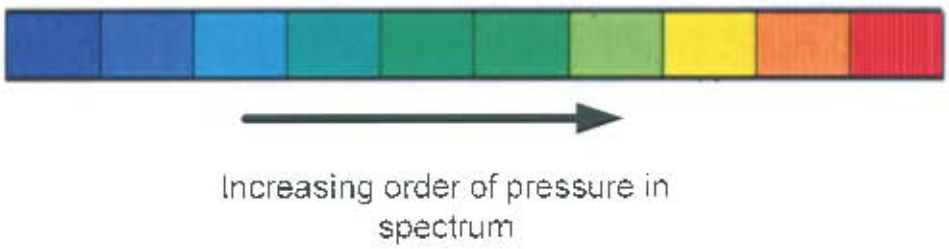

Figure 6.29: Figure showing spectrum of colours corresponding to pressure variation in finite element model ranging from 0 to 33GPa.

Step II

In this step, interrogation of the contact of the explosive and the plate top surface is carried out. Figure 6.31 shows interaction of the expanding detonation products and the plate surface. The figure also shows pressure and stress distribution with explosive and plate respectively as indicated by the colour variation. In figure 6.31, more area of contact is made by the CY explosive on the plate at a time of 4.6μs, compared to the TC and ITC explosives. At 8.2μs and 10.2μs, the area of contact by the ITC explosive is more than that created by the TC and CY explosives due to the proximity of the slant sides to the plate. Figure 6.31 also shows that the load by the ITC is less localised compared to the CY and TC explosives. Although not very clear from the diagrams in figure 6.31 however, it can also be seen at a time of 26.4μs, that the vertical deformation of the plate by the TC explosive is greater than those of the CY and ITC explosive indicating a more localised effect. This shows that the TC and CY explosive loads are more localised compared to the ITC explosive which is in agreement with the experiment and theory discussed earlier.

Results of the detonation process of 25mm CY, TC and ITC explosives of mass 3.0g are also shown in figures 6.32 and 6.33. The results show similar load distribution compared to the 18mm load cases. At times of 8.2μs, 10.2μs, and 17.29μs, it is shown in figure 6.33, that the ITC explosive is more uniformly distributed compared to the TC and CY explosives which show more localised load distribution on the plate surface. It is also shown that due to the problem of contact interaction between the explosive and plate, which is related to mesh density, the deformation of the plate subjected to CY and TC explosives are not well predicted.

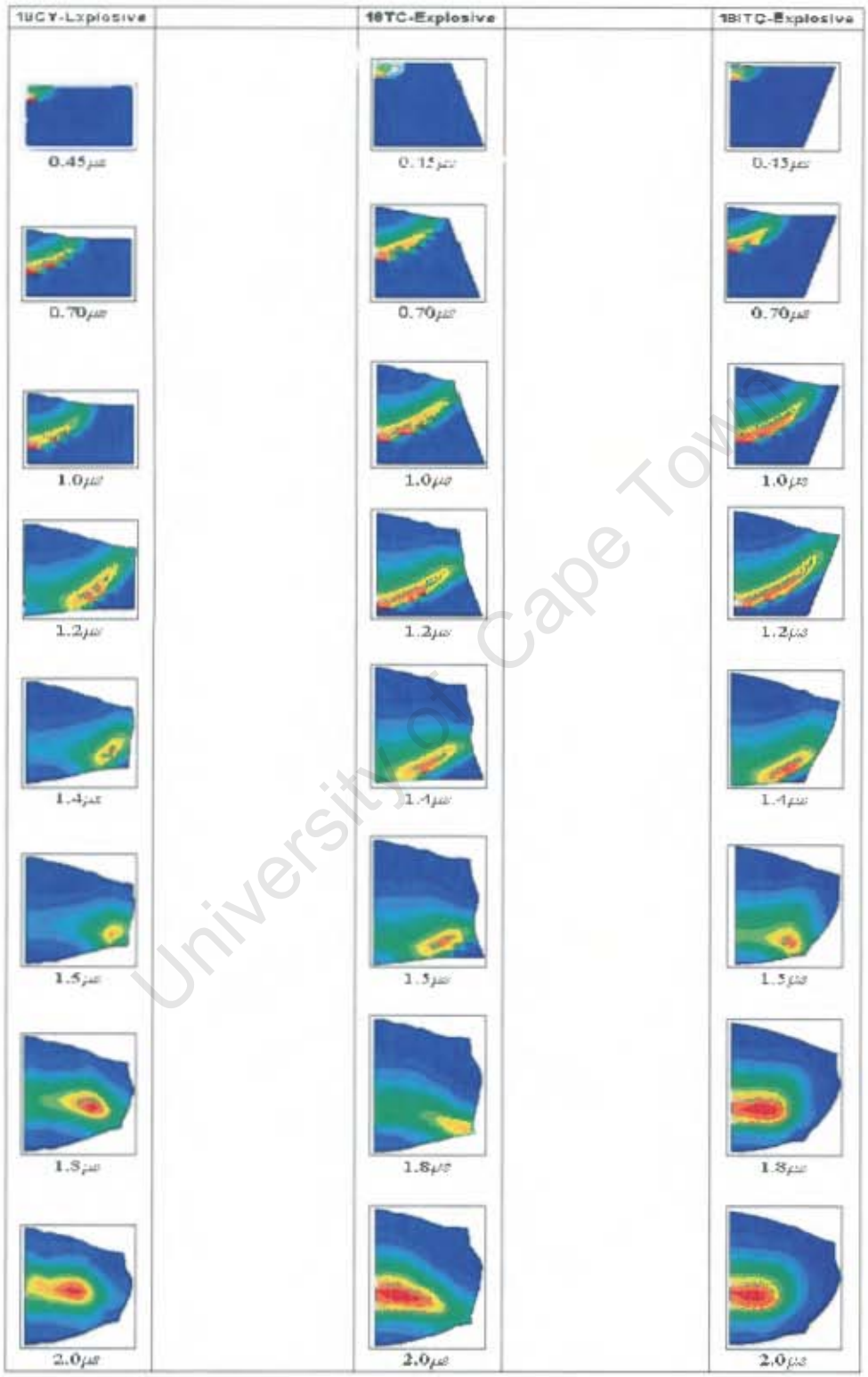

Figure 6.30: Figure showing detonation process and pressure distribution within 18mm CY, TC and ITC explosives of mass 2.6g each from ABAQUS/Explicit 6.4.

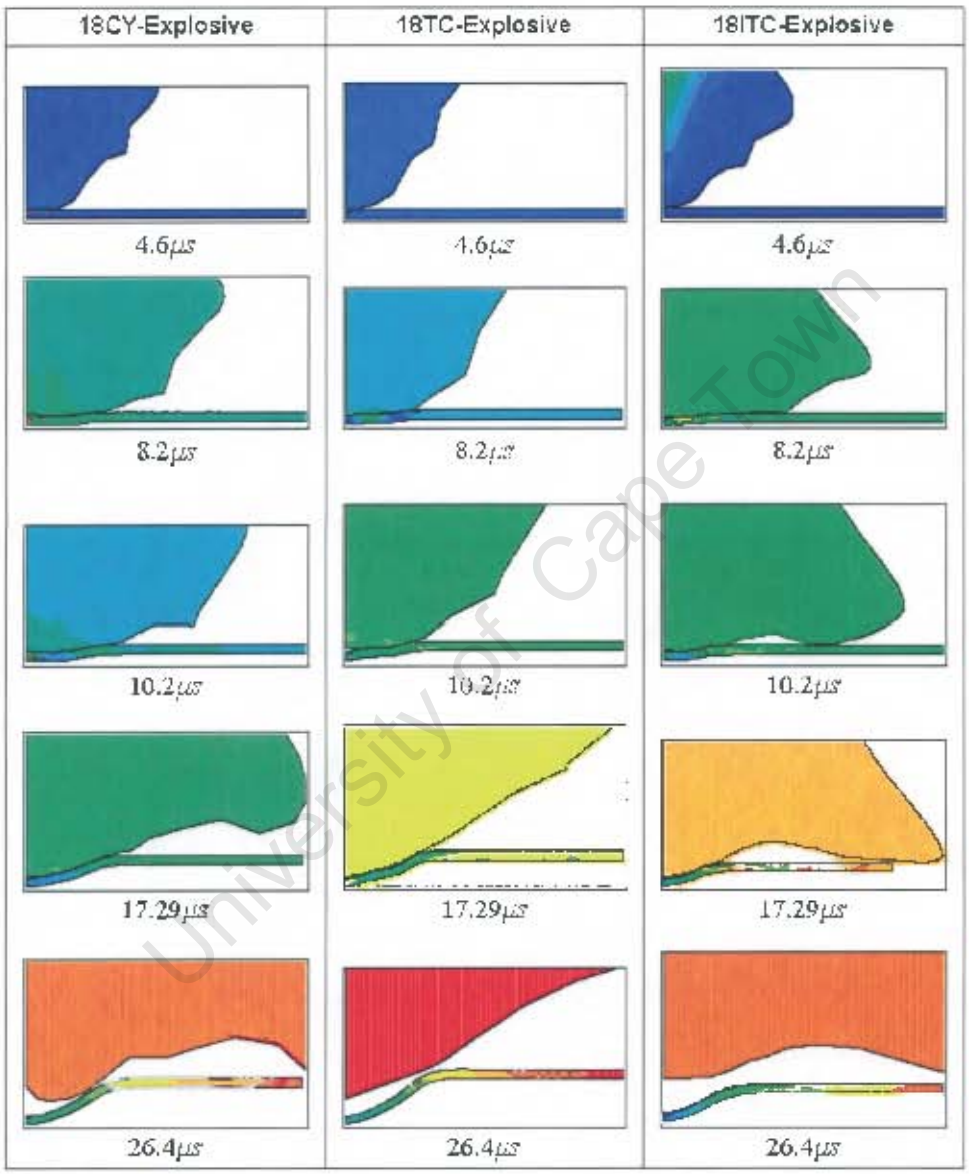

Figure 6.31: Figure showing interaction of expanding 2.6g of CY, TC and ITC explosives and contour plot of pressure (stress) on plate in Step II of the simulation from ABAQUS/Explicit 6.4.

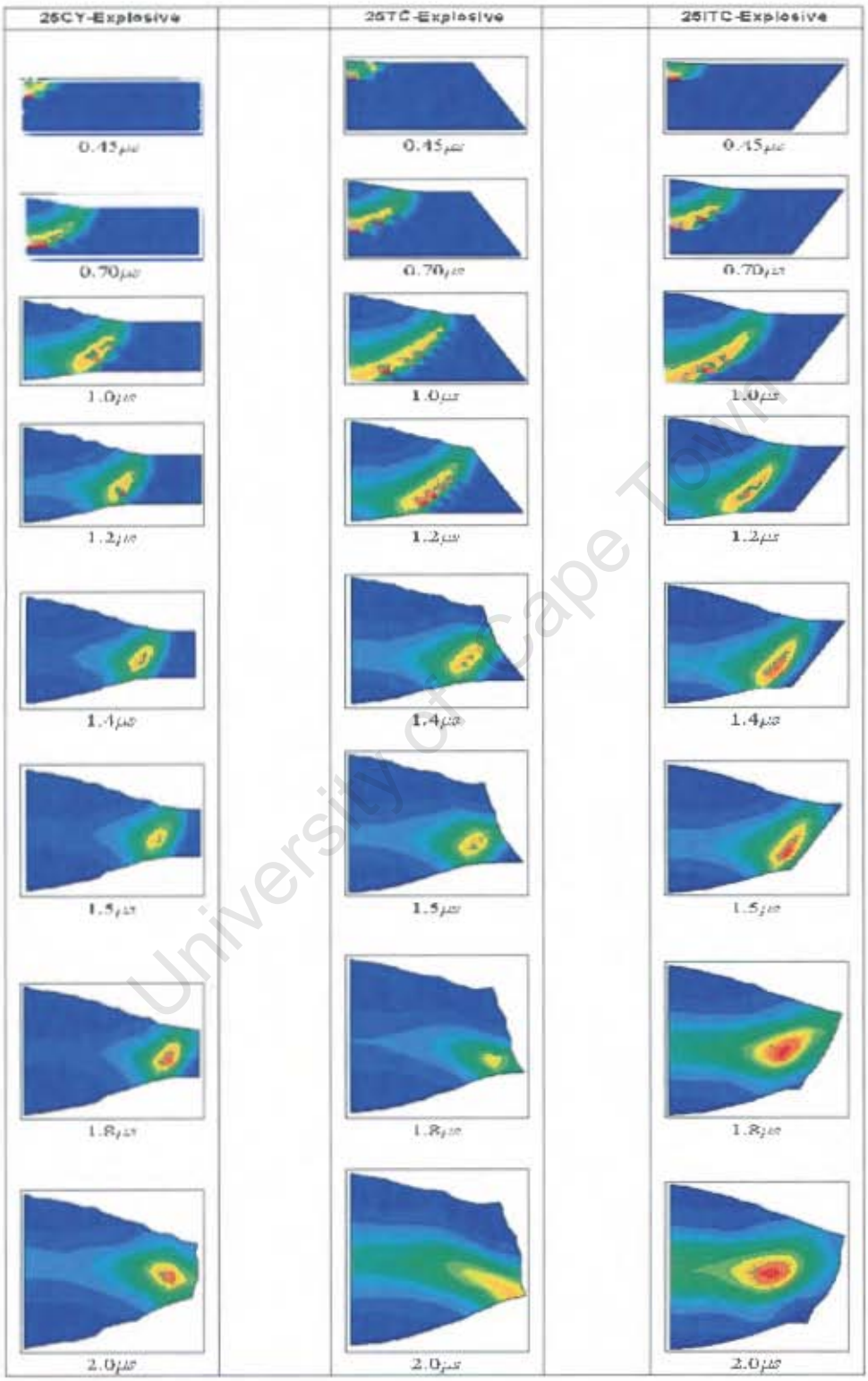

Figure 6.32: Figure showing detonation process and pressure distribution within 25mm CY, TC and ITC explosives of mass 3.0g each from ABAQUS/Explicit 6.4 (Step I).

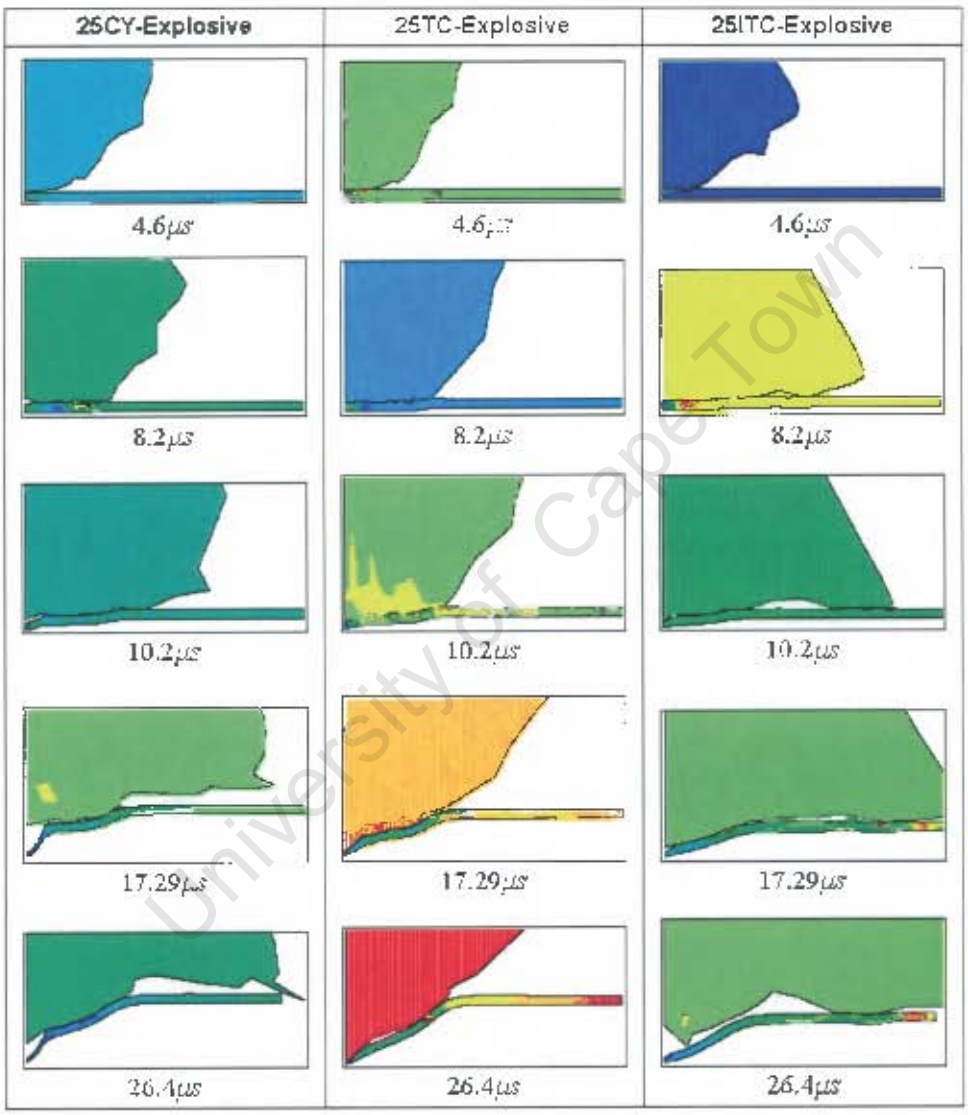

Figure 6.33: Figure showing interaction of expanding explosive and contour plot of pressure (stress) on plate in Step II of the ABAQUS/Explicit 6.4 simulation.

Step III

Step III is the final step of the simulation process, wherein no contact between the explosive is made with the plate. The explosive is then "frozen" as no contact is made with the plate. The plate absorbs the energy from the explosive for 1000μs. The final deformed plates are shown in figure 6.34, where the central deformation subjected to the TC explosive is higher than that of the CY and far greater than that of the ITC explosive. Thinning can also be observed for the plate subjected to the TC explosive which may be realistic as deformation becomes excessively large.

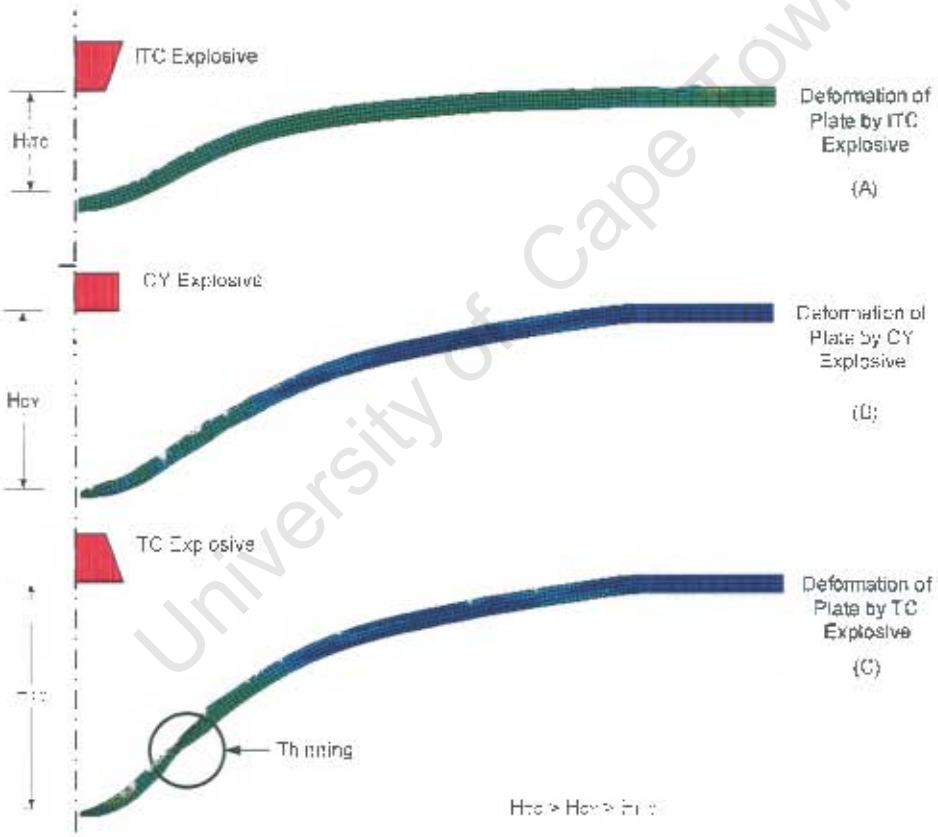

Figure 6.34: Figure showing deformation of plates subjected to ITC, CY and TC explosives of mass 2.6g in (A), (B) and (C) respectively (Step III) from ABAQUS/Explicit 6.4.

6.7 Investigating the Detonation Process in AUTODYN 6.0

The detonation process of the CY, TC and ITC explosives from the AUTODYN 6.0 code, is shown in figure 6.35. It is seen that the detonation process is similar to that generated in ABAQUS/Explicit 6.4 as regards the shape of the wave front. The simulation is shown to run from 0.25μs to 24.4μs in order to investigate the load distribution on the steel plate. The wave front remains circular during the detonation process until the explosive charge is completely consumed. The CY explosive is consumed much earlier than the TC and ITC explosive along its axis at 0.69μs. At 1.0μs, the CY explosive has been fully consumed whilst the TC and ITC explosive are completely detonated at a time of 1.2μs. It can be seen that the high pressure region within the explosive after complete detonation, moves toward the axis. This may be due to the fact that a considerable amount of pressure is still within the explosive after the generation of the first primary shock wave as it expands as seen more clearly at a time of 2.0μs.

Expansion of the explosive detonation particles continue until interaction is made with the plate surface as shown in figure 6.36. At 5.0μs, the explosives have still not made any contact whilst contact is visible at 5.9μs. At 5.9μs, it can be seen in figure 6.36 that the load by the ITC explosive is much more distributed on the plate compared to the CY and TC explosives. It can also be seen that the TC explosive load is more localised at a time of 7.8μs compared to the CY and ITC explosives.

Similar observations of the expansion and load distribution of the blast on the plate can be made as shown in figures 6.37 and 6.38 for 25mm load cases and in figures 6.39 and 6.40, for 33mm load cases.

The final deformation at a time of 1000μs from the AUTODYN 6.0 simulation is shown in figure 6.41. It is shown numerically, that the central deformation of the plate subjected to a TC explosive is higher than those of the CY and ITC explosive. From figure 6.41, no significant thinning is observed in all three plates. This can be associated with a lower deformation of the plate which is less than that given by ABAQUS/Explicit 6.4.

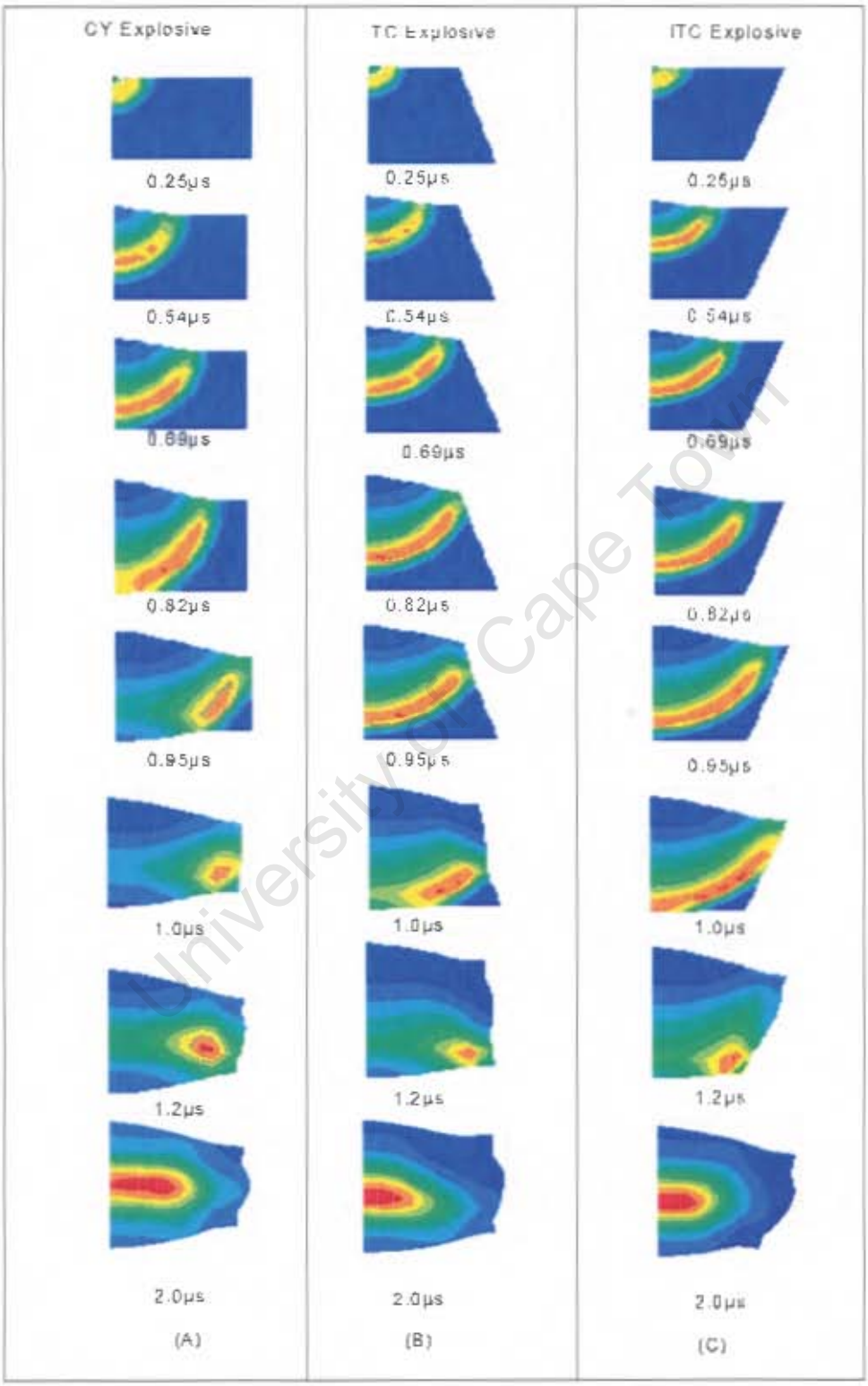

Figure 6.35: Figure showing detonation process and pressure distribution within 18mm CY, TC and ITC explosives of mass 2.6g each from AUTODYN 6.0.

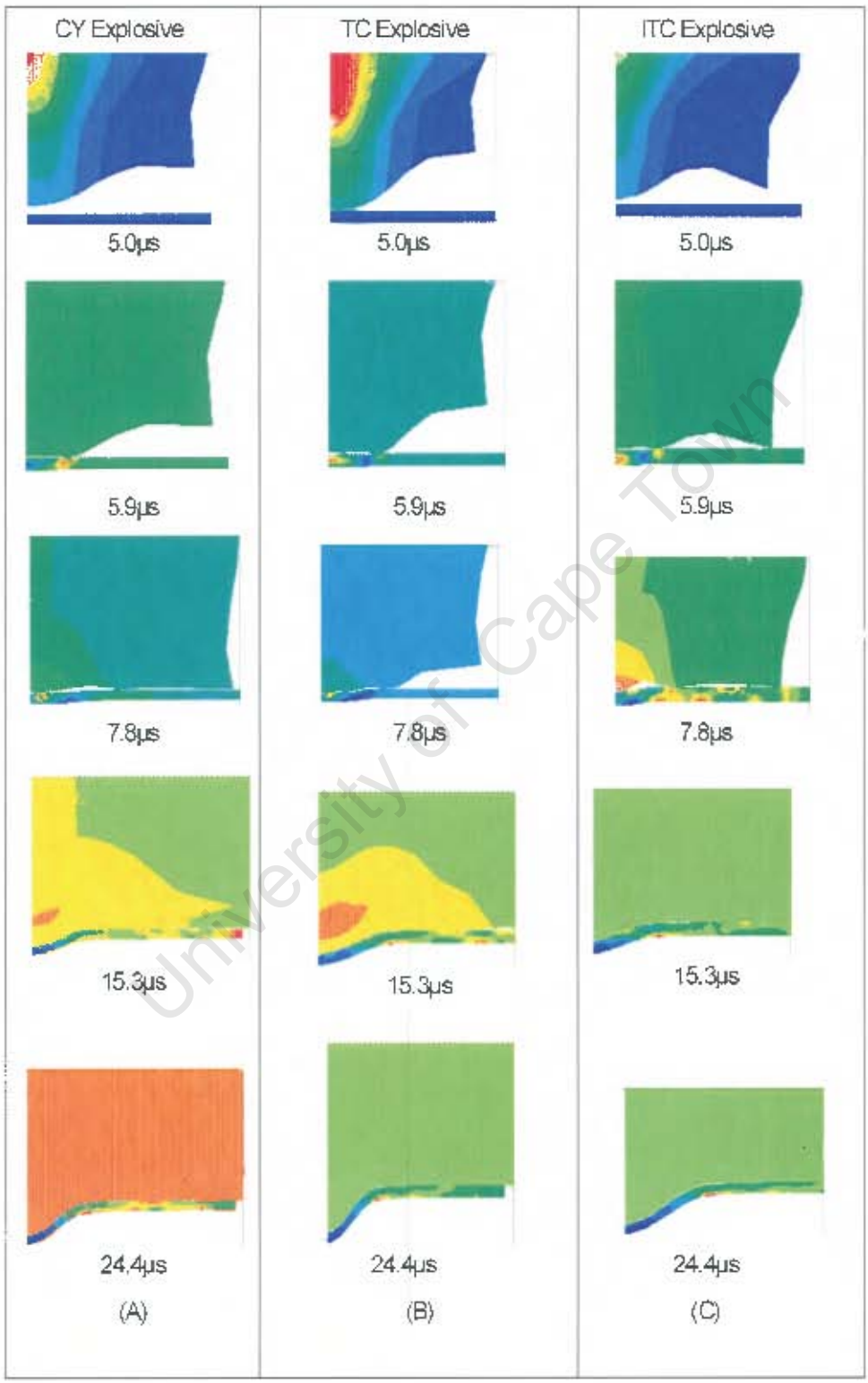

Figure 6.36: Figure showing interaction of expanding 2.6g of 18mm CY, TC and ITC explosives and contour plot of pressure (stress) on plate from AUTODYN 6.0.

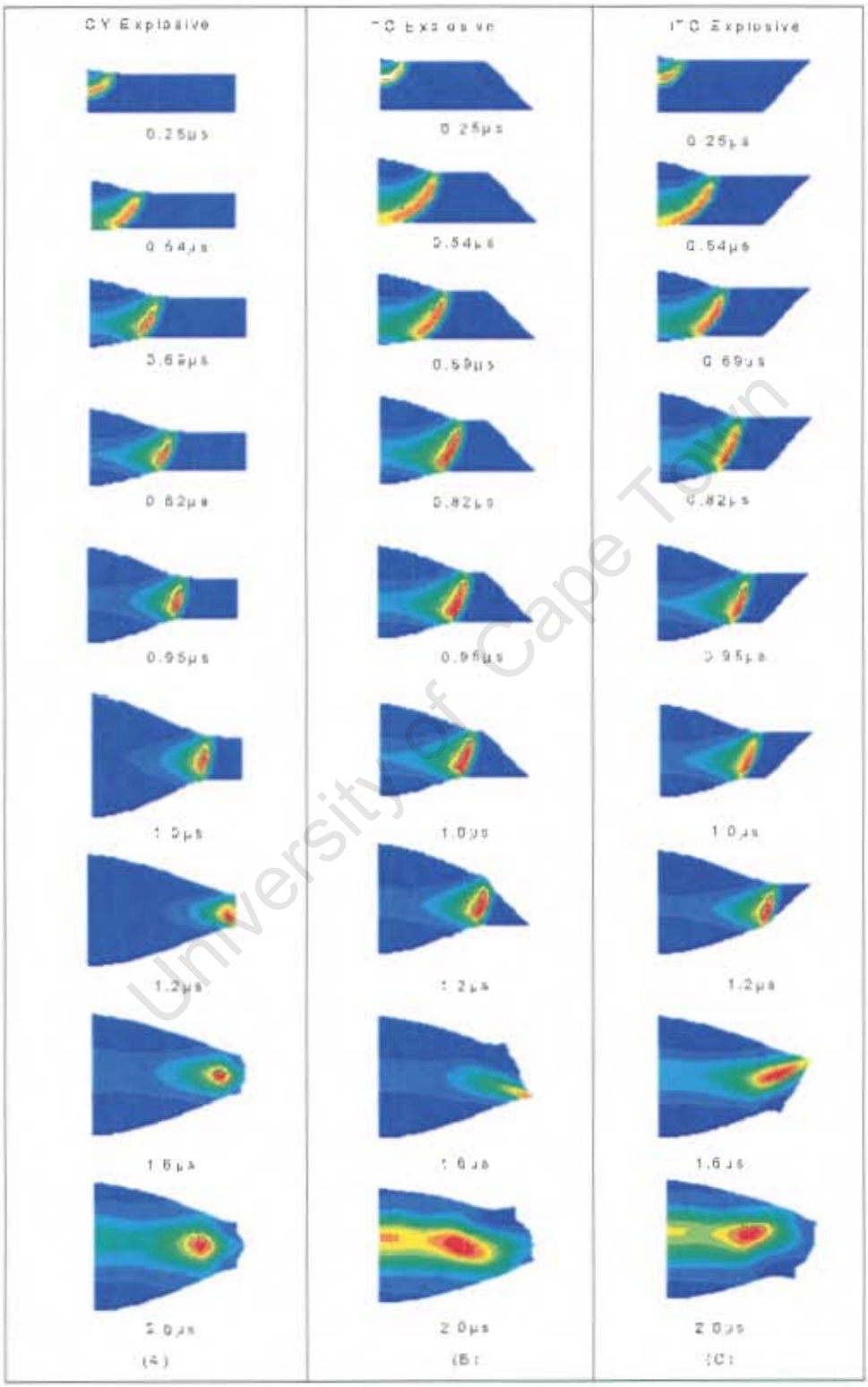

Figure 6.37: Figure showing detonation process and pressure distribution within 25mm CY, TC and ITC explosives of mass 3.0g each from AUTODYN 6.0.

Figure 6.38: Figure showing interaction of expanding 3.0g of 25mm CY, TC and ITC explosives and contour plot of pressure (stress) on plate from AUTODYN 6.0.

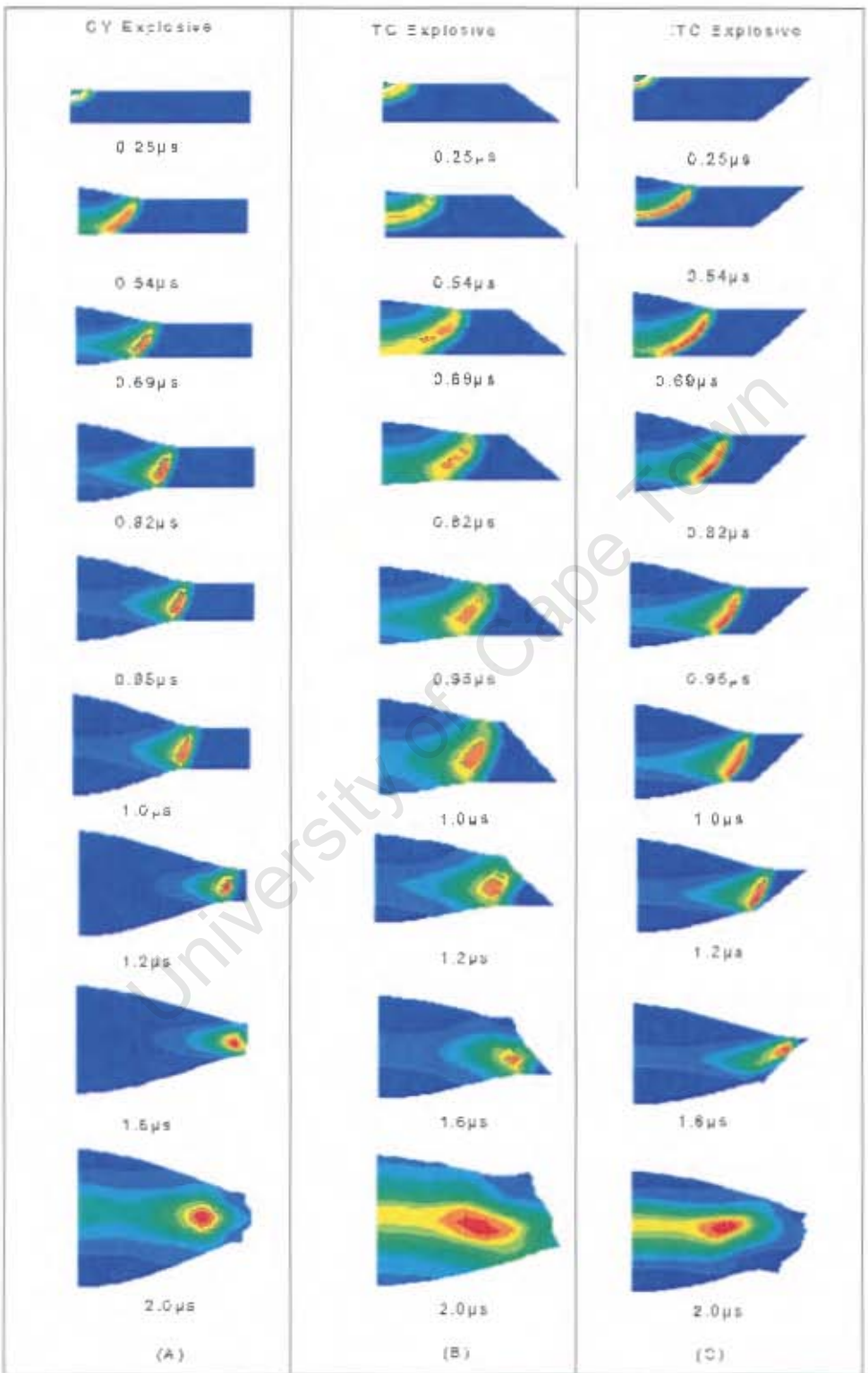

Figure 6.39: Figure showing detonation process and pressure distribution within 33mm CY, TC and ITC explosives of mass 3.0g each from AUTODYN 6.0.

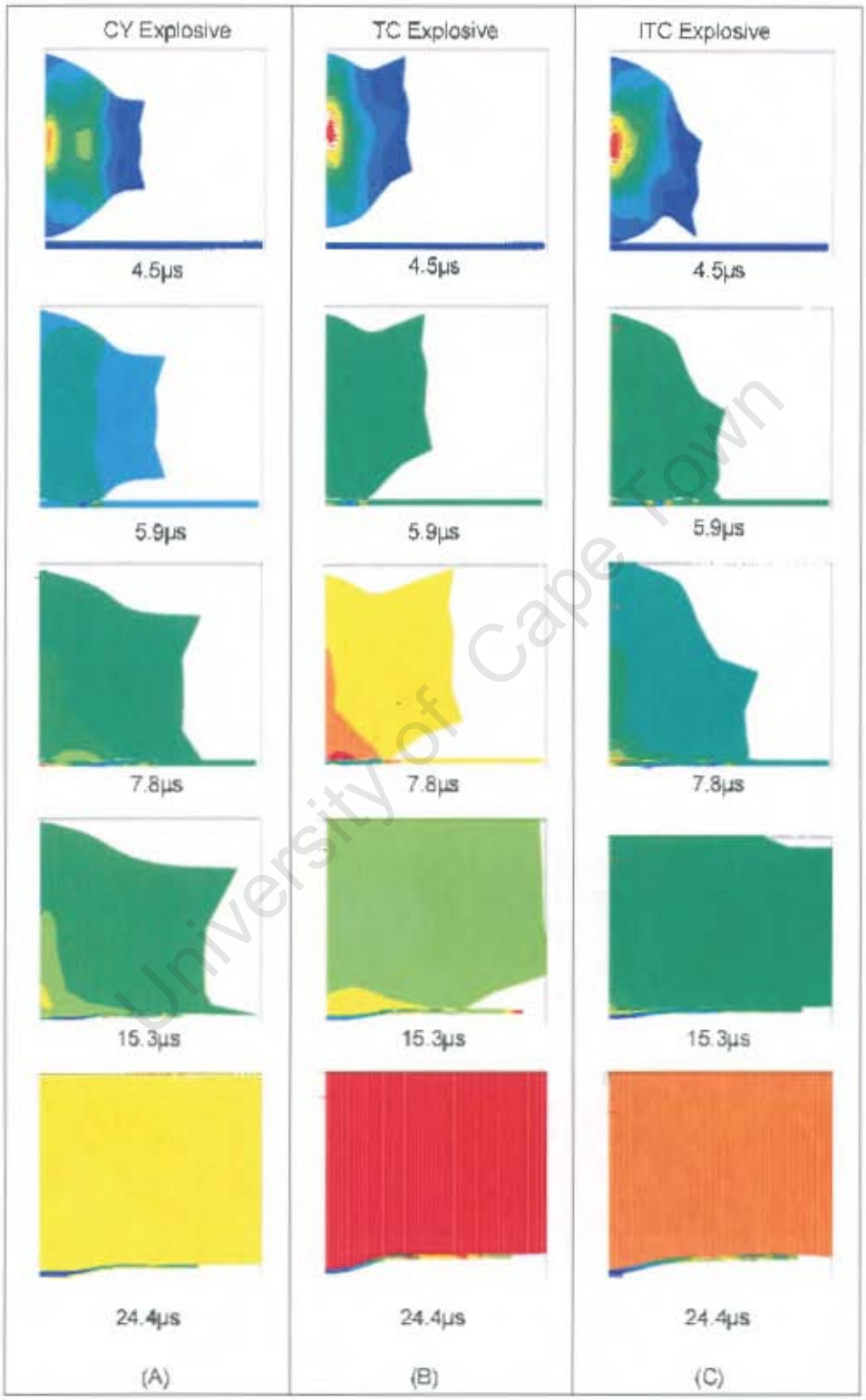

Figure 6.40: Figure showing interaction of expanding 3.0g of 33mm CY, TC and ITC explosives and contour plot of pressure (stress) on plate from AUTODYN 6.0.

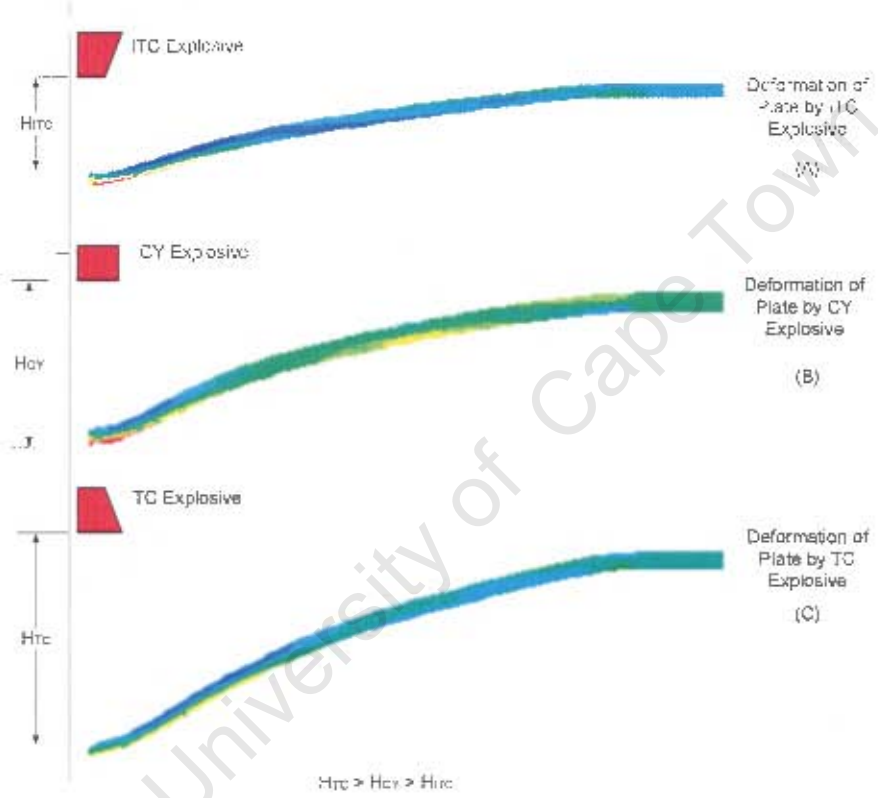

Figure 6.41: Figure showing deformation of plates from AUTODYN 6.0, subjected to ITC, CY and TC explosives of mass 2.6g in (A), (B) and (C) respectively.

6.8 Stress Distribution in Plate

6.8.1 Stress Distribution in Plate From ABAQUS/Explicit 6.4

The stress distribution in the plate by the 18mm, 25mm and 33mm CY, TC and ITC explosives of mass 2.6g, 3.0g and 3.6g each, are shown in figure 6.42, 6.43 and 6.44 respectively. The load distribution are generally similar indicating localised loading with the maximum pressure occurring around the central area of the plate. However, the load distribution on the plate away from the central area by the ITC explosive is higher than those of the TC and CY loaded plates for the 18mm and 25mm load cases. The 33mm load cases show the lowest stress away from the centre of the plate. The maximum stress around the central area of the plate by the CY and TC explosives are higher than that subjected by the ITC explosive. This indicates that the maximum axial momentum of the TC and CY explosives are higher than that of the ITC explosive. It can also be seen that the pressure distribution by the 25mm TC explosive is not shown, indicating the problem of excessive element deformation which terminated the simulation.

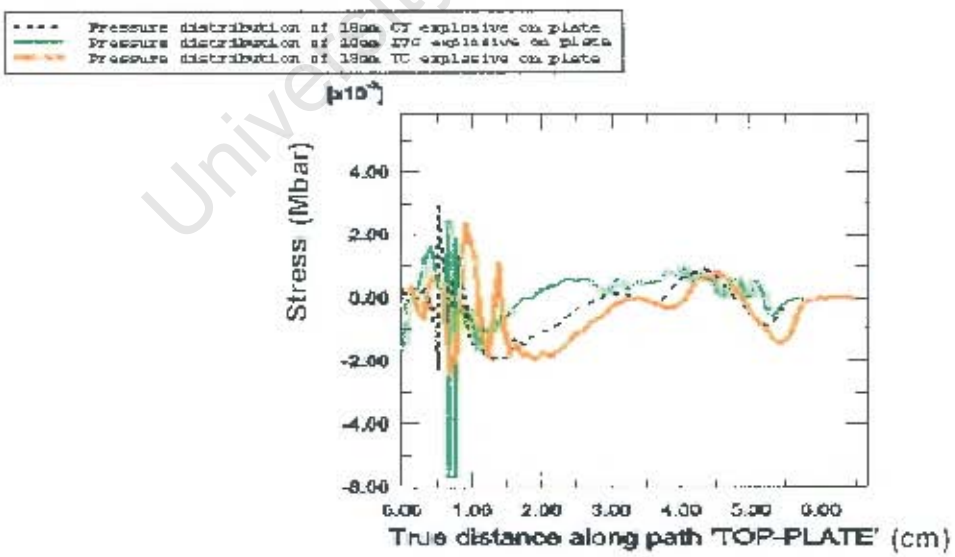

Figure 6.42: Figure showing stress distribution of 18mm TC, CY and ITC explosives along plate radius from ABAQUS/Explicit 6.4 simulation.

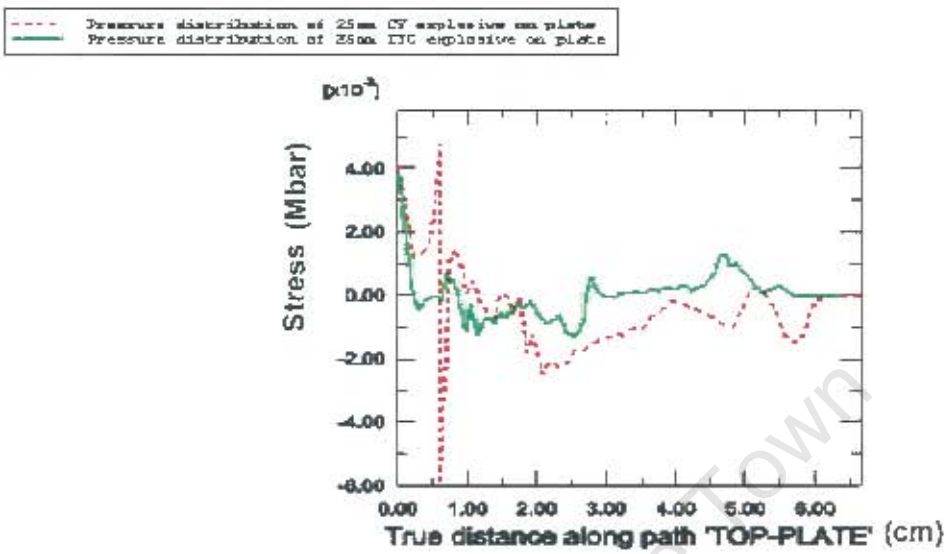

Figure 6.43: Figure showing stress distribution of 25mm, CY and ITC explosives along plate radius from ABAQUS/Explicit 6.4 simulation.

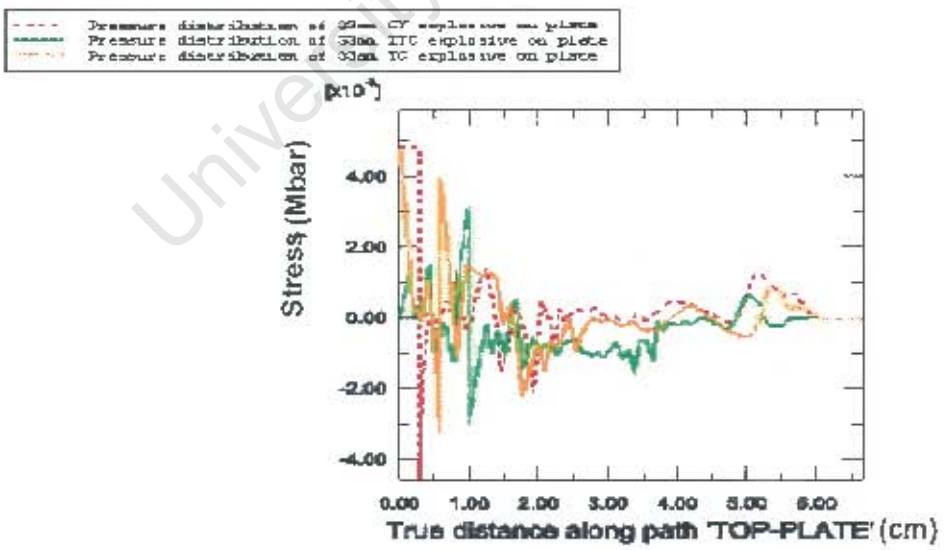

Figure 6.44: Figure showing stress distribution of 33mm TC, CY and ITC explosives along plate radius from ABAQUS/Explicit 6.4 simulation.

6.8.2 Stress Distribution in Plate From AUTODYN 6.0

The stress distribution in the plate subjected to CY, TC and ITC explosives of mass 2.6g are shown in figure 6.45. As shown, the maximum stress at the point of contact of the explosive and plate centre, is higher for the ITC explosive compared to the CY and TC explosives. This is in contrast to the theory in which the pressure at the point of contact by the TC explosive with the highest effective mass is expected. The reason for this is not very clear and needs further investigations both numerically and experimentally. It can be seen that the loads on the structure are highly localised on the plate for all three explosives. The area of load distribution also increases as the diameter of the charge increases. The load profile of the CY and TC explosives are similar due to the similarity in the shock-wave profiles discussed in chapter 5.

6.8.3 Comparison of Theoretical and Predicted Shock-Wave Profiles

Comparison of the pressure profiles (shock-waves) from the simulations and the theory as explained in chapter 5 are shown in figure 6.46. The figure shows similarity between the theory and simulation of the explosive with regard to the shape of the load profiles during interaction with the plate. Diagrams (A) and (B) of figure 6.46 show that the load distribution of the TC and CY explosives are more localised compared to diagram (C) for the ITC explosive in which the load interaction area on the plate is much wider.

6.9 Summary

Investigations of the numerical simulations have been well carried out. It is found that the shape of the shock-wave profile from theory compares well with the numerical simulation wave profiles obtained in both codes. It is found in both numerical codes, that an element size of 0.8mm×0.8mm for the explosive predicted the central deformation and total plate deformation reasonable well for ABAQUS/Explicit 6.4 code and an explosive element size of 0.8mm×0.4mm for the AUTODYN 6.0 code while the plate element size is kept uniform at 0.8mm×0.4mm in both codes. Investigations of the energies of the plate in relation to the explosive shape are also investigated. It is found that the internal

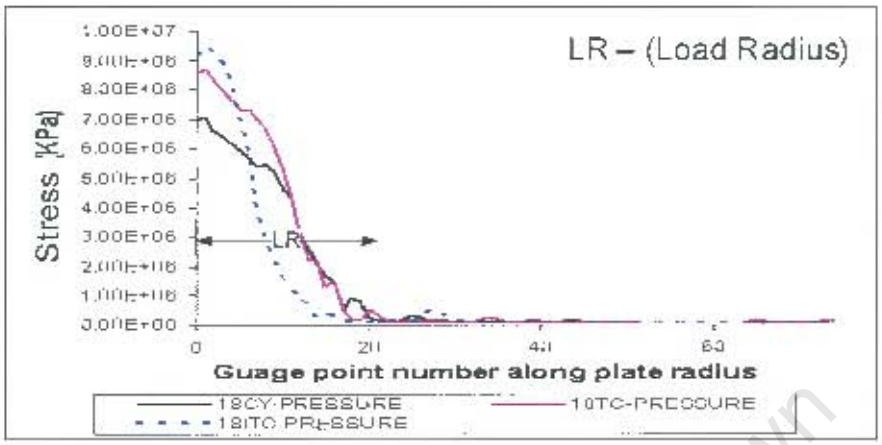

(A) Stress Distribution of 18mm Charge on Plate

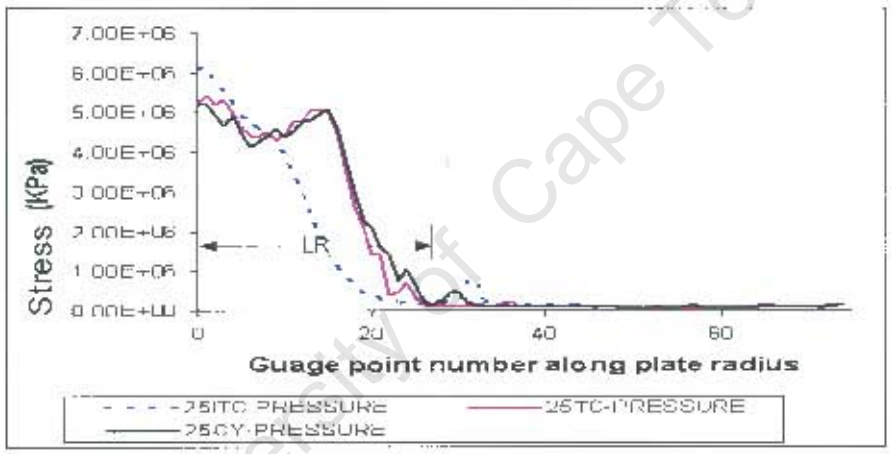

(B) Stress Distribution of 25mm Charge on Plate

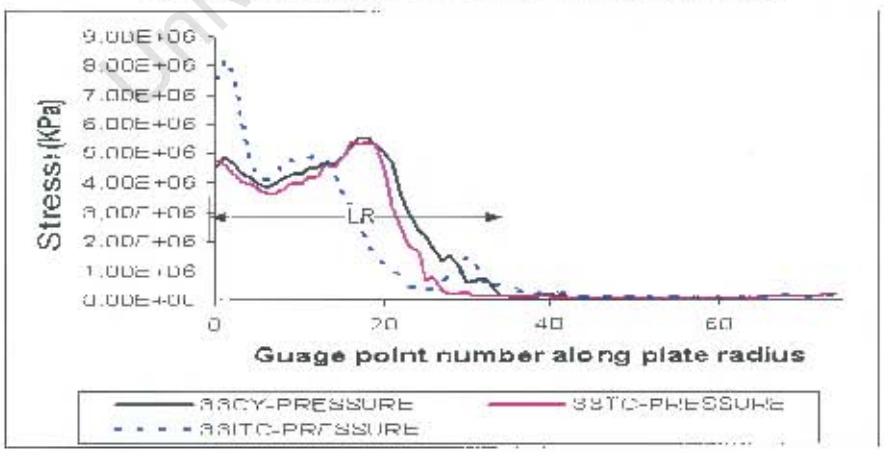

(C) Stress Distribution of 33mm Charge on Plate

Figure 6.45: Graphs showing stress distribution of 18mm, 25mm and 33mm TC, CY and ITC explosives along plate radius from AUTODYN 6.0 simulation.

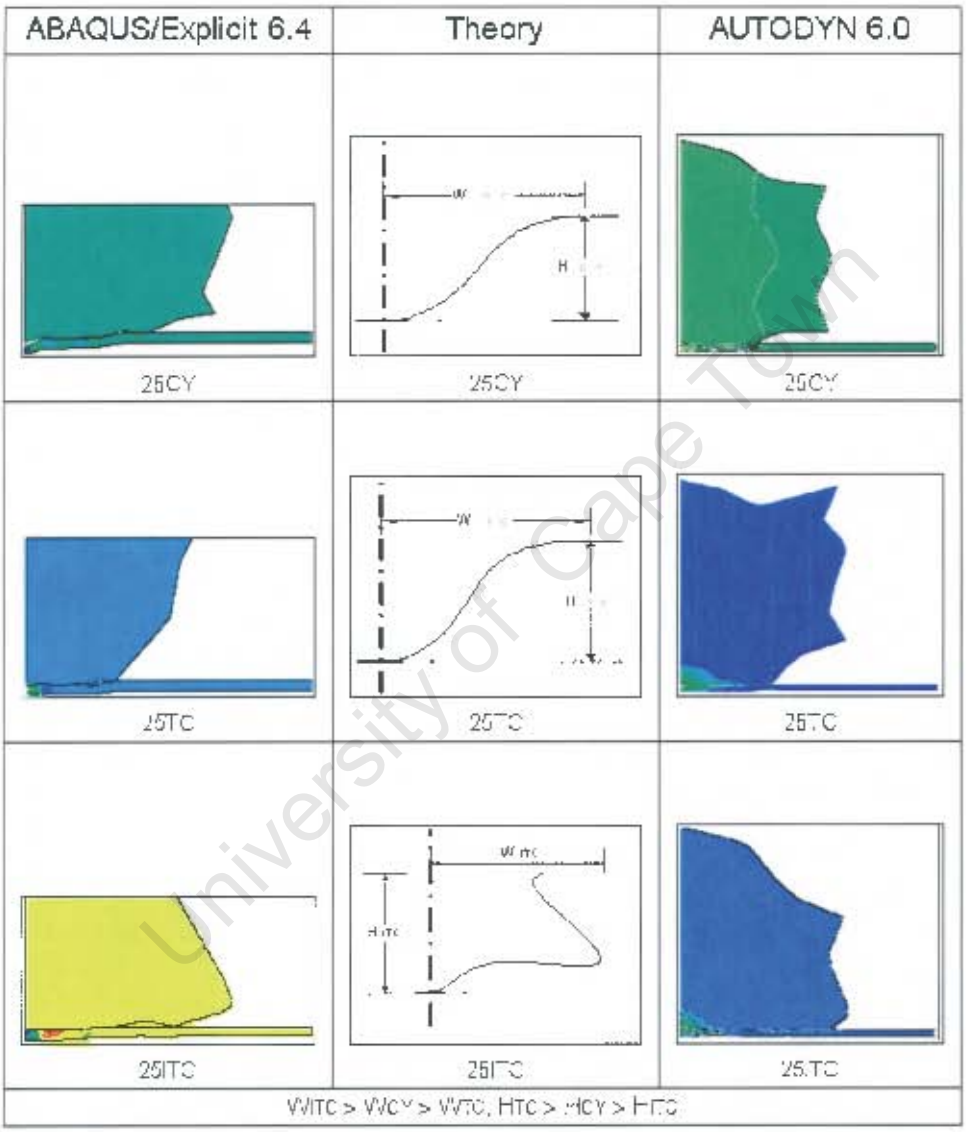

Figure 6.46: Figure showing comparison of load profiles from ABAQUS, AUTODYN and theory for 25mm CY, TC and ITC explosives in (A), (B) and (C).

energies of the plate is related to the central deformation of the plate. From the all the numerical results presented for the internal energy, the TC explosive which generally causes the biggest central deformation, also causes the highest internal energies of the plate.

Chapter 7

Numerical Results

7.1 Introduction

Results of the numerical simulations are presented in this chapter. The reliability of the ABAQUS/Explicit 6.4 and AUTODYN 6.0 programmes to predict the experimental deformation of the plate is the main objective of this chapter.

It should be noted however, that the central deformation varies with time due to the continual oscillation of the plate as shown in figure 7.1 for the lowest centre node of the plate. The values of the central deformation as time varies are shown at points A and B. The point A indicates the maximum deformation and also the point at which the total energy of the plate is reached. Because the plate continues to oscillate with the highest point at B, the values at A and B of the central deformation are averaged so as to approximate the central deformation of the plate. Some of the plate profile results are not presented in this chapter in order to avoid duplication. The rest of the results are presented in chapter 8 in which the plate profiles are compared to those of the experiments.

7.2 Central Deformation Results from ABAQUS/Explicit 6.4

7.2.1 18mm Load Cases

Predictions of the central deformation of the plates subjected to 18mm load cases are presented as shown in table 7.1 with figure 7.2 showing a plot of the results.

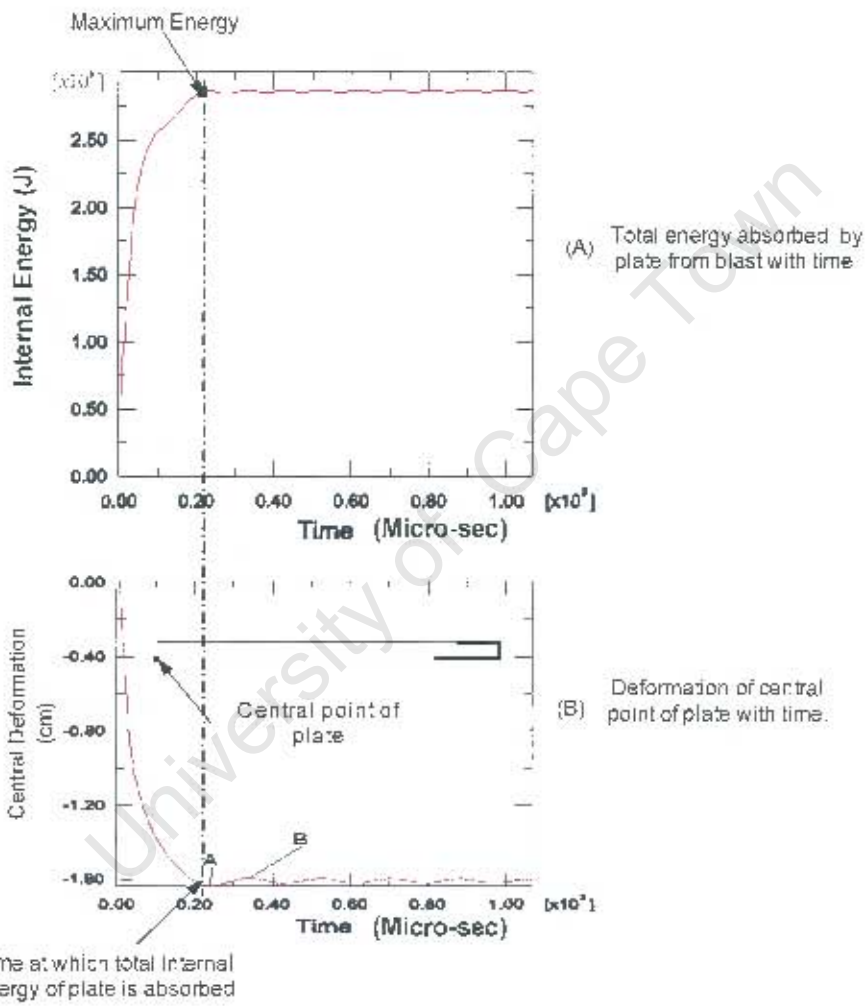

Figure 7.1: Figure showing internal energy absorption and central deformation of plate with time from ABAQUS/Explicit 6.4 for a 2.6g of 18mm CY explosive.

It can be seen that the TC explosive causes the largest central deformation compared to the CY and ITC explosives. This is in agreement with the experimental results in which the central deformation of the TC loaded plates are generally higher than those of the CY and ITC explosive.

Mass(g)	Def. TC(mm)	Def. CY(mm)	Def. ITC(mm)
2.6	18.32	15.40	9.70
3.2	20.30	17.20	10.20
3.7	-	19.07	11.38
4.3	-	-	11.18

Table 7.1: Predicted central deformation of plate subjected to 18mm TC, CY and ITC explosives from ABAQUS/Explicit 6.4.

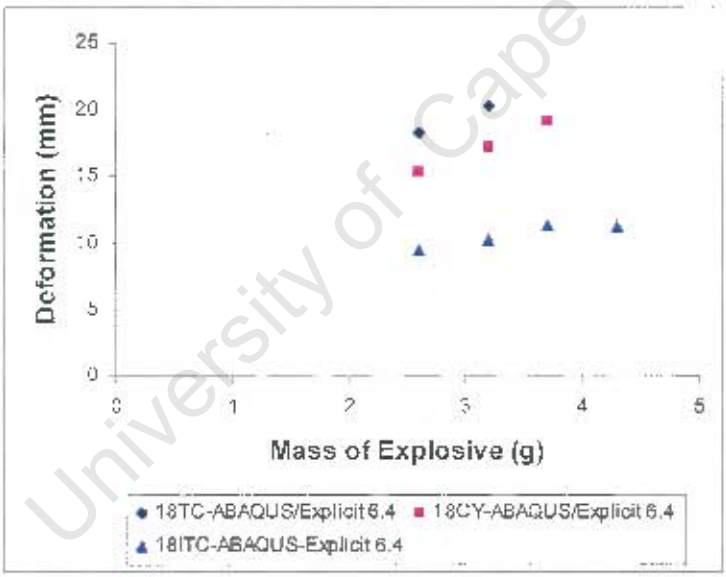

Figure 7.2: Graph showing predicted central deformation of plate from ABAQUS/Explicit 6.4 subjected to varying masses of 18mm TC, CY and ITC explosives.

7.2.2 25mm Load Cases

Prediction of the central deformation of the plate subjected to 25mm load cases are presented as shown in table 7.2 with figure 7.3 showing a plot of the results. It can be seen that the TC explosive caused the largest central deformation compared to the CY and ITC explosives as in the case of the 18mm load cases. Simulation of the experimental results in which capping or partial tearing occurred are not carried out and hence are not recorded as indicated in table 7.2.

Mass(g)	Def. TC(mm)	Def. CY(mm)	Def. ITC(mm)
3.0	26.40	18.76	14.75
3.6	26.50	24.80	16.00
4.7	-	-	18.40

Table 7.2: Table showing predicted central deformation of plate from ABAQUS/Explicit 6.4 subjected to 25mm TC, CY and ITC explosives.

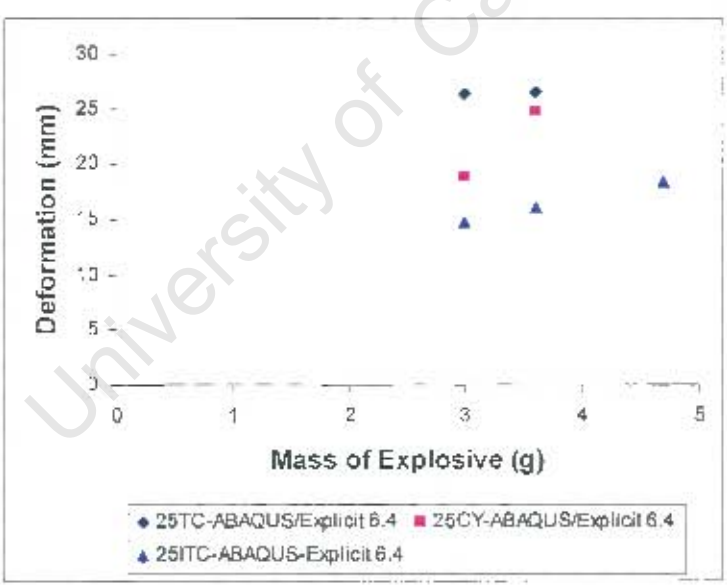

Figure 7.3: Graph showing predicted central deformation of plate from ABAQUS/Explicit 6.4 subjected to varying masses of 25mm TC, CY and ITC explosives.

7.2.3 33mm Load Cases

Prediction of the central deformation of the plate subjected to 33mm load cases are presented as shown in table 7.3 with figure 7.4 showing a plot of the results. Only one point is recorded for the 33TC explosive due to termination of the simulation caused by excessive element deformation. Although the results show only one value of central deformation by the TC explosive at a mass of 3.6g, it can be seen that the TC explosive caused the largest central deformation of the plates compared to the CY and ITC explosives.

Mass(g)	Def. TC(mm)	Def. CY(mm)	Def. ITC(mm)
3.0	-	18.90	15.06
3.6	26.20	20.00	17.90
4.7	-	-	22.10
5.9	-	-	24.40

Table 7.3: Predicted central deformation of plate subjected to 33mm TC, CY and ITC explosives.

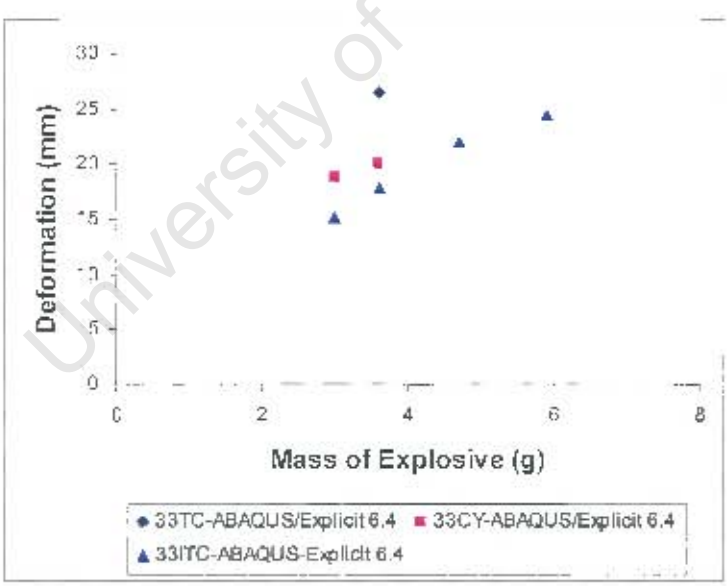

Figure 7.4: Graph showing predicted central deformation of plate from ABAQUS/Explicit 6.4 subjected to varying masses of 33mm TC, CY and ITC explosives.

Numerically, the results of the central deformation of the plates subjected to varying masses and shapes of explosives have been investigated using the

ABAQUS/Explicit 6.4 code. The results show that the shape of an explosive does have an effect on the total deformation of a structure.

7.3 Central Deformation Results from AUTODYN 6.0

7.3.1 18mm Load Cases

The predicted results from the simulations using AUTODYN 6.0 for 18mm load cases are shown in table 7.4 and figure 7.5. The results show that the central deformation of the plates subjected to TC explosives are generally higher than those of the ITC explosives and are slightly higher than those of the CY explosively loaded plates.

Mass(g)	Def. TC(mm)	Def. CY(mm)	Def. ITC(mm)
2.6	15.70	15.60	9.80
3.2	17.60	17.40	10.60
3.7	-	18.90	11.20
4.3	-	-	11.60

Table 7.4: Table showing predicted central deformation of plate subjected to 18mm TC, CY and ITC explosives from AUTODYN 6.0.

7.3.2 25mm Load Cases

Results of the central deformation of the plates for 25mm charges are presented in table 7.5 and figure 7.6. The results from the AUTODYN simulations show that the central deformation of the plates subjected to TC explosive is generally higher than those of the CY and ITC explosively loaded plates.

Mass(g)	Def. TC(mm)	Def. CY(mm)	Def. ITC(mm)
3.0	20.40	18.70	15.30
3.6	23.30	21.70	17.00
4.7	-	-	20.10

Table 7.5: Table showing predicted central deformation of plate from AUTODYN 6.0 subjected to 25mm TC, CY and ITC explosives.

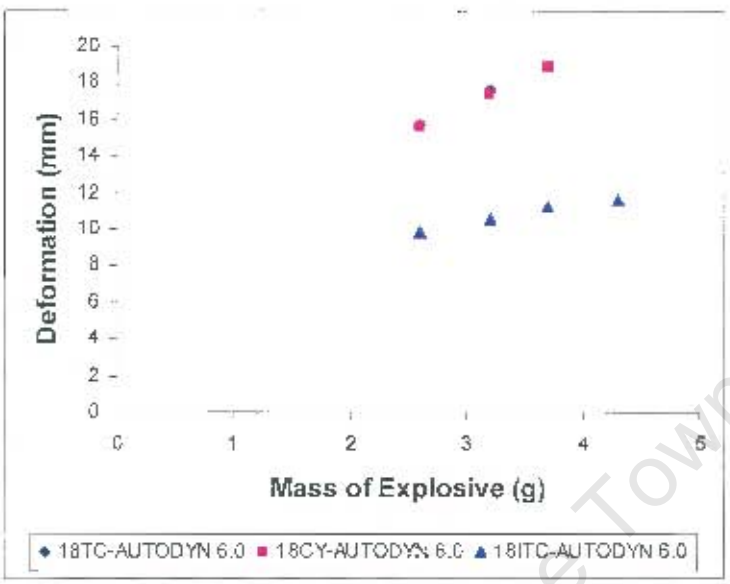

Figure 7.5: Graph showing predicted central deformation of plate from AUTODYN 6.0 subjected to varying masses of 18mm TC, CY and ITC explosives.

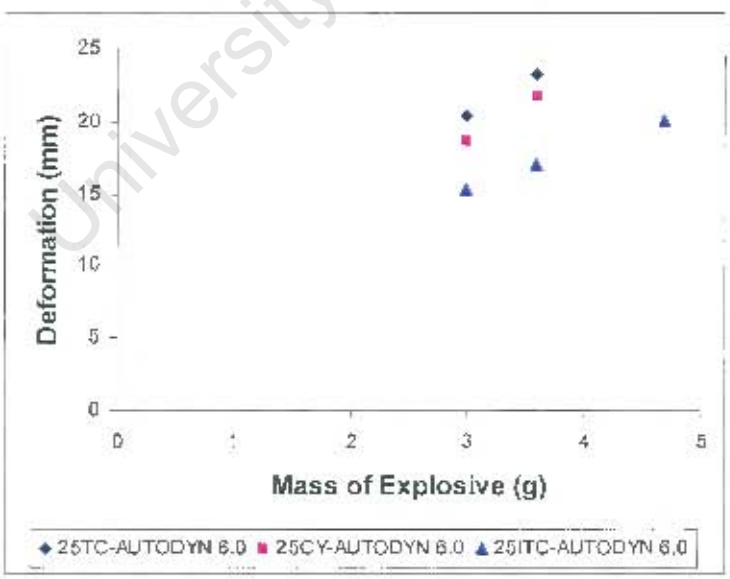

Figure 7.6: Graph showing predicted central deformation of plate from AUTODYN 6.0 subjected to varying masses of 25mm TC, CY and ITC explosives.

7.3.3 33mm Load Cases

Results of the central deformation of the plates subjected to 33mm charges from the AUTODYN simulations are shown in table 7.6 and figure 7.7. The results show similar trend compared to the 18mm and 25mm load cases in that the TC explosive gives a higher central deformation compared to the CY and ITC explosives.

Mass(g)	Def. TC(mm)	Def. CY(mm)	Def. ITC(mm)
3.0	19.90	17.70	15.40
3.6	22.70	20.40	17.60
4.7	-	-	22.10
5.9	-	-	25.90

Table 7.6: Table showing predicted central deformation of plate from AUTODYN 6.0 subjected to 33mm TC, CY and ITC explosives.

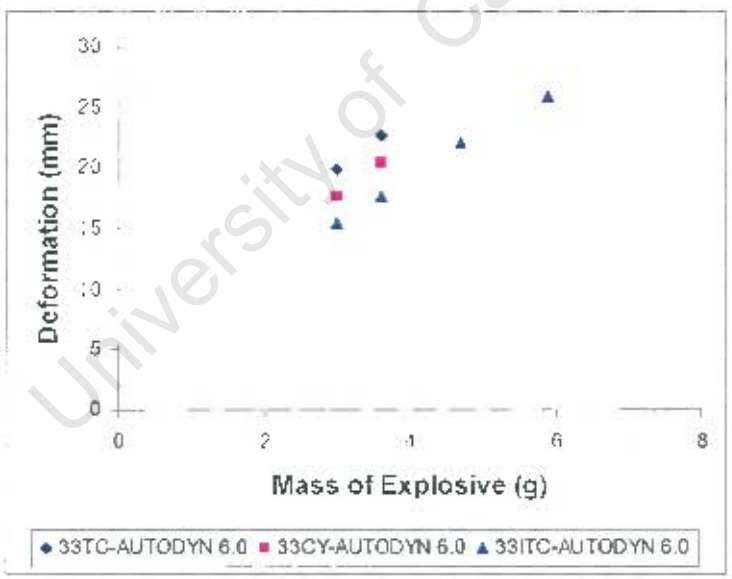

Figure 7.7: Graph showing predicted central deformation of plate from AUTODYN 6.0 subjected to varying masses of 33mm TC, CY and ITC explosives.

The numerical predictions of the experiments from the AUTODYN 6.0 code show that the TC explosive generally gives the biggest central deformation of the plate with the ITC explosive given the lowest central deformation.

7.4 Plate Profile Results Subjected to CY, TC and ITC explosives

7.4.1 ABAQUS/Explicit 6.4 Results

In this section, comparison of the plate profiles subjected to CY, TC and ITC explosives of the same mass are presented as shown in figures 7.8, 7.9 and 7.10. The results are presented in this section in order to numerically highlight the difference in deformation of the plate subjected to different shapes of explosives. Not all the results of the plate profiles are presented in this chapter in order to avoid repetition. The rest of the results are presented in chapter 8. The numerical results show that the overall deformation of the plates subjected to TC explosives are higher than those subjected to CY and ITC explosives.

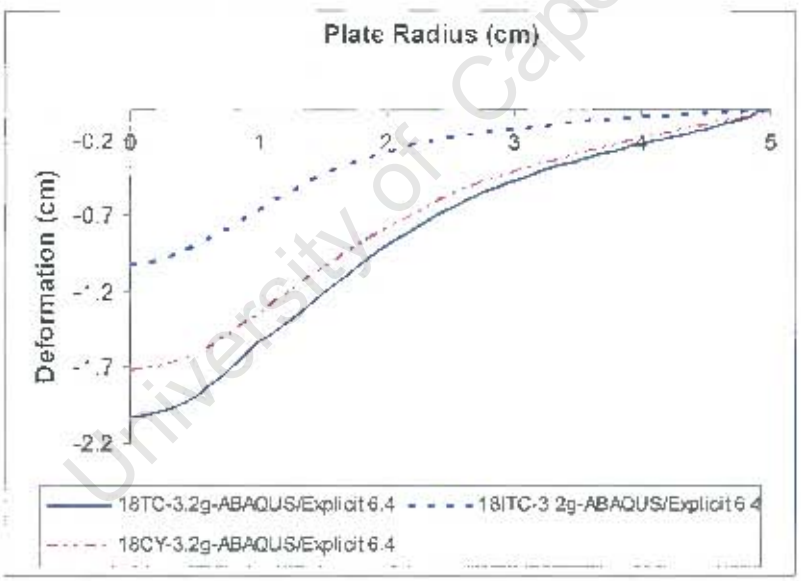

Figure 7.8: Graphs showing comparison of plate profiles subjected to 18mm CY, TC and ITC explosives of mass 3.2g each.

7.4.2 AUTODYN 6.0 Results

Comparison of the plate profile results subjected to the same mass of explosives of various diameters from AUTODYN 6.0 are given in figures 7.11, 7.12 and 7.13. Results of the CY and TC explosive are generally higher than those of

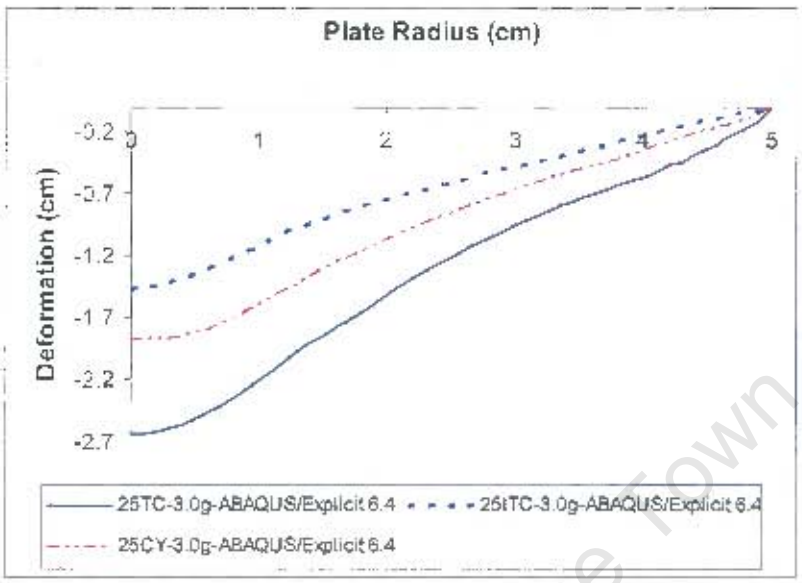

Figure 7.9: Graphs showing comparison of plate profiles subjected to 25mm CY, TC and ITC explosives of mass 3.0g each.

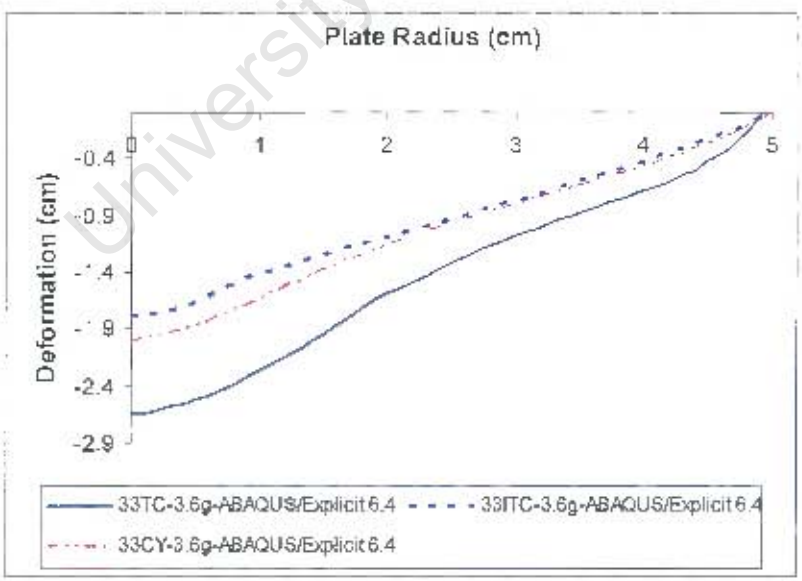

Figure 7.10: Graphs showing comparison of plate profiles subjected to 33mm CY, TC and ITC explosives of mass 3.6g each.

the ITC loaded plate. With the exception of the results in figure 7.11, the TC explosive generally gives a higher deformation compared to the CY and ITC as shown in figures 7.12 and 7.13. This is in agreement with the experiments in which the TC loaded plates have a higher deformation compared to the CY and ITC loaded plates.

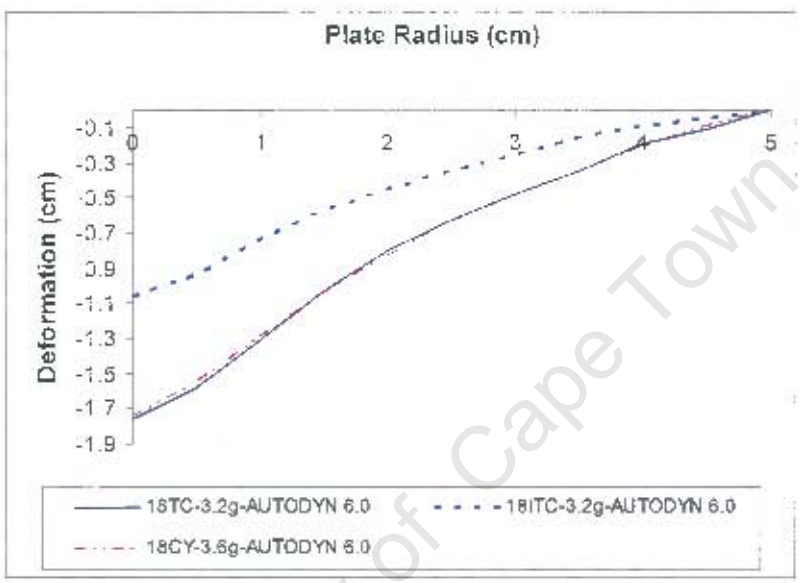

Figure 7.11: Graphs showing comparison of plate profiles subjected to 18mm CY, TC and ITC explosives of mass 3.2g each from AUTODYN 6.0.

7.5 Summary

Results of the predicted plate deformation from the simulations have been presented in tabular and graphical forms, with the central deformation of the TC loaded plates generally showing a higher value compared to the CY and ITC explosively loaded plates. The rest of the results of the plate deformation are presented in chapter 8.

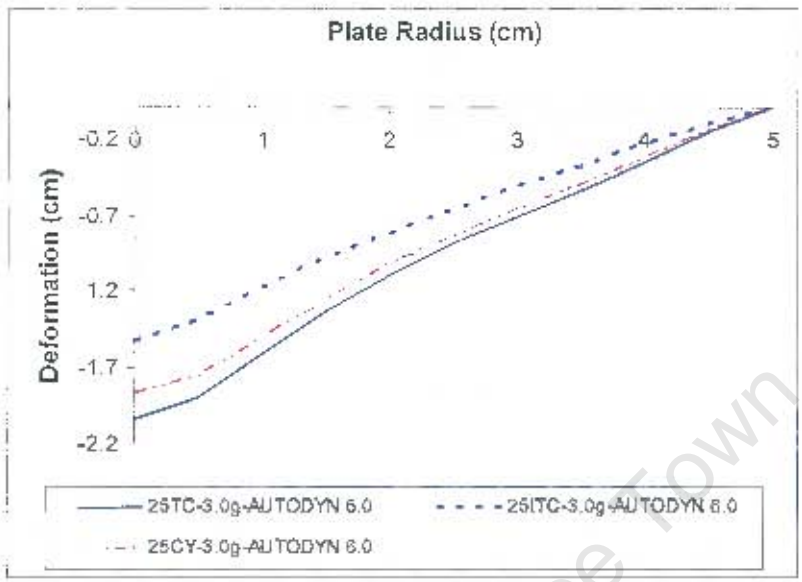

Figure 7.12: Graphs showing comparison of plate profiles subjected to 25mm CY, TC and ITC explosives of mass 3.0g each from AUTODYN 6.0.

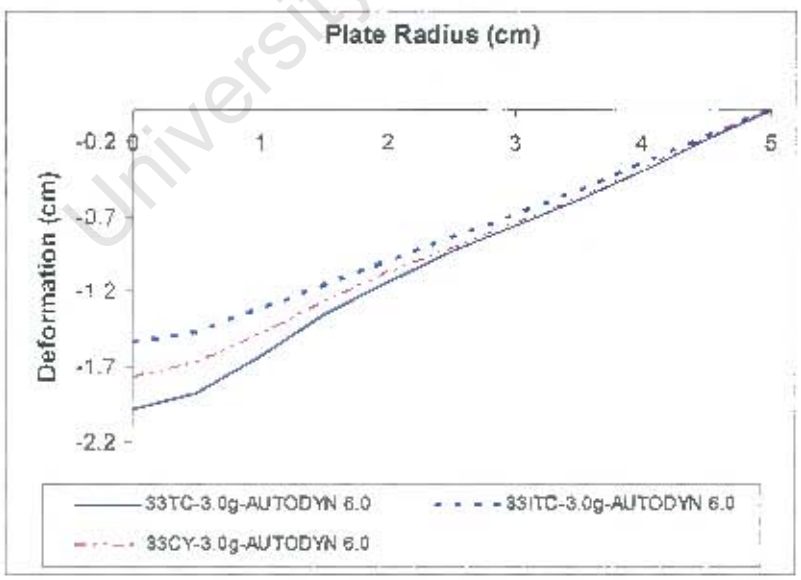

Figure 7.13: Graphs showing comparison of plate profiles subjected to 33mm CY, TC and ITC explosives of mass 3.0g each from AUTODYN 6.0.

Chapter 8

Comparison of Numerical and Experimental Results

8.1 Introduction

Comparison of the central deformation and profile of the plate are experimentally and numerically presented in this chapter. Points within the 90% band show reasonable correlation of the predicted results with those of the experiments. The plates from the experiments are cut into two equal halves and the profiles measured by mapping the boundary of the cross-sections on a graph paper. Points at intervals of 2.5mm along the plate radius (x-coordinates) corresponding to points along the profile of the plates (y-coordinates) are recorded and plotted. The plate profiles from the numerical simulations are compared with those from the experiment in order to predict the total deformation of the structure. Results from the ABAQUS and AUTODYN simulations are also presented on the same axes.

8.2 Central deformation Results of Plate from AUTODYN 6.0 and ABAQUS/Explicit 6.4

Results from all the experiments and simulations are given in the form of a table and graphs. Table 8.1 shows the summary of all the results with their corresponding masses. The impulses recorded are those obtained from the experiments. The results are also presented graphically for each charge diameter.

Shape	Explo. Mass (g)	Exp-Def. (mm)	ABQ-Def. (mm)	AUT-Def. (mm)	Impulse (Ns)
18CY	2.6	16.50	15.30	15.80	6.10
	3.2	17.47	17.20	17.40	7.09
	3.7	18.00	19.10	18.90	7.60
	4.3	-	-	-	8.71
25CY	3.0	20.67	18.76	18.70	8.10
	3.6	22.81	24.80	21.7	9.20
	4.7	-	-	-	10.70
33CY	3.0	19.92	18.90	17.70	8.48
	3.6	21.88	20.04	20.40	10.00
	4.7	-	-	-	12.07
	5.9	-	-	-	13.90
18TC	2.6	17.50	18.30	15.70	6.10
	3.2	18.59	20.30	17.60	6.30
	3.7	-	-	-	6.90
	4.3	-	-	-	7.17
25TC	3.0	20.21	26.40	20.40	7.81
	3.6	24.03	26.50	23.30	8.93
	4.7	-	-	-	10.39
33TC	3.0	19.50	0	19.90	8.12
	3.6	23.05	26.50	22.70	9.92
	4.7	-	-	-	11.22
	5.9	-	-	-	12.98
18ITC	2.6	10.79	9.40	9.80	6.90
	3.2	11.88	10.20	10.60	7.20
	3.7	10.40	11.40	11.20	7.85
	4.3	11.66	11.18	11.60	8.86
25ITC	3.0	15.08	14.75	15.30	8.62
	3.6	16.69	16.00	17.00	9.47
	4.7	20.79	18.40	20.10	11.46
33ITC	3.0	17.24	15.20	15.40	8.48
	3.6	18.63	17.90	17.60	10.00
	4.7	22.60	22.10	22.10	11.97
	5.9	26.92	24.50	25.90	14.89

Figure 8.1: Table of values showing experimental and numerical results for 18mm, 25mm and 33mm CY, TC and ITC explosives.

8.2.1 18mm Load Cases

Results of comparing the predicted and experimental central deformations for 18mm CY, TC and ITC explosively loaded plates are shown in figure 8.2. The results in (A) and (B) show that the central deformation of the plate for 18mm load cases is in good agreement with the experiments. Less number of points are plotted for the TC and CY explosives compared to those of the ITC explosive due to capping or partial tearing of the plate around the central area.

The points plotted outside the band means that the model overpredicted or underpredicts the experimental central deformation. The results show good correlation by both ABAQUS/Explicit 6.4 and AUTODYN 6.0 codes, with almost all the points falling within the 90% confidence band.

8.2.2 25mm Load Case

Results for the 25mm load cases, are also generally good with two points predicted outside the 90% confidence band as shown in figure 8.3. All the points from the AUTODYN simulations fall within the band compared to the ABAQUS/Explicit simulation which far over-predicts one of the TC loaded plates and under-predicts one of the ITC explosively loaded plates. Nonetheless, the central deformation is generally well predicted by both codes as shown in figure 8.3.

It is also shown that the central deformation of the plate caused by the TC explosive is higher than those caused be the CY and ITC explosive of the same mass. For partial tearing (Mode II*c) and capping, (Mode II) the central deformation is assumed infinite and therefore ignored. In this regard, no comparison of the prediction is made with the experiment.

8.2.3 33mm Load Case

Results of the central deformation for 33mm load cases are shown in figures 8.4. The results are generally good and similar to those of the 18mm and 25mm load cases in which most of the points fall within the 90% prediction band. The AUTODYN 6.0 code shows better prediction of the central deformation compared to ABAQUS/Explicit 6.4 code.

8.2.1 18mm Load Cases

Results of comparing the predicted and experimental central deformations for 18mm CY, TC and ITC explosively loaded plates are shown in figure 8.2. The results in (A) and (B) show that the central deformation of the plate for 18mm load cases is in good agreement with the experiments. Less number of points are plotted for the TC and CY explosives compared to those of the ITC explosive due to capping or partial tearing of the plate around the central area.

The points plotted outside the band means that the model overpredicted or underpredicts the experimental central deformation. The results show good correlation by both ABAQUS/Explicit 6.4 and AUTODYN 6.0 codes, with almost all the points falling within the 90% confidence band.

8.2.2 25mm Load Case

Results for the 25mm load cases, are also generally good with two points predicted outside the 90% confidence band as shown in figure 8.3. All the points from the AUTODYN simulations fall within the band compared to the ABAQUS/Explicit simulation which far over-predicts one of the TC loaded plates and under-predicts one of the ITC explosively loaded plates. Nonetheless, the central deformation is generally well predicted by both codes as shown in figure 8.3.

It is also shown that the central deformation of the plate caused by the TC explosive is higher than those caused be the CY and ITC explosive of the same mass. For partial tearing (Mode II*c) and capping, (Mode II) the central deformation is assumed infinite and therefore ignored. In this regard, no comparison of the prediction is made with the experiment.

8.2.3 33mm Load Case

Results of the central deformation for 33mm load cases are shown in figures 8.4. The results are generally good and similar to those of the 18mm and 25mm load cases in which most of the points fall within the 90% prediction band. The AUTODYN 6.0 code shows better prediction of the central deformation compared to ABAQUS/Explicit 6.4 code.

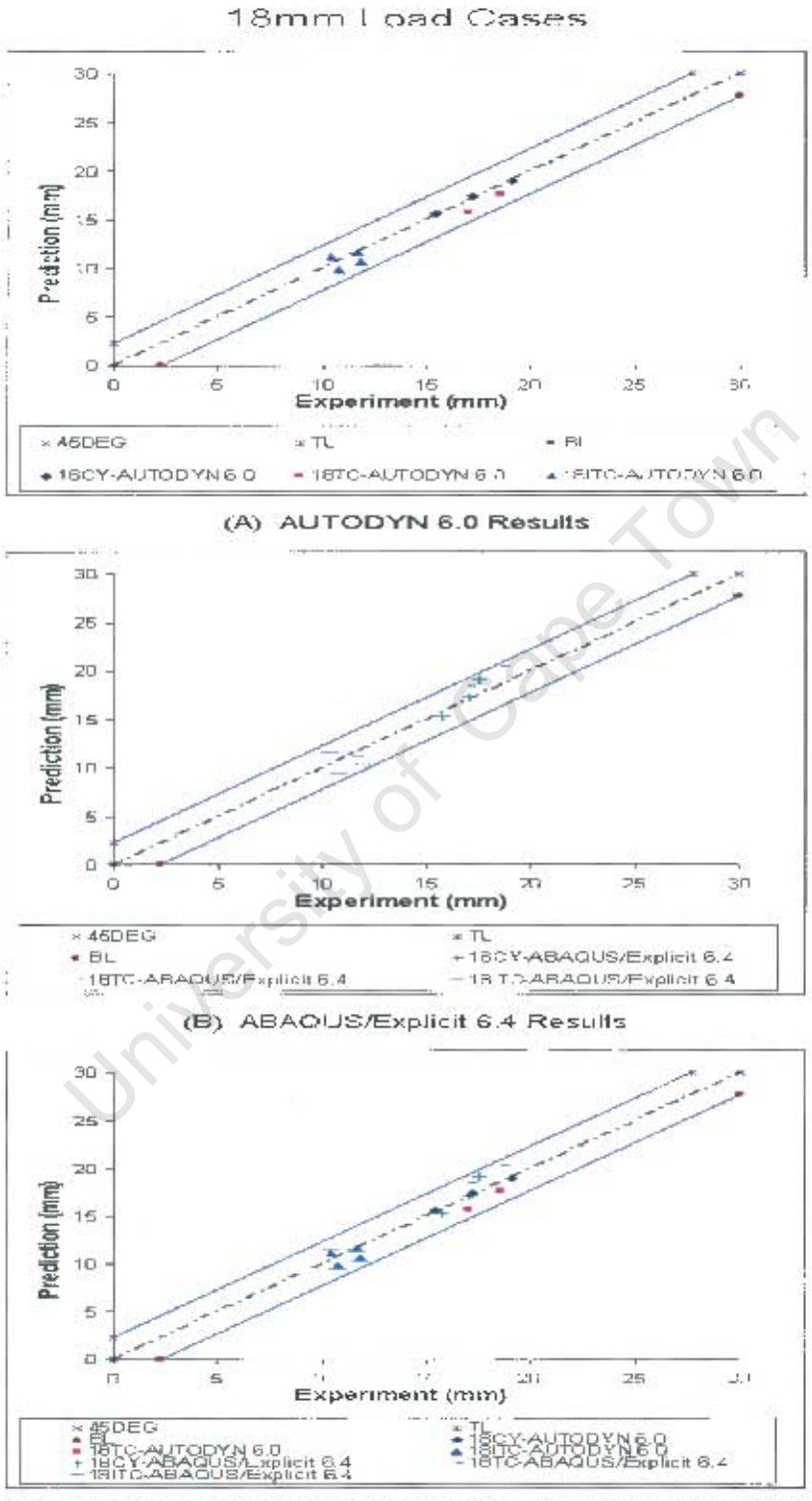

Figure 8.2: Graphs showing comparison of predicted and experimental central deformation results, from AUTODYN 6.0 and ABAQUS/Explicit 6.4, for 18mm load cases.

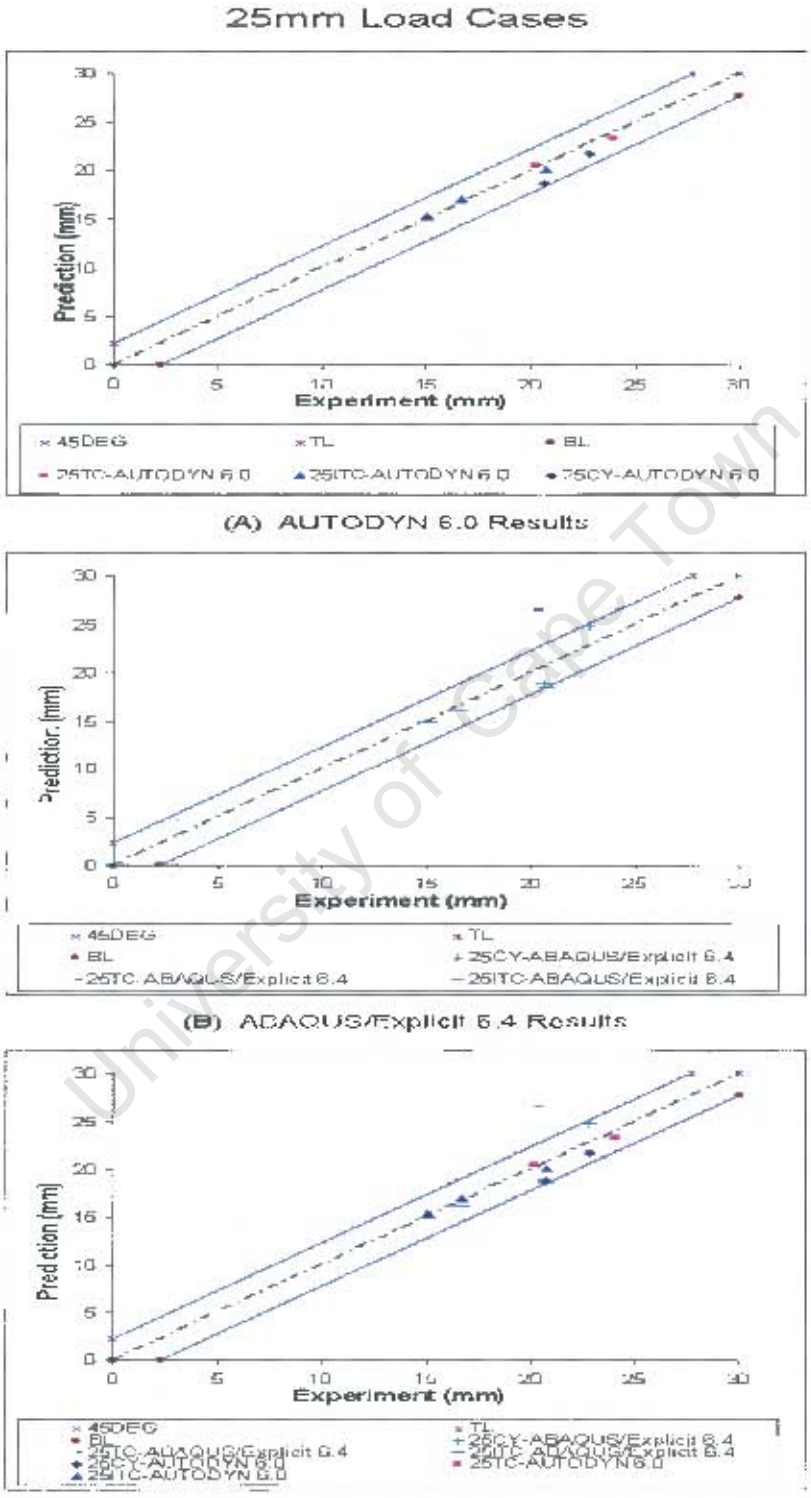

Figure 8.3: Graphs showing comparison of predicted and experimental central deformation results, from AUTODYN 6.0 and ABAQUS/Explicit 6.4, for 25mm load cases.

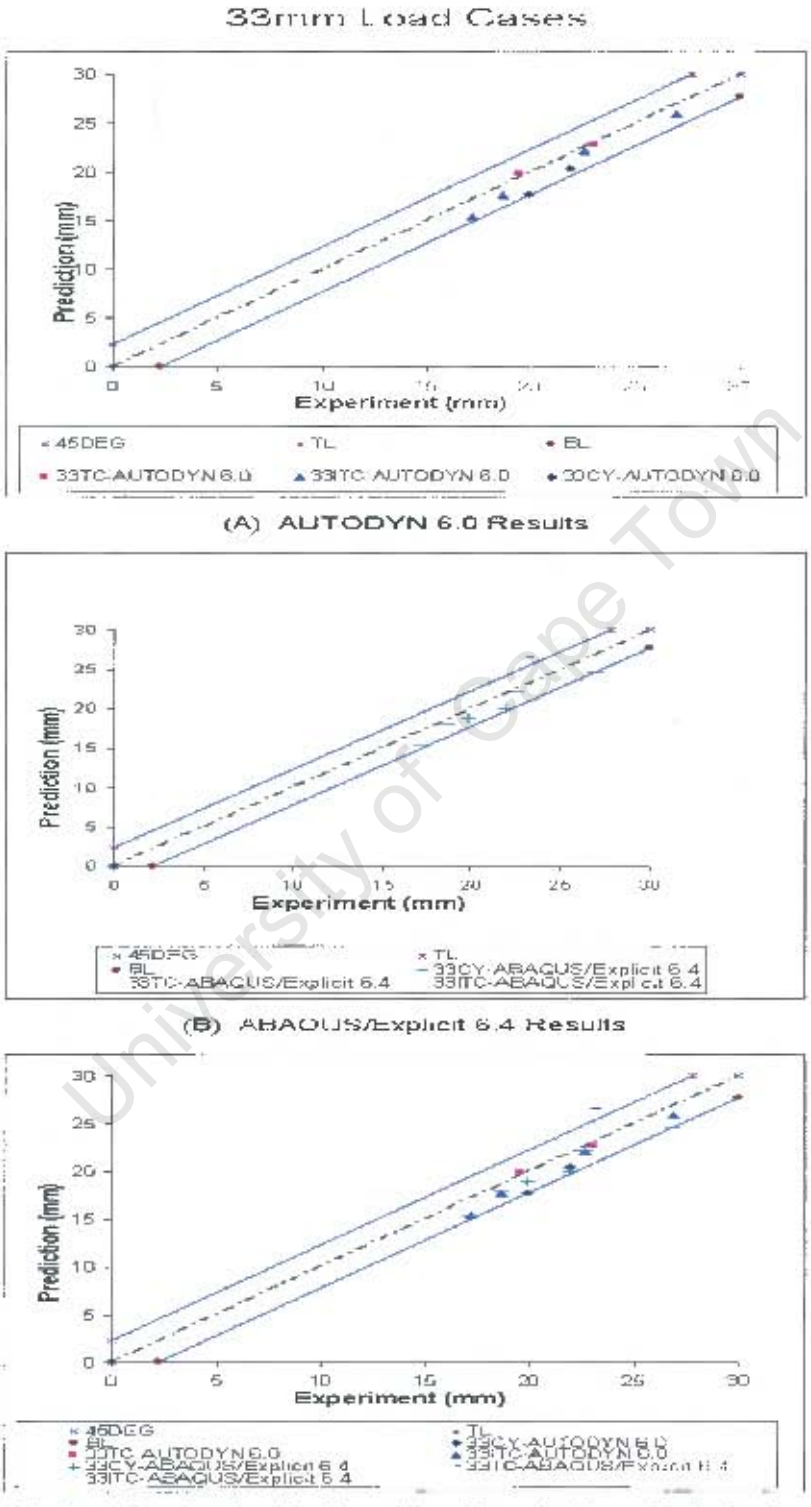

Figure 8.4: Graphs showing comparison of predicted and experimental central deformation results, from AUTODYN 6.0 and ABAQUS/Explicit 6.4, for 25mm load cases.

8.3 Plate Profile Results

Comparison of the predicted and experimental central deformation is a necessary condition for validating the effectiveness of the finite element programme but not a sufficient condition. Prediction of the plate profiles considers the total deformation of the plate and therefore should be considered as a sufficient condition for the prediction of plate deformation. Comparison of the plate profiles in this work is limited to Mode I deformation. Comparison of the results from ABAQUS/Explicit 6.4, AUTODYN 6.0 and experimental plate profiles are presented.

In addition, the profiles of the simulations and experiments are obtained from the underside of the plates as the deformation is smoother compared to the top surface which is normally not smooth due to excessive element deformation and node penetration of the master surface into the slave node. This problem is observed from the ABAQUS/Explicit simulation as can be seen in figure 8.5 where the surface of a plate after interaction with an explosive is distorted. The problem of indentation is not observed in the AUTODYN 6.0 simulations.

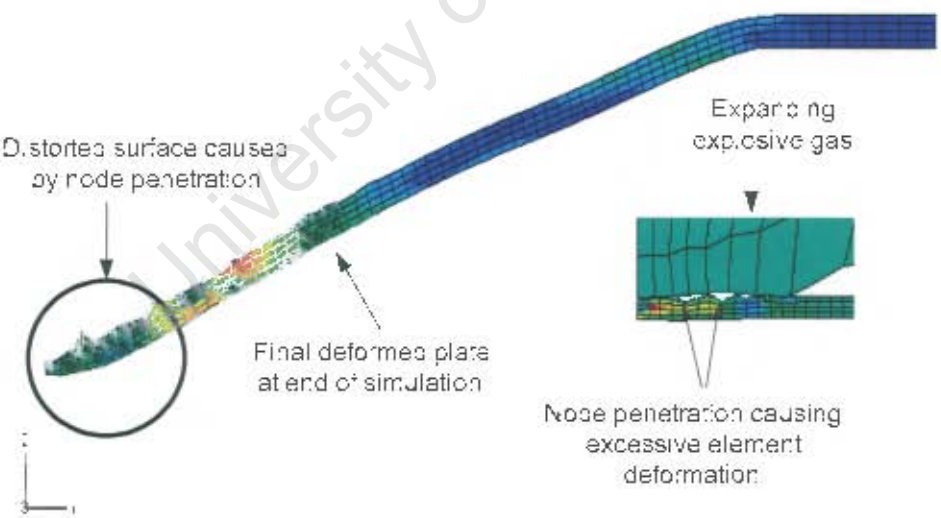

Figure 8.5: Figure showing distortion of plate surface from ABAQUS/Explicit 6.4, due to node penetration from the explosive.

8.3.1 Plate Profile Results for 18mm CY Explosives

Comparison of the experimental and predicted plate profile results from both AUTODYN 6.0 and ABAQUS/Explicit codes subjected to 18mm CY explosives of varying masses are shown in figures 8.6, 8.7 and 8.8. As shown, the results compare well with the experiment as regards the total deformation and shape of the experimental plate profiles.

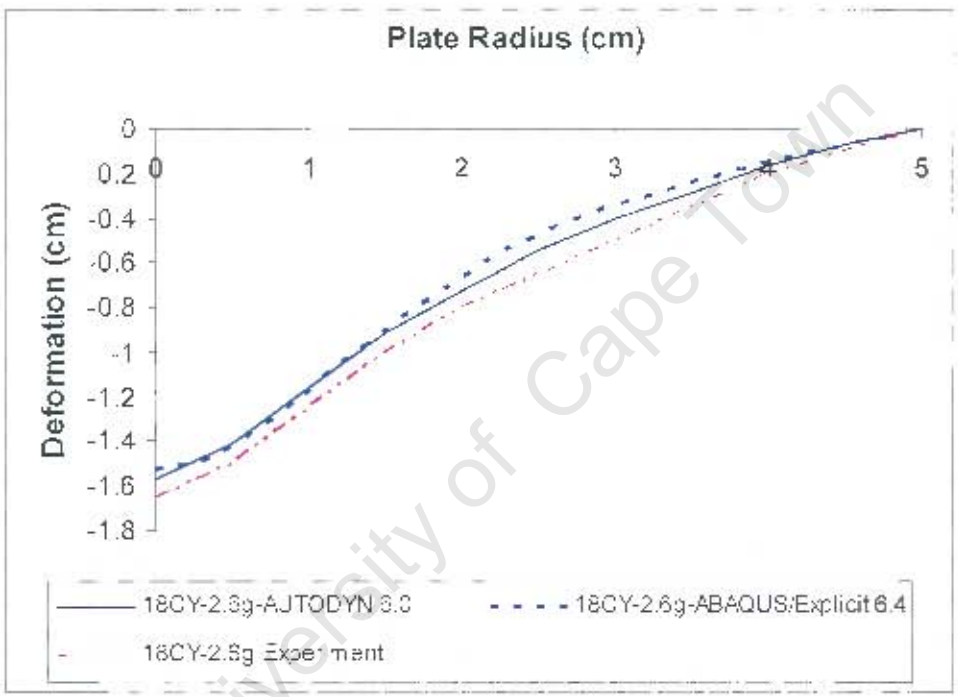

Figure 8.6: Graphs showing comparison of plate profiles from ABAQUS/Explicit 6.4, AUTODYN 6.0 and experiment for 2.6g of 18CY explosive.

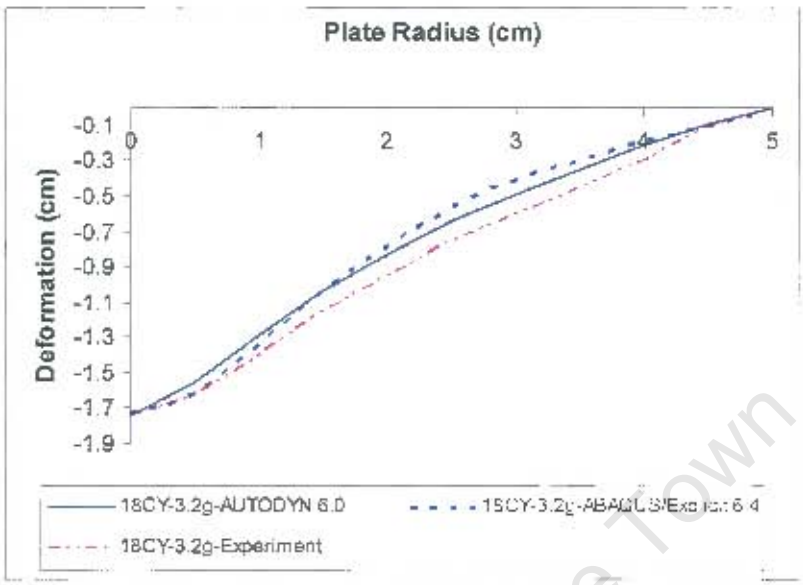

Figure 8.7: Graphs showing comparison of plate profiles from ABAQUS/Explicit 6.4, AUTODYN 6.0 and experiment for 3.2g of 18CY explosive.

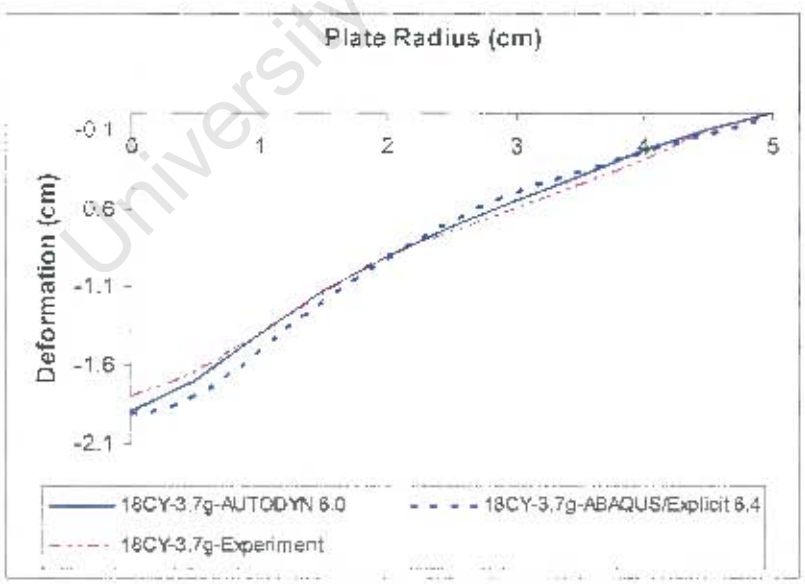

Figure 8.8: Graphs showing comparison of plate profiles from ABAQUS/Explicit 6.4, AUTODYN 6.0 and experiment for 3.7g of 18CY explosive.

8.3.2 Plate Profile Results for 18mm TC Explosives

Comparison of the predicted and experimental plate profiles subjected to 18mm TC explosive loadings are shown in figures 8.9 and 8.10. The shape of the plate is generally better predicted with AUTODYN 6.0 compared to the ABAQUS/Explicit 6.4 code. The central deformation of the plate is slightly over-predicted by the ABAQUS/Explicit 6.4 code and underpredicted by the AUTODYN 6.0 code. The deformation towards the edge of the plate shows that both codes underpredicted the deformation.

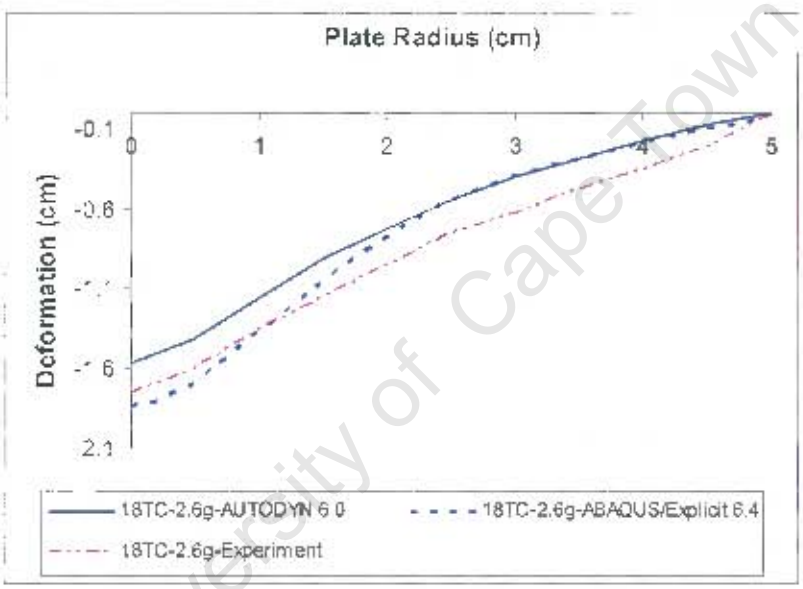

Figure 8.9: Graphs showing comparison of plate profiles from ABAQUS/Explicit 6.4, AUTODYN 6.0 and experiment for 2.6g of 18TC explosive.

8.3.3 Plate Profile Results for 18mm ITC Explosives

Results of the predicted plate profiles subjected to ITC explosives by both codes are not generally good compared to the experiment as shown in figures 8.11, 8.12 and 8.13. The deformation is largely under predicted by both codes around the central area of the plate radius. The shape of the plate is however, better predicted by the AUTODYN 6.0 code compared ABAQUS/Explicit 6.4 code. As shown in the results, comparison of the predicted and experimental central

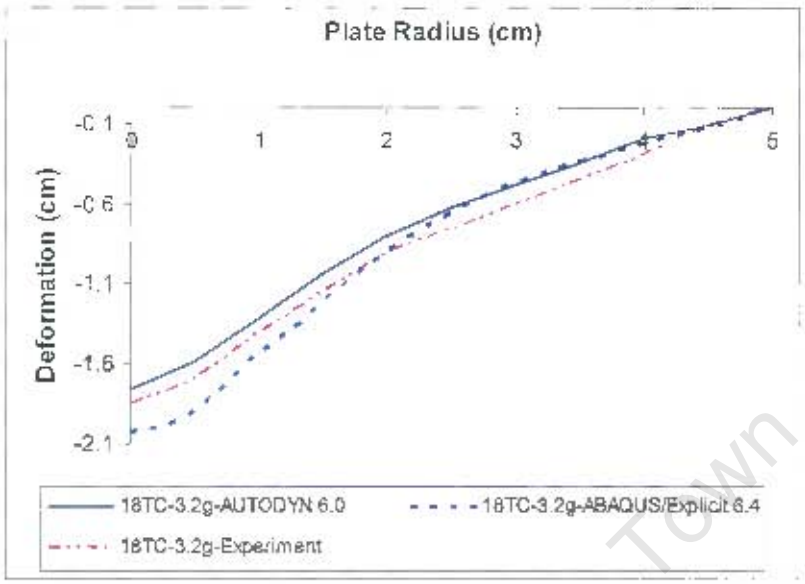

Figure 8.10: Graphs showing comparison of plate profiles from ABAQUS/Explicit 6.4, AUTODYN 6.0 and experiment for 3.2g of 18TC explosive.

deformation is not a sufficient parameter to validate the plate prediction. The total deformation also has to be considered in order to make meaningful predictions. Although both codes predicts the central deformation of the plate, however, the total deformation of the plate is better predicted with the AUTODYN code compared to the ABAQUS/Explicit 6.4 code. In addition, the shape of the plate is better predicted for localised loading conditions.

8.3.4 Plate Profile Results for 25mm CY Explosives

Comparison of predicted and experimental plate profiles are shown in figures 8.14 and 8.15. The results are generally good for both cases showing that accurate prediction can be obtained for CY explosive loaded plates. Both codes predicts the total deformation and shape of the plate. The results are similar to those for the 18mm CY load cases as regards predicting the total deformation of the plates and shape of the plate.

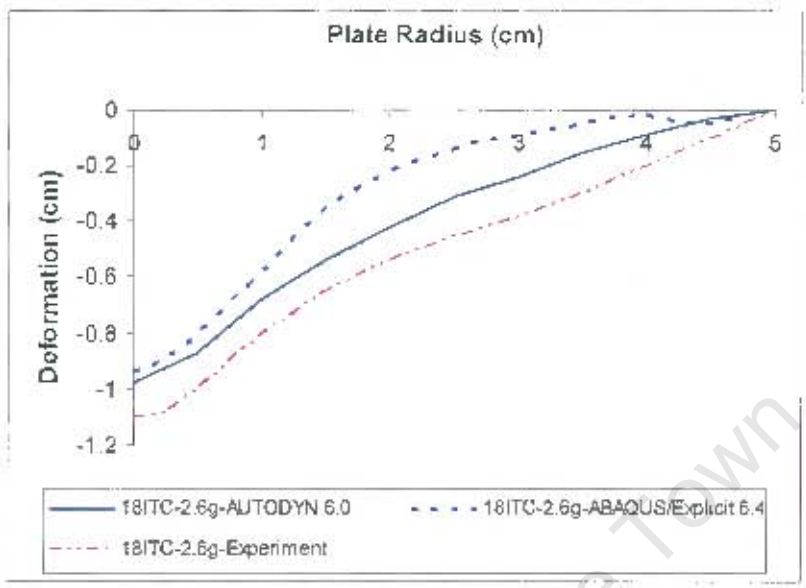

Figure 8.11: Graphs showing comparison of plate profiles from ABAQUS/Explicit 6.4, AUTODYN 6.0 and experiment for 2.6g of 18ITC explosive.

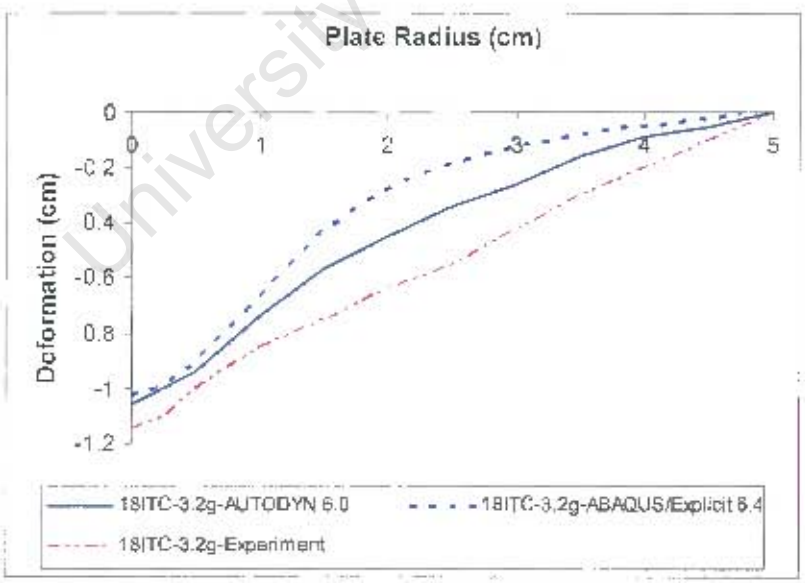

Figure 8.12: Graphs showing comparison of plate profiles from ABAQUS/Explicit 6.4, AUTODYN 6.0 and experiment for 3.2g of 18ITC explosive.

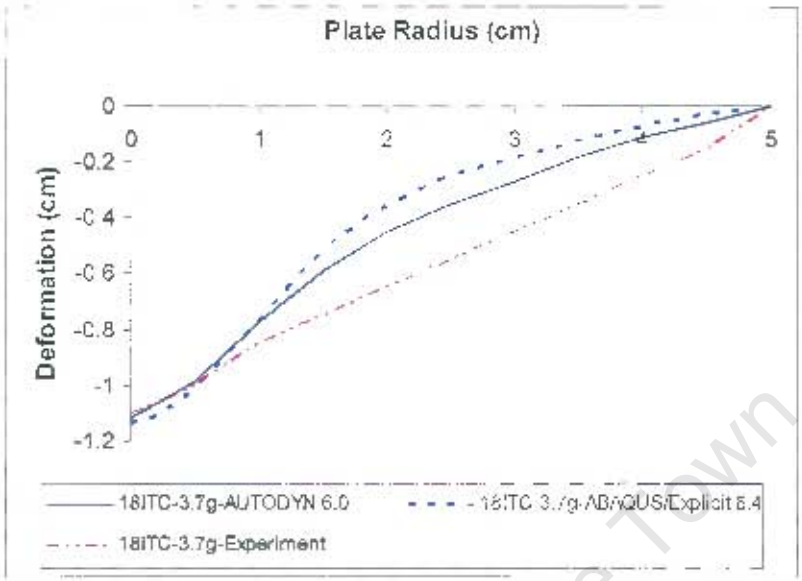

Figure 8.13: Graphs showing comparison of plate profiles from ABAQUS/Explicit 6.4, AUTODYN 6.0 and experiment for 3.7g of 18ITC explosive.

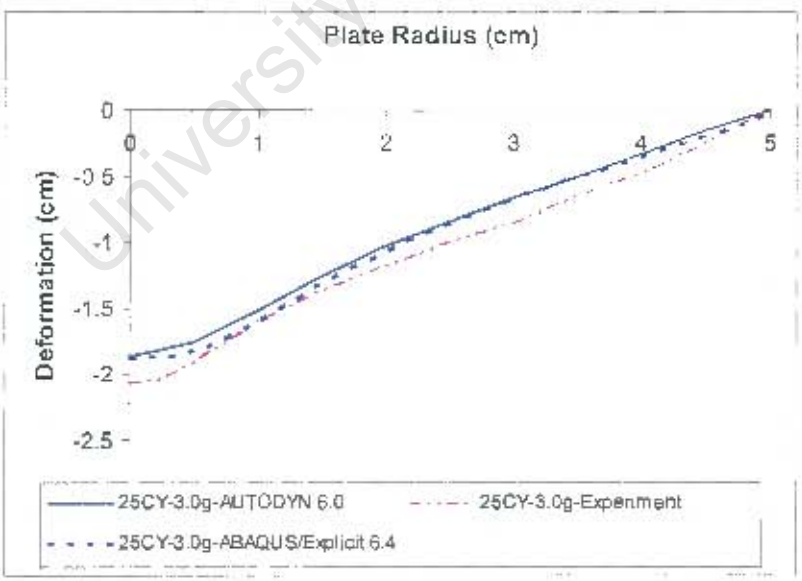

Figure 8.14: Graphs showing comparison of plate profiles from ABAQUS/Explicit 6.4, AUTODYN 6.0 and experiment for 3.0g of 25CY explosive.

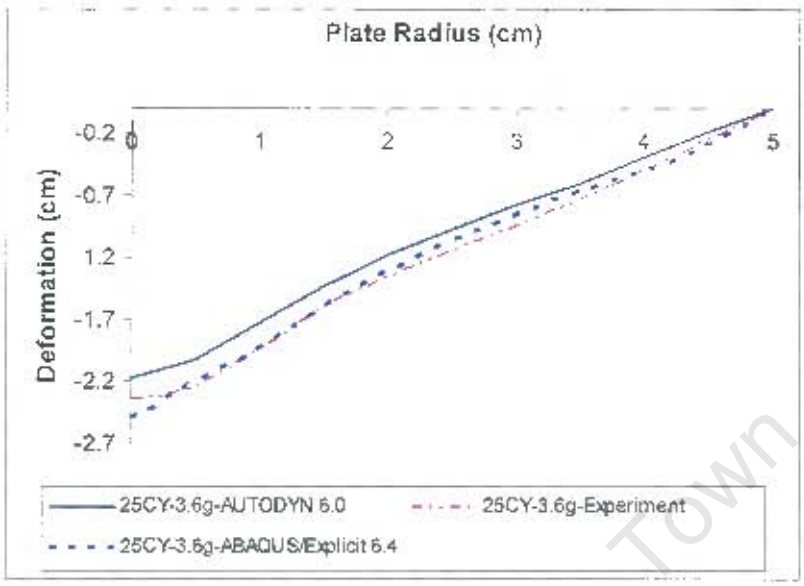

Figure 8.15: Graphs showing comparison of plate profiles from ABAQUS/Explicit 6.4, AUTODYN 6.0 and experiment for 3.6g of 25CY explosive.

8.3.5 Plate Profile Results for 25mm TC Explosives

Results of the plate profiles subjected to 25mm TC explosives are shown in figures 8.16 and 8.17. The results show an over-prediction of the total deformation from the ABAQUS/Explicit 6.4 code compared to the AUTODYN 6.0 code which accurately predicts the total deformation and the shape of the plate. The results are also similar to those given by the 18mm TC explosives in which deformation of the plate is over-predicted by the ABAQUS code.

8.3.6 Plate Profile Results for 25mm ITC Explosives

Figures 8.18 and 8.19 show comparison of the predicted and experimental plate profiles subjected to 3.0g and 3.6g of explosives respectively. The results show that the predicted deformations are similar for both AUTODYN 6.0 and ABAQUS/Explicit 6.4 codes. The central deformation is reasonably predicted unlike the profile of the plate which both codes do not well predict.

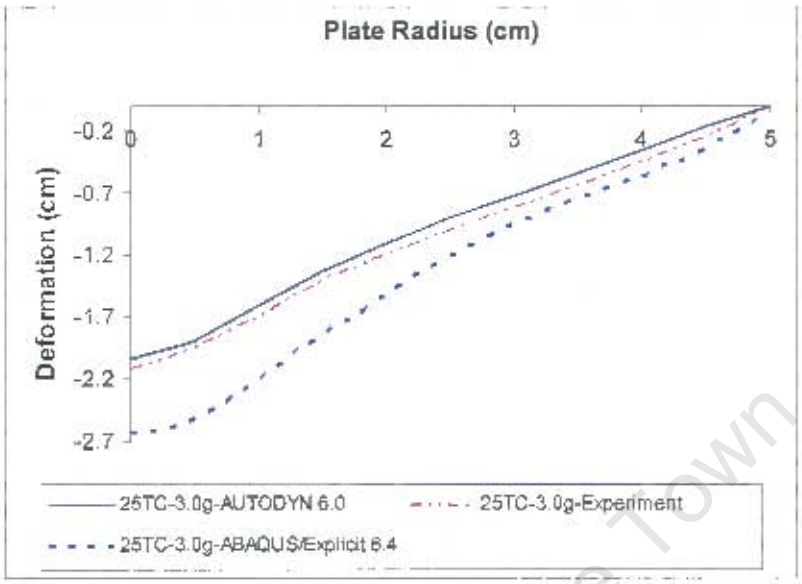

Figure 8.16: Graphs showing comparison of plate profiles from ABAQUS/Explicit 6.4, AUTODYN 6.0 and experiment for 3.0g of 25TC explosive.

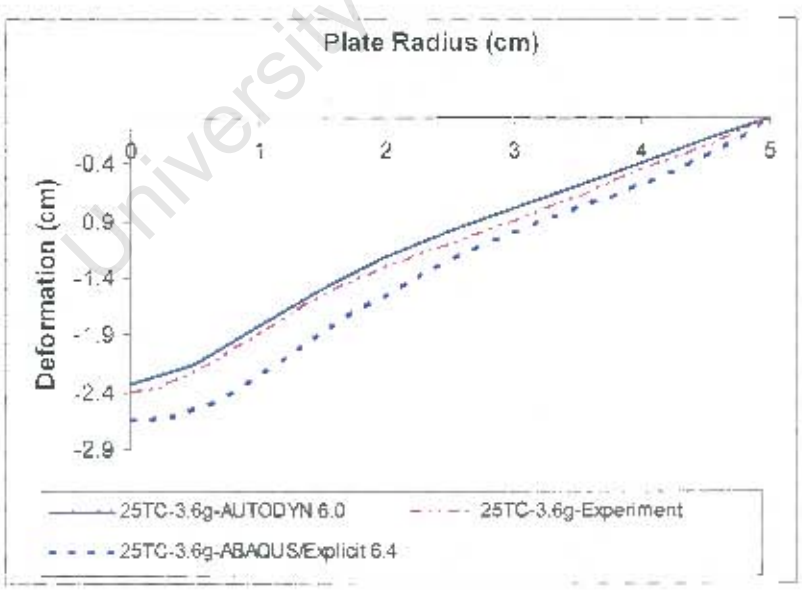

Figure 8.17: Graphs showing comparison of plate profiles from ABAQUS/Explicit 6.4, AUTODYN 6.0 and experiment for 3.6g of 25TC explosive.

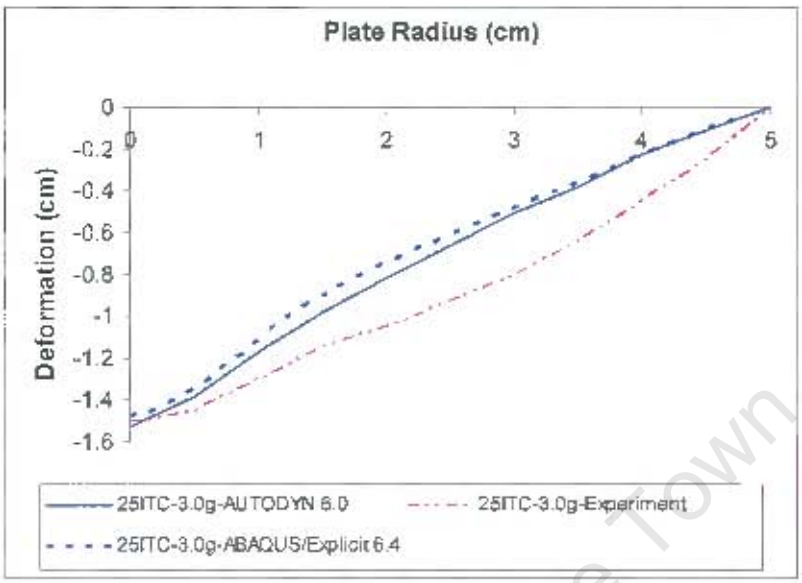

Figure 8.18: Graphs showing comparison of plate profiles from ABAQUS/Explicit 6.4, AUTODYN 6.0 and experiment for 3.0g of 25ITC explosive.

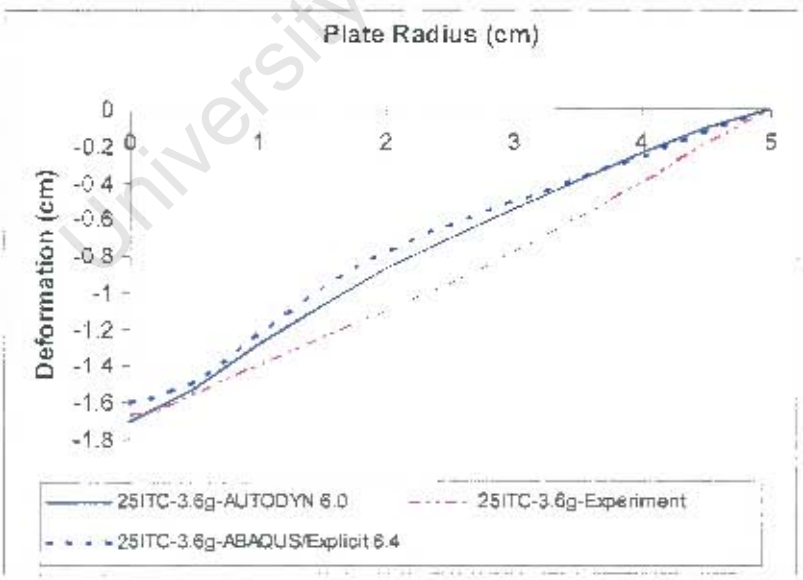

Figure 8.19: Graphs showing comparison of plate profiles from ABAQUS/Explicit 6.4, AUTODYN 6.0 and experiment for 3.6g of 25ITC explosive.

8.3.7 Plate Profile Results for 33mm CY Explosives

Result of the plate profile for 33mm CY explosive is generally good and similar to those of 25mm CY and 18mm explosively loaded plates as shown in figures 8.20 and 8.21. The central deformation and plate profile can be seen to be reasonably predicted with slight underprediction of the central deformation by both the ABAQUS/Explicit 6.4 and AUTODYN 6.0 codes.

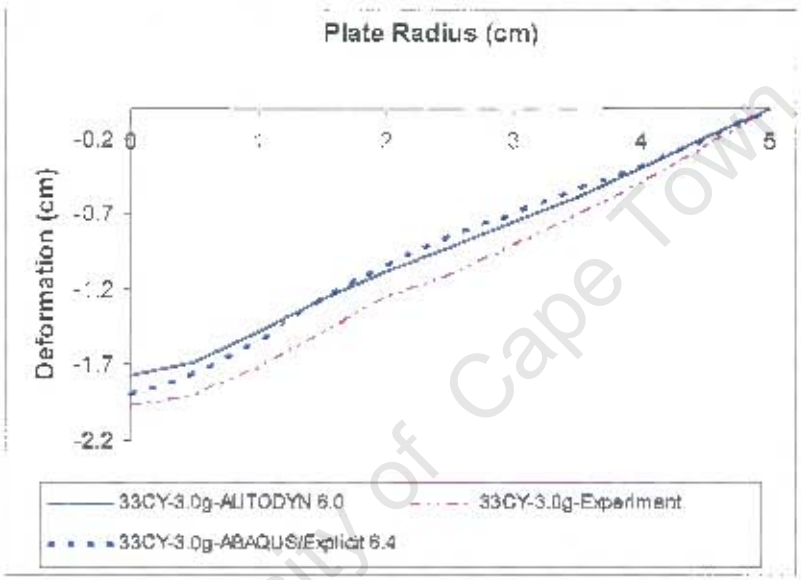

Figure 8.20: Graphs showing comparison of plate profiles from ABAQUS/Explicit 6.4, AUTODYN 6.0 and experiment for 3.0g of 33CY explosive.

8.3.8 Plate Profile Results for 33mm TC Explosives

Figure 8.22 shows comparison of the plate profiles subjected to 33mm TC explosives. The total deformation and plate profiles by the AUTODYN code shows a good match with an overestimation of the central deformation by the ABAQUS/Explicit code.

8.3.9 Plate Profile Results for 33mm ITC Explosives

Results of the plate profiles subjected to 33mm ITC explosives are shown in figures 8.23, 8.24, 8.25 and 8.26. The codes reasonably predict the profile of the

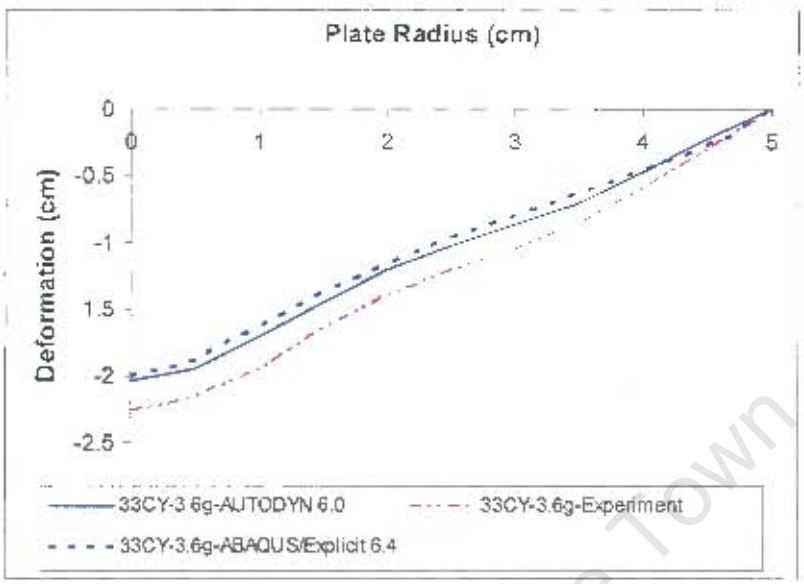

Figure 8.21: Graphs showing comparison of plate profiles from ABAQUS/Explicit 6.4, AUTODYN 6.0 and experiment for 3.6g of 33CY explosive.

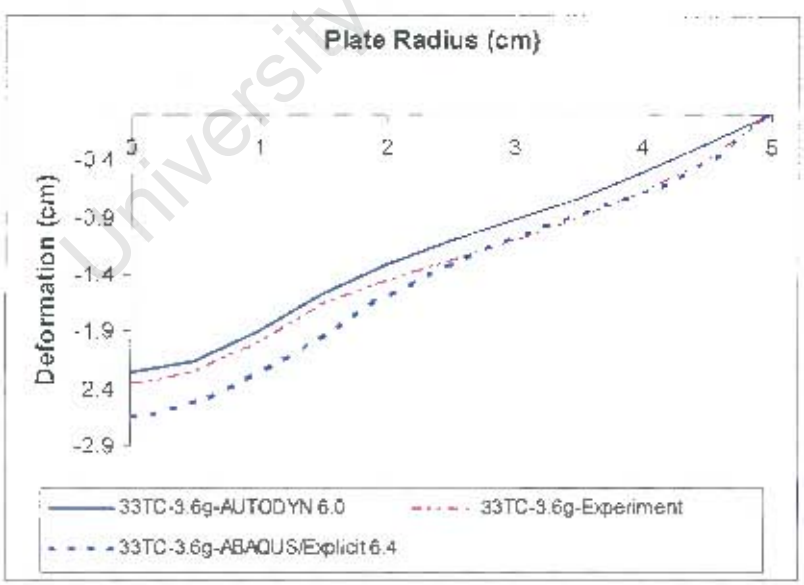

Figure 8.22: Graphs showing comparison of plate profiles from ABAQUS/Explicit 6.4, AUTODYN 6.0 and experiment for 3.6g of 33TC explosive.

plate but largely under predict the deformation as can be seen in figures 8.25 and 8.26.

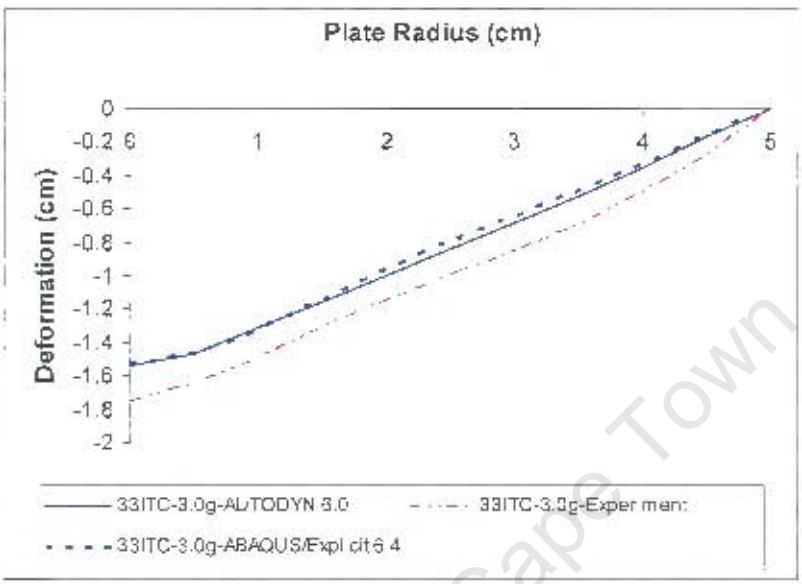

Figure 8.23: Graphs showing comparison of plate profiles from ABAQUS/Explicit 6.4, AUTODYN 6.0 and experiment for 3.0g of 33ITC explosive.

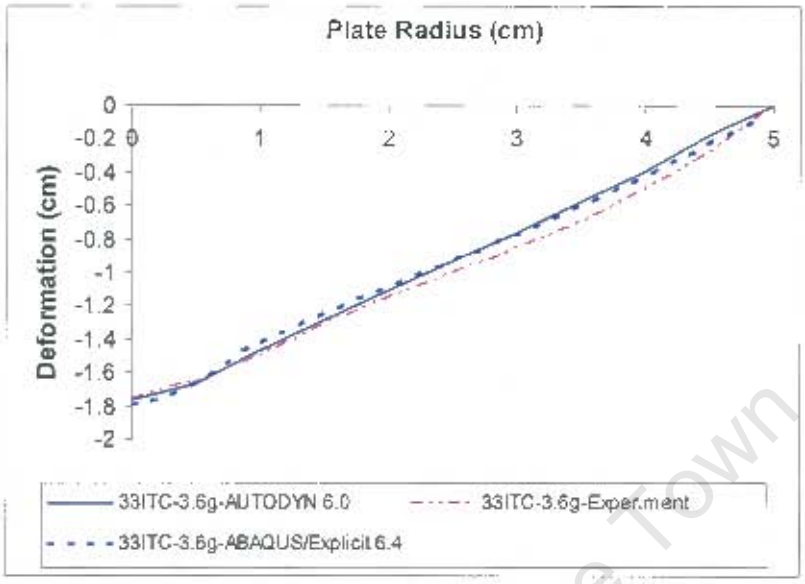

Figure 8.24: Graphs showing comparison of plate profiles from ABAQUS/Explicit 6.4, AUTODYN 6.0 and experiment for 3.6g of 33ITC explosive.

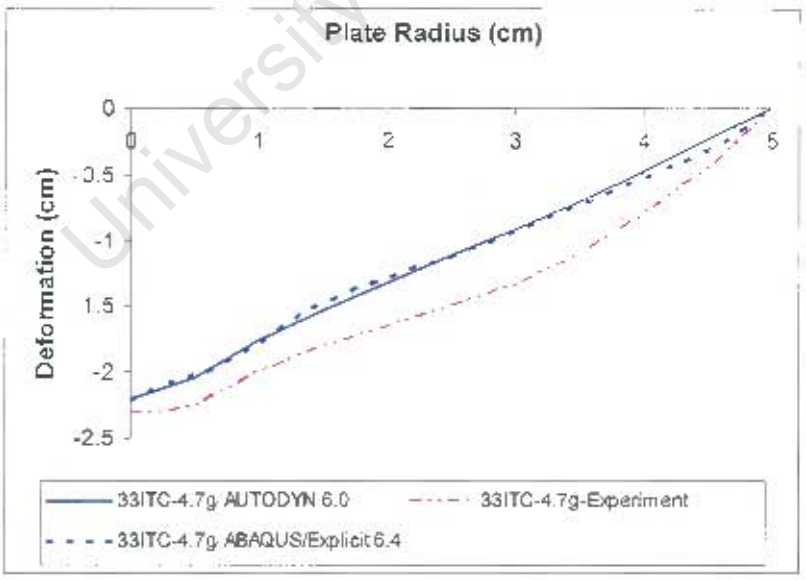

Figure 8.25: Graphs showing comparison of plate profiles from ABAQUS/Explicit 6.4, AUTODYN 6.0 and experiment for 4.7g of 33ITC explosive.

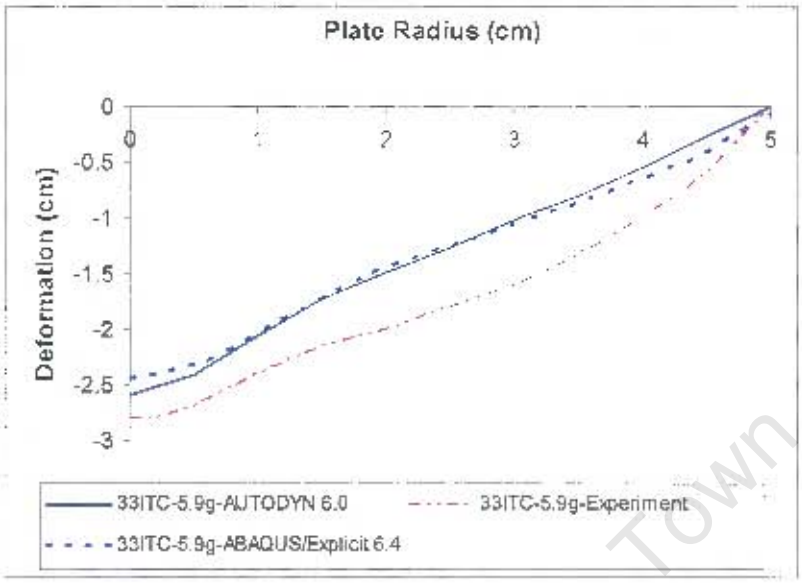

Figure 8.26: Graphs showing comparison of plate profiles from ABAQUS/Explicit 6.4, AUTODYN 6.0 and experiment for 5.9g of 33ITC explosive.

8.4 Summary

Comparison of both the central deformation and plate profiles from the simulation with the experiments have been carried out. The results show some success by the codes in predicting localised loading but fail in some cases to predict deformation caused by the ITC explosive of smaller diameters. However, it is recommended that more research needs to be carried out for other shapes of explosives and also to improve the results of the plate deformation for ITC explosives.

Chapter 9

Discussion of Experimental and Predicted Results

9.1 Introduction

Results from the experiments and simulations are discussed in this chapter. The effects of shape and mass of the explosives on the total plate deformation and impulse results are discussed.

9.2 Discussion of Experimental Results

9.2.1 Effects of Shape and Mass of Explosive on Central Deformation of Plate

As discussed in chapter 5, the shape of the shock-wave profile which depends on the shape of the explosive charge, determines the load distribution on the structure during interaction. For a TC explosive, the effective mass is higher than those of the CY and ITC explosives and load is highly localised, generally causing a higher central deformation of the plate.

The central deformation of the plates is dependent upon the effective mass of the explosive as discussed in chapter 5. The effective mass of the explosives as discussed earlier, are repeated here for clarity in figure 9.1. The effective mass of the explosives in figure 9.1 is shown for 18mm, 25mm and 33mm load cases of masses 2.6g, 3.0g and 3.6g respectively where L_{TC} is the depth of the shock-

wave by the TC explosive. The shapes are drawn to scale in order to relate the relative central deformation of the plate obtained from the experiment and the effective mass of the explosives. Since the effective mass of the TC explosive charge is bigger than those of the CY and ITC explosives, it is expected that the deformation of the TC loaded plates are generally higher compared to those of the CY and ITC explosives.

For the 25mm load cases, the height of the explosives are lower than those of the 18mm load cases. It can be seen that all the explosives of the TC charge contribute to the axial momentum of the plate as opposed to the CY and ITC explosives. Due to the higher effective mass of the TC explosive, it can be seen that the TC loaded plate causes the highest central deformation compared to the CY and ITC loaded plates.

For the 33mm load cases in which the effective mass of the TC explosive is maximum, the depth of the shock-wave is bigger than those of the CY and ITC explosives. As shown for the 33mm load cases, side loss of the 33CY explosive is reduced significantly, meaning that a bigger central deformation of the 33TC loaded plates slightly higher than that of the 33CY explosively loaded plates is expected. Although the effective mass of the TC explosive is higher than that of the CY explosive, however, the central deformation of the 33TC loaded plate is slightly less than that of the 33CY loaded plate which may be attributed to an experimental error. The effective mass of the explosives can be increased by increasing the charge diameter and decreasing the height of the explosive.

Because the axial momentum at the centre of the explosive is generally higher for the TC explosive than those of the CY and ITC explosives, the central deformation of the plate subjected to the TC loaded plates is expected to be higher. The results also show that the bigger the mass of explosive, the bigger the central deformation of the plate. This is also confirmed from the results presented in previous results in the literature as reported by Nurick and Radford [2]. The results clearly show that the deformation of a structure subjected to explosive loads is influenced both by the shape and mass of the explosive.

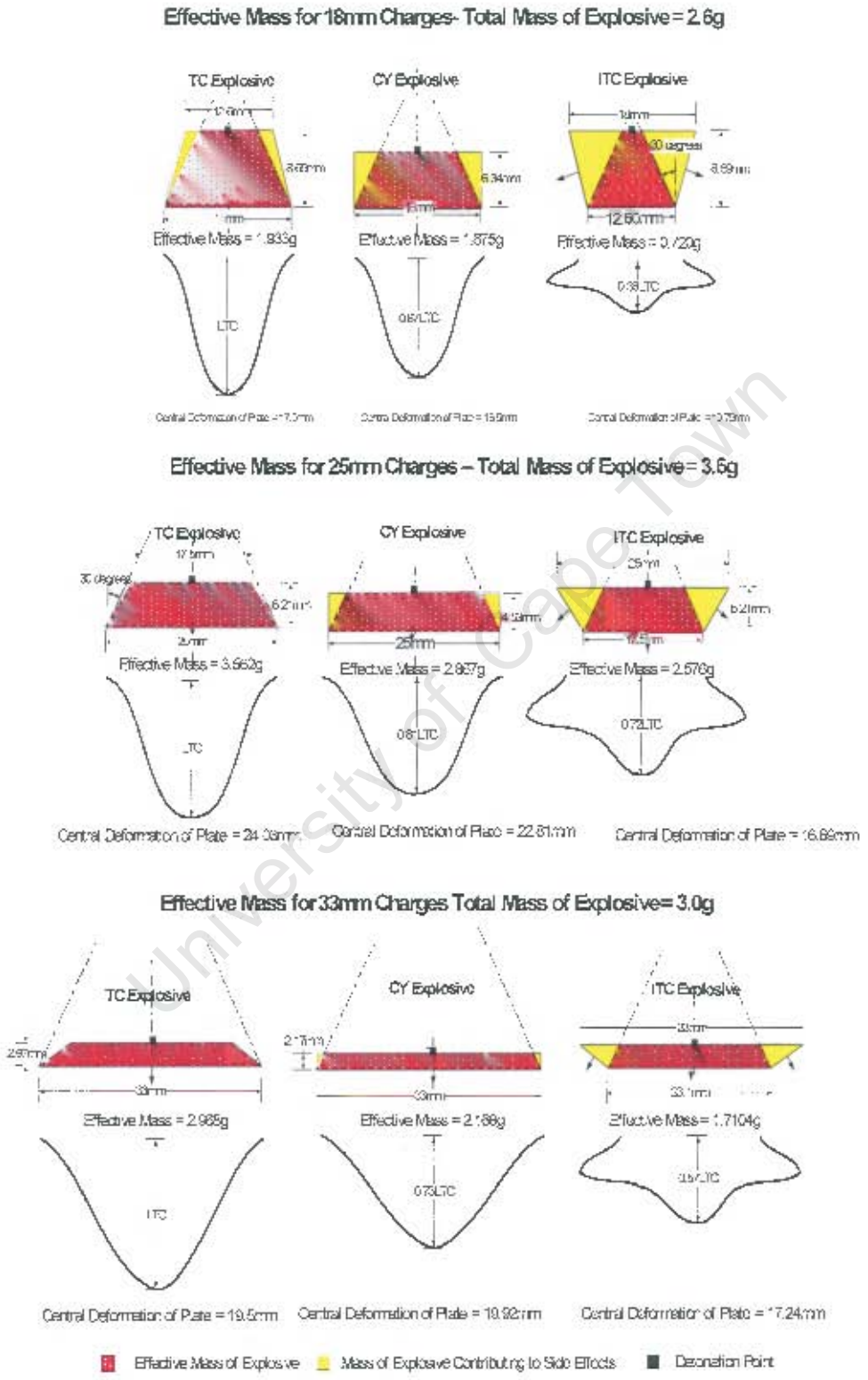

Figure 9.1: Figure showing schematics of the effective mass of 18mm, 25mm and 33mm explosive charges contributing to the axial momentum of a structure.

9.2.2 Comparison of the Experimental and Predicted Plate Profile Results

From the ABAQUS/Explicit 6.4 simulations, the experimental and predicted plate profiles generally show good correlation for all diameters and shapes of explosive, with the exception of the 18mm ITC explosives which failed to predict the experiment as regards the profile. The reason for this is not quite clear but may be attributed to the problem of unrealistic pressure distribution on the surface of the plate or that of mesh problem. Some of the results of the predicted central deformation of the plate subjected to TC explosives in the ABAQUS/Explicit 6.4 code show slight over-prediction compared to the experiment, indicating a highly localised load during the simulation. Unlike the ABAQUS/Explicit 6.4 code, no over-prediction of the experimental deformation is observed from the AUTODYN 6.0 simulations. With the exception of the 18mm ITC explosives, the results are generally good as regards the central deformation and shape of the plate profiles as the diameter of the charge increases with corresponding decrease in charge height.

Results from the AUTODYN 6.0 simulations show a similar trend to those predicted by the ABAQUS/Explicit 6.4 code and experiments in that the TC explosive loaded plates show a higher deformation compared to the CY and ITC explosives. The deformation and shape are reasonably predicted compared to the experiment with the exception of the ITC explosively loaded plates that were largely underpredicted predicted by both codes. The problem of element deformation of the plate is not reported for the AUTODYN 6.0 simulations, as opposed to the ABAQUS/Explicit 6.4 simulations in which the simulation sometimes terminates due to element deformation.

Although the codes do not reasonably predict the deformation caused by the ITC explosive, however, results from the simulations show that both numerical codes show the influence of shape of solid explosives on interaction with a structure. The results also show that the central deformation of the plate is not a sufficient condition to investigate the influence of shape of the explosive, but the entire plate deformation (profile) should be investigated.

Results of the ratio of the predicted central deformation of the plate by the CY and ITC explosives to those of the TC explosives against the ratio of their corresponding effective masses are given in figures 9.2 and 9.3. The results in

figures 9.2 obtained from the AUTODYN 6.0 code show a reasonable correlation between the ratio of the central deformation with those of the ratio of their respective effective masses compared to the results by the ABAQUS/Explicit 6.4 code which do not show good correlation. It can also be observed that the ratio of the CY to TC central deformation is higher than the ratio of the central deformation of the ITC to TC loaded plates in both codes.

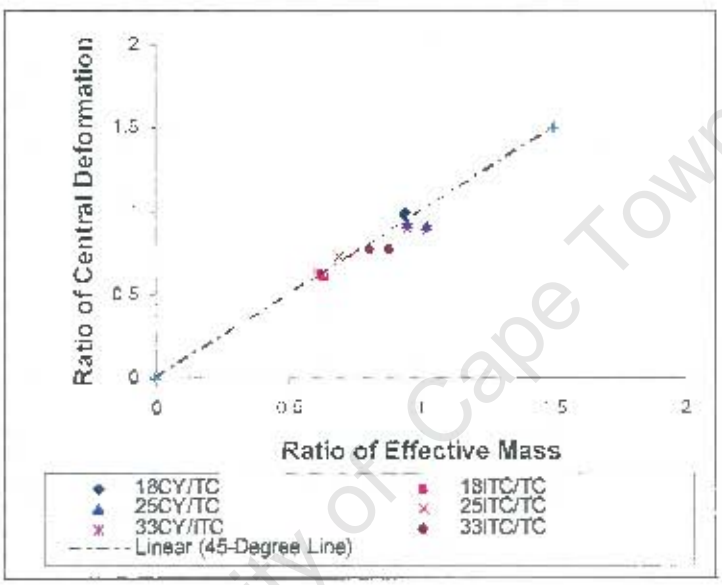

Figure 9.2: Figure showing ratio of the central deformations (CY/TC, ITC/TC) from AUTODYN against ratio of their respective effective masses.

9.2.3 Effect of Shape of Explosive Charge on Impulse

It is generally shown in all the results of the impulse, that the ITC explosive gives the highest impulse of the blast from the experiments with the TC explosives given the lowest values as given in chapter 4. For the ITC explosives however, the strength of the shock-wave is less axially, but stronger on the slant sides due to the close proximity to the plate as the detonation products are mostly directed to the plate. This means that most of the detonation products from the slant sides will interact with the plate in a much wider area compared to the CY and TC explosive charges. Although the effective mass of the TC explosive charge is generally higher than those of the CY and ITC charges, results of the impulse by the TC explosives are generally lower than those of the CY and ITC

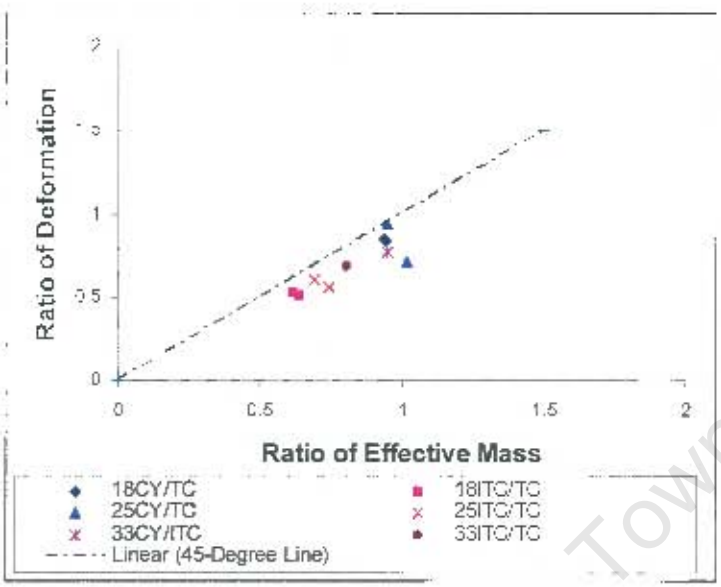

Figure 9.3: Figure showing ratio of the central deformations (CY/TC, ITC/TC) from ABAQUS against ratio of their respective effective masses.

charges. This means that the area of interaction influences the impulse much more than the mass of the charge as discussed in the next sections.

9.2.4 Effect of Diameter of Charge on Impulse

The effect of diameter of load application on impulse can be experimentally investigated. In order to achieve this, the mases and shapes of the explosives should be the same with varying diameters. Figure 9.4 shows plots of the impulse and mass of explosives for 25mm and 33mm load cases. Results of the 18mm load cases are not included due to the fact that the masses are not the same with those of the 25mm and 33mm load cases. The impulse can be seen to increases as the mass of the charges of each shape increases. However, it can also be seen in figure 9.4, that although the masses and shapes of the explosives are the same, the 33mm load cases show a higher impulse than the 25mm load cases due to the higher load area of the 33mm load cases than the 25mm load cases. It is also expected that the impulse of the 18mm load cases of the same masse as those of the 25mm and 33mm load cases are lower, due to the smaller load area. For example, the impulse measured by an 18mm CY charge of mass 3.2g is 7.09Ns compared to impulses of 8.10Ns and 8.48Ns by the 25mm CY and 33mm CY

charges of mass 3.0g each. Likewise, the impulse of the 18mm TC explosive charge of mass 3.2g is 6.1Ns, compared to impulses of 7.81Ns and 8.12Ns for the 25mm and 33mm charges respectively. Furthermore, the impulse of the 18mm ITC explosive charge is 6.9Ns compared to 8.62Ns and 8.48Ns for 25mm and 33mm ITC charges of mass 3.0g each.

From the results presented in figure 9.4, it can be seen that the impulse increases as the mass of explosive increases. Theoretically, equation 9.1 shows that the impulse is directly proportional to the product of square of the radius and height of explosive, where I is impulse of blast, r is minimum radius of load area on the target structure h the height and ρ the density of explosive. This means that the impulse is more sensitive to the radius than the height of the charge. Although, the height of the 25mm charges is higher than those of the 33mm load cases, it can be seen in figure 9.4 that at the same masses, the influence of the area of load application is greater than that of the height of the explosive. However, it should be acknowledged that determining the impulse theoretically is a challenging and complex issue and therefore needs further investigations.

$$I \propto [\pi r^2 h \rho] \tag{9.1}$$

9.2.5 Effect of Height of Explosive Charge on Impulse

Although results of the impulse shown in figure 9.4 is related to the diameter of the charges, however, the height of the charge should also be considered. As discussed in chapter 2, the thicker the explosive, the lower the momentum of the detonation products at the rear end. Because the height of the 25mm charges are bigger than those of the 33mm charges, it is expected that the detonation products at the rear end of the 33mm load cases are much higher in momentum than those of the 25mm load cases. The effect of the bigger height may contribute to the lower impulse measured by the 25mm charges compared to the 33mm load cases. The height of the 18mm load cases are much bigger than those of the 25mm and 33mm load cases. In this regard, a lower impulse of the blast by an 18mm load charge of the same mass and shape as those of the 25mm and 33mm load cases is expected.

Results of the ratio of mass to impulse from the experiments against height

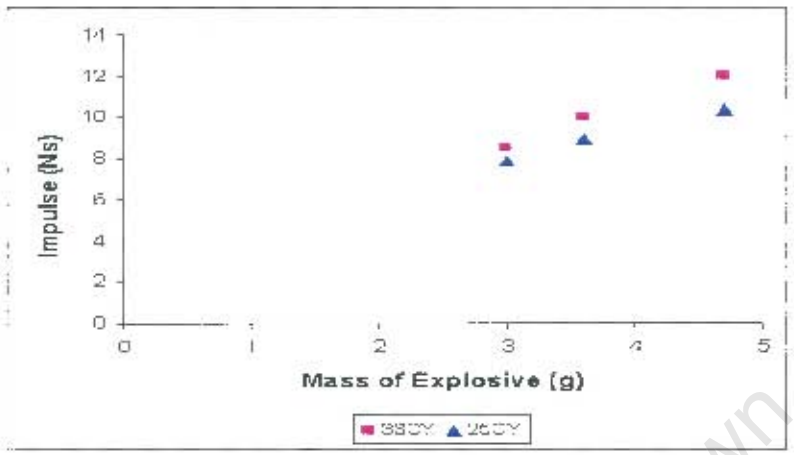

(A) Impulse vs. Mass for 25mm and 33mm CY Load Cases

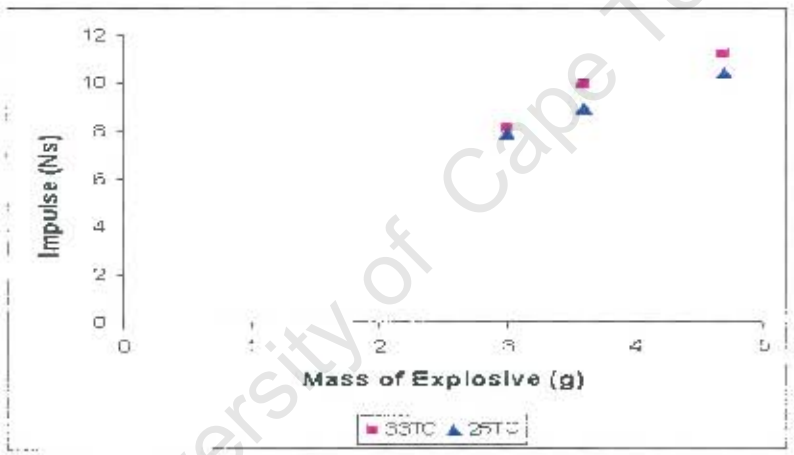

(B) Impulse vs. Mass for 25mm and 33mm TC Load Cases

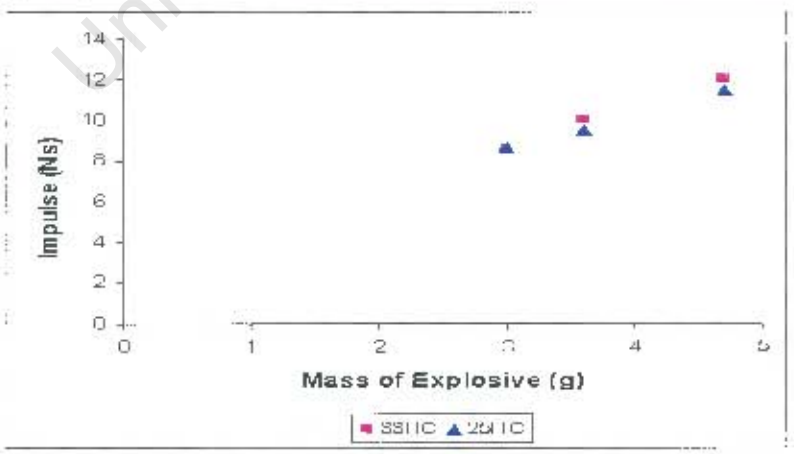

(C) Impulse vs. Mass for 25mm and 33mm ITC Load Cases

Figure 9.4: Graphs showing impulse vs. mass of explosive at the same mass for 25mm and 33mm load cases.

of explosive are plotted as shown in figure 9.5. The range of ratio of explosive mass to impulse of blast is 0.32 to 0.59(g/Ns). The results also show that as the charge diameter increases with a corresponding decrease in charge height, the ratio of mass to impulse increases with the TC explosive given the highest value.

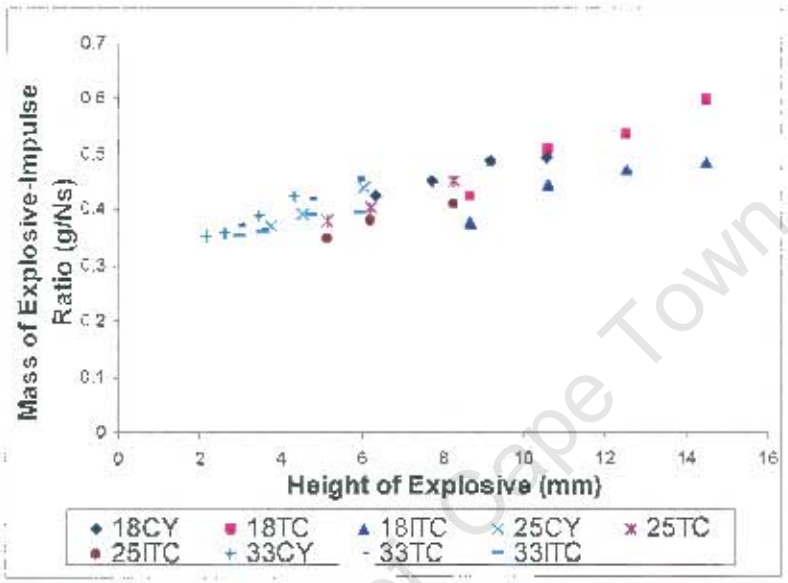

Figure 9.5: Figure showing ratio of explosive mass-impulse vs. height of explosive.

9.3 Summary

Attempts have been made to try to address the influence of shape of a solid explosive on the deformation of the plate and the impulse measured by the pendulum. It is found that the central deformation of the plate is dependent on the effective mass of the explosive whilst the impulse is dependent on the mass, height and diameter of the explosive charge. It is generally observed that the bigger the explosive charge, the bigger the impulse for explosives of the same mass. It is also generally found that the load area influences the impulse much more than the mass of the explosive irrespective of the shape of the explosives. In this regard, conclusions and recommendations are made following these observations.

Chapter 10

Conclusions

10.1 Introduction

Conclusions and recommendations in this work are based on the results from the experiments and predictions. The influence of shape of an explosive on the deformation of the plates and impulse measured by the pendulum has been thoroughly investigated experimentally, theoretically and numerically, which is the main objective of this research.

10.2 Conclusions on the experiments

10.2.1 Conclusion on Plate Deformation

It can be generally observed, that plates subjected to TC explosives give the highest deformation followed by the CY and ITC explosives respectively. This conclusion from the experiments can be drawn from the fact the axial momentum related to the effective mass of the explosive in the central area of the charges is higher for the TC explosive than those of the CY and ITC explosives. Because the TC explosives generally gives the highest effective mass compared to the CY and ITC explosives, it can be concluded that the TC loaded plate will give the biggest deformation of the plate. It can also be concluded that the TC explosive causes a more localised load than those of the CY and ITC explosives due to their initial shapes. This means that the Taylor-wave which is related to the flow of particles of the explosion is generally longer for the TC explosive than those of the CY and ITC explosives at their respective axes. In this regard, it can be

concluded that the shape of an explosive does have an effect on the deformation of the target structure.

10.2.2 Conclusion on Impulse of Blast

It can be concluded as found from the experimental results of the impulses, that both the mass and shape of the explosive do influence the impulse measured by the pendulum. The influence of the area of load interaction is found to have a greater effect on the impulse more than the height of the explosive. This is so because the impulse is related to the square of the radius of the load area compared to the height which is linearly related to the impulse given in equation 9.1. As found in the results, the ITC explosive which normally gives the smallest effective mass, but with a much wider load area, gives the highest impulse.

10.3 Conclusions on the Numerical Simulations

The numerical simulations are carried out for all Mode I deformation from the experiments in order to confirm the validity of the prediction of blast loads on structures using the ABAQUS/Explicit 6.4 and AUTODYN 6.0 codes. It is shown numerically, that the deformation of the plate is influenced by the shape of the explosive and that both codes predicts the deformation of the plates reasonably well.

10.3.1 Conclusion on the Prediction of Central Deformation

For both numerical codes, it is found that prediction of the central deformation of circular plates subjected to CY, TC and ITC explosives in comparison to the experiments are good within the 90% confidence band for all sizes of explosives.

10.3.2 Conclusion on the Prediction of Plate Profiles

From all the results presented, it can be seen that the plate profiles caused by the CY and TC explosives are generally good in comparison with the experiments from both codes. However, for the ITC explosive, the codes do not predict the overall deformation of the plate well and therefore requires more investigations.

It can be concluded that both codes model reasonably well, localised loading on structures better than non-localised load which is related to the ITC explosive. It can also be concluded that comparison of the central deformation of the plate is a necessary condition, but not a sufficient one for the prediction of plate deformation. This means that the entire plate profile should be investigated as a necessary and sufficient condition for the prediction of plate deformation. As regards the effectiveness of the codes to predict the plate profiles, it can be generally concluded from all the results, that the AUTODYN 6.0 code better predicts the experiment compared to the ABAQUS/Explicit 6.4 code.

10.4 Recommendations and Future Work

It is recommended from the findings of this research, that experiments carried out for explosively loaded structures, must take account of the shape of the explosive and not only the mass for small charges and near-blast field experiments. The moulds used in this research give the opportunity to reproduce the shape of the explosive for future experiments in order to achieve repeatability. In this regard, proper moulds for forming the shapes of the explosives must be used especially for near-field blast experiments. Although results of the deformation of the plate and impulse are conclusive based on the data presented, however, it is recommended that additional experiments need to to carried out in order to get a wider spread of the results. Further research is recommended into the interaction of explosives of other shapes with a structure.

It is also recommended that a reaction rate model be incorporated in the numerical model in order to model the detonation shock of the explosive. For an approximation of the system, the polystyrene can be replaced with air because of the low density of the polystyrene foam. This will give an opportunity to investigate the presence of a mach stem formation in relation to localised loading.

Bibliography

[1] S.B., Menkes and H.J., Opat, "Tearing and Shear failures in explosively loaded broken beams", *Explosion Mechanics*, 13, 480 – 486 (1973).

[2] G.N., Nurick, A.M., Radford, "Deformation and Tearing of Clamped Circular Plates Subjected to Localised Central Blast Loads", Recent Development in Computational and Applied Mechanics (ed. B.D Reddy). A Volume in Honour of John B Martin, pp. 276 - 301, April (1997).

[3] G.N., Nurick, M.E., Gelman and N.S., Marshall "Tearing of blast loaded plates with clamped boundary conditions", *International Journal of Impact Engineering*, Volume 18, Nos. 7-8, pp 803 – 827, November (1996).

[4] W. P., Grobbelaar and G.N., Nurick, "An investigation of structures subjected to blast loads incorporating an equation of state to model the material behaviour of the explosive", *Proceedings of the 7th International symposium on structural failure and plasticity* (IMPLAST), Melbourne, Australia, 4-6 October 2000, pp 185-194, (2000).

[5] S., Chung Kim Yuen, "Deformation and tearing of uniformly blast-loaded quadrangular stiffened plates", MSc Thesis, Department of Mechanical, (2000).

[6] R.E., Bimha, G.N., Nurick, G.P., Mitchell, "Modelling the deformation of blast-loaded Stiffened Square Plates", 1st South African Conference on Applied Mechanics '96, Gauteng, pp 260 – 267, July (1996).

[7] E.L., Lee, H.C., Horning, J.W., Lawrence, "Adiabatic Expansion of High Explosive Detonation Products", Livermore Laboratory, Report UCRL-50422, (1968).

[8] I.C., Skidmore, "The Physics of Detonation", *Sci. Prog.*, Oxf. 55, 239-257, (1967).

[9] A.N., Dremin, "Discovery in Detonation of Molecular Condensed Explosives in the 20th Century", Combustion Explosion and Shock Waves, Vol. 36 No. 6, (2000).

[10] M.A., Meyers, "Dynamic Behaviour of Materials", University of California, San Diego, John Wiley and Sons, Inc.(1994).

[11] E.L., Baker, A.S., Daniels, K.W., Ng, V.O., Martin, and J.P., Orosz, "Barnie: A Unitary Demolition Warhead", *19th International Symposium of Ballistics*, 7-11 May, Interlaken, Switzerland (2001).

[12] M., Katayama, A., Takeba, S., Toda and S., Kibe, "Analysis of Jet Formation and Penetration By Conical Shaped Charge with The Inhibitor", *International Journal of Impact Engineering*, 23. 443-454 (1999).

[13] J., Molinari, "Finite Element Simulation of Shaped Charges", *Finite Element in Analysis and Design*, 38 921-936 (2000).

[14] R.E., Brown, M.E., Majerus, and J.S., Lewis, "Building Characteristics Into a Shaped Charge To Achieve Unique Performance Requirements", *International Journal of Impact Engineering,* Vol. 17. pp. 121 130, (1995).

[15] M., Held, "Verification of The Equation For Radial Crater Growth By Shaped Charge Jet Penetration" *International Journal of Impact Engineering,* Vol. 17. pp 387-398, (1995).

[16] Livermore Scientists, "Unravelling the Mystery of Detonation", High Explosive Detonation Research, http://www.llnl.gov/str/Simpson99.html. Science and Technology Review (1999).

[17] A.R., Shouman, "A Very Simple Yet Accurate Solution to The Thermal Explosion Problem" Journal of Loss Prevention in the Process Industries 11. 383-390 (1998).

[18] T.F., Jenkins, D.C., Leggett, P.H., Miyares, M.E., Walsh, T.A., Ranney, H., Cragin and V., George, "Chemical Signatures of TNT-Filled Land Mines", Talanta 54. 501-513, (2001).

[19] R.N., Rogers and J.L., Rogers, "Explosive Science", Los Alamos, NM (http://home.att.net/~rnrogers, (2005).

[20] S.K., Chidester, C.M., Tarver, L.G., Green and P.A., Urtiew, "On the Violence of Thermal Explosion in Solid Explosives", Defence Technologies Engineering Division, Lawrence Livermore National Laboratory L-282, Livermore, CA 94550, Combustion and Flame 110:264-280, (1997).

[21] J.S., Rinehart, J., Pearson, "Explosive working of metals", Pergamon Press, (1963).

[22] W., Ficket and W.C., Davis, "Detonation Theory and Experiment", Dover Publications, Inc, Mineola, Ney York, (2000).

[23] H., Langweiler, "The Hydrodynamic Theory of Detonation", National Advisory Committee for Aernautics, Technical Memorandum No. 899. Vol. 19, (1938).

[24] R., Guirguis, A., Landsburg, H., Sandusky and A., Wardlaw, "Propagation of Detonation Waves in Radially Graded Explosives", Naval Surface Warfare Center, Indian Head, MD 20640-5035, www.math.rpi.edu/faculty/kapila (2000).

[25] B., Leal-Crouzet, G., Baudin and H.N., Presles, "Shock Initiation of Detonation in Nitromethane", DGA/Centre d'Etudes de Gramat, 46500 Gramat, France (2000).

[26] S.N., Lubyatinsky and B.G., Loboiko, "Detonation Reaction Zones of Solid Explosives", Russian Federal Nuclear Center, Institute of Technical Physics, 11th International Symposium on Detonation, (2002).

[27] J.A., Zukas and W., Walters, "Explosive effects and Applications", Springer-Verlag New York, (2003).

[28] T.D., Aslam and J.B., Bdzil, "Numerical and Theoretical Investigations on Detonation-Inert Confinement Interactions", Los Alamos National Laboratory, Los Alamos, NM 87545, USA, www.intdetsymp.org/detsym2002, International Symposium on Detonation, (2002).

[29] R.J., Swinton, T., Bussell and L., McVay, "A Critical Diameter Study of the Australian Manufactured Underwater Explosive Composition H6", Weapons Systems Division Aeronautical and Maritime Research Laboratory, DSTO-TN-0049, Department of Defence (1996).

[30] D.S., Stewart and J., Yao, "The Normal Detonation Shock Velocity-Curvature Relationship for Materials With Non-ideal Equation of State and Multiple Turning Points", Department of Theoretical and Applied Mechanics (D.S.S) and Aeronautical and Astronautical Engineering (J.Y), University of Illinois, Urban, IL 61801, USA, Combustion and Flame113:224-235 (1998).

[31] P.W., Cooper, S.R., Kurowski, "Introduction to the technology of explosives", WILEY-VCH, (1996).

[32] N.F., Scilly, "Measurement of the explosive performance of high explosives" *Journal of loss Prev. Process* Ind. Vol. 8. No. 5. pp. 265-273, (1995).

[33] W.C., Davis, "Equation of State for Detonation Products", Tenth International Detonation Symposium, pp-369-376, (1993).

[34] W.C., Davis, "Complete Equation of State for Unreacted Solid Explosive", Los Alamos National Laboratory, Los Alamos, NM 87545, USA, Combustion and Flame, 120:399-403, (2000).

[35] D.J., Pastine, "(E),V,T and P,V,T Equations of State of Reaction Products at High Pressure and Temperature", Enig Associates, Inc. Silverspring, Maryland, 11th International Symposium on Detonation, (2002).

[36] O., Huezé, "A Complete Equation of State for Detonation Products in Hydrocodes", CEA DAM/ IIe de France, B.P 12, 91680 Bruyères-le-Châtel, France.

[37] W.B., Brown and M.,Braithwaite, "Development of the Williamburg Equation of State to Model Non-Ideal Detonation", 10th International Detonation Symposium, pp. 377-385, (1993).

[38] J.D., Dunnett, D.C., Swift and M., Braithwaite, "Comparison of Williamburg and JWL Equation of State for Nitromethane", Proceedings For The 11th International Symposium on Detonation, (1951-1998).

[39] H.D., Jones, P.K., Gaustavson and F.J., Zerilli, "Analytic Equation of State For SX-2", Naval Surface Warfare Centre, Indian Head Division, Indian Head, MD 20640-5035, 11th International Symposium on Detonation, (2002).

[40] W., Byers-Brown, M., Braithwaite, "Development of the Williamburg Equation of State to Model None-Ideal Detonation", Proc 10th Symposium (International) On Detonation, ONR 33395-12, (1995).

[41] W.C., Davis, "Equation of State for Detonation Products", Tenth International Detonation Symposium, pp-369-376, (1993).

[42] R.D., Cowan and W., Ficket, "Calculation of the Detonation Properties of Solid Explosives with the Kistiakowsky-Wilson Equation of State", Journal of Chem. Phys. 24 932 (1956).

[43] W., Ficket and W.W., Woods, "A Detonation-Product Equation of State Obtained From Hydrocode Data", Physics of Fluids 1, 528 (1958).

[44] M.L., Wilkins, "The Equation of State of PBX 9404 and LX04-01", Lawrence Radiation Laboratory, Livermore, Rept. UCRL-7797 (1964).

[45] H., Jones and A.R., Miller, "The Detonation of Solid Explosives", Proc. Roy. Soc. London, A-194 480, (1948).

[46] Z., Yang, "Finite Element Simulation of Response of Buried Shelters to Blast Loading", Finite Elements in Analysis and Design 24 113-132 (1997).

[47] P.W., Merchant, S.J., White and A.M., Collyer, "A WBL-Consistent Equation of State For The HMX-Based Explosive EDC37 From Cylinder Tests", Atomic Weapons Establishment, Aldermaston, Berkshire, RG7 4PR, UK, 12th International Symposium Detonation, (2002).

[48] D.J., Whelan, R., Swinton and G., Bocksteiner, "Velocity of Detonation and Charge Diameter in Some RDX-Driven Heterogenous Explosives: PBXW-115, PBXN-111, H-6 and Composition B", Weapons Systems Division Aeronautical and Maritime Research Laboratory, DSTO-TR-0400, (1996).

[49] N.J. Robertson, C.J., Hayhurst, and G.E., Fairlie, "Numerical Simulation of Explosion Phenomena", IJCAT, Twenty Years of Finite Element Analysis: Review and Future Prospects, International Journal of Computer Applications in Technology, Vol. 7. Nos 3-6, pp. 316-329, (1994).

[50] G.I., Taylor, "The Propagation of Blast Waves", Vol. 3, pp. 221-235, (1958-1971).

[51] T., Krauthammer, A., Altenberg, "Negative Phase Blast Effects on Glass Panels" *International Journal of Impact Engineering,* 24 1-17, (2000).

[52] Z., Whenhui, X., Honglu, Z., Guangquan, and G.K., Schleyer, "Dynamic Response of Cylindrical Explosives chamber to Internal Loading Produced by a Concentrated Charge" *International Journal of Impact Engineering,* Vol. 19, Nos. 9-10, pp. 831-845, (1997).

[53] S., Guruprasad, A., Mukherjee, "Layered Sacrificial Claddings Under Blast Loading Part II - Experimental Studies", *International Journal of Impact Engineering,* 24. 975-984 (2000).

[54] T.C., Chapman, T.A., Rose and P.D., Smith, "Reflected Blast wave Resultants Behind Cantilever Walls: A New Prediction Technique", *International Journal of Impact Engineering,* Vol. 16, No. 3, pp. 397-403, (1995).

[55] G.F., Kinney and K.G., Graham, "Explosive Shocks in Air", 2nd Edition, Springer-Verlag, New York (1985).

[56] T., Hiroe, H., Matsuo, K., Fujiwara, T., Abe, K., Kusumegi, T., Katoh, "Dynamic Behaviour of Materials Induced by Explosive Loadings Initiated Using Wire Explosion Technique", Journal of Materials Processing Technology 85, 56-59 (1985).

[57] P.D., Smith, P., Vismeg, L.C., Teo and L., Tingey, "Blast Wave Transmission Along Rough-Walled Tunnels", *International Journal of Impact Engineering,* Vol. 21, No. 6, pp. 419-432, (1998).

[58] O., Olatidoye, S., Sarathy, G., Jones, C., McIntyre, L., Milligan, "A Representative Survey of Blast LoadingModels and Damage Assessment Methods for Buildings Subjected to Explosive Blast", CEWES MSRC/PET TR/98-36 (2005).

[59] M.S., Agabian, "Design of Structures to Resist Nuclear Weapon Effects", ASCE Manual on Engineering Practice, No. 42. asce, New York (1985).

[60] W.E., Baker, "Explosions in Air", University of Texas Press, Austin, TX, (1973).

[61] A.C., Jacinto, R.D., Ambrosini and R.F., Danesi, "Experimental and Computational Analysis of Plates under Air Blast Loading", *International Journal of Impact Engineering*, 25. 927-947 (2001).

[62] S.A., Formby, R.K., Wharton, "Blast Characteristics and TNT equivalence values for some commercial explosives detonated at ground level", *Journal of Harzadous Materials*, A50. 183-198, (1996).

[63] I.A., Naumyenko, I.G., Petroskyi, "The Shock Wave of Nuclear Explosions" (1956).

[64] R.K., Wharton, S.A., Formby and R., Merrifield, "Airblast TNT Equivalence for a Range of Commercial Blasting Explosives", *Journal of Hazardous Materials* A79 31-39 (2000).

[65] H.L., Brode, "Numerical Solutions of Spherical Blast Waves", Journal of Applied Physics, 6. (1956).

[66] J., Henrych, "The Dynamics of Explosions and its Use", Amsterdam: Elsevier, (1979).

[67] C.A., Mills, "The design of Concrete Structures to Resist Explosions and Weapon Effects", International Proceedings of The First International Conference For Harzard Protection, Edinburgh, (1987).

[68] R.W., Gurney, "The Initial Velocities of Fragments From Bombs, Shells and Grenades", BRI Report 405. (1943).

[69] M.H., Kashavarz, "Simple determination of Performance of Explosives Without using any Experimental Data" *Journal of Hazardous Materials,* A119, 25-29 (2005).

[70] J.E., Kennedy, "Behaviour and Utilisation of Explosives in Engineering Design," 12th Annual Symposium, ASME, UNM, Albuquerque, NM (1972).

[71] H.U., Mair, "Review: Hydrocodes For Structural Response To Underwater Explosions", Shock and Vibration 6/2 81-96, (1999).

[72] T., Frank and K., Gruber, "Numerical Simulation of Frontal Offset Collisions," Cray Channels, 13, 4, 2-6, (1992).

[73] P.C., Galbraith and Finn, "Supercomputer Simulation of Automative Sheet-Metal Forming" Cray Channels 16,2. 16-21 (1994).

[74] C.L., Mader, "Numerical Modelling of Detonations", University of California Press, (1979).

[75] M.L., Wilkins, "Calculations of Elastic-plastic flow", Lawrence Radiation Laboratory, Report UCRL–7322, (1969).

[76] J.M., Walsh, M.H., Rice, R.G., McQueen, F.L., Yarger. "HELP: A Multiple Material Eulerian Programme for Compressible Fluid and Elastic Plastic Flows in Two Space Dimensions and Time, Vols. 1 and 2, Systems, Science and Software Inc., Report 3SR-350, (1970).

[77] G.N., Nurick and J.B., Martin, "Deformation of Thin Plates Subjected to Impulsive Loading – A Review Part I: Theoretical Considerations", *International Journal of Impact engineering.* 8, (2), 159-169 (1989).

[78] G.N., Nurick and J.B., Martin, "Deformation of thin plates subjected to impulsive loading – A Review Part II: Experimental Studies", *International journal of Impact engineering.* 8, (2), 171-186 (1989).

[79] M.D., Olson, G.N., Nurick, and J.R., Fagnan "Deformation and Rupture of Blast Loaded Plates – Predictions and Experiments", *International Journal on Impact Engineering.* 13, (2), 279-291 (1993).

[80] R. G., Teeling-Smith, G.N., Nurick, , "Predicting the Onset of Necking and Hence Tearing of Thin Plates Subjected to Impulsive Loading-An experimental view", Structures under shock and Impact (ed. P. Bulson). Published by computational Mechanics Publications and Thomas Telford, pp 431 – 445, (1992).

[81] G.N., Nurick, and D.M., Lump, "Deflection and Tearing of Clamped Stiffened Circular Plates Subjected to Uniform Impulsive Loads", Structures

Under Shock and Impact IV, (Ed. N Jones, CA Brebbia, AJ Watson), Published by Computational mechanics publications, pp 393 – 402, (1996).

[82] Y., Pan and L.A., Louca, "Experimental and Numerical Studies on the Response of Stiffened Plates Subjected to Gas Explosions", *Journal of Constructional Steel Research*, 52, 171-193, (1999).

[83] N.S., Rudrapatna, R., Vaziri and M.D., Olson, "Deformation of Stiffened Plates", *International Journal of Impact Engineering*, 24, 457-474, (2000).

[84] G.K., Schleyer and S.S., Hsu, "A modelling Scheme for Predicting the Response of Elastic-Plastic Structures to Pulse Pressure Loading", *International Journal of Impact Engineering*, 24, 759-777, (2000).

[85] T., Wierzbicki, G.N., Nurick, "Large Deformation of Thin Plate under Localised Impulsive Loading", *International Journal of Impact Engineering*, Vol. 18, Nos.. 7 – 8, pp. 899 – 918, November (1996).

[86] P.S., Symonds and T., Wierzbicki, "Membrane Mode Solution for impulsively loaded circular plates", Journal of Applied Mechanics 46, 58-64 (1979).

[87] S., Chung Kim Yuen, G.N., Nurick, "The significance of thickness of a plate when subjected to localized blast load", 16th International Symposium on military Aspects of Blast and shock, (MABS16), Oxford, UK, 10-15 September, pp 491-499, (2000).

[88] E., Muluh, "Analysis of Deformation and Tearing of Uniformly Blast-Loaded Circular and Square Plates, Rectangular Beams and T-Beams" Msc Thesis, University of Cape Town, (2003).

[89] V.H., Balden, G.N., Nurick, "Numerical Simulation of the Post-Failure Motion of Steel Plates Subjected to Blast Loading", *International Journal of Impact Engineering*, 32. 14-34, (2005).

[90] G.N., Nurick and MW., Bryant, "Fragmentation Damage As a Result of An Explosion"In N.K., Gupta, Editor, Plasticity and Impact Mechanics, New Delhi, India, pp. 484-498, (1996).

[91] S., Chung Kim Yuen, G.N., Nurick, "Experimental and Numerical Studies on Quadrangular Stiffened Plates: Part I, Uniform Blast Loading", *International Journal of Impact Engineering*, 31. 55-83, (2005).

[92] G.S., Langdon, S., Chung Kim Yuen, G.N., Nurick, "Experimental and Numerical Studies on Quadrangular Stiffened Plates: Part II, Localised Blast Loading", *International Journal of Impact Engineering*, 31. 85-111, (2005).

[93] L., Lain, O., Ranestad, A., Sandvik and A., Snekkevik, "Numerical Simulations of Anti-Tank Mine Detonations" Presented at *12th APS Topical Group Conference on Shock Compressed Matter*, Atlanta, USA, June 24-29, (2001).

[94] X., Wang, Z., Zhuang and W., Yang, "Simulation of Absorbtive Tripple-Layer Structures Against Shock-Wave Blast", Department of Engineering Mechanics, Tsinghua University, Beijing 100084, PR. China, ABAQUS User Conference, (2000).

[95] J.L., O'Daniel, T., Krauthammer, "Assessment of Numerical Simulation Capabilities for Medium-Structure Interaction Systems Under Explosive Loads", *Computers and Structures,* Vol. 63, No. 5. pp. 875-887, (1997).

[96] B.M., Thomas, and G.N., Nurick, "The Effect of Boundary Conditions on Thin Plates Subjected to Impulsive Loads", The 15th International Symposium on Plasticity and its Current Application, Osaka, Japan, July, pp 85-88 (1995).

[97] M.E., Gelman, G.N., Nurick, G.P., Mitchell, "A Numerical Study of Inelastic Failure of Impulsively Loaded Circular Plates, With Various Boundary Conditions", Proceedings of the first South African Conference on Applied Mechanics (SACAM) 96, 1-5 July, Midrand South Africa (1996).

[98] L., Daykin, "Numerical modelling of explosively loaded steel V-Plates using the Jones-Wilkins-Lee equation of state", MSc Thesis University of Cape Town (2002).

[99] Hibbit, Karlson, and Sorenson, INC. "ABAQUS/Explicit 6.4 example problems manual", (1996).

[100] C.G., Soares, J.M., Gordo, and A.P, Teixeira, "Elasto-Plastic Behaviour of Plates Subjected to Heat Loads", Journal of Construction Steel Res. Vol. 45, No. 2, pp. 179-198, (1998).

[101] G.R., Johnson and W.H., Cook, "A Constitutive Model and Data for Metals Subjected to Large Strains, High Strain Rates and High Temperatures", Proceedings of the Seventh International Symposium on Ballistics, The Hague, The Netherlands, pp. 541-547 (1983).

[102] F.J., Zerilli and R.W., Armstrong, "Dislocation-Mechanism-Based Constitutive Relations for Material Dynamics Calculations", Journal of Applied Physics 61 (5), 1816 -1825 (1987).

[103] N., Jones, "Structural Impact". Cambridge University Press, Cambridge (1989).

[104] T., Masui, T., Nunokawa, T., Hiramatsu., "Shape correction of hot rolled steel using an on line leveler", Journal of Japan Society for technology of plasticity, (1), (1987).

[105] D., Bonorchis, "Implementation of Material Models for High Strain Rate Applications as User-Subroutines in ABAQUS/Explicit", Msc Thesis, Department of Mechanical Engineering, University of Cape Town, (2003).

[106] T.J., Holmquist and G.G., Johnson, "Determination of Constants and Comparison of Results for Various Constitutive Models", Journal de Phyique III, Vol. 1, pp. 853 - 860, (1991).

[107] W.K., Rule and S.E., Jones, "A Revised form of the Johnson-Cook Strength Model", *International Journal of Impact Engineering*, Vol. 21. No. 8, pp. 609-624, (1998).

[108] R., Liang, A.S., Khan, "A Critical Review of Experimental Results and Constitutive Models for BCC and FCC metals Over a Wide Range of Strain Rates and Temperatures", International Journal of Plasticity, 15. 963-980, (1999).

[109] S.R., Bodner and P.S., Symonds, "Experiments on visco-plastic response of Circular plates to impulsive loading", Journal of Mechanics and Physics of Solids, 27, 91 – 113 (1979).

[110] M.V., Dharaneepathy, M.N.K., Rao and A.R., Santhakumar, "Critical Distance For Blast-Resistance Design", Computers and Structures, Vol. 54, No. 4, pp. 587-595, (1995).

[111] G.A., Leiper, D.L., Kennedy, "Reactive Flow Analysis and its Application", Ninth Symposium (International) on Detonation, Vol. 2, (1989).

[112] S.J., Schraml, R.L., Summers, R.M., Mudd, "Close-In Blast of End-Detonated Cylindrical Charges", AMSRL-WM-TC www.intdetsymp.org/detsym2002, International Symposium on Detonation, (1989).

[113] M.A., Wiehahn, G.N., Nurick, and H.C., Bowles, "Some insight into the mechanism of the deformation and tearing of thin plates at high strain rates incorporating temperature dependent material properties", Structures under shock and impact (SUSI), (Ed P Bulson), Published by computational mechanics publications, pp 207-220, (2000).

[114] C., Anderson Jr., "An Overview of the Theory of Hydrocodes", *International Journal of Impact Engineering*, 15, 33-59, (1987).

[115] K., Ohashi, H., Kleine, K., Takayama, "Characteristics of Blast Wave Generated by milligram charges", Department of Aeronautics and Space Engineering, Tohoku University, Aoba Aramaki 01, Aoba-ku, Sendai, Miyagi, 980-8579, Japan (2003).

[116] C.A., Forest and C.L., Mader, "Two Dimensional Homogeneous and Heterogeneous Detonation Wave Propagation", LA 6259, (1976).

[117] K., Bathe, "Finite Element Procedures in Engineering Analysis", Prentice-Hall, Inc., Englewood Cliffs, New Jersey, (1982).

Appendix A

Explosive Dimensions Table

Height of Explosive	Mass	Top diameter	Bottom Diameter
6.34mm	2.6g	18mm	18mm
7.74mm	3.2g	18mm	18mm
9.15mm	3.7g	18mm	18mm
10.56mm	4.3g	18mm	18mm

Table A.1: Dimensions of 18mm Cylinder Explosives

Height of Explosive	Mass	Top diameter	Bottom Diameter
8.69mm	2.6g	12.6mm	18mm
10.60mm	3.2g	12.6mm	18mm
12.53mm	3.7g	12.6mm	18mm
14.47mm	4.3g	12.6mm	18mm

Table A.2: Dimensions of 18mm Truncated Cone Explosives

Height of Explosive	Mass	Top diameter	Bottom Diameter
8.69mm	2.6g	18mm	12.6mm
10.60mm	3.2g	18mm	12.6mm
12.53mm	3.7g	18mm	12.6mm
14.47mm	4.3g	18mm	12.6mm

Table A.3: Dimensions of 18mm Inverted Truncated Cone Explosives

Height of Explosive	Mass	Top diameter	Bottom Diameter
3.77mm	3.0g	25mm	25mm
4.53mm	3.6g	25mm	25mm
6.04mm	4.7g	25mm	25mm

Table A.4: Dimensions of 25mm Diameter Cylinder Explosives

Height of Explosive	Mass	Top diameter	Bottom Diameter
5.16mm	3.0g	17.5mm	25mm
6.21mm	3.6g	17.5mm	25mm
8.27mm	4.7g	17.5mm	25mm

Table A.5: Dimensions of 25mm Truncated Cone Explosives

Height of Explosive	Mass	Top diameter	Bottom Diameter
5.16	3.0g	25mm	17.5mm
6.21mm	3.6g	25mm	17.5mm
8.27mm	4.7g	25mm	17.5mm

Table A.6: Dimensions of 25mm Inverted Truncated Cone Explosives

Height of Explosive	Mass	Top diameter	Bottom Diameter
2.17mm	3.0g	33mm	33mm
2.6mm	3.6g	33mm	33mm
3.46mm	4.7g	33mm	33mm
4.33mm	5.9g	33mm	33mm

Table A.7: Dimensions of 33mm Diameter Cylinder Explosives

Height of Explosive	Mass	Top diameter	Bottom Diameter
2.97mm	3.0g	23.1mm	33mm
3.56mm	3.6g	23.1mm	33mm
4.74mm	4.7g	23.1mm	33mm
5.96mm	5.9g	23.1mm	33mm

Table A.8: Dimensions of 33mm Truncated Cone Explosives

Height of Explosive	Mass	Top diameter	Bottom Diameter
2.97mm	3.0g	33mm	23.1mm
3.56mm	3.6g	33mm	23.1mm
4.74mm	4.7g	33mm	23.1mm
5.96mm	5.9g	33mm	23.1mm

Table A.9: Dimensions of 33mm Inverted Truncated Cone Explosives

A.1 Photographs of Explosive Moulds

Table A.10: Photographs of moulds for 18mm CY, TC and ITC explosive charges

Table A.11: Photographs of moulds for 25mm CY, TC and ITC explosive charges

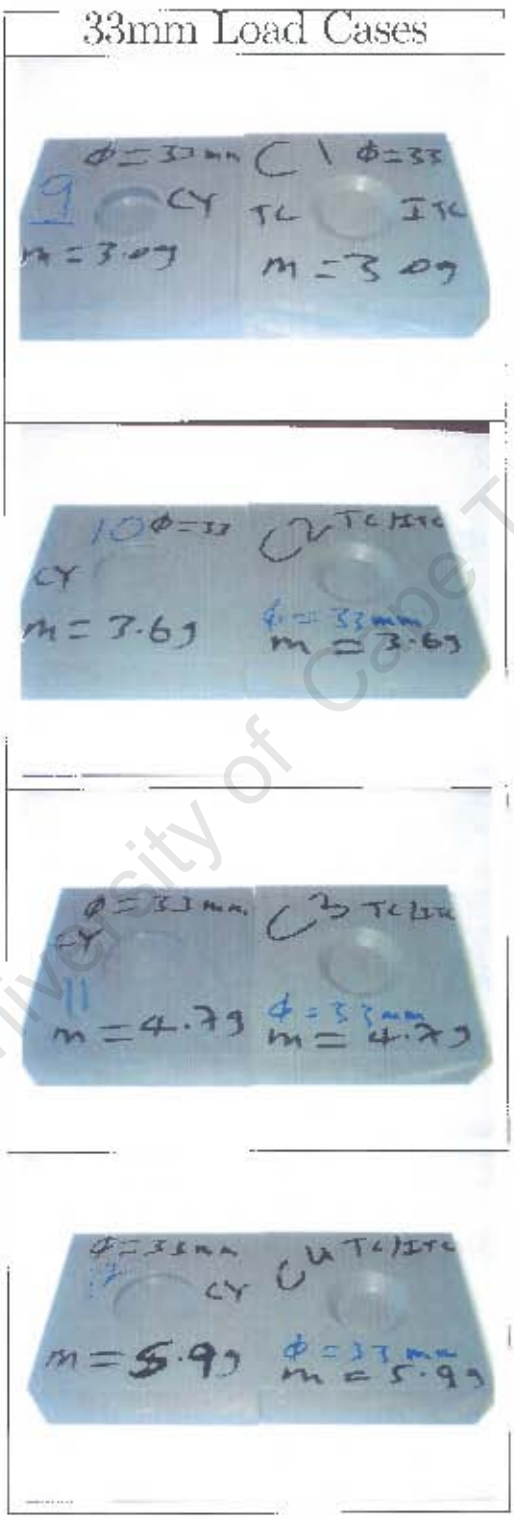

Table A.12: Photographs of moulds for 33mm CY, TC and JTC explosive charges

Appendix B

Impulse Calculation

Figure B.1 shows the pendulum when displaced by the blast wave. The impulse of an object is generally given as shown in equation B.1.

$$I - M \cdot \dot{x}_o \tag{B.1}$$

where M is the total mass, and $\dot{x}_o$is the initial velocity. For the pendulum, the equation of motion of is given as shown in equation B.2.

$$M\frac{d^2x}{dt^2} + C\frac{dx}{dt} - \frac{M}{R}gx = 0 \tag{B.2}$$

where x is the horizontal displacement, C is the damping coefficient, and R the radius of the pendulum motion. The solution for the horizontal displacement is given in equation B.3.

$$x = e^{-\beta t}\frac{\dot{x}_o}{w_d}\sin(w_d t) \tag{B.3}$$

$\beta = \frac{C}{M}$, $w_n = \frac{2\pi}{t}$, T is the period of the oscillation of the pendulum. If x_1 is the displacement of the pendulum for a time of $t = \frac{T}{4}$ and x_2 for a time of $t = \frac{3T}{4}$, then solving for x_1 and x_2 yields the solutions in B.4 and B.5.

$$x_1 = e^{-\frac{\beta T}{4}}\dot{x}_o\frac{T}{2\pi} \tag{B.4}$$

$$x_2 = e^{-\frac{3\beta T}{4}}\dot{x}_o\frac{T}{2\pi} \tag{B.5}$$

$$\frac{x_1}{x_2} = e^{\frac{\beta T}{2}} \tag{B.6}$$

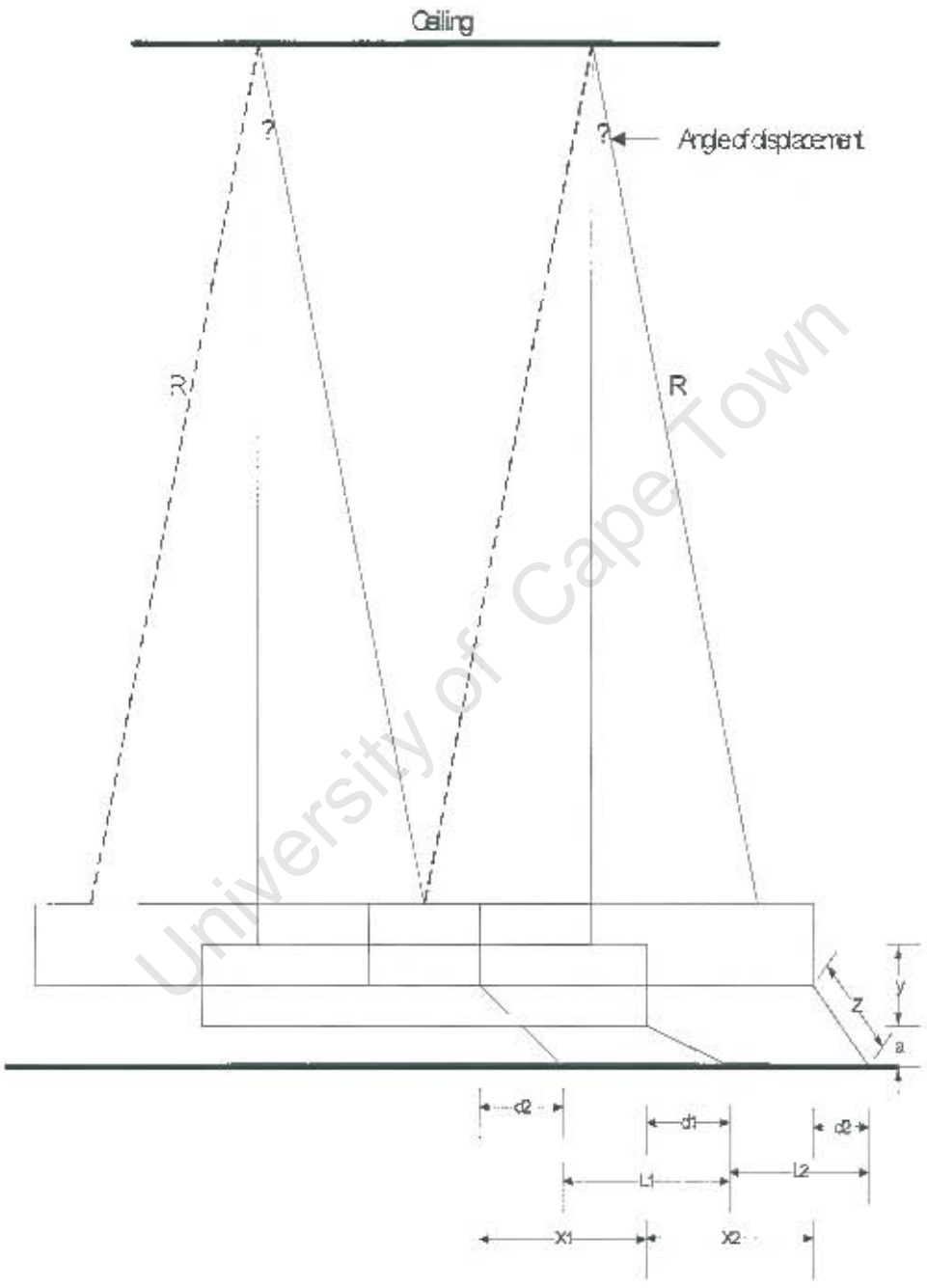

Figure B.1: Displaced pendulum geometry.

$$\beta = \frac{2 \ln \frac{x_1}{x_2}}{T} \tag{B.7}$$

If the value of β, x_1 and x_2 are known, then the initial velocity given in equation B.8 can be estimated, hence, the Impulse.

$$\dot{x}_o = x_1 \frac{2\pi}{T} e^{\frac{\beta T}{4}} \tag{B.8}$$

In this experiment, the value of $\beta = 0.028$. $M = 82.64Kg$, $T = 3.4s$, $Z = 0.21$, $R = 2.92m$, $a = 0.14$.

Appendix C

Input Decks of Simulations

C.1 Input Deck for Cylinder Explosive-Plate simulation in ABAQUS/Explicit 6.4

```
*Heading
    ** Job name: explo Model name: NEW MODEL
    *Preprint, echo=NO, model=NO, history=NO, contact=NO
    **
    ** PARTS
    **
    *Part, name=EXPLOSIVE
    *End Part
    *Part, name=PLATE
    *End Part
    **
    ** ASSEMBLY
    **
    *Assembly, name=Assembly
    **
    *Instance, name=EXPLO-1, part=EXPLO
    0., 2., 0.
    *Node
    1, 0., 0.
    2, 0.05624999, 0.
```

3, 0.1125, 0.
4, 0.16875, 0.
5, 0.225, 0.
6, 0.28125, 0.
7, 0.3375, 0.
8, 0.39375, 0.
9, 0.45, 0.
10, 0.50625, 0.
11, 0.5625, 0.
12, 0.61875, 0.
13, 0.675, 0.
14, 0.73125, 0.
15, 0.7875, 0.
16, 0.84375, 0.
17, 0.9, 0.
18, 0., 0.05283333
19, 0.05625, 0.05283333
20, 0.1125, 0.05283333
21, 0.16875, 0.05283333
22, 0.225, 0.05283333
23, 0.28125, 0.05283333
24, 0.3375, 0.05283333
25, 0.39375, 0.05283333
26, 0.45, 0.05283333
27, 0.50625, 0.05283333
28, 0.5625, 0.05283333
29, 0.61875, 0.05283333
30, 0.675, 0.05283333
31, 0.73125, 0.05283333
32, 0.7875, 0.05283333
33, 0.84375, 0.05283333
34, 0.9, 0.05283333
35, 0., 0.1056667
36, 0.05625, 0.1056667
37, 0.1125, 0.1056667

38, 0.16875, 0.1056667
39, 0.225, 0.1056667
40, 0.28125, 0.1056667
41, 0.3375, 0.1056667
42, 0.39375, 0.1056667
43, 0.45, 0.1056667
44, 0.50625, 0.1056667
45, 0.5625, 0.1056667
46, 0.61875, 0.1056667
47, 0.675, 0.1056667
48, 0.73125, 0.1056667
49, 0.7875, 0.1056667
50, 0.84375, 0.1056667
51, 0.9, 0.1056667
52, 0., 0.1585
53, 0.05625, 0.1585
54, 0.1125, 0.1585
55, 0.16875, 0.1585
56, 0.225, 0.1585
57, 0.28125, 0.1585
58, 0.3375, 0.1585
59, 0.39375, 0.1585
60, 0.45, 0.1585
61, 0.50625, 0.1585
62, 0.5625, 0.1585
63, 0.61875, 0.1585
64, 0.675, 0.1585
65, 0.73125, 0.1585
66, 0.7875, 0.1585
67, 0.84375, 0.1585
68, 0.9, 0.1585
69, 0., 0.2113333
70, 0.05625, 0.2113333
71, 0.1125, 0.2113333
72, 0.16875, 0.2113333

73, 0.225, 0.2113333
74, 0.28125, 0.2113333
75, 0.3375, 0.2113333
76, 0.39375, 0.2113333
77, 0.45, 0.2113333
78, 0.50625, 0.2113333
79, 0.5625, 0.2113333
80, 0.61875, 0.2113333
81, 0.675, 0.2113333
82, 0.73125, 0.2113333
83, 0.7875, 0.2113333
84, 0.84375, 0.2113333
85, 0.9, 0.2113333
86, 0., 0.2641667
87, 0.05625, 0.2641667
88, 0.1125, 0.2641667
89, 0.16875, 0.2641667
90, 0.225, 0.2641667
91, 0.28125, 0.2641667
92, 0.3375, 0.2641667
93, 0.39375, 0.2641667
94, 0.45, 0.2641667
95, 0.50625, 0.2641667
96, 0.5625, 0.2641667
97, 0.61875, 0.2641667
98, 0.675, 0.2641667
99, 0.73125, 0.2641667
100, 0.7875, 0.2641667
101, 0.84375, 0.2641667
102, 0.9, 0.2641667
103, 0., 0.317
104, 0.05625, 0.317
105, 0.1125, 0.317
106, 0.16875, 0.317
107, 0.225, 0.317

108, 0.28125, 0.317
109, 0.3375, 0.317
110, 0.39375, 0.317
111, 0.45, 0.317
112, 0.50625, 0.317
113, 0.5625, 0.317
114, 0.61875, 0.317
115, 0.675, 0.317
116, 0.73125, 0.317
117, 0.7875, 0.317
118, 0.84375, 0.317
119, 0.9, 0.317
120, 0., 0.3698333
121, 0.05625, 0.3698333
122, 0.1125, 0.3698333
123, 0.16875, 0.3698333
124, 0.225, 0.3698333
125, 0.28125, 0.3698333
126, 0.3375, 0.3698333
127, 0.39375, 0.3698333
128, 0.45, 0.3698333
129, 0.50625, 0.3698333
130, 0.5625, 0.3698333
131, 0.61875, 0.3698333
132, 0.675, 0.3698333
133, 0.73125, 0.3698333
134, 0.7875, 0.3698333
135, 0.84375, 0.3698333
136, 0.9, 0.3698333
137, 0., 0.4226667
138, 0.05625, 0.4226667
139, 0.1125, 0.4226667
140, 0.16875, 0.4226667
141, 0.225, 0.4226667
142, 0.28125, 0.4226667

143, 0.3375, 0.4226667
144, 0.39375, 0.4226667
145, 0.45, 0.4226667
146, 0.50625, 0.4226667
147, 0.5625, 0.4226667
148, 0.61875, 0.4226667
149, 0.675, 0.4226667
150, 0.73125, 0.4226667
151, 0.7875, 0.4226667
152, 0.84375, 0.4226667
153, 0.9, 0.4226667
154, 0., 0.4755
155, 0.05625, 0.4755
156, 0.1125, 0.4755
157, 0.16875, 0.4755
158, 0.225, 0.4755
159, 0.28125, 0.4755
160, 0.3375, 0.4755
161, 0.39375, 0.4755
162, 0.45, 0.4755
163, 0.50625, 0.4755
164, 0.5625, 0.4755
165, 0.61875, 0.4755
166, 0.675, 0.4755
167, 0.73125, 0.4755
168, 0.7875, 0.4755
169, 0.84375, 0.4755
170, 0.9, 0.4755
171, 0., 0.5283334
172, 0.05625, 0.5283333
173, 0.1125, 0.5283333
174, 0.16875, 0.5283333
175, 0.225, 0.5283333
176, 0.28125, 0.5283333
177, 0.3375, 0.5283333

178, 0.39375, 0.5283333
179, 0.45, 0.5283333
180, 0.50625, 0.5283333
181, 0.5625, 0.5283333
182, 0.61875, 0.5283333
183, 0.675, 0.5283333
184, 0.73125, 0.5283333
185, 0.7875, 0.5283333
186, 0.84375, 0.5283334
187, 0.9, 0.5283334
188, 0., 0.5811667
189, 0.05624999, 0.5811667
190, 0.1125, 0.5811667
191, 0.16875, 0.5811667
192, 0.225, 0.5811667
193, 0.28125, 0.5811667
194, 0.3375, 0.5811667
195, 0.39375, 0.5811667
196, 0.45, 0.5811667
197, 0.50625, 0.5811667
198, 0.5625, 0.5811667
199, 0.61875, 0.5811667
200, 0.675, 0.5811667
201, 0.73125, 0.5811667
202, 0.7875, 0.5811667
203, 0.84375, 0.5811667
204, 0.9, 0.5811667
205, 0., 0.634
206, 0.05624999, 0.634
207, 0.1125, 0.634
208, 0.16875, 0.634
209, 0.225, 0.634
210, 0.28125, 0.634
211, 0.3375, 0.634
212, 0.39375, 0.634

213, 0.45, 0.634
214, 0.50625, 0.634
215, 0.5625, 0.634
216, 0.61875, 0.634
217, 0.675, 0.634
218, 0.73125, 0.634
219, 0.7875, 0.634
220, 0.84375, 0.634
221, 0.9, 0.634
*Element, type=CAX4R
1, 1, 2, 19, 18
2, 2, 3, 20, 19
3, 3, 4, 21, 20
4, 4, 5, 22, 21
5, 5, 6, 23, 22
6, 6, 7, 24, 23
7, 7, 8, 25, 24
8, 8, 9, 26, 25
9, 9, 10, 27, 26
10, 10, 11, 28, 27
11, 11, 12, 29, 28
12, 12, 13, 30, 29
13, 13, 14, 31, 30
14, 14, 15, 32, 31
15, 15, 16, 33, 32
16, 16, 17, 34, 33
17, 18, 19, 36, 35
18, 19, 20, 37, 36
19, 20, 21, 38, 37
20, 21, 22, 39, 38
21, 22, 23, 40, 39
22, 23, 24, 41, 40
23, 24, 25, 42, 41
24, 25, 26, 43, 42
25, 26, 27, 44, 43

26, 27, 28, 45, 44
27, 28, 29, 46, 45
28, 29, 30, 47, 46
29, 30, 31, 48, 47
30, 31, 32, 49, 48
31, 32, 33, 50, 49
32, 33, 34, 51, 50
33, 35, 36, 53, 52
34, 36, 37, 54, 53
35, 37, 38, 55, 54
36, 38, 39, 56, 55
37, 39, 40, 57, 56
38, 40, 41, 58, 57
39, 41, 42, 59, 58
40, 42, 43, 60, 59
41, 43, 44, 61, 60
42, 44, 45, 62, 61
43, 45, 46, 63, 62
44, 46, 47, 64, 63
45, 47, 48, 65, 64
46, 48, 49, 66, 65
47, 49, 50, 67, 66
48, 50, 51, 68, 67
49, 52, 53, 70, 69
50, 53, 54, 71, 70
51, 54, 55, 72, 71
52, 55, 56, 73, 72
53, 56, 57, 74, 73
54, 57, 58, 75, 74
55, 58, 59, 76, 75
56, 59, 60, 77, 76
57, 60, 61, 78, 77
58, 61, 62, 79, 78
59, 62, 63, 80, 79
60, 63, 64, 81, 80

61, 64, 65, 82, 81
62, 65, 66, 83, 82
63, 66, 67, 84, 83
64, 67, 68, 85, 84
65, 69, 70, 87, 86
66, 70, 71, 88, 87
67, 71, 72, 89, 88
68, 72, 73, 90, 89
69, 73, 74, 91, 90
70, 74, 75, 92, 91
71, 75, 76, 93, 92
72, 76, 77, 94, 93
73, 77, 78, 95, 94
74, 78, 79, 96, 95
75, 79, 80, 97, 96
76, 80, 81, 98, 97
77, 81, 82, 99, 98
78, 82, 83, 100, 99
79, 83, 84, 101, 100
80, 84, 85, 102, 101
81, 86, 87, 104, 103
82, 87, 88, 105, 104
83, 88, 89, 106, 105
84, 89, 90, 107, 106
85, 90, 91, 108, 107
86, 91, 92, 109, 108
87, 92, 93, 110, 109
88, 93, 94, 111, 110
89, 94, 95, 112, 111
90, 95, 96, 113, 112
91, 96, 97, 114, 113
92, 97, 98, 115, 114
93, 98, 99, 116, 115
94, 99, 100, 117, 116
95, 100, 101, 118, 117

96, 101, 102, 119, 118
97, 103, 104, 121, 120
98, 104, 105, 122, 121
99, 105, 106, 123, 122
100, 106, 107, 124, 123
101, 107, 108, 125, 124
102, 108, 109, 126, 125
103, 109, 110, 127, 126
104, 110, 111, 128, 127
105, 111, 112, 129, 128
106, 112, 113, 130, 129
107, 113, 114, 131, 130
108, 114, 115, 132, 131
109, 115, 116, 133, 132
110, 116, 117, 134, 133
111, 117, 118, 135, 134
112, 118, 119, 136, 135
113, 120, 121, 138, 137
114, 121, 122, 139, 138
115, 122, 123, 140, 139
116, 123, 124, 141, 140
117, 124, 125, 142, 141
118, 125, 126, 143, 142
119, 126, 127, 144, 143
120, 127, 128, 145, 144
121, 128, 129, 146, 145
122, 129, 130, 147, 146
123, 130, 131, 148, 147
124, 131, 132, 149, 148
125, 132, 133, 150, 149
126, 133, 134, 151, 150
127, 134, 135, 152, 151
128, 135, 136, 153, 152
129, 137, 138, 155, 154
130, 138, 139, 156, 155

131, 139, 140, 157, 156
132, 140, 141, 158, 157
133, 141, 142, 159, 158
134, 142, 143, 160, 159
135, 143, 144, 161, 160
136, 144, 145, 162, 161
137, 145, 146, 163, 162
138, 146, 147, 164, 163
139, 147, 148, 165, 164
140, 148, 149, 166, 165
141, 149, 150, 167, 166
142, 150, 151, 168, 167
143, 151, 152, 169, 168
144, 152, 153, 170, 169
145, 154, 155, 172, 171
146, 155, 156, 173, 172
147, 156, 157, 174, 173
148, 157, 158, 175, 174
149, 158, 159, 176, 175
150, 159, 160, 177, 176
151, 160, 161, 178, 177
152, 161, 162, 179, 178
153, 162, 163, 180, 179
154, 163, 164, 181, 180
155, 164, 165, 182, 181
156, 165, 166, 183, 182
157, 166, 167, 184, 183
158, 167, 168, 185, 184
159, 168, 169, 186, 185
160, 169, 170, 187, 186
161, 171, 172, 189, 188
162, 172, 173, 190, 189
163, 173, 174, 191, 190
164, 174, 175, 192, 191
165, 175, 176, 193, 192

166, 176, 177, 194, 193
167, 177, 178, 195, 194
168, 178, 179, 196, 195
169, 179, 180, 197, 196
170, 180, 181, 198, 197
171, 181, 182, 199, 198
172, 182, 183, 200, 199
173, 183, 184, 201, 200
174, 184, 185, 202, 201
175, 185, 186, 203, 202
176, 186, 187, 204, 203
177, 188, 189, 206, 205
178, 189, 190, 207, 206
179, 190, 191, 208, 207
180, 191, 192, 209, 208
181, 192, 193, 210, 209
182, 193, 194, 211, 210
183, 194, 195, 212, 211
184, 195, 196, 213, 212
185, 196, 197, 214, 213
186, 197, 198, 215, 214
187, 198, 199, 216, 215
188, 199, 200, 217, 216
189, 200, 201, 218, 217
190, 201, 202, 219, 218
191, 202, 203, 220, 219
192, 203, 204, 221, 220
*Nset, nset=all, generate
1, 221, 1
*Elset, elset=all, generate
1, 192, 1
** Region: (EXPLO:Picked)
*Elset, elset=_PickedSet2, internal, generate
1, 192, 1
** Section: EXPLO

*Solid Section, elset=_PickedSet2, material=EXPLO
1.,
*End Instance
**
*Instance, name=PLATE-1, part=PLATE
*Node
1, 0., 0.
2, 0.07619048, 0.
3, 0.152381, 0.
4, 0.2285714, 0.
5, 0.3047619, 0.
6, 0.3809524, 0.
7, 0.4571429, 0.
8, 0.5333334, 0.
9, 0.6095238, 0.
10, 0.6857143, 0.
11, 0.7619048, 0.
12, 0.8380952, 0.
13, 0.9142857, 0.
14, 0.9904762, 0.
15, 1.066667, 0.
16, 1.142857, 0.
17, 1.219048, 0.
18, 1.295238, 0.
19, 1.371429, 0.
20, 1.447619, 0.
21, 1.52381, 0.
22, 1.6, 0.
23, 1.67619, 0.
24, 1.752381, 0.
25, 1.828571, 0.
26, 1.904762, 0.
27, 1.980952, 0.
28, 2.057143, 0.
29, 2.133333, 0.

30, 2.209524, 0.
31, 2.285714, 0.
32, 2.361905, 0.
33, 2.438095, 0.
34, 2.514286, 0.
35, 2.590476, 0.
36, 2.666667, 0.
37, 2.742857, 0.
38, 2.819048, 0.
39, 2.895238, 0.
40, 2.971429, 0.
41, 3.047619, 0.
42, 3.12381, 0.
43, 3.2, 0.
44, 3.276191, 0.
45, 3.352381, 0.
46, 3.428571, 0.
47, 3.504762, 0.
48, 3.580952, 0.
49, 3.657143, 0.
50, 3.733333, 0.
51, 3.809524, 0.
52, 3.885714, 0.
53, 3.961905, 0.
54, 4.038095, 0.
55, 4.114286, 0.
56, 4.190476, 0.
57, 4.266667, 0.
58, 4.342857, 0.
59, 4.419048, 0.
60, 4.495238, 0.
61, 4.571429, 0.
62, 4.647619, 0.
63, 4.72381, 0.
64, 4.8, 0.

65, 4.92, 0.
66, 5.04, 0.
67, 5.16, 0.
68, 5.28, 0.
69, 5.4, 0.
70, 5.52, 0.
71, 5.64, 0.
72, 5.76, 0.
73, 5.88, 0.
74, 6., 0.
75, 0., 0.04
76, 0.07619048, 0.04
77, 0.152381, 0.04
78, 0.2285714, 0.04
79, 0.3047619, 0.04
80, 0.3809524, 0.04
81, 0.4571429, 0.04
82, 0.5333334, 0.04
83, 0.6095238, 0.04
84, 0.6857143, 0.04
85, 0.7619048, 0.04
86, 0.8380952, 0.04
87, 0.9142857, 0.04
88, 0.9904762, 0.04
89, 1.066667, 0.04
90, 1.142857, 0.04
91, 1.219048, 0.04
92, 1.295238, 0.04
93, 1.371429, 0.04
94, 1.447619, 0.04
95, 1.52381, 0.04
96, 1.6, 0.04
97, 1.67619, 0.04
98, 1.752381, 0.04
99, 1.828571, 0.04

100, 1.904762, 0.04
101, 1.980952, 0.04
102, 2.057143, 0.04
103, 2.133333, 0.04
104, 2.209524, 0.04
105, 2.285714, 0.04
106, 2.361905, 0.04
107, 2.438095, 0.04
108, 2.514286, 0.04
109, 2.590476, 0.04
110, 2.666667, 0.04
111, 2.742857, 0.04
112, 2.819048, 0.04
113, 2.895238, 0.04
114, 2.971429, 0.04
115, 3.047619, 0.04
116, 3.12381, 0.04
117, 3.2, 0.04
118, 3.276191, 0.04
119, 3.352381, 0.04
120, 3.428571, 0.04
121, 3.504762, 0.04
122, 3.580952, 0.04
123, 3.657143, 0.04
124, 3.733333, 0.04
125, 3.809524, 0.04
126, 3.885714, 0.04
127, 3.961905, 0.04
128, 4.038095, 0.04
129, 4.114286, 0.04
130, 4.190476, 0.04
131, 4.266667, 0.04
132, 4.342857, 0.04
133, 4.419048, 0.04
134, 4.495238, 0.04

135, 4.571429, 0.04
136, 4.647619, 0.04
137, 4.72381, 0.04
138, 4.8, 0.04
139, 4.92, 0.04
140, 5.04, 0.04
141, 5.16, 0.04
142, 5.28, 0.04
143, 5.4, 0.04
144, 5.52, 0.04
145, 5.64, 0.04
146, 5.76, 0.04
147, 5.88, 0.04
148, 6., 0.04
149, 0., 0.08
150, 0.07619048, 0.08
151, 0.152381, 0.08
152, 0.2285714, 0.08
153, 0.3047619, 0.08
154, 0.3809524, 0.08
155, 0.4571429, 0.08
156, 0.5333334, 0.08
157, 0.6095238, 0.08
158, 0.6857143, 0.08
159, 0.7619048, 0.08
160, 0.8380952, 0.08
161, 0.9142857, 0.08
162, 0.9904762, 0.08
163, 1.066667, 0.08
164, 1.142857, 0.08
165, 1.219048, 0.08
166, 1.295238, 0.08
167, 1.371429, 0.08
168, 1.447619, 0.08
169, 1.52381, 0.08

170, 1.6, 0.08
171, 1.67619, 0.08
172, 1.752381, 0.08
173, 1.828571, 0.08
174, 1.904762, 0.08
175, 1.980952, 0.08
176, 2.057143, 0.08
177, 2.133333, 0.08
178, 2.209524, 0.08
179, 2.285714, 0.08
180, 2.361905, 0.08
181, 2.438095, 0.08
182, 2.514286, 0.08
183, 2.590476, 0.08
184, 2.666667, 0.08
185, 2.742857, 0.08
186, 2.819048, 0.08
187, 2.895238, 0.08
188, 2.971429, 0.08
189, 3.047619, 0.08
190, 3.12381, 0.08
191, 3.2, 0.08
192, 3.276191, 0.08
193, 3.352381, 0.08
194, 3.428571, 0.08
195, 3.504762, 0.08
196, 3.580952, 0.08
197, 3.657143, 0.08
198, 3.733333, 0.08
199, 3.809524, 0.08
200, 3.885714, 0.08
201, 3.961905, 0.08
202, 4.038095, 0.08
203, 4.114286, 0.08
204, 4.190476, 0.08

205, 4.266667, 0.08
206, 4.342857, 0.08
207, 4.419048, 0.08
208, 4.495238, 0.08
209, 4.571429, 0.08
210, 4.647619, 0.08
211, 4.72381, 0.08
212, 4.8, 0.08
213, 4.92, 0.08
214, 5.04, 0.08
215, 5.16, 0.08
216, 5.28, 0.08
217, 5.4, 0.08
218, 5.52, 0.08
219, 5.64, 0.08
220, 5.76, 0.08
221, 5.88, 0.08
222, 6., 0.08
223, 0., 0.12
224, 0.07619048, 0.12
225, 0.152381, 0.12
226, 0.2285714, 0.12
227, 0.3047619, 0.12
228, 0.3809524, 0.12
229, 0.4571429, 0.12
230, 0.5333334, 0.12
231, 0.6095238, 0.12
232, 0.6857143, 0.12
233, 0.7619048, 0.12
234, 0.8380952, 0.12
235, 0.9142857, 0.12
236, 0.9904762, 0.12
237, 1.066667, 0.12
238, 1.142857, 0.12
239, 1.219048, 0.12

240, 1.295238, 0.12
241, 1.371429, 0.12
242, 1.447619, 0.12
243, 1.52381, 0.12
244, 1.6, 0.12
245, 1.67619, 0.12
246, 1.752381, 0.12
247, 1.828571, 0.12
248, 1.904762, 0.12
249, 1.980952, 0.12
250, 2.057143, 0.12
251, 2.133333, 0.12
252, 2.209524, 0.12
253, 2.285714, 0.12
254, 2.361905, 0.12
255, 2.438095, 0.12
256, 2.514286, 0.12
257, 2.590476, 0.12
258, 2.666667, 0.12
259, 2.742857, 0.12
260, 2.819048, 0.12
261, 2.895238, 0.12
262, 2.971429, 0.12
263, 3.047619, 0.12
264, 3.12381, 0.12
265, 3.2, 0.12
266, 3.276191, 0.12
267, 3.352381, 0.12
268, 3.428571, 0.12
269, 3.504762, 0.12
270, 3.580952, 0.12
271, 3.657143, 0.12
272, 3.733333, 0.12
273, 3.809524, 0.12
274, 3.885714, 0.12

275, 3.961905, 0.12
276, 4.038095, 0.12
277, 4.114286, 0.12
278, 4.190476, 0.12
279, 4.266667, 0.12
280, 4.342857, 0.12
281, 4.419048, 0.12
282, 4.495238, 0.12
283, 4.571429, 0.12
284, 4.647619, 0.12
285, 4.72381, 0.12
286, 4.8, 0.12
287, 4.92, 0.12
288, 5.04, 0.12
289, 5.16, 0.12
290, 5.28, 0.12
291, 5.4, 0.12
292, 5.52, 0.12
293, 5.64, 0.12
294, 5.76, 0.12
295, 5.88, 0.12
296, 6., 0.12
297, 0., 0.16
298, 0.07619048, 0.16
299, 0.152381, 0.16
300, 0.2285714, 0.16
301, 0.3047619, 0.16
302, 0.3809524, 0.16
303, 0.4571429, 0.16
304, 0.5333334, 0.16
305, 0.6095238, 0.16
306, 0.6857143, 0.16
307, 0.7619048, 0.16
308, 0.8380952, 0.16
309, 0.9142857, 0.16

310, 0.9904762, 0.16
311, 1.066667, 0.16
312, 1.142857, 0.16
313, 1.219048, 0.16
314, 1.295238, 0.16
315, 1.371429, 0.16
316, 1.447619, 0.16
317, 1.52381, 0.16
318, 1.6, 0.16
319, 1.67619, 0.16
320, 1.752381, 0.16
321, 1.828571, 0.16
322, 1.904762, 0.16
323, 1.980952, 0.16
324, 2.057143, 0.16
325, 2.133333, 0.16
326, 2.209524, 0.16
327, 2.285714, 0.16
328, 2.361905, 0.16
329, 2.438095, 0.16
330, 2.514286, 0.16
331, 2.590476, 0.16
332, 2.666667, 0.16
333, 2.742857, 0.16
334, 2.819048, 0.16
335, 2.895238, 0.16
336, 2.971429, 0.16
337, 3.047619, 0.16
338, 3.12381, 0.16
339, 3.2, 0.16
340, 3.276191, 0.16
341, 3.352381, 0.16
342, 3.428571, 0.16
343, 3.504762, 0.16
344, 3.580952, 0.16

345, 3.657143, 0.16
346, 3.733333, 0.16
347, 3.809524, 0.16
348, 3.885714, 0.16
349, 3.961905, 0.16
350, 4.038095, 0.16
351, 4.114286, 0.16
352, 4.190476, 0.16
353, 4.266667, 0.16
354, 4.342857, 0.16
355, 4.419048, 0.16
356, 4.495238, 0.16
357, 4.571429, 0.16
358, 4.647619, 0.16
359, 4.72381, 0.16
360, 4.8, 0.16
361, 4.92, 0.16
362, 5.04, 0.16
363, 5.16, 0.16
364, 5.28, 0.16
365, 5.4, 0.16
366, 5.52, 0.16
367, 5.64, 0.16
368, 5.76, 0.16
369, 5.88, 0.16
370, 6., 0.16
*Element, type=CAX4R
1, 1, 2, 76, 75
2, 2, 3, 77, 76
3, 3, 4, 78, 77
4, 4, 5, 79, 78
5, 5, 6, 80, 79
6, 6, 7, 81, 80
7, 7, 8, 82, 81
8, 8, 9, 83, 82

9, 9, 10, 84, 83
10, 10, 11, 85, 84
11, 11, 12, 86, 85
12, 12, 13, 87, 86
13, 13, 14, 88, 87
14, 14, 15, 89, 88
15, 15, 16, 90, 89
16, 16, 17, 91, 90
17, 17, 18, 92, 91
18, 18, 19, 93, 92
19, 19, 20, 94, 93
20, 20, 21, 95, 94
21, 21, 22, 96, 95
22, 22, 23, 97, 96
23, 23, 24, 98, 97
24, 24, 25, 99, 98
25, 25, 26, 100, 99
26, 26, 27, 101, 100
27, 27, 28, 102, 101
28, 28, 29, 103, 102
29, 29, 30, 104, 103
30, 30, 31, 105, 104
31, 31, 32, 106, 105
32, 32, 33, 107, 106
33, 33, 34, 108, 107
34, 34, 35, 109, 108
35, 35, 36, 110, 109
36, 36, 37, 111, 110
37, 37, 38, 112, 111
38, 38, 39, 113, 112
39, 39, 40, 114, 113
40, 40, 41, 115, 114
41, 41, 42, 116, 115
42, 42, 43, 117, 116
43, 43, 44, 118, 117

44, 44, 45, 119, 118
45, 45, 46, 120, 119
46, 46, 47, 121, 120
47, 47, 48, 122, 121
48, 48, 49, 123, 122
49, 49, 50, 124, 123
50, 50, 51, 125, 124
51, 51, 52, 126, 125
52, 52, 53, 127, 126
53, 53, 54, 128, 127
54, 54, 55, 129, 128
55, 55, 56, 130, 129
56, 56, 57, 131, 130
57, 57, 58, 132, 131
58, 58, 59, 133, 132
59, 59, 60, 134, 133
60, 60, 61, 135, 134
61, 61, 62, 136, 135
62, 62, 63, 137, 136
63, 63, 64, 138, 137
64, 64, 65, 139, 138
65, 65, 66, 140, 139
66, 66, 67, 141, 140
67, 67, 68, 142, 141
68, 68, 69, 143, 142
69, 69, 70, 144, 143
70, 70, 71, 145, 144
71, 71, 72, 146, 145
72, 72, 73, 147, 146
73, 73, 74, 148, 147
74, 75, 76, 150, 149
75, 76, 77, 151, 150
76, 77, 78, 152, 151
77, 78, 79, 153, 152
78, 79, 80, 154, 153

79, 80, 81, 155, 154
80, 81, 82, 156, 155
81, 82, 83, 157, 156
82, 83, 84, 158, 157
83, 84, 85, 159, 158
84, 85, 86, 160, 159
85, 86, 87, 161, 160
86, 87, 88, 162, 161
87, 88, 89, 163, 162
88, 89, 90, 164, 163
89, 90, 91, 165, 164
90, 91, 92, 166, 165
91, 92, 93, 167, 166
92, 93, 94, 168, 167
93, 94, 95, 169, 168
94, 95, 96, 170, 169
95, 96, 97, 171, 170
96, 97, 98, 172, 171
97, 98, 99, 173, 172
98, 99, 100, 174, 173
99, 100, 101, 175, 174
100, 101, 102, 176, 175
101, 102, 103, 177, 176
102, 103, 104, 178, 177
103, 104, 105, 179, 178
104, 105, 106, 180, 179
105, 106, 107, 181, 180
106, 107, 108, 182, 181
107, 108, 109, 183, 182
108, 109, 110, 184, 183
109, 110, 111, 185, 184
110, 111, 112, 186, 185
111, 112, 113, 187, 186
112, 113, 114, 188, 187
113, 114, 115, 189, 188

114, 115, 116, 190, 189
115, 116, 117, 191, 190
116, 117, 118, 192, 191
117, 118, 119, 193, 192
118, 119, 120, 194, 193
119, 120, 121, 195, 194
120, 121, 122, 196, 195
121, 122, 123, 197, 196
122, 123, 124, 198, 197
123, 124, 125, 199, 198
124, 125, 126, 200, 199
125, 126, 127, 201, 200
126, 127, 128, 202, 201
127, 128, 129, 203, 202
128, 129, 130, 204, 203
129, 130, 131, 205, 204
130, 131, 132, 206, 205
131, 132, 133, 207, 206
132, 133, 134, 208, 207
133, 134, 135, 209, 208
134, 135, 136, 210, 209
135, 136, 137, 211, 210
136, 137, 138, 212, 211
137, 138, 139, 213, 212
138, 139, 140, 214, 213
139, 140, 141, 215, 214
140, 141, 142, 216, 215
141, 142, 143, 217, 216
142, 143, 144, 218, 217
143, 144, 145, 219, 218
144, 145, 146, 220, 219
145, 146, 147, 221, 220
146, 147, 148, 222, 221
147, 149, 150, 224, 223
148, 150, 151, 225, 224

149, 151, 152, 226, 225
150, 152, 153, 227, 226
151, 153, 154, 228, 227
152, 154, 155, 229, 228
153, 155, 156, 230, 229
154, 156, 157, 231, 230
155, 157, 158, 232, 231
156, 158, 159, 233, 232
157, 159, 160, 234, 233
158, 160, 161, 235, 234
159, 161, 162, 236, 235
160, 162, 163, 237, 236
161, 163, 164, 238, 237
162, 164, 165, 239, 238
163, 165, 166, 240, 239
164, 166, 167, 241, 240
165, 167, 168, 242, 241
166, 168, 169, 243, 242
167, 169, 170, 244, 243
168, 170, 171, 245, 244
169, 171, 172, 246, 245
170, 172, 173, 247, 246
171, 173, 174, 248, 247
172, 174, 175, 249, 248
173, 175, 176, 250, 249
174, 176, 177, 251, 250
175, 177, 178, 252, 251
176, 178, 179, 253, 252
177, 179, 180, 254, 253
178, 180, 181, 255, 254
179, 181, 182, 256, 255
180, 182, 183, 257, 256
181, 183, 184, 258, 257
182, 184, 185, 259, 258
183, 185, 186, 260, 259

184, 186, 187, 261, 260
185, 187, 188, 262, 261
186, 188, 189, 263, 262
187, 189, 190, 264, 263
188, 190, 191, 265, 264
189, 191, 192, 266, 265
190, 192, 193, 267, 266
191, 193, 194, 268, 267
192, 194, 195, 269, 268
193, 195, 196, 270, 269
194, 196, 197, 271, 270
195, 197, 198, 272, 271
196, 198, 199, 273, 272
197, 199, 200, 274, 273
198, 200, 201, 275, 274
199, 201, 202, 276, 275
200, 202, 203, 277, 276
201, 203, 204, 278, 277
202, 204, 205, 279, 278
203, 205, 206, 280, 279
204, 206, 207, 281, 280
205, 207, 208, 282, 281
206, 208, 209, 283, 282
207, 209, 210, 284, 283
208, 210, 211, 285, 284
209, 211, 212, 286, 285
210, 212, 213, 287, 286
211, 213, 214, 288, 287
212, 214, 215, 289, 288
213, 215, 216, 290, 289
214, 216, 217, 291, 290
215, 217, 218, 292, 291
216, 218, 219, 293, 292
217, 219, 220, 294, 293
218, 220, 221, 295, 294

219, 221, 222, 296, 295
220, 223, 224, 298, 297
221, 224, 225, 299, 298
222, 225, 226, 300, 299
223, 226, 227, 301, 300
224, 227, 228, 302, 301
225, 228, 229, 303, 302
226, 229, 230, 304, 303
227, 230, 231, 305, 304
228, 231, 232, 306, 305
229, 232, 233, 307, 306
230, 233, 234, 308, 307
231, 234, 235, 309, 308
232, 235, 236, 310, 309
233, 236, 237, 311, 310
234, 237, 238, 312, 311
235, 238, 239, 313, 312
236, 239, 240, 314, 313
237, 240, 241, 315, 314
238, 241, 242, 316, 315
239, 242, 243, 317, 316
240, 243, 244, 318, 317
241, 244, 245, 319, 318
242, 245, 246, 320, 319
243, 246, 247, 321, 320
244, 247, 248, 322, 321
245, 248, 249, 323, 322
246, 249, 250, 324, 323
247, 250, 251, 325, 324
248, 251, 252, 326, 325
249, 252, 253, 327, 326
250, 253, 254, 328, 327
251, 254, 255, 329, 328
252, 255, 256, 330, 329
253, 256, 257, 331, 330

254, 257, 258, 332, 331
255, 258, 259, 333, 332
256, 259, 260, 334, 333
257, 260, 261, 335, 334
258, 261, 262, 336, 335
259, 262, 263, 337, 336
260, 263, 264, 338, 337
261, 264, 265, 339, 338
262, 265, 266, 340, 339
263, 266, 267, 341, 340
264, 267, 268, 342, 341
265, 268, 269, 343, 342
266, 269, 270, 344, 343
267, 270, 271, 345, 344
268, 271, 272, 346, 345
269, 272, 273, 347, 346
270, 273, 274, 348, 347
271, 274, 275, 349, 348
272, 275, 276, 350, 349
273, 276, 277, 351, 350
274, 277, 278, 352, 351
275, 278, 279, 353, 352
276, 279, 280, 354, 353
277, 280, 281, 355, 354
278, 281, 282, 356, 355
279, 282, 283, 357, 356
280, 283, 284, 358, 357
281, 284, 285, 359, 358
282, 285, 286, 360, 359
283, 286, 287, 361, 360
284, 287, 288, 362, 361
285, 288, 289, 363, 362
286, 289, 290, 364, 363
287, 290, 291, 365, 364
288, 291, 292, 366, 365

289, 292, 293, 367, 366
290, 293, 294, 368, 367
291, 294, 295, 369, 368
292, 295, 296, 370, 369
*Nset, nset=REACTION
64, 65, 66, 67, 68, 69, 70, 71, 72, 73, 74, 148, 222, 296, 365, 366
367, 368, 369, 370
*Elset, elset=REACTION
64, 65, 66, 67, 68, 69, 70, 71, 72, 73, 146, 219, 288, 289, 290, 291
292,
** Region: (PLATE:Picked)
*Elset, elset=_PickedSet7, internal, generate
1, 292, 1
** Section: PLATE
*Solid Section, elset=_PickedSet7, material=PLATE
1.,
*End Instance
*Nset, nset=reaction, instance=PLATE-1
64, 65, 66, 67, 68, 69, 70, 71, 72, 73, 74, 148, 222, 296, 370
*Elset, elset=reaction, instance=PLATE-1
64, 65, 66, 67, 68, 69, 70, 71, 72, 73, 146, 219, 292
*Nset, nset=reaction2, instance=PLATE-1, generate
64, 74, 1
*Elset, elset=reaction2, instance=PLATE-1, generate
64, 73, 1
*Nset, nset=reaction3, instance=PLATE-1, generate
297, 370, 1
*Elset, elset=reaction3, instance=PLATE-1, generate
220, 292, 1
*Nset, nset=_PickedSet42, internal, instance=PLATE-1
64, 65, 66, 67, 68, 69, 70, 71, 72, 73, 74, 148, 222, 296, 365, 366
367, 368, 369, 370
*Elset, elset=_PickedSet42, internal, instance=PLATE-1
64, 65, 66, 67, 68, 69, 70, 71, 72, 73, 146, 219, 288, 289, 290, 291
292,

```
*Nset, nset=_PickedSet43, internal, instance=PLATE-1, generate
1, 297, 74
*Elset, elset=_PickedSet43, internal, instance=PLATE-1, generate
1, 220, 73
*Nset, nset=_PickedSet44, internal, instance=EXPLO-1, generate
1, 205, 17
*Elset, elset=_PickedSet44, internal, instance=EXPLO-1, generate
1, 177, 16
*Nset, nset=_PickedSet45, internal, instance=EXPLO-1, generate
1, 221, 1
*Elset, elset=_PickedSet45, internal, instance=EXPLO-1, generate
1, 192, 1
*Nset, nset=_PickedSet46, internal, instance=PLATE-1, generate
1, 370, 1
*Elset, elset=_PickedSet46, internal, instance=PLATE-1, generate
1, 292, 1
*Elset, elset=__PickedSurf34_S1, internal, instance=EXPLO-1, generate
1, 16, 1
*Elset, elset=__PickedSurf34_S2, internal, instance=EXPLO-1, generate
16, 192, 16
*Surface, type=ELEMENT, name=_PickedSurf34, internal
__PickedSurf34_S1, S1
__PickedSurf34_S2, S2
*Elset, elset=__PickedSurf35_S3, internal, instance=PLATE-1, generate
220, 292, 1
*Surface, type=ELEMENT, name=_PickedSurf35, internal
__PickedSurf35_S3, S3
*End Assembly
**
** MATERIALS
**
*Material, name=EXPLOSIVE
*Density
1.6,
*Eos, type=JWL
```

```
0.819, 6.0977, 0.1295, 0.25, 4.5, 1.4, , 0.
*DetonationPoint
0., 2.987, 0., 0.
*Material, name=PLATE
*Density
7.846,
*Elastic
2.1, 0.3
*Inelastic Heat Fraction
0.9,
*Plastic, hardening=JOHNSON COOK
0.0023, 0.0032857, 0.5603, 0.55, 1811., 300.
*Rate Dependent, type=JOHNSON COOK
0.022,1.
*Specific Heat
0.000452,
**
** INTERACTION PROPERTIES
**
*Surface Interaction, name=IntProp-1
*Friction
0.,
*Surface Behavior, pressure-overclosure=HARD
*Surface Interaction, name=IntProp-2
*Surface Behavior, pressure-overclosure=HARD
**
** BOUNDARY CONDITIONS
**
** Name: BC-1 Type: Symmetry/Antisymmetry/Encastre
*Boundary
_PickedSet42, ENCASTRE
** Name: BC-2 Type: Symmetry/Antisymmetry/Encastre
*Boundary
_PickedSet43, XSYMM
** Name: BC-3 Type: Symmetry/Antisymmetry/Encastre
```

```
*Boundary
_PickedSet44, XSYMM
**
** FIELDS
**
** Name: Field-1 Type: Temperature
*Initial Conditions, type=TEMPERATURE
_PickedSet46, 300.
*Initial Conditions, type=SPECIFIC ENERGY
EXPLO-1.all, 0.09
** ----------------------------------------------------------------
**
** STEP: Step-1
**
*Step, name=Step-1
*Dynamic, Explicit, adiabatic
, 2.
*Bulk Viscosity
0.06, 1.2
**
** INTERACTIONS
**
** Interaction: Int-1
*Contact Pair, interaction=IntProp-1, mechanical constraint=KINEMATIC,
weight=0.4, cpset=Int-1
_PickedSurf35, _PickedSurf34
**
** OUTPUT REQUESTS
**
*Restart, write, number interval=1, time marks=NO
**
** FIELD OUTPUT: F-Output-1
**
*Output, field, number intervals=200
*Node Output
```

```
A, RF, U, V
*Element Output
LE, PE, PEEQ, S, TEMP, TSHR
*Contact Output
CSTRESS,
*Output, history, frequency=0
*End Step
** ----------------------------------------------------------------
**
** STEP: Step-2
**
*Step, name=Step-2
*Dynamic, Explicit, adiabatic
, 65.
*Bulk Viscosity
0.06, 1.2
**
** OUTPUT REQUESTS
**
*Restart, write, number interval=1, time marks=NO
**
** FIELD OUTPUT: F-Output-1
**
*Output, field, number intervals=200
*Node Output
A, RF, U, V
*Element Output
LE, PE, PEEQ, S, TEMP, TSHR
*Contact Output
CSTRESS,
*Output, history, frequency=0
*End Step
** ----------------------------------------------------------------
**
** STEP: Step-3
```

```
**
*Step, name=Step-3
*Dynamic, Explicit, adiabatic
, 1000.
*Bulk Viscosity
0.06, 1.2
**
** BOUNDARY CONDITIONS
**
** Name: BC-4 Type: Symmetry/Antisymmetry/Encastre
*Boundary
_PickedSet45, ENCASTRE
**
** OUTPUT REQUESTS
**
*Restart, write, number interval=1, time marks=NO
**
** FIELD OUTPUT: F-Output-1
**
*Output, field, number intervals=200
*Node Output
A, RF, U, V
*Element Output
LE, PE, PEEQ, S, TEMP, TSHR
*Contact Output
CSTRESS,
*Output, history, frequency=0
*End Step
```